

Particle Deposition Behavior from Coal-Derived Syngas in Gas
Turbines at Modern Turbine Inlet Temperatures

Robert Laycock

A dissertation submitted to the faculty of
Brigham Young University
in partial fulfillment of the requirements for the degree of

Doctor of Philosophy

Thomas H. Fletcher, Chair
Larry L. Baxter
Jeffrey P. Bons
Morris D. Argyle
David O. Lignell

Department of Chemical Engineering
Brigham Young University

Copyright © 2017 Robert Laycock

All Rights Reserved

ABSTRACT

Particle Deposition Behavior from Coal-Derived Syngas in Gas Turbines at Modern Turbine Inlet Temperatures

Robert Laycock

Department of Chemical Engineering, BYU

Doctor of Philosophy

Certain types of fuel used for combustion in land-based gas turbines can contain traces of ash when introduced into a gas turbine. Examples include synfuel, from the gasification of coal, and heavy fuel oil. When these ash particles travel through the hot gas path of the gas turbine they can deposit on turbine vanes and blades. As deposits grow, they can reduce turbine efficiency and damage turbine hardware. As turbine inlet temperatures increase, ash deposition rates increase as well.

Experiments were conducted in the Turbine Accelerated Deposition Facility (TADF) at Brigham Young University to better understand ash deposition behavior at modern turbine inlet temperatures. Experiments were conducted that varied deposition duration, gas temperature, surface temperature, ash type and characteristics, and film-cooling blowing ratio. Analysis included measuring and calculating the capture efficiency, deposit surface roughness, deposit density, and deposit surface temperature. Test results indicate that capture efficiency increases with time and as the gas temperature increases. Previous studies have shown that the capture efficiency increases with increasing surface temperature as well, but the results from this study show that at a gas temperature of 1400°C, the capture efficiency of the ash used in these tests initially increased but then began to decrease with increasing surface temperature. It was also shown that different ashes, with differing ash chemistries and densities, deposit at very different rates and produce different surface structures. The film-cooling tests showed that film cooling does reduce the capture efficiency at modern turbine temperatures, but has a smaller relative effect than at lower temperatures. Tests performed with heavy fuel oil ash and increased SO₂ levels (similar to those found in heavy fuel oil combustion environments) indicate that the increased sulfur levels result in the formation of more sulfur compounds in the deposit and change which elements are dissolved by water, but has little effect on the amount of deposit that dissolves.

CFD simulations were performed to model the fluid dynamics and particle trajectories in the TADF. The resulting particle impact data (particle impact velocity, temperature, diameter, etc.) were used in sticking models to evaluate the models' performance at high temperatures. Results indicate that while the models can be fit fairly well to specific data, they need to be able to better account for changing surface conditions and high temperature particle behavior to accurately model deposition at high temperatures.

Keywords: coal, ash, deposition, turbines, IGCC, HFO, film cooling, high temperature

ACKNOWLEDGEMENTS

I would like to thank all those who have helped me along my path to completing this work and achieving what I have. In particular I would like to thank my advisor, Dr. Thomas Fletcher, for his support (intellectual, spiritual and financial), guidance and patience throughout this process. I would also like to thank the other members of my graduate committee (Dr. Jeffrey Bons, Dr. Larry Baxter, Dr. David Lignell, and Dr. Morris Argyle) for their insights and encouragement along the way. It would also be a mistake to overlook the assistance of the Chemical Engineering Department secretaries, Serena Jacobson, Arlene Cleverley and formerly Linda Bosley. They keep the department and projects running and no student would graduate without their help and the work they perform.

Kevin Cole provided invaluable help in providing access to machinery and equipment and all sorts of technical support. Ken Forster provided assistance in manufacturing, repairing, and altering equipment and materials used for this research and provided valuable design insight.

Several undergraduate students worked on this project and contributed valuable help in performing experiments, analyzing data, researching methods and materials, and creating solutions to various problems we faced. These individuals include Spencer Harding, Devin Rappleye, Jonathan Gallacher, Daniel Parker, McKaye Dennis, Matt Sharp, Sam Nielsen, Ben Olvera and Ryan Gillis. I am grateful for their help and for the friendships that were developed in the process. I am also grateful for the friendships that I have developed with various graduate students with whom I have interacted over the years.

I would also like to thank my Heavenly Father for the many blessings that I have received from him and the miracles that I have seen in my life that have helped me in all aspects of my life, including the ability to finish this work.

Finally, I would like to thank my wife, Katie, for all of the love and support that she has given me as I have finished this project. She has been by my side for only a fraction of the time that I have been in the program, but she has been a major driving force in my efforts to finish. She helped me to stay on task and I would not have gotten to this point without her. I love her and am forever grateful for her love, guidance and support.

This project was funded in part by the U.S. Department of Energy under Award No. DE-NT0005055 and by the General Electric Corporation. The views expressed in this dissertation are those of the author and do not reflect the official policy or position of the Department of Energy, the U.S. Government or the General Electric Corporation.

TABLE OF CONTENTS

| | |
|---|------|
| LIST OF TABLES | xi |
| LIST OF FIGURES | xiii |
| NOMENCLATURE | xix |
| 1 Introduction | 1 |
| 1.1 Objective | 3 |
| 2 Literature Review | 5 |
| 2.1 Accelerated Deposition | 5 |
| 2.2 Temperature Effects on Deposition..... | 6 |
| 2.3 Particle Size Effects | 13 |
| 2.4 Ash Chemistry Effects | 14 |
| 2.5 High Temperature Strategies..... | 16 |
| 2.5.1 Thermal Barrier Coatings (TBC)..... | 16 |
| 2.5.2 Film Cooling..... | 17 |
| 2.5.3 Effects of Deposits on Heat Transfer..... | 19 |
| 2.6 Transient Deposition | 22 |
| 2.7 Modeling | 22 |
| 2.7.1 Critical Velocity Model | 24 |
| 2.7.2 Critical Viscosity Model..... | 26 |
| 2.7.3 Elasto-Plastic Model..... | 28 |
| 2.7.4 Non-Spherical Model..... | 28 |
| 2.8 Summary | 30 |
| 3 Description of Experimental Facilities | 33 |
| 3.1 Deposition Facility | 33 |
| 3.2 Upgrades..... | 36 |
| 3.2.1 Holder | 37 |
| 3.2.2 Acceleration Cone and Equilibration Tube..... | 38 |
| 3.3 Coupons..... | 39 |
| 3.4 Ash Properties and Preparation | 40 |
| 3.5 Particle Feeding System | 45 |
| 3.6 Temperature Measurement..... | 47 |
| 3.7 Deposit Analysis | 53 |

| | | |
|---------|--|-----|
| 3.7.1 | Capture Efficiency | 53 |
| 3.7.2 | Surface Roughness, Deposit Thickness and Deposit Density | 57 |
| 4 | Comparison with the Original Facility | 59 |
| 4.1 | Test Conditions | 59 |
| 4.2 | Results and Discussion..... | 59 |
| 4.3 | Summary and Conclusions..... | 63 |
| 5 | Transient Characteristics | 65 |
| 5.1 | Test Conditions | 65 |
| 5.2 | Analysis..... | 67 |
| 5.3 | Results and Discussion..... | 68 |
| 5.3.1 | Surface Temperature..... | 68 |
| 5.3.2 | Capture Efficiency | 70 |
| 5.3.3 | Deposit Thickness..... | 72 |
| 5.3.4 | Deposit Roughness and Density | 73 |
| 5.3.5 | Ash Viscosity and Sticking Probability | 76 |
| 5.4 | Summary and Conclusions..... | 80 |
| 6 | Temperature-Dependent Characteristics | 83 |
| 6.1 | Test Conditions | 83 |
| 6.2 | Analysis..... | 85 |
| 6.3 | Results and Discussion..... | 86 |
| 6.3.1 | Constant $T_{s,i}$ Series..... | 87 |
| 6.3.1.1 | Capture Efficiency..... | 87 |
| 6.3.1.2 | Surface Roughness and Density..... | 88 |
| 6.3.1.1 | Surface Temperature | 90 |
| 6.3.1.2 | Physical Structure and Appearance..... | 93 |
| 6.3.2 | Constant T_g Series..... | 94 |
| 6.3.2.1 | Capture Efficiency..... | 94 |
| 6.3.2.1 | Surface Roughness and Density..... | 95 |
| 6.3.2.2 | Physical Structure and Appearance..... | 97 |
| 6.3.3 | Equilibration Tube Capture Efficiency..... | 97 |
| 6.4 | Summary and Conclusions..... | 100 |
| 7 | Ash-Dependent Characteristics | 103 |
| 7.1 | Test Conditions | 103 |

| | | |
|----------|---|-----|
| 7.2 | Analysis..... | 103 |
| 7.3 | Results and Discussion..... | 104 |
| 7.3.1 | Capture Efficiency | 104 |
| 7.3.2 | Surface Roughness and Density..... | 106 |
| 7.3.3 | Surface Temperature..... | 110 |
| 7.3.4 | Physical Structure and Appearance | 114 |
| 7.4 | Summary and Conclusions..... | 115 |
| 8 | Heavy Fuel Oil..... | 117 |
| 8.1 | Test Conditions | 117 |
| 8.2 | Analysis..... | 120 |
| 8.3 | Results and Discussion..... | 123 |
| 8.3.1 | Mass Loss..... | 123 |
| 8.3.2 | Capture Efficiency | 124 |
| 8.3.3 | Surface Roughness..... | 127 |
| 8.3.4 | Chemical Composition..... | 128 |
| 8.3.1 | Surface Temperature..... | 132 |
| 8.4 | Summary and Conclusions..... | 133 |
| 9 | Film-Cooling Characteristics..... | 135 |
| 9.1 | Test Conditions | 135 |
| 9.2 | Analysis..... | 136 |
| 9.3 | Results and Discussion..... | 136 |
| 9.3.1 | Capture Efficiency | 137 |
| 9.3.2 | Surface Roughness and Density..... | 141 |
| 9.3.1 | Surface Temperature..... | 142 |
| 9.3.2 | Physical Structure and Appearance | 144 |
| 9.4 | Summary and Conclusions..... | 144 |
| 10 | Deposition Modeling | 147 |
| 10.1 | Computational Setup..... | 147 |
| 10.1.1 | Gas Phase Simulation | 148 |
| 10.1.1.1 | Mesh Refinement | 148 |
| 10.1.1.1 | Temperature Cases | 151 |
| 10.1.2 | Particle Phase Simulation | 151 |
| 10.1.1 | Sticking and Detachment Models..... | 155 |

| | | |
|------------|--|-----|
| 10.1.1.1 | Critical Velocity Model..... | 156 |
| 10.1.1.2 | Non-Spherical Model..... | 157 |
| 10.1.2 | Determination of Final Capture Efficiency..... | 158 |
| 10.2 | Results and Discussion..... | 159 |
| 10.2.1 | Critical Velocity Model..... | 159 |
| 10.2.2 | Non-Spherical Model..... | 167 |
| 10.3 | Summary and Conclusions..... | 173 |
| 11 | Summary and Conclusions..... | 175 |
| 11.1 | Transient Characteristics..... | 176 |
| 11.2 | Temperature-Dependent Characteristics..... | 176 |
| 11.3 | Ash-Dependent Characteristics..... | 177 |
| 11.4 | Heavy Fuel Oil Characteristics..... | 178 |
| 11.5 | Film-Cooling Characteristics..... | 179 |
| 11.6 | Deposition Modeling..... | 180 |
| 11.7 | Recommendations for Future Work..... | 180 |
| References | | 183 |
| Appendix A | Test Data..... | 191 |
| A.1 | Verification Test Series..... | 191 |
| A.2 | Transient Test Series..... | 192 |
| A.3 | Constant $T_{s,i}$ Test Series..... | 194 |
| A.4 | Constant T_g Test Series..... | 196 |
| A.5 | Various Coal Ashes Test Series..... | 198 |
| A.6 | Heavy Fuel Oil Test Series..... | 200 |
| A.7 | Film-Cooling Test Series..... | 201 |
| Appendix B | Additional Figures..... | 203 |
| B.1 | Particle Size Distributions..... | 203 |
| B.2 | Deposit Photos..... | 205 |
| Appendix C | Temperature Measurement..... | 213 |
| C.1 | Thermocouple Radiation Correction..... | 213 |
| C.2 | RGB Camera Calibration..... | 217 |
| C.2.1 | First Calibration (2-Color, Red/Blue)..... | 217 |
| C.2.2 | Second Calibration (2-Color, Red/Green)..... | 220 |
| C.2.3 | Third Calibration (1-Color, Red)..... | 223 |

| | | |
|------------|--|-----|
| Appendix D | Deposition Model Codes..... | 229 |
| D.1 | Importing Data and Calling Models..... | 229 |
| D.2 | Critical Velocity Model..... | 231 |
| D.3 | Non-Spherical Model..... | 237 |

LIST OF TABLES

| | |
|--|-----|
| Table 2-1: Recent ash deposition studies..... | 7 |
| Table 3-1: Chemical composition and physical characteristics of the various ash samples..... | 42 |
| Table 5-1: Summary of test conditions for the transient test series..... | 66 |
| Table 6-1: Test conditions and data for the test series varying T_g | 84 |
| Table 6-2: Test conditions and data for the test series varying $T_{s,i}$ | 85 |
| Table 6-3: Dependence of the increase in average surface temperature on gas temperature | 92 |
| Table 7-1: Summary of test conditions using various types of coal ash..... | 104 |
| Table 7-2: Averages of the capture efficiency, mass of deposit, and change in surface temperature recorded for each type of ash | 112 |
| Table 7-3: Average values of L for the deposits of the various ash samples, including the sample standard deviation of L | 113 |
| Table 8-1: HFO ash test conditions | 118 |
| Table 8-2: Calculated equilibrium and outlet SO_3 mol% over the range of planned gas temperatures | 119 |
| Table 8-3: Summary of the conditions of the tests used to develop the kinetic model (Burdett et al., 1984) and the conditions in the TADF to which the kinetic model was applied | 121 |
| Table 9-1: Summary of test conditions for the film-cooling series | 136 |
| Table 9-2: Average $T_{s,i}$ at each blowing ratio (M)..... | 141 |
| Table 9-3: Average final surface temperature ($T_{s,f}$) at each blowing ratio, including standard error on the mean | 143 |
| Table 10-1: Boundary conditions for the gas phase CFD simulation..... | 149 |
| Table 10-2: Cell count in each of the grids used in the grid study | 150 |
| Table 10-3: Temperature cases for the gas-phase simulations | 153 |
| Table 10-4: Average particle injection temperature and velocity for each temperature case..... | 154 |
| Table 10-5: Impact efficiency of particles with different particle sizes and at different quantities of particle trajectories | 155 |
| Table 10-6: SSE values for the results from the critical velocity model for the constant $T_{s,i}$, constant T_g , and transient test series using both Young's modulus fits..... | 161 |
| Table 10-7: SSE values for the results from the non-spherical model for the constant $T_{s,i}$, constant T_g , and transient test series using both Young's modulus fits..... | 170 |
| Table A-1: Deposition data for the verification test series | 191 |
| Table A-2: Temperature data for the verification test series | 192 |
| Table A-3: Deposition data for the transient test series..... | 192 |
| Table A-4: Temperature data for the transient test series | 193 |
| Table A-5: Surface scan data for the transient test series | 193 |
| Table A-6: Deposition data for the constant $T_{s,i}$ test series | 194 |
| Table A-7: Temperature data for the constant $T_{s,i}$ test series..... | 195 |
| Table A-8: Surface scan data for the constant $T_{s,i}$ test series..... | 195 |
| Table A-9: Deposition data for the constant T_g test series..... | 196 |

| | |
|--|-----|
| Table A-10: Temperature data for the constant T_g test series..... | 197 |
| Table A-11: Surface scan data for the constant T_g test series..... | 198 |
| Table A-12: Deposition data for the various coal ash type test series | 198 |
| Table A-13: Temperature data for the various coal ash type test series | 199 |
| Table A-14: Surface scan data for the various coal ash type test series | 199 |
| Table A-15: Deposition data for the HFO test series..... | 200 |
| Table A-16: Temperature data for the HFO test series..... | 200 |
| Table A-17: Surface scan data for the HFO test series..... | 201 |
| Table A-18: Deposition data for the film-cooling test series..... | 201 |
| Table A-19: Temperature data for the film-cooling test series..... | 202 |
| Table A-20: Surface scan data for the film-cooling test series..... | 202 |
| Table C-1: Radiation view factors from the thermocouple to the other visible surfaces. The temperature of each surface is also provided | 214 |
| Table C-2: Values of c and m for Eq. (C-8), based on the value of Re | 216 |
| Table C-3: Approximate mass flows of air, natural gas and sulfur dioxide for each desired gas temperature..... | 217 |
| Table C-4: Temperatures calculated using the three combinations of color signal, plus the sensitivity constants for each color..... | 220 |
| Table C-5: S_R table used for the single-color calibration | 224 |
| Table C-6: Coupon temperature measured by an IR thermometer | 226 |
| Table C-7: Coupon temperature calculated from RGB images | 226 |

LIST OF FIGURES

| | |
|--|----|
| Figure 2-1: Capture efficiency with respect to particle diameter at various gas temperatures, adapted from Ai and Fletcher (2011). | 15 |
| Figure 3-1: Schematic of the TADF at BYU. | 34 |
| Figure 3-2: Radial temperature profile across the exit of the equilibration tube as measured by and adapted from Crosby (2007). The thermocouple traversed the tube in the $-r/R$ direction. | 36 |
| Figure 3-3: Redesigned coupon holder. | 37 |
| Figure 3-4: SiO ₂ faceplate protecting the redesigned coupon holder from high gas temperatures. | 37 |
| Figure 3-5: One-piece SiC cone and tube configuration and 2-piece SiC cone and quartz tube configuration. | 39 |
| Figure 3-6: Coupon dimensions showing film-cooling holes. | 40 |
| Figure 3-7: Particle size distribution of the JB2 ash. | 43 |
| Figure 3-8: Picture of the particle feeding system. | 46 |
| Figure 3-9: Graphs displaying the results from the process used to filter the periodic T_g measurements. The T_g data shown here is from test G3. | 49 |
| Figure 3-10: Example, from test F4, of potentially valid data being filtered out from the T_g measurements. | 50 |
| Figure 3-11: RGB camera setup for obtaining coupon and deposit surface temperatures via optical pyrometry. | 52 |
| Figure 3-12: Temperature map of test G8 (which will be discussed in Chapter 6) and the spatially-averaged temperature ($T_s = 1109^\circ\text{C}$). | 54 |
| Figure 3-13: (a) Representation of the projected area of the coupon to the area of the equilibration tube outlet, with the shading indicating the distance of the coupon from the tube outlet (darker = closer). (b) Coupon and faceplate before any deposition occurred. (c) Coupon and faceplate after deposition. The circle represents the coupon area. Only ash deposited within this circle was included in m_{dep} | 56 |
| Figure 3-14: CFD results of particle impact efficiency vs. particle size at varying gas temperatures in the TADF. | 57 |
| Figure 3-15: (a) 3D surface map of the scan of test T3. (b) Side view of the surface scan. (c) Area used to determine R_a for test T3. | 58 |
| Figure 4-1: Screen captures from the video of test S1. A large deposit can be seen to first form at the edge of the faceplate and then advance onto the coupon. | 60 |
| Figure 4-2: Comparison of adjusted capture efficiencies obtained from tests on the upgraded (new) TADF and the previous (old) TADF. | 62 |
| Figure 5-1: Surface temperature maps, at 10 minute increments for test T3 ($T_g = 1302^\circ\text{C}$, $\text{MMD} = 14 \mu\text{m}$). | 68 |
| Figure 5-2: Increase of spatially-averaged coupon surface temperature with respect to time. | 69 |
| Figure 5-3: T_g and T_s measurements over time for test T3 ($\text{MMD} = 14 \mu\text{m}$) and tests T8 and T9 ($\text{MMD} = \mu\text{m}$). | 70 |

| | |
|---|----|
| Figure 5-4: Time-dependent growth of capture efficiency. 95% confidence band is shown for the 14 μm fit..... | 71 |
| Figure 5-5: Deposit thickness growth with respect to time. 95% confidence band is shown for the 14 μm fit..... | 73 |
| Figure 5-6: Average surface roughness (R_a) development over time. The 95% confidence band is shown for the 14 μm fit and is extrapolated to $t = 0$ | 74 |
| Figure 5-7: Deposit bulk density vs. time..... | 75 |
| Figure 5-8: Histogram of particle temperatures (T_p) obtained from CFD simulations as the particles impact the coupon. The dotted black line indicates the softening temperature of the JB2 ash and the numbers in parentheses indicate the number of particles that impacted the coupon..... | 77 |
| Figure 5-9: Change in average P_s of the surface ash with time. | 78 |
| Figure 5-10: Change in the maximum P_s of the surface ash with time..... | 79 |
| Figure 5-11: Change in the minimum P_s of the surface ash with time. | 79 |
| Figure 5-12: Distribution of sticking probability for pixels over the observed face of the coupon as a function of time. | 81 |
| Figure 6-1: Capture efficiency vs. mass of ash delivered for T_g close to 1300°C. The corresponding $T_{s,i}$ for each test are also shown. | 87 |
| Figure 6-2: Variation in capture efficiency with respect to gas temperature. The red squares represent tests that had a similar m_{del} (G3, G6, G8, and G9). The blue circles represent the rest of the tests included from Table 6-1. | 88 |
| Figure 6-3: Average surface roughness with respect to gas temperature. The red squares represent tests that had a similar m_{del} (G3, G6, G8, and G9). The blue circles represent the rest of the tests included from Table 6-1. | 89 |
| Figure 6-4: Deposit bulk density with respect to gas temperature. The red squares represent tests that had a similar m_{del} (G3, G6, G8, and G9). The blue circles represent the rest of the tests included from Table 6-1. | 89 |
| Figure 6-5: ESEM images of deposits from test G3 ($T_g = 1261^\circ\text{C}$). (a) Outer surface and (b) cross-section..... | 91 |
| Figure 6-6: ESEM images of deposits from test G8 ($T_g = 1413^\circ\text{C}$). (a) Outer surface and (b) cross-section..... | 91 |
| Figure 6-7: Increase in average surface temperature with respect to time for tests G3 ($T_g = 1261^\circ\text{C}$), G6 ($T_g = 1311^\circ\text{C}$), G8 ($T_g = 1413^\circ\text{C}$), and G9 ($T_g = 1361^\circ\text{C}$). | 92 |
| Figure 6-8: Surface temperature profiles measured during test G8 ($T_g = 1413^\circ\text{C}$). | 92 |
| Figure 6-9: Photos of ash deposits collected from tests G3, G6, G9, and G8 respectively. The arrows indicate the direction of the gas flow during deposition. | 93 |
| Figure 6-10: Capture efficiency versus initial surface temperature of the coupon..... | 95 |
| Figure 6-11: Deposit detachment during test S2 ($T_g = 1402^\circ\text{C}$, $T_{s,i} = 899^\circ\text{C}$), (a) before detachment occurs and (b) after detachment occurs. The arrows indicate the locations where the detachment occurs..... | 96 |
| Figure 6-12: Surface roughness versus initial surface temperature of the coupon. | 96 |
| Figure 6-13: Deposit density versus initial surface temperature of the coupon. | 97 |
| Figure 6-14: Photos of ash deposits collected from tests S4, S3, S6, and S14 respectively..... | 98 |

| | |
|---|-----|
| Figure 6-15: Equilibration tube capture efficiency data. | 99 |
| Figure 7-1: Capture efficiency vs. gas temperature for 5 different coal ash samples..... | 105 |
| Figure 7-2: Capture efficiency vs. ash apparent density for 5 different coal ash samples. | 106 |
| Figure 7-3: Surface roughness vs. gas temperature for 4 different coal ash samples..... | 107 |
| Figure 7-4: Surface roughness vs. ash apparent density for 4 different coal ash samples..... | 107 |
| Figure 7-5: Cross-sectional view of deposits from tests using ash from various coal types. The arrows indicate the direction of gas flow as it approaches the coupon and deposit..... | 108 |
| Figure 7-6: Deposit density vs. gas temperature for 4 different coal ash samples. | 109 |
| Figure 7-7: Deposit density vs. ash apparent density for 4 different coal ash samples. | 109 |
| Figure 7-8: Ratio of deposit density to ash apparent density vs. ash apparent density for 4 different coal ash samples. | 110 |
| Figure 7-9: Spatially-averaged surface temperature vs. time for various coal ash deposits with (a) $T_{s,i} \sim 1100^{\circ}\text{C}$ and (b) $T_{s,i} \sim 1000^{\circ}\text{C}$ | 111 |
| Figure 7-10: Photographs of deposits formed from the four ashes used in this test series plus a deposit formed from the JB2 ash for comparison. The red square in the JB2 image outlines the area shown in the JB2 – zoomed image. | 114 |
| Figure 8-1: Location of markings for scan locations on the HFO ash deposits..... | 122 |
| Figure 8-2: Mass loss after washing the HFO flyash deposits. The error bars represent the propagated measurement uncertainty from the mass balances used to weigh the coupons..... | 124 |
| Figure 8-3: Capture efficiency vs. T_g from the HFO tests. The error bars represent the propagated measurement uncertainty from the mass balances used to weigh the coupons. Data from Crosby et al. (2008) is also included for comparison. | 125 |
| Figure 8-4: Initial surface temperature versus gas temperature for the HFO test series..... | 126 |
| Figure 8-5: Average % ash release after baking the HFO ash samples. The error bars represent the standard error of the mean. | 127 |
| Figure 8-6: Average surface roughness (pre-wash and post-wash) data for the HFO deposits. Error bars show the standard error of the mean. | 128 |
| Figure 8-7: wt% of sulfur and magnesium in the HFO deposits with respect to T_g | 130 |
| Figure 8-8: wt% of potassium and calcium in the HFO deposits with respect to T_g | 130 |
| Figure 8-9: Relative change in wt% of Mg, K, and Ca as a function of the pre-wash wt% of S. | 131 |
| Figure 8-10: Average surface temperature of the HFO ash deposits during the deposit tests.... | 132 |
| Figure 9-1: Capture efficiency vs. blowing ratio (M) and density ratio for the film-cooling test series. | 137 |
| Figure 9-2: Momentum flux ratio (I) vs. blowing ratio (M) for the film-cooling test series..... | 139 |
| Figure 9-3: Particle size distributions of the ground JB1 and JB2 ash samples. | 140 |
| Figure 9-4: The effect of $T_{s,i}$ on capture efficiency during the film-cooling and constant T_g tests series..... | 142 |
| Figure 9-5: Surface roughness and density of deposits formed at $M = 0.5 - 2.1$ | 142 |
| Figure 9-6: Average surface temperature (T_s) vs. deposition time. | 143 |
| Figure 9-7: Photos of deposits formed at $M = 0.5 - 2.1$ (tests F4, F9, F7 and F8 respectively). | 144 |

| | |
|---|-----|
| Figure 10-1: Holder and gas phase geometry used in STAR-CCM+. The yellow arrows represent the direction of flow at the flow inlet. | 149 |
| Figure 10-2: Regions of greatest importance in the CFD simulation: (a) Faceplate, (b) Jet and (c) Coupon. The yellow arrows represent the direction of flow at the flow inlet..... | 150 |
| Figure 10-3: % Change in RMS between grid solutions for (a) Faceplate, (b) Jet and (c) Coupon. | 152 |
| Figure 10-4: (a) Temperature and (b-d) velocity profiles across the centerline of the coupon. | 153 |
| Figure 10-5: Injection points for 50 particle trajectories. | 156 |
| Figure 10-6: Capture efficiency data from the constant $T_{s,i}$ test series and the results from the critical velocity model using the linear and exponential Young's modulus fits. | 160 |
| Figure 10-7: Comparison of experimental data and model results for (a) the constant T_g test series and (b) the transient test series using the critical velocity model and Young's modulus fits from the constant $T_{s,i}$ test series..... | 161 |
| Figure 10-8: Graphs showing the model predictions using four combinations of ρ_{app} and particle size distribution for the (a) constant $T_{s,i}$ test series and (b) transient test series using the critical velocity model and exponential Young's modulus fit (Eq. (10-3))...... | 163 |
| Figure 10-9: Size distributions of the unground JB1 ash and the JB2 ash. | 164 |
| Figure 10-10: Average normal impact velocity (v_n) as a function of particle diameter (d_p). Also included is the average normal component of the critical velocity ($v_{cr,n}$) as a function of d_p , calculated with constant values of R (0.3 and 0.5) and using the exponential Young's modulus fit Eq. (10-3) ($T_g = 1294^\circ\text{C}$, $T_s = 1136^\circ\text{C}$)...... | 165 |
| Figure 10-11: Particle sticking efficiency as a function of particle size (d_p) calculated with the critical velocity model using constant values of R (0.5 and 1.0) and using the exponential Young's modulus fit Eq. (10-3) ($T_g = 1288^\circ\text{C}$)...... | 166 |
| Figure 10-12: Constant $T_{s,i}$ capture efficiency data and the non-spherical model results using Eqs. (10-1) and (10-4) for the yield stress relationship. | 168 |
| Figure 10-13: Capture efficiency data from the constant $T_{s,i}$ test series and the results from the non-spherical model using the linear and exponential Young's modulus fits..... | 169 |
| Figure 10-14: Comparison of experimental data and model results for (a) the constant T_g test series and (b) the transient test series using the non-spherical model and Young's modulus fits from the constant $T_{s,i}$ test series..... | 170 |
| Figure 10-15: Average particle temperature from the constant T_g test series plotted against surface temperature. | 171 |
| Figure 10-16: Graphs showing the model predictions using four combinations of ρ_{app} and particle size distribution for the (a) constant $T_{s,i}$ test series and (b) transient test series using the non-spherical model and linear Young's modulus fit (Eq. (10-5))...... | 172 |
| Figure 10-17: Particle sticking efficiency as a function of particle size (d_p) calculated with the non-spherical model and using the linear Young's modulus fit Eq. (10-5) ($T_g = 1288^\circ\text{C}$). | 173 |
| Figure B-1: Particle size distributions for the JB1 (MMD = 3 μm and 14 μm), JB2 and PRB ash samples. | 203 |

| | |
|--|-----|
| Figure B-2: Particle size distributions for the lignite, bituminous, petcoke and HFO ash samples. | 204 |
| Figure B-3: Photos of the deposits collected during the verification test series. | 205 |
| Figure B-4: Photos of the deposits collected during the transient test series. | 206 |
| Figure B-5: Photos of the deposits collected during the constant $T_{s,i}$ test series. | 207 |
| Figure B-6: Photos of the deposits collected during the constant T_g test series. | 208 |
| Figure B-7: Photos of the deposits collected during the various coal ash type test series. | 209 |
| Figure B-8: Photos of the deposits collected during the HFO test series. | 210 |
| Figure B-9: Photos of the deposits collected during the film-cooling test series. | 211 |
| Figure C-1: Placement of the thermocouple tip in the CFD geometry for calculating the radiation view factors. The heat shield is not shown in this view. | 214 |
| Figure C-2: Spectral responsivity curve for the Sony RGB camera. | 219 |
| Figure C-3: Spectral sensitivity data obtained for the UNIQ RGB camera. | 222 |
| Figure C-4: Calculated vs. blackbody temperatures (a) without the temperature correction and (b) with the temperature correction. | 222 |
| Figure C-5: Example of temperature maps created from images taken at different exposure times and the final temperature map created by splicing/averaging the images together. ... | 225 |
| Figure C-6: Map showing how many temperature maps overlapped at each pixel of the final temperature map shown in Figure C-5. | 225 |
| Figure C-7: Difference between the T_s calculated with the RBG camera and measured with the IR camera vs. emissivity. | 227 |
| Figure C-8: Calculated vs. blackbody temperatures for the single color calibration, with a temperature correction of -11.24°C applied to the calculated temperatures. | 228 |

NOMENCLATURE

| | |
|-----------------|--|
| A | Heat transfer area |
| c | Speed of light |
| c_p | Specific heat capacity |
| CCSEM | Computer controlled scanning electron microscopy |
| CFD | Computational fluid dynamics |
| CMM | Coordinate measuring machine |
| CO ₂ | Carbon dioxide |
| d | Film-cooling hole diameter |
| d_p | Particle diameter |
| E | Young's modulus |
| $E_{b\lambda}$ | Spectral radiance of a blackbody |
| EDS | Energy-dispersive x-ray spectroscopy |
| ESEM | Environmental scanning electron microscopy |
| f | Friction factor |
| F_b | Buoyant force |
| F_D | Drag force |
| F_g | Gravitational force |
| F_T | Total force acting on an ash particle |
| g | Gravitational acceleration, 9.81 m/s ² |
| h | Convective heat transfer coefficient or Planck constant |
| h_{dep} | Deposit thickness |
| HFO | Heavy fuel oil |
| I | Momentum flux ratio, $I = \rho_c U_c^2 / \rho_\infty U_\infty^2$ |
| IGCC | Integrated gasification combined cycle |
| k | Thermal conductivity or roughness height |

| | |
|-----------------|---|
| k_s | Equivalent sand grain roughness height |
| k_b | Boltzmann constant |
| L | Average deposit thickness |
| l_c | Characteristic length in Stokes number equation |
| LOI | Loss on ignition |
| M | Blowing ratio, $M = \rho_c U_c / \rho_\infty U_\infty$ |
| m_{acc} | Mass of ash accumulated in the TADF |
| m_{del} | Mass of ash delivered (mass exiting the equilibration tube) |
| m_{dep} | Mass of ash deposited on the coupon surface |
| m_{fed} | Mass of ash fed into the TADF |
| $m_{tube,e}$ | Mass of ash deposited in the equilibration tube |
| $m_{tube,f}$ | Mass of ash remaining in the ash feed tube |
| $Mg_3V_2O_8$ | Magnesium orthovanadate |
| MgO | Magnesium oxide |
| $MgSO_4$ | Magnesium sulfate |
| MMD | Mass mean particle diameter |
| P/d | Pitch-to-diameter ratio (film-cooling hole spacing) |
| P_s | Sticking probability |
| R | Thermal resistance or coefficient of restitution |
| R_a | Centerline average surface roughness |
| RANS | Reynolds –Averaged Navier-Stokes |
| Re | Reynolds number |
| RMS | Root mean square |
| SiC | Silicon Carbide |
| SO ₂ | Sulfur dioxide |
| SO ₃ | Sulfur trioxide |
| St | Stokes number |
| t | Time or test duration |
| T_∞ | Mainstream or freestream gas temperature |
| TADF | Turbine Accelerated Deposition Facility |

| | |
|-----------------------|---|
| TBC | Thermal barrier coating |
| T_c | Coolant air temperature |
| T_g | Gas temperature |
| T_p | Particle temperature |
| TIT | Turbine inlet temperature |
| T_s | Surface temperature |
| $T_{s,i}$ | Initial surface temperature |
| T_{soft} | Softening temperature |
| U_∞ | Mainstream or freestream gas velocity |
| U_c | Coolant air velocity |
| V_2O_5 | Vanadium Pentoxide |
| V_{dep} | Deposit bulk volume |
| v_g | Gas velocity |
| V_i | Characteristic velocity in Stokes number equation |
| v_p | Particle velocity |
| z | Height of an individual roughness element |
| \bar{z} | Mean height of roughness elements |
| μ | Viscosity |
| γ | Surface free energy |
| ε | Emissivity |
| ε_λ | Spectral emissivity |
| λ | Wavelength |
| η | Overall film-cooling effectiveness |
| η_{cap} | Capture efficiency |
| ρ_∞ | Mainstream or freestream gas density |
| ρ_{app} | Ash apparent density |
| ρ_c | Coolant air density |
| ρ_{dep} | Deposit density |
| ρ_p | Particle density |

1 INTRODUCTION

According to the U.S. Energy Information Administration, coal provided 40% of total world electricity generation in 2012. Although the total share of electricity generated by coal is projected to fall to 28% in 2040, the net electricity generation by coal is projected to increase by 23% from 8.6 trillion kWh in 2012 to 10.6 trillion kWh in 2040 (U.S. Energy Information Administration 2016). According to the International Energy Administration, electricity and commercial heat generation from coal grew from 6.2 trillion kWh in 1971 to 27.7 trillion kWh in 2014 and the overall share of electricity and commercial heat generation from coal, after falling to about 35% in 1991, has risen to about 40% in 2014 (Agency, 2016). As coal will continue to be an important source of electricity, and due to increasing environmental concerns, there is a continuous effort to seek out cleaner and more efficient forms of energy production from coal. One technology of interest is the integrated gasification combined cycle (IGCC). IGCC processes combine the abundance of coal resources with the efficiency of a gas turbine combined cycle system. IGCC also allows for cleaner use of coal because the fuel stream can be cleaned and many of the coal contaminants removed prior to combustion. IGCC therefore facilitates CO₂ capture (Pruschek et al., 1997), and also reduces SO_x, NO_x, and particulate emissions (Topper et al., 1994; Franco and Diaz, 2009).

Despite particulate filtration, some fine coal flyash particles remain in the fuel stream. As the fuel is burned and the gases pass through the gas turbine, the ash particles heat up and stick on

the turbine guide vanes and blades. Over time (8000+ operating hours), particle deposition can lead to significant ash deposits inside the turbine. Particle deposition in gas turbines can adversely affect turbine performance in a variety of ways: clogging film cooling holes, thus reducing film cooling effectiveness (Lawson et al., 2012); changing flow patterns around turbine airfoils and decreasing efficiency (Kurz and Brun, 2001); and depositing corrosive elements such as Na and V (Wenglarz and Fox Jr, 1990b). Even at low ash content, particle deposition is a concern. Cleaned syngas can have an ash concentration close to 0.1 ppmw.

Gas turbine environments can be harsh. Typical flow velocities at the first stage inlet of a turbine are Mach 0.2-0.4 (Jensen et al., 2005; Kurz, 2005). The effort to increase gas turbine efficiency has resulted in increased turbine inlet temperatures. Modern gas turbines can reach turbine inlet temperatures (TIT) from 1400°C to 1500°C and there are continual efforts to further increase TIT (Lebedev and Kostennikov, 2008). As temperatures increase, it is important to know how they will affect all aspects of gas turbine operation, including particle deposition. Due to material considerations, many of the deposition experiments that have previously been conducted were at gas temperatures below 1200°C.

Another fuel used in land-based gas turbines is heavy fuel oil (HFO). HFO is a heavy residue collected from the refining of crude oil. Heavy fuel oil, however, can have ash contents that are several orders of magnitude higher than cleaned syngas (Schmidt, 1985). Tovar et al. (2013) performed combustion experiments with an HFO with 0.21 wt% ash and provided ash samples for the deposition experiments to be described in this work.

1.1 Objective

The purpose of this study is to expand upon the current knowledge of ash deposition behavior in first stage rotors and stators in gas turbines. The primary focus is deposition behavior at gas temperatures up to 1400°C, approaching modern turbine inlet temperatures. This portion of the study can be summarized by the following goals:

1. Investigate the independent effects of gas and surface temperature on ash deposition at elevated gas temperatures.
2. Investigate the deposition behavior of ash samples from different types of coal and with different chemical compositions at 1400°C gas temperature.
3. Investigate the effect of film-cooling on ash deposition at 1400°C gas temperature.
4. Compare the performance of current ash deposition models at elevated temperatures.

In addition, this study also seeks to contribute to understanding the time-dependent nature of the growth of ash deposits. Work was also conducted to investigate the deposition behavior of flyash produced from the combustion of HFO in gas turbines and the effect of elevated levels of SO₂ on the deposit composition.

2 LITERATURE REVIEW

The following chapter presents a review of literature concerning the particle deposition process and various processes and conditions that affect particle deposition behavior and overall deposit growth, as well as methods used to study the deposition process.

2.1 Accelerated Deposition

To facilitate deposition studies, an accelerated deposition process can be used to create representative ash deposits in a fraction of the time required for deposits to form in operating turbines. Kim et al. (1993) showed that capture efficiency is independent of ash concentration (particle loading), but rather that the mass of deposition is a function of the mass of ash fed. It follows that increasing the particle loading in the gas stream to feed the same mass of ash in a shorter time period will produce deposits representative of those produced over a longer time period and lower ash concentrations.

Jensen et al. (2005) developed and validated the use of an accelerated deposition facility to simulate deposits formed in a gas turbine. By increasing the particle loading, they were able to produce deposits in 4 hours that were similar to deposits found on in-service hardware after 10000 hours of operation. The flow conditions in the experiments (gas temperature = 1150°C, Mach number = 0.33) were meant to represent those found in a gas turbine environment. They studied the surface topography, internal structure, and chemical composition of the deposits formed in the

accelerated tests and compared them to deposits obtained from serviced hardware. They found that the accelerated deposits were visually similar in topography to the serviced deposits and that the surface statistics (centerline-averaged roughness, maximum peak-to-valley height, etc.) were similar as well. The accelerated and serviced deposits were also determined to have similar internal structures by examining SEM images of deposit cross-sections. The chemical composition of the accelerated deposits varied from that of the serviced deposits, but this may have been due to differences in the chemistry of the seed particles. This same facility was used to perform the experiments reported in this document and will be described in greater detail in Section 3.1.

The practice of accelerated deposition has been widely implemented in deposition studies. There are currently several accelerated deposition facilities, of various configurations, in operation that are used to study the characteristics of ash deposition in gas turbines. Several of these facilities and studies, as well as other deposition studies, are summarized in Table 2-1.

2.2 Temperature Effects on Deposition

Wenglarz and Fox (1990a) studied the effect of gas and surface temperature on deposition on test specimens downstream from a staged rich-quench-lean (RQL) combustor burning coal-water fuels. Test specimens were placed at two locations downstream from the combustor: a high gas temperature region (1100°C) and a low gas temperature region (980°C). In the high gas temperature region, test samples ranged in surface temperature from 900°C (max coolant) to 1100°C (uncooled). The rate of deposition increased with increased surface temperature, with specimen weight gain (measured in mg/cm²) at 1100°C being about 2.5 times greater than that at 900°C. In the low gas temperature region, test samples ranged in surface temperature from 800°C to 980°C. There was no trend in deposition with surface temperature seen in the low gas

Table 2-1: Recent ash deposition studies

| Source | Particle Characteristics | Surface Type | Cooling (d = hole diameter, P/d = pitch to hole diameter ratio, M = blowing ratio) | Gas Temp (°C) | Gas Velocity (m/s) |
|--------------------------------------|---|--|---|--|--------------------|
| Anderson et al. (1990) | Pulverized bituminous coal particles (Arkwright and Blue Gem) | Platinum surface, perpendicular to flow | Backside impingement cooling Surface temperature maintained at 780°C - 960°C | 1100, 1200, 1300 | 152, 300 |
| Wenglarz and Fox Jr (1990b), (1990a) | Pulverized coal, 3 different ash levels | TBC and SiC 10°, 30°, and 45° impact angles | TBC samples: internally cooled Surface temperature maintained at 980°C, 900°C, 880°C, 800°C SiC sample: uncooled Surface temperature at 1100°C | 980, 1100 | 183 |
| Richards et al. (1992) | Pulverized bituminous coal particles (Arkwright and Blue Gem) | Platinum surface, perpendicular to flow | Backside impingement cooling Surface temperature maintained at 780°C – 980°C | 1100, 1200, 1300 | 300 |
| Kim et al. (1993) | Volcanic ash (Mt. St. Helens, black scoria) | High pressure turbine vanes | 2 vanes internally cooled, independent of other vanes | 949-1371 | - |
| Jensen et al. (2005) | Commercially manufactured particle blend | TBC 30° - 90° to flow | None | 900-1150 | 220 |
| Crosby et al. (2008) | Subbituminous coal ash MMD = 3, 8, 13, 16 µm MMD = 3 µm Petcoke/coal ash blend MMD = 6 µm | TBC 45° to flow | None, insulated backside Backside impingement cooling Initial surface temperatures of 1000°C-1100°C None, insulated backside | 1183 (860 – 1183 for 3 µm) 1183 1183 | 170 |

Table 2-1 Continued

| Source | Particle Characteristics | Surface Type | Cooling (d = hole diameter, P/d = pitch to hole diameter ratio, M = blowing ratio) | Gas Temp (°C) | Gas Velocity (m/s) |
|--------------------------|---|--|---|---------------------------------------|--------------------|
| Wammack et al. (2008) | Commercially manufactured particle blend | Bare metal and TBC coated 45° to flow | None | 1150 | 220 |
| Ai et al. (2011a) | Subbituminous coal ash MMD = 4 μm, 13 μm | Bare Metal 30°, 45° to flow Bare Metal w/ Trench 15°, 30°, 45° to flow | Cylindrical holes d = 1 mm, P/d = 3.375, 4.5 M = 0, 0.5, 1.0, 2.0 Cylindrical holes d = 1 mm, P/d = 4.5 M = 0.5, 1.0, 2.0 | 1183 | 170 |
| Ai et al. (2011b) | Subbituminous coal ash MMD = 13 μm | Bare metal 45° to flow TBC 45° to flow | Cylindrical holes d = 1.0 mm, P/d = 3.375, M = 0, 0.5, 1.0, 2.0 P/d = 4.5, M = 0, 0.5, 1.0, 2.0, 4.0 Cylindrical holes d = 1.0 mm, P/d = 2.25, 4.5 M = 0, 0.5, 2.0, 4.0 | 1183 | 180 |
| Ai et al. (2011c) | Subbituminous coal ash MMD = 16 μm | Bare metal 45° to flow TBC 45° to flow | Cylindrical and shaped holes d = 1.5 mm, P/d = 3 M = 0, 0.5, 1.0, 1.5, 2.0 Cylindrical holes d = 1.0 mm, P/d = 2.25 and 4.5 M = 0, 0.5, 2.0, 4.0 | 1183 | 180 |
| Albert and Bogard (2012) | Wax droplets d _p = 8-80 μm | Epoxy leading edge model | Cylindrical holes d = 3.18 mm, P/d = 7.6; M ≈ 0, 1.0, 2.0 | 21-40 (scaled to wax melting temp) | 15 |

Table 2-1 Continued

| Source | Particle Characteristics | Surface Type | Cooling (d = hole diameter, P/d = pitch to hole diameter ratio, M = blowing ratio) | Gas Temp (°C) | Gas Velocity (m/s) |
|--------------------------|--|--|--|------------------------------------|--------------------|
| Lawson and Thole (2012) | Wax droplets $d_p = 1-100 \mu\text{m}$ | Polyurethane endwall model with an external balsawood layer | Cylindrical holes (endwall cooling) $d = 4.6 \text{ mm}$ $M = 0.5, 1.0, 2.0$ Trench depth = 0.4d, 0.8d, 1.2d | 65 (scaled to wax melting temp) | 6.3 |
| Lawson et al. (2012) | Wax droplets MMD = 175 μm | Cylindrical leading edge model | Cylindrical holes (showerhead configuration) $d = 1.24 \text{ cm}$, P/d = 3.6 $M = 0.5, 1.0, 1.8$ | 42 (scaled to wax melting temp) | 6.7 |
| Webb et al. (2012) | 4 coal ash samples: 1 lignite 2 subbituminous 1 bituminous MMD = 12-18 μm | CFM56-5B aero engine nozzle guide vanes (NGV) ; bare metal | None (all 4 coals) Cylindrical holes: Bituminous – 11.60% film cooling Lignite - 8.30% film cooling | 1041 – 1112 1037 | 64 |
| Albert and Bogard (2013) | Wax droplets $d_p = 8-80 \mu\text{m}$ | Polyurethane (adiabatic) vane model Corian (conjugate heat transfer) vane model | Cylindrical holes, showerhead (SH) and pressure side (PS) row $d = 4.22 \text{ mm}$ $M (\text{PS}/\text{SH}) = 1.0/0.75, 2.0/2.0$ Pressure side row of cooling holes with and without trench | 32 (scaled to wax melting temp) | 5.8 |
| Davidson et al. (2013) | Wax droplets $d_p = 10-200 \mu\text{m}$ | Cork | Round holes, showerhead (SH) and pressure side (PS) row; $d = 4.2 \text{ mm}$, $M (\text{PS}/\text{SH}) = 0.7/0.0, 2.0/2.0$ Round holes with crater; $M = 2.0$ Round holes with trench; $M = 2.0$ Round holes with modified trench; $M = 2.0$ P/d (PS) = 3.0, P/d (SH) = 5.6 | 28 (scaled to wax melting temp) | 5.8 |

Table 2-1 Continued

| Source | Particle Characteristics | Surface Type | Cooling (d = hole diameter, P/d = pitch to hole diameter ratio, M = blowing ratio) | Gas Temp (°C) | Gas Velocity (m/s) |
|------------------------|--|---|--|----------------------|---------------------------|
| Casaday et al. (2014) | Subbituminous coal ash MMD = 11.6 μm | Annular turbine vane cascade | No vane cooling Cold jets added to core flow to simulate “hot streaks,” or non-uniform inlet temperatures | 1093 | 79 |
| Prenter et al. (2014) | Subbituminous coal ash MMD = 6.48 μm | Annular turbine vane cascade | Film-cooling, spanwise slot instead of holes Slot thickness = 0.24 mm 30° exit angle M = 1.16 – 2.67 | 1080 | - |
| Delimont et al. (2015) | Arizona road dust d _p = 20-40 μm | Hastelloy X 30° to 80° to flow (10° increments) | None | 800-1050 | 70 |
| Prenter et al. (2016) | Subbituminous coal ash MMD = 6.48 μm | Annular turbine vane cascade | Film-cooling, spanwise slot instead of holes Slot thickness = 0.254 mm 30° exit angle M = 2.78 Cold jets added to core flow to simulate “hot streaks,” or non-uniform inlet temperatures | 1067-1102 | - |

temperature region. The specimen weight gain in the low temperature region was 2 orders of magnitude lower than that in the high temperature region, indicating that gas temperature plays an important role in particle deposition. Some of this reduction in weight gain, however, may also be due to reduced particle impaction as the low temperature region is located downstream of the high temperature region and some of the particles had already stuck to the samples in the high temperature region.

Anderson et al. (1990) studied the effect of reactor and target temperature on particle deposition in direct coal-fired turbines. Pulverized coal particles were fed into a heated reactor and directed through a nozzle to a target coupon situated perpendicular to the flow. The target coupon was cooled from the backside and the flow rate of coolant was varied. They observed that the sticking coefficient (the fraction of impacting particles that adhere to the surface) decreased with increasing reactor temperature from 1100°C to 1300°C. Target temperature had no effect on sticking coefficient at the lower reactor temperatures, but did have an effect at the highest reactor temperature of 1300°C. In this case, the sticking coefficient increased with increasing target temperature.

Kim et al. (1993) investigated the deposition behavior of various volcanic materials in the hot section of test engines. For one ash sample, they performed deposition test at turbine inlet temperatures from 955°C to 1233°C while keeping particle concentration and exposure time constant. As the turbine inlet temperature increased, there was no deposition until the threshold temperature (~1094°C) was exceeded. After this point, the capture efficiency increased from 2.8% at 1121°C to 3.8% at 1233°C. There were, however, not enough data to determine the functionality of this relationship. The authors also observed, however, that for a different ash sample increasing the TIT actually decreased the capture efficiency once deposition started to occur. The authors

concluded that this reduction of capture efficiency was because the ash was molten at the higher temperatures and molten material was blowing off of the vane during the test.

Kim et al. (1993) also tested the hypothesis that the vane metal temperature was significant in the process of particle deposition. They decreased the amount of coolant air that flowed to an independently cooled vane (ICV) and noted that the amount of deposits on the ICV increased significantly. They determined that the two major parameters that determine whether or not a particle will deposit are the turbine inlet temperature and the temperature of the surface on which the particles impact. They reported that, for both of these parameters, there is a threshold temperature below which no deposition occurs.

A series of deposition tests was also conducted by Crosby et al. (2008) in which gas temperature was varied in an accelerated deposition facility. These studies showed that deposition rates increased exponentially with gas temperature over the temperature range 860°C – 1183°C, with no deposition occurring at 860°C. Crosby et al. suggested that while the deposition rate would continue to increase with increasing temperature, the increase might not be exponential at higher temperatures more representative of actual turbine operation due to some constituents in the ash potentially being vaporized at temperatures above 1500°C.

Crosby et al. (2008) also conducted tests where the flow rate of backside impingement cooling was increased, effectively lowering the temperature of the deposit surface. The gas temperature was held constant at 1183°C while the mass flow of coolant air was varied from 0 g/s to 8.33 g/s. Two test series were conducted: one with subbituminous coal ash and one with a petcoke/coal blend particulate. As the coolant flow was increased, the net capture efficiency for the coal ash decreased from 3.68% (no coolant) to 0% (max coolant) and the net capture efficiency for the petcoke/coal blend decreased from 4.79% (no coolant) to 0.65% (max coolant).

2.3 Particle Size Effects

Richards et al. (1992) performed deposition studies at coal-fired gas turbine conditions in which they burned coal in a drop tube furnace and then accelerated the combustion products (including the coal ash) toward a perpendicular deposition surface. They found that as particle size increased, the deposition rate became less influenced by surface temperature. They reported that larger particles were not cooled quickly in the boundary layer before impacting, whereas smaller particles were cooled to the surface temperature before impacting.

The effect of particle size on deposition was also studied by Crosby et al. (2008). They performed deposition tests at a gas exit temperature of 1183°C, but varied the mass averaged particle size from 3 μm to 16 μm. The results of these tests showed that the amount of deposition increased linearly with particle size. This increase in deposition with increasing particle size could be attributed to the momentum of larger particles causing them to impact more frequently than smaller particles and could also be due to the cooling effects reported by Richards et al. (1992). As particle temperatures increase, cooling rates through the boundary layer will change, which could affect the differences in deposition behavior between large and small particles.

Barker et al. (2013) discussed the relationship between Stokes number and a particle's probability to impact a surface. The Stokes number is the ratio of the characteristic time of a particle suspended in fluid flow to the characteristic time of the flow around an obstacle and is expressed as

$$St_k = \frac{\rho_p d_p^2 V_i}{18\mu l_c} \quad (2-1)$$

where ρ_p is the particle density, d_p is the particle diameter, μ is the fluid viscosity, V_i is a characteristic velocity and l_c is a characteristic length. Particles with larger Stokes number are less

likely to follow fluid streamlines around an object and are thus more likely to impact the surface. Barker et al. conducted CFD simulations of particles in flow around a GE-E³ turbine vane geometry. To illustrate the effects of Stokes number, they calculated the impact efficiency for particles ranging from 1-100 μm in diameter. They found that all particles above a Stokes number of 1.0, corresponding to a particle diameter of 10 μm in their setup, impacted the surface and that the impact efficiency decreased as the Stokes number decreased below 1.0.

Ai and Fletcher (2011) and Barker et al. (2013) used modified versions of the critical velocity particle sticking model developed by Brach and Dunn (1992) to predict which particles will stick to the surface after impacting. Each used a different CFD geometry representative of their own experimental setups, but each still obtained similar trends in their results. While the impact efficiency increased with particle diameter, the sticking efficiency decreased with increased particle size, resulting in a trend where capture efficiency increased initially with particle size but then peaked at a value specific to the process conditions before decreasing with increased particle diameter, as shown in Figure 2-1.

2.4 Ash Chemistry Effects

Just as coal chemistry varies from one coal to another, the chemical composition of coal ash varies from one coal to another. Anderson et al. (1990) conducted experiments on a combustion/deposition entrained reactor in which coal particles were entrained in a hot gas stream and burned. The resulting particle-laden gas was accelerated toward a platinum disk and the particles impinged on the disk. Two types of coals were used in this study: an Arkwright Pittsburgh bituminous coal and a highly cleaned Kentucky Blue Gem bituminous coal. The Blue Gem coal exhibited a higher sticking efficiency than the Arkwright coal. The Arkwright coal had high silica

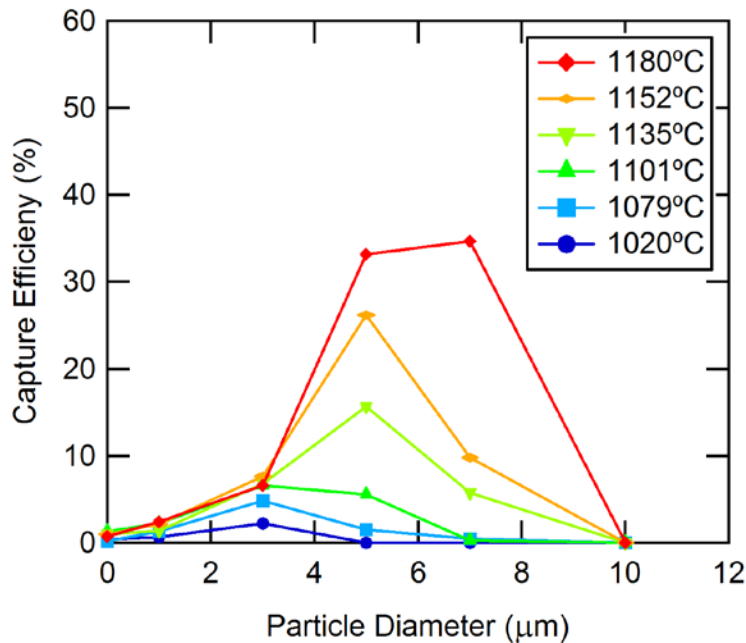


Figure 2-1: Capture efficiency with respect to particle diameter at various gas temperatures, adapted from Ai and Fletcher (2011).

content and a softening temperature of 1421°C and the Blue Gem coal had high iron content and a softening temperature of 1385°C. Thus, this difference in sticking efficiency could be explained by either the difference in ash softening temperature or other chemistry effects.

Additionally, Anderson et al. (1990) observed that at reactor temperatures of 1100°C and 1200°C the target surface temperature had no effect on sticking efficiency. However, Crosby et al. (2008) observed surface temperature effects at gas temperatures of 1183°C. One possible explanation for the different observations between these studies was that Crosby and coworkers used a subbituminous coal ash with a different ash chemistry than that of the bituminous Arkwright coal used by Anderson and coworkers.

HFO often contains significant levels of corrosive elements such as sodium, sulfur, and vanadium. In an effort to change ash and deposit characteristics and reduce corrosion, magnesium-based additives can be added to HFO (Pequeno and Severin, 1999; Rocca et al., 2003; Barroso et al., 2004). A primary goal is to prevent deposition of vanadium pentoxide (V_2O_5) by instead forming magnesium orthovanadate ($Mg_3V_2O_8$). When sulfur is present in the HFO, sulfur dioxide and sulfur trioxide (SO_2/SO_3) are produced during combustion. The SO_3 can react with magnesium oxide (MgO) to produce magnesium sulfate ($MgSO_4$). This formation of $MgSO_4$ can inhibit the formation of magnesium vanadate by depleting the amount of available magnesium in the system. However, $MgSO_4$ is water-soluble and is desirable over MgO deposits, which can also form and which are non-soluble in water.

2.5 High Temperature Strategies

Current turbine inlet temperatures exceed the softening and melting temperatures of metals and alloys used in land based gas turbines. Various technologies have been employed to help protect turbine materials from these high temperatures and prevent mechanical failures due to melting. These technologies include thermal barrier coatings (TBC) on the surface of the turbine blades along with internal and film cooling

2.5.1 Thermal Barrier Coatings (TBC)

TBC is applied to turbine blades to reduce heat flux to the blade, thus reducing the temperature of the metal and preventing failure due to softening and melting. Particle deposition can have a detrimental effect on TBC. Borom et al. (1996) studied the role of deposits in spallation of TBC. Spallation occurs when molten phases infiltrate the TBC layer, solidify, and then pull the TBC layer off as the deposit flakes away from the surface. Borom et al. found that, regardless of

operating conditions or type of particulate matter entering the turbine, spallation was linked to the presence of CaO, MgO, Al₂O₃, and SiO₂ in the molten phase.

Ai et al. (2011b) compared deposits formed on bare metal coupons with those formed on TBC coated coupons. It was found that capture efficiency, under the same testing conditions, was higher on TBC coated coupons than on bare metal coupons. It was also observed that the average surface temperature of the TBC coated coupons was approximately 76°C higher than that of the bare metal coupons, which would account for some of the increase in capture efficiency. It was also noted that the deposits that formed on the TBC were much more tenacious (i.e. much harder to remove) than those that formed on the bare metal.

Wenglarz and Fox (1990a) suggested that once a deposit has started to form, the original surface composition has little effect on the rate of deposition because the ash is only depositing on an existing layer of ash and that temperature is the more important factor.

Wammack et al. (2008) reported that TBC surfaces tend to be rougher and more porous than bare metal surfaces, allowing deposits to penetrate and become better anchored to the coupon surface. Spallation was also observed in these experiments and, upon examining cross-sections of the coupon and of a spalled portion of TBC, it was determined that the spallation was initiated by particles penetrating into cracks in the TBC.

2.5.2 Film Cooling

Another technique used to cool turbine blades is film cooling. Film cooling involves passing cooling air through the turbine blade which then exits out the blade through small film-cooling holes. The coolant air then passes over the surface of the turbine blade. Through film cooling, the blade is cooled both internally and externally.

Albert and Bogard (2012) used a wax droplet deposition method to study deposition on the leading edge of a film-cooled turbine airfoil. The airfoil model used in the experiments included three rows of film-cooling holes: one along the stagnation region of the leading edge and two rows offset 25° from the stagnation region (one on each side). They showed that deposit formation was dependent upon the location on the airfoil. Along the stagnation region, wax deposits formed along the path of the film cooling jets due to the film cooling jets separating from the airfoil surface and the wax particles being transported to the region underneath the film cooling jets via vortices that formed around the coolant jets. In the off stagnation regions of the airfoil the coolant jets remained at least partially attached to the airfoil surface, preventing deposits from forming underneath the coolant jets and resulting in deposit free regions along the coolant jet paths and areas of deposition between the coolant jets.

Ai et al. (2011b) studied the effect of hole spacing and blowing ratio on deposition. Blowing ratio (M) is defined as the ratio of the mass flux of the cooling jets to the mass flux of the mainstream flow, or $M = \rho_c U_c / \rho_\infty U_\infty$ where ρ is density, and U is velocity. These tests showed that capture efficiency and surface roughness decreased with increasing blowing ratio due to increased cooling of the coupon, and also due to a larger number of particles being swept away from the surface by the coolant jets at high blowing ratios (Ai, 2009). At low blowing ratios ($M \leq 1.0$), the coolant holes of a TBC coated coupon became partially or fully blocked with deposit, significantly decreasing film cooling performance. It was also shown that the capture efficiency and surface roughness decreased when the cooling holes were spaced closer together. The smaller spacing between holes improved coolant coverage as a result of neighboring cooling jets interacting with each other. The effect of hole spacing on capture efficiency and surface roughness, however, was not as substantial as the effect of blowing ratio.

Davidson et al. (2013) conducted deposition experiments using the same wax droplet deposition method as Albert and Bogard (2012) to study the effect of TBC and various film cooling hole geometries. In their scaled up facility, they used a layer of cork to simulate the TBC layer on an actual turbine blade. They noticed that, in general, the use of film cooling increased the thickness of the deposit that formed on the blade surface downstream of the film-cooling holes. While an overall capture efficiency was not calculated, this observation appears to be in contrast with those made by Ai et al. (2011b).

2.5.3 Effects of Deposits on Heat Transfer

Bogard et al. (1998) performed experiments investigating the effect of surface roughness on heat transfer to turbine blades. They performed wind tunnel studies on scaled-up models of turbine vanes from engines in military aircraft that had seen 500 hours of service. The scaled up models were designed to match various roughness parameters of the turbine vanes, including centerline-averaged surface roughness (R_a), roughness height (k), and equivalent sand grain roughness height (k_s). The Stanton number (St) was used to evaluate effect of roughness on heat transfer. The Stanton number is evaluated as

$$St = \frac{h}{\rho_{\infty} u_{\infty} c_p} \quad (2-2)$$

where h is the convective heat transfer coefficient, ρ_{∞} is the density of the freestream, u_{∞} is the velocity of the freestream and c_p is the specific heat capacity of the freestream fluid. They found that the rough surfaces experienced heat transfer rates 50 to 60 percent higher than a smooth surface. They also found that increased surface roughness increased heat transfer rates at low and high freestream turbulence levels, indicating that the effects of surface roughness are not overwhelmed

at high turbulence levels and should be taken into account. They also determined that R_a alone is not sufficient to determine the effect of surface roughness on heat transfer. They tested two different rough surfaces with different R_a values, but similar k_s values and found that the heat transfer rates increased by similar amounts for both surfaces.

Bons et al. (2008) similarly performed wind tunnel experiments to determine the effect of surface roughness on heat transfer to turbine blades. Deposition experiments had been performed in which a TBC coated coupon was exposed to deposition in 4 successive tests. The surface roughness was measured between each test and 3D surface maps were generated. These surface maps were used to create scaled up models matching the surface geometry of the deposit surface that were then studied in the wind tunnel. The Stanton number was found to increase with increasing roughness statistics, including R_a .

The thermal conductivity of flyash has been measured by Robinson et al. (2001) and Anderson et al. (1987). Both of these studies were in relation to ash deposits formed on heat transfer tubes in coal fired power plants. The ash in coal fired boilers is moving at velocities much lower than that in gas turbines, so the deposit structures can vary. However, both of these studies looked at the effects of sintering and increased bulk density of the deposit. The highest thermal conductivities reported were at least an order of magnitude lower than the thermal conductivities of most metals. Therefore, as the ash deposits on the turbine blade a thermally insulating layer is created. The idea that the ash layer is thermally insulating is supported by observations made by Kim et al. (1993) that a layering of phases occurred where the deposit close to the turbine surface was an agglomeration whereas the outer layers on thicker deposits were molten. A thermally insulating layer is also evidenced by observations that surface temperatures in a region of deposition increased due to increased deposit thickness (Ai et al., 2011b; Ai et al., 2011c).

The development of ash deposits on turbine blades affects the cooling effectiveness of applied cooling techniques and the temperature of the turbine blade. Lawson et al. (2012) conducted wax droplet deposition studies (simulating ash deposition) on a turbine vane model with a showerhead film-cooling configuration. They used an IR camera to measure the surface temperature of the vane model before any deposition occurred. They then injected ash particles in 100 g increments and measured the surface temperature again after each deposition session. They showed that as the wax deposit grew the film-cooling effectiveness decreased. This was due to hole blockage by wax particles and altered film-cooling coverage by deposits downstream of the film-cooling holes.

Davidson et al. (2013) reported two types of cooling effectiveness for their studies on film cooling with a TBC layer. They measured the temperature of both the exterior cork TBC surface and the vane surface that was covered by the cork TBC. This allowed them to calculate a TBC surface cooling effectiveness, $\tau = (T_{\infty} - T_{TBC}) / (T_{\infty} - T_c)$, and a vane surface cooling effectiveness, $\phi = (T_{\infty} - T_v) / (T_{\infty} - T_c)$ where T_{∞} is the mainstream temperature, T_v is the vane surface temperature, T_{TBC} is the cork TBC surface temperature, and T_c is the coolant air temperature. They determined that the formation of deposits decreased τ for most cooling geometries. However, for the case of round holes at a blowing ratio of 2.0, deposits formed on the upstream edge of the holes and arched over the exits of the holes. This created a sort of barrier that helped the cooling jets to not lift off of the surface and actually increased τ . The formation of deposits actually served to increase ϕ because the deposits formed an insulating layer that reduced heat transfer to the vane surface under the cork TBC.

2.6 Transient Deposition

Kim et al. (1993) studied the time-dependent deposition of volcanic materials on hot turbine components. These studies showed that the capture efficiency (the ratio of the mass of material deposited to the mass of material fed through the system) increased with exposure time. However, their studies only included two variations of exposure time, so the true functionality of capture efficiency with respect to exposure time could not be determined. The layering of phases observed by Kim et al. also suggests that surface conditions change throughout the formation process, which could affect the deposition behavior as time progresses.

In their experiments with molten wax droplets, Albert and Bogard (2012) varied the wax spray duration and measured the final deposit thickness for several experiments. They found that the final deposit thickness reached an equilibrium state after about 20 minutes of spray duration, or about 80 grams of wax sprayed.

To improve existing deposition models, a better understanding of ash deposition as a function of time is required. A better understanding could be achieved by measuring the time-dependent nature of surface temperature, capture efficiency, deposit thickness, deposit roughness, and ash viscosity. These data can be used to improve upon existing deposition models.

2.7 Modeling

There has been a large amount of research performed in the coal community on fly ash formation and deposition in coal-fired burners. While the geometry, operating conditions, and flow dynamics within a gas turbine differ from that of a coal-fired boiler, the deposition models developed to describe fly ash deposition in boilers can serve as a great resource and outline in

model development for gas turbines. While each model is different, the general and simplified modeling procedure is as follows:

1. Characterize the inorganic component of the coal
2. Describe inorganic transformations and ash development
3. Track particle trajectories due to the flow field and transport mechanisms
4. Predict ash sticking and deposit development based on particle properties
5. Characterize the resulting ash deposit

Beer et al. (1992) developed a model in which the coal particles are characterized and fly ash size and composition distributions are obtained by computer controlled scanning electron microscopy (CCSEM). The CCSEM data are then used in a URN model to create a representation of the source coal that models the particle-to-particle variation of mineral properties. The inorganic transformations are then predicted through combustion and coalescence models and the resulting ash particles trajectories are tracked and ash sticking upon impaction is predicted. Inertial impaction is the only transport mechanism considered in this model.

In discussing ash deposition during coal combustion, Baxter (1993) stated that there are four main mechanisms by which ash particles are deposited: inertial impaction, thermophoresis, condensation, and chemical reactions. The ADLVIC (Ash Deposit Local Viscosity, Index of refraction, and Composition) model incorporates all four of these deposition mechanisms and incorporates boiler design and operating conditions to model deposition in coal-fired boilers. It was used to predict deposit rates and properties in one pilot-scale and one utility-scale coal combustor. The qualitative and quantitative predictions agreed well with experimental results

obtained from the two coal combustors. ADLVIC is different from other ash deposition models in that a mineralogical description, rather than an ASTM analysis or elemental description, of the inorganic matter is required. Baxter states that a mineralogical description is important because there is variation in the behavior of different minerals with similar elemental composition. Also, the mass rate of deposition is predicted based on two different time scales. One time scale is the residence time of the ash. The residence time of the particle determines the thermal history and final deposit location of the ash in the boiler geometry. The second time scale is the elapsed time. Varying the elapsed time allows the model to account for total throughput of ash and the deposit development in a particular location over a period of time.

Due to the high gas velocities inside a gas turbine, particle deposition occurs primarily by inertial impaction. Thermophoresis, condensation, and chemical reactions are not incorporated into current gas turbine ash deposition models. Barker et al. (2013) tracked individual particle trajectories using a computational model of a GE-E³ high pressure turbine vane passage. They found that all particles with a Stokes number of about 1.0 impacted the surface and the probability of impact decreased with decreasing Stokes number. They also found that particles with Stokes numbers greater than 1.0 impacted multiple surfaces after rebounding, showing that one individual particle may have multiple opportunities to deposit on the turbine surface

2.7.1 Critical Velocity Model

Sticking models have been developed to simulate and predict if an ash particle will deposit upon impacting the turbine blade surface. Brach and Dunn (1992) developed an impact and adhesion model for microspheres in low velocity impact. The model uses classical impact theory to describe the approach and rebound phases of the particle impact, Hertzian contact mechanics

(which do not include the effects of adhesion) to describe the particle deformation upon impact, and an adhesion model proposed by Johnson et al. (1971) to describe the adhesive forces that are overcome during rebound. The model can be used to determine a critical velocity (v_{cr}). The critical velocity is the initial impact velocity for which the magnitude of the rebound velocity is 0. If a particle impacts with a velocity below v_{cr} , no rebound occurs. The v_{cr} is calculated generally as follows:

$$v_{cr}^2 = -\frac{1 + \eta^2}{R^2} \frac{2W_A}{m} \quad (2-3)$$

$$\eta = \frac{v_t}{v_n} \quad (2-4)$$

$$W_A = -\left[\frac{5}{4}\rho\pi^2(k_1 + k_2)\right]^{\frac{5}{2}} \gamma r^2 |v_n|^{\frac{4}{5}} \quad (2-5)$$

$$k_1 = \frac{1 - \nu_s^2}{\pi E_s} \quad (2-6)$$

$$k_2 = \frac{1 - \nu_p^2}{\pi E_p} \quad (2-7)$$

where d_p is the particle diameter, R is the particle coefficient of restitution in the absence of adhesion forces, γ is the surface free energy, v_t and v_n are the tangential and normal impact velocities respectively, E_s is the Young's modulus of the deposit surface, E_p is the Young's modulus of the particle, and ν_s and ν_p are the Poisson's ratio of the surface and particle respectively. W_A is the work of adhesion that must be overcome in order for a particle to rebound from the surface. The model has been applied to high velocity impact in turbine systems by El-Batsh and Haselbacher (2002) and Ai and Fletcher (2011).

El-Batsh and Haselbacher (2002) and Ai and Fletcher (2011) also applied a critical moment detachment model in conjunction with the critical velocity adhesion model. A critical wall shear velocity (u_{tc}) is calculated as

$$u_{tc}^2 = \frac{Cu \cdot \gamma}{\rho D_p} \left(\frac{\gamma}{d_p K_c} \right)^{\frac{1}{3}} \quad (2-8)$$

where Cu is the Cunningham Correction Factor, d_p is the particle diameter, ρ is the gas density and K_c is defined as

$$K_c = \frac{4}{3} \left[\frac{(1 - \nu_s^2)}{E_s} + \frac{(1 - \nu_p^2)}{E_p} \right]^{-1} \quad (2-9)$$

A particle will detach if the wall friction velocity (u_w) is greater than the critical wall shear velocity. The u_w is calculated according to Eq. (2-10), where τ_w is the wall shear stress,

$$u_w = \sqrt{\frac{\tau_w}{\rho}} \quad (2-10)$$

2.7.2 Critical Viscosity Model

Sreedharan and Tafti (2011) developed a composition-dependent sticking model. This model predicts particle deposition based on a sticking probability (P_s) defined as

$$P_s = \frac{\mu_{crit}}{\mu_{T_p}} \quad (2-11)$$

* The symbol γ is used here for continuity within this document but is represented as W_A in El-Batsch and Haselbacher (2002) and Ai and Fletcher (2011).

where μ_{crit} is the critical viscosity and is calculated as the viscosity at the softening temperature of the ash and μ_{Tp} is the viscosity of the particle at the actual particle temperature. The viscosity is temperature dependent and is calculated using a model developed by Senior and Srinivasachar (1995) given in Eq. (2-12) where μ is viscosity, T is temperature (either particle or softening temperature), and A and B are parameters dependent upon ash composition. This viscosity model is most reliable in predicting viscosities in the $10^4 - 10^9$ Pa·s range.

$$\log\left(\frac{\mu}{T}\right) = A + \frac{10^3 B}{T} \quad (2-12)$$

The softening temperature is also dependent upon the chemical composition of the ash and was calculated according to the following regression formula (Yin et al., 1998):

$$T_{soft} = 92.55 \cdot SiO_2 + 97.83 \cdot Al_2O_3 + 84.52 \cdot Fe_2O_3 + 83.67 \cdot CaO + 81.04 \cdot MgO + 91.92 \cdot a - 7891 \quad (2-13)$$

$$a = 100 - (SiO_2 + Al_2O_3 + Fe_2O_3 + CaO + MgO), \quad (2-14)$$

where SiO_2 , Al_2O_3 , Fe_2O_3 , CaO and MgO are the weight percent of the respective oxides in the ash.

Barker et al. (2013) utilized the sticking models from Ai and Fletcher (2011) and Sreedharan and Tafti (2011) in their computational deposition studies. They found that both models worked well during the initial stages of deposition, but not at later stages of deposition, stating that transient deposition effects need to be taken into account to accurately model ash deposition.

2.7.3 Elasto-Plastic Model

Singh and Tafti (2013) developed a model for predicting the coefficient of restitution of particle wall collisions in gas turbines. This model breaks the particle-wall interaction into 4 stages:

1. An elastic compression stage incorporating Hertzian theory
2. An elasto-plastic compression stage that uses the work of Jackson and Green (2005) to incorporate plastic deformation once the particle starts to yield
3. A restitution stage in which the sphere begins to rebound but only recovers a portion of its original kinetic energy due to energy losses from plastic deformation
4. An adhesion breakup stage which follows the adhesion model of Brach and Dunn (1992) to incorporate adhesion losses and determine a final coefficient of restitution.

The final normal coefficient of restitution (e_n) is calculated as

$$e_n = \frac{V_{2n}}{V_{1n}} = e_{ep} \left(1 + \frac{2W_A}{e_{ep}^2 m V_1^2} \right)^{\frac{1}{2}}, \quad (2-15)$$

where e_{ep} is the coefficient of restitution after the elasto-plastic phases, V_{1n} is the initial normal impact velocity, V_{2n} is the final normal rebound velocity, and m is the mass of the particle. In this study, the e_n is calculated for each particle and the particle rebounds if e_n is greater than zero, otherwise the particle adheres and deposits on the surface.

2.7.4 Non-Spherical Model

Bons et al. (2016) developed a non-spherical impact model in which the ash particles are modeled as a cylinder that contacts the surface end-on rather than employing the usual spherical particle assumption. The model assumes that, upon contact with the deposition surface, the

cylindrical particle responds primarily as a 1-D spring with spring constant $E_c A / \ell$ where A is the cross-sectional area of the cylinder and ℓ is the length of the cylinder equal to $2d_p/3$ (which corresponds to a volume equal to that of a sphere of diameter d_p), and E_c is the composite Young's modulus

$$E_c = (\pi k_1 + \pi k_2)^{-1}, \quad (2-16)$$

where k_1 and k_2 are as previously defined in Eqs. (2-6) and (2-7). When the particle impacts the surface, the particle first experiences elastic deformation and impact normal kinetic energy ($E_{k,n1}$) is converted to elastic energy. Constant cylinder geometry is assumed during elastic deformation and the elastic energy (E_{el}) that corresponds to elastic deformation (w_{el}) is defined as

$$E_{el} = \int_0^{w_{el}} \frac{E_c A}{l} w dw = \left(\frac{E_c A}{l} \right) \frac{w_{el}^2}{2}. \quad (2-17)$$

Plastic deformation begins when the yield stress (σ_y) is reached. The point of deformation at which plastic deformation begins is referred to as w_{crit} . After this point, plastic deformation continues until the remaining $E_{k,n1}$ is expended. The maximum deformation (w_{max}) can then be calculated by solving the following expression

$$E_{k,n1} = E_{el,crit} + \int_{w_{crit}}^{w_{max}} \sigma_y A dw, \quad (2-18)$$

where $E_{el,crit}$ is the maximum elastic energy stored, or the E_{el} evaluated at w_{crit} .

After plastic deformation, the particle rebounds and the rebound normal kinetic energy ($E_{k,n2}$) is determined by subtracting the work of adhesion from $E_{el,crit}$. W_A in this case is calculated according to Eq. (2-19) where A_{cont} is the contact area at the maximum deformation and γ is the surface free energy and is considered constant at 0.8 J/m^2 . A_{cont} is obtained from the semi-empirical

derivation shown in Eq. (2-20), where $a = 0.1$, $b = 1/7$, and $c = 0.5$ and A_{crit} is the contact area at w_{crit} . If the resulting kinetic energy, and thus the rebound normal velocity, is greater than zero the particle will rebound. Otherwise, the particle sticks.

$$W_A = A_{cont}\gamma \quad (2-19)$$

$$\frac{A_{cont}}{A_{crit}} = a + b \left(\frac{w_{max}}{w_{crit}} \right)^c \quad (2-20)$$

To account for shear removal, a drag moment around the cylindrical particle is calculated according to Eq. (2-21). This drag moment is multiplied by 1.7 to account for wall effects. Unlike the detachment model used by El-Batsh and Haselbacher (2002) and Ai and Fletcher (2011) where shear removal was calculated after the particle had adhered to the surface, the drag moment is applied at the point of maximum deformation (w_m) during the deposition process. M_{drag}/a_{cont} , where a_{cont} is the radius of the contact surface area, represents the shear force working against the adhesion forces. This shear force is added to the elastic force of the compressed cylinder and increases the available rebound kinetic energy.

$$M_{drag} = \frac{\rho_f^3 u_\tau^4 d l^4}{8\mu^2} + \frac{3\rho_f^{\frac{5}{3}} d^{\frac{1}{3}} u_\tau^{\frac{8}{3}} l^{\frac{10}{3}}}{2\mu^{\frac{2}{3}}} \quad (2-21)$$

2.8 Summary

A summary of the recent turbine deposition studies was shown in Table 2-1. Some deposition studies have been conducted at high temperatures representative of actual turbine inlet temperatures (1400°C - 1500°C), but only enough to learn some general effects of turbine inlet temperature and surface temperature on deposition rates. More detailed testing has been performed at temperatures up to 1183°C. One goal of this research is to study deposition trends at higher

temperatures, up to 1400°C, and to better distinguish between the effects of gas temperature and surface temperature. The effect of particle size, film cooling, and ash fuel type and transient deposition behavior will also be studied at high temperatures and at gas velocities representative of those at first-stage turbine blades.

3 DESCRIPTION OF EXPERIMENTAL FACILITIES

The following chapter describes the experimental facilities and materials used to create ash deposits as well as the types of analysis performed on the ash deposits.

3.1 Deposition Facility

Experiments were performed in the Turbine Accelerated Deposition Facility (TADF) at Brigham Young University, shown in Figure 3-1. The TADF is used to simulate deposition that occurs in gas turbines using syngas (such as in an IGCC power plant) on a laboratory scale. The deposition occurs in an accelerated manner, simulating 8000 hours of exposure time in 1 hour by increasing particle loading in the exhaust gas. The use of accelerated deposition testing was validated by Jensen et al. (2005).

The TADF has undergone a number of redesigns and modifications since it was originally built. The design and construction of the original TADF is outlined in Jensen (2004). Afterward, several modifications were made to the TADF. These included improvements to the air supply line (allowing for easier control of the air supply and the inclusion of a coolant air line), increasing the equilibration tube diameter from 1.6 cm to 2.6 cm, modifications to the gas inlets to improve flame stability, implementation of a more reliable particle feeding system, and the design of a new coupon holder to allow for backside impingement cooling (Crosby, 2007). Additional modifications were made to the coupon holder to allow for backside film cooling in addition to

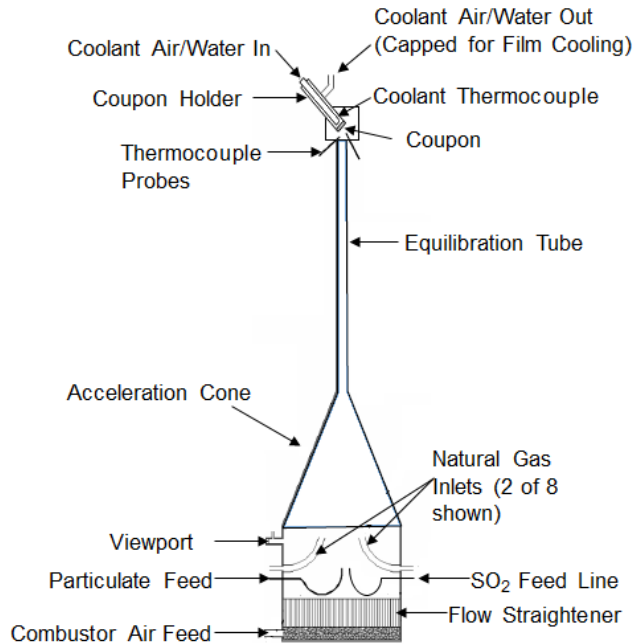


Figure 3-1: Schematic of the TADF at BYU.

backside impingement cooling (Ai et al., 2011c). The remainder of this chapter outlines the current setup of the TADF and modifications that were made specifically for this study.

The combustion chamber is located at the base of the TADF. Natural gas is burned in the combustor and the facility is capable of reaching gas temperatures (T_g) of 1400°C , similar to the TIT of modern gas turbines. Coal ash is fed into the base of the combustor and flows up with the combustion gases to simulate particulate in exhaust gas from syngas combustion. The hot combustion gases flow up through a cone that converges toward an equilibration tube. The cone accelerates the gas to velocities of 200 m/s and greater. The equilibration tube is 0.8 m long. When operating at T_g near 1183°C , the absolute pressure inside the combustor was measured as 90.7 kPa (assuming an atmospheric pressure of 86 kPa).

The particulate laden gas exits out the top of the equilibration tube and impinges on a nickel superalloy coupon held at a 45° angle directly above the equilibration tube. This coupon is the surface upon which deposition occurs. The rate at which deposition occurs is dependent upon the impingement angle of the gas stream on the coupon, with deposit thickness increasing as impingement angle increases (Jensen et al., 2005). The 45° angle was chosen to allow for an appreciable amount of deposit to be collected in the 1 hour time frame and is representative of the leading edge portion of turbine vanes and blades. Coolant air can be introduced at the back of the coupon holder allowing for backside impingement cooling of the coupon or film cooling if there are film cooling holes in the coupon. The end of the coolant air inlet tube was located 4 cm from the back of the coupon for the tests discussed in Chapters 4 and 5, and 2.5 cm from the back of the coupon for the remainder of the tests. A water line was also added to the coupon holder to allow for additional backside cooling for better control of T_s at high T_g .

In order to more closely simulate the combustion environment for the heavy fuel oil (HFO) ash experiments, an additional feed line was added to the base of the TADF. This feed line allowed for the introduction of SO_2 into the combustion chamber. The necessity to maintain the levels of SO_2 in the system for the HFO tests is discussed in Chapter 8.

After the changes outlined in Crosby (2007) were made, the radial temperature profile was measured at the standard operating conditions used in those tests ($T_g = 1183^\circ\text{C}$, Mach = 0.25) and is shown in Figure 3-2, where r/R is the ratio of the radial location of the thermocouple to the radius of the equilibration tube, with $r/R = 0$ representing the center of the tube. The temperature profile exhibited turbulent behavior as it was flat away from the edges of the tube. The drop in temperature from $r/R = 0$ to $r/R = -0.8$ was the result of the thermocouple moving vertically away from the exit of the equilibration tube. The approximate path of the thermocouple is also shown in

Figure 3-2. The temperature profile of the TADF was not measured at the new conditions used for the tests presented in this work, but the calculated Reynolds number for flow in the equilibration tube ranged from $1.7 \cdot 10^4$ to $2.1 \cdot 10^4$, indicating turbulent flow. It was then assumed that there was little radial variation in temperature, velocity and particle concentration in the equilibration tube.

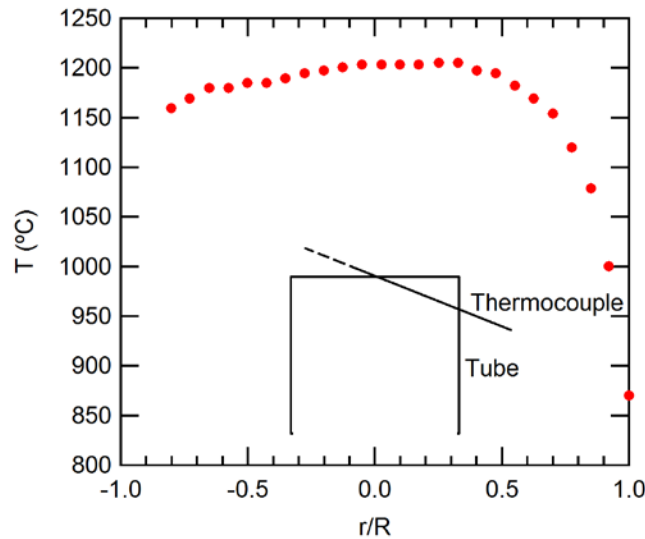


Figure 3-2: Radial temperature profile across the exit of the equilibration tube as measured by and adapted from Crosby (2007). The thermocouple traversed the tube in the $-r/R$ direction.

3.2 Upgrades

The original TADF was constructed of Inconel 601 and had a maximum operating temperature of 1200°C (Jensen et al., 2005). To allow for testing at T_g up to 1400°C , the design and materials of the TADF had to be modified and upgraded as outlined in the following sections.

3.2.1 Holder

The coupon holder was rebuilt so that a SiO₂ faceplate could be attached to the front side of the holder. The new holder design is shown in Figure 3-3. The faceplate was made in two halves that closed around the front of the coupon holder and could be secured in place with two bolts. Springs were placed on the bolts to help continue to hold the two halves together when the bolts expanded at the high temperatures. When installed, the front surface of the faceplate was flush with the front surface of the coupon. The SiO₂ faceplate is shown in Figure 3-4.

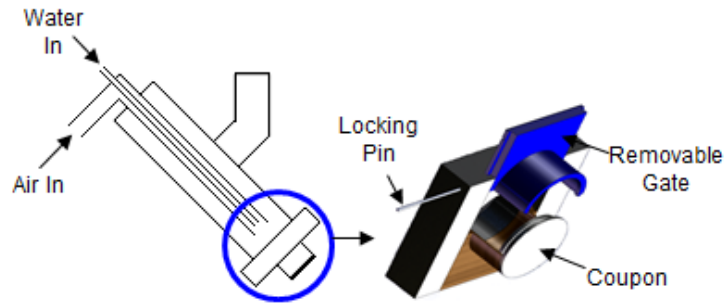


Figure 3-3: Redesigned coupon holder.

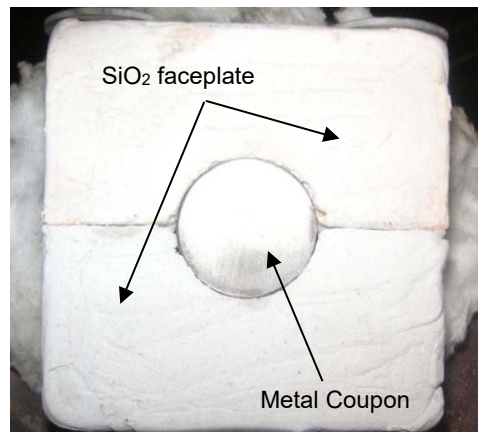


Figure 3-4: SiO₂ faceplate protecting the redesigned coupon holder from high gas temperatures.

The faceplate was made from Rescor 750TM castable SiO₂ from Cotronics Corp. The castable ceramic had a maximum operating temperature of 1482°C and came in two parts: a powder base and a liquid activator. The two parts were combined according to the provided instructions and the mixture was placed in 3D-printed molds, manufactured by the BYU Rapid Prototype Lab, and allowed to cure. After curing, the faceplate halves were removed from the molds and the interior surfaces were ground until the faceplate halves fit properly over the coupon holder and could be secured in place. The use of the castable ceramic made it possible to make a new faceplate in the laboratory whenever a replacement was needed.

The previous holder included an air line that entered the back of the holder and provided coolant air for either impingement or film-cooling. Increasing the gas temperature to 1400°C created a need for increased cooling capacity to maintain the desired surface temperatures. A water line was added through the back of the coupon to provide this extra cooling capacity when needed.

3.2.2 Acceleration Cone and Equilibration Tube

To allow for testing at higher T_g , the Inconel acceleration cone and equilibration tube portion of the combustor was initially replaced with a silicon carbide (SiC) cone and tube. The Grade SC-2 reaction bonded silicon carbide has a maximum temperature limit of 1500°C. However, due to the cost of the SiC cone and tube and the time required to produce and ship a new cone and tube when needed, the tube portion was replaced by a quartz tube. This modification resulted in a SiC cone that remained attached to the combustor and a quartz tube that could be attached to the top of the SiC cone. The quartz equilibration tube could be removed and replaced quickly and affordably. The maximum operating temperature of the quartz tube, for short-term use, was 1400°C. Diagrams of each setup are shown in Figure 3-5.

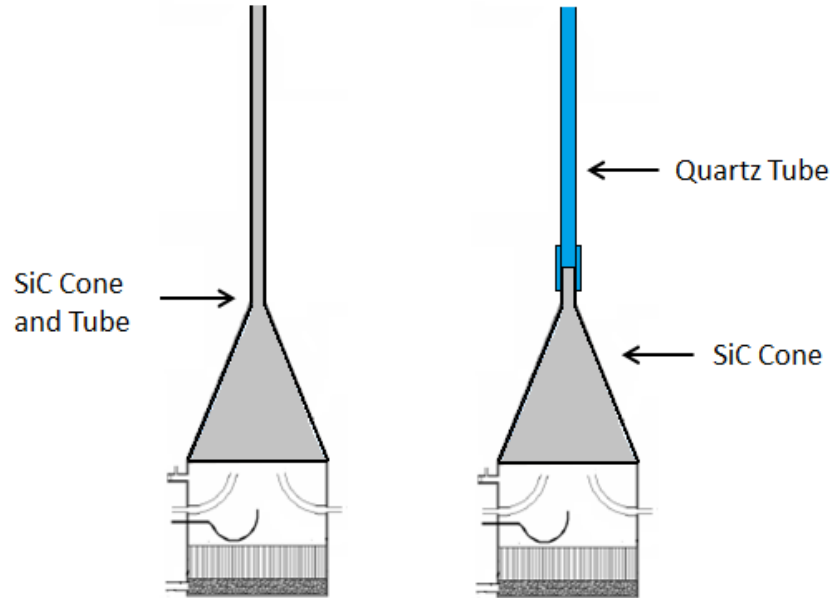


Figure 3-5: One-piece SiC cone and tube configuration and 2-piece SiC cone and quartz tube configuration.

3.3 Coupons

Metal coupons were provided by industrial contacts. The coupons are made of a nickel based superalloy specific to the turbine manufacturer. An example of the coupons used in this study can be seen in Figure 3-4. Each coupon has a front side diameter of 2.5 cm and is 0.3 cm thick. A groove was cut into the edge of the coupon to facilitate attaching the coupon to the coupon holder.

Film-cooling holes were added to some of the coupons. The holes were cut at a 30° angle and emerge along the centerline on the front side of the coupon. The hole configuration, along with the coupon dimensions are shown in Figure 3-6.

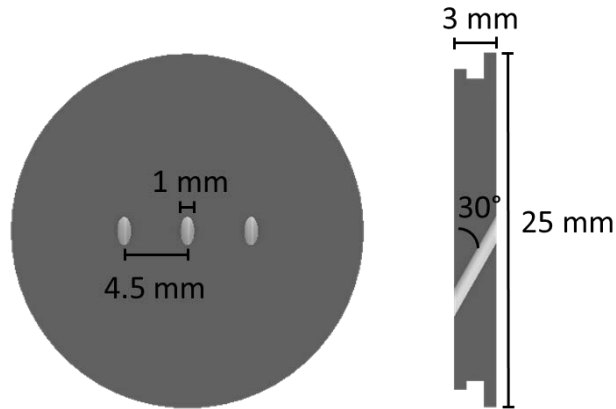


Figure 3-6: Coupon dimensions showing film-cooling holes.

3.4 Ash Properties and Preparation

Seven different ashes were used to generate ash deposits: three subbituminous coal ashes, one lignite ash from Mississippi, one bituminous coal ash from coal mined in West Virginia, one petcoke/coal blend ash, and one heavy fuel oil ash. Two of the three subbituminous coal ashes were received from the Jim Bridger Power Plant in Wyoming. These two ashes were received several years apart in two separate batches and have different chemical compositions and are labeled JB1 and JB2. The majority of the experiments in this study were conducted using the JB2 ash. The third subbituminous coal ash was obtained from coal mined in the Powder River Basin (PRB) in Wyoming. All of the coal ash samples originated from operating power plants.

The HFO ash was a blend of ash samples produced by the combustion of HFO in the Burner Flow Reactor (BFR) at Brigham Young University (Tovar et al., 2013). Raw HFO was first washed to reduce sodium and potassium levels to typically 2 ppm or less and then filtered. The HFO was then burned in the BFR, which is a downward-fired combustor. Prior to entering the burner nozzle of the combustor, a magnesium additive was injected into the HFO. During the combustion process,

portions of the flue gas were directed through two bag filters and a cyclone separator in order to collect the ash for analysis and testing. The process is described in greater detail in Tovar et al. (2013).

The chemical composition and physical properties of the different ash samples are summarized in Table 3-1. The apparent density was estimated by measuring the tap density of the ash and then dividing this value by an estimated packing factor of 0.5. While applied generally, this method was not ideal for each sample. For example, the apparent density of the PRB subbituminous ash was estimated to be 0.8 g/cm^3 , which is less dense than water. The PRB ash, however, does not float on water when dispersed, indicating that the apparent density should be greater than 1.0 g/cm^3 . The mass mean diameter (MMD) was measured in a Beckman-Coulter LS-100 laser diffraction particle size analyzer. The apparent density and MMD of the HFO ash was measured using the as-received ash, which had a high loss on ignition (LOI, 67.11 wt% dry). The ash fusion temperatures were determined by ASTM method D1857. The ash fusion temperature analysis was performed by Wyoming Analytical Laboratories, Inc.

To accurately replicate the deposition process that occurs in industry turbines, the particle diameter of the ash used in the TADF must be similar to that which would be present in a gas turbine after fuel cleanup and filtration. Modern particulate removal systems can reduce particulate content to 0.1 ppmw and can remove 99.9% of particles smaller than $1 \text{ }\mu\text{m}$ (Sharma et al., 2008). The MMD after properly functioning filtration systems can be on the order of $1 \text{ }\mu\text{m}$, or higher with inadequate or degraded filtration systems (Bons et al., 2005). To achieve similar particle sizes, the as-received ash was ground in one of two ways. For the first batch of Jim Bridger ash and the petcoke ash, the ash was passed through a wheat grinder and the fine particulate exiting the exhaust of the wheat grinder was collected. The remaining ash samples were milled with spherical milling

Table 3-1: Chemical composition and physical characteristics of the various ash samples

| <i>Chemical Composition</i> | | | | | | | |
|--|------------------------|------------------------|------------------------|----------------------------|-------------------------------|----------------------------|------------------------|
| <i>wt%, dry, hydrocarbon free</i> | | | | | | | |
| | JB1¹ | JB2² | PRB¹ | Lignite¹ | Bituminous¹ | Petcoke³ | HFO² |
| SiO ₂ | 49.9 | 63.6 | 22.1 | 32.8 | 25.3 | 46.5 | 4.38 |
| Al ₂ O ₃ | 11.5 | 17.3 | 10.5 | 14.2 | 13.5 | 15.6 | 2.16 |
| Fe ₂ O ₃ | 14.5 | 4.22 | 6.1 | 9.8 | 52.7 | 18.6 | 22.7 |
| CaO | 9.4 | 5.04 | 42.2 | 31.7 | 2.3 | 6.0 | 7.02 |
| MgO | 1.7 | 1.55 | 6.9 | 3.6 | 0.6 | 2.1 | 14.6 |
| TiO ₂ | 3.0 | 1.04 | 2.2 | 2.6 | 1.9 | 0.8 | 0.33 |
| Na ₂ O | 3.7 | 2.53 | 1.8 | 0.8 | 0.3 | 3.3 | 0.58 |
| K ₂ O | 1.6 | 0.93 | 0.5 | 1.0 | 2.0 | 1.7 | 3.98 |
| SO ₃ | 1.2 | 0.39 | 5.7 | 1.2 | 0.6 | 1.4 | 25.6 |
| P ₂ O ₅ | - | 0.43 | - | - | - | 0 | 2.58 |
| V ₂ O ₅ | - | - | - | - | - | 3.45 | 11.1 |
| NiO | - | - | - | - | - | 0.65 | 4.23 |
| BaO | - | 0.42 | - | - | - | - | 0.09 |
| SrO | 0.7 | 0.18 | 0.3 | 1.3 | 0.1 | - | 0.06 |
| MnO ₂ | - | 0.03 | - | - | - | - | 0.49 |
| <i>Physical Characteristics</i> | | | | | | | |
| | JB1 | JB2 | PRB | Lignite | Bituminous | Petcoke | HFO |
| ρ_{app} (g/cm ³) | 2.8 | 2.1 | 0.8 | 1.3 | 2.5 | 2.2 | 0.5 |
| MMD (μ m) | 3.2, 14 | 4.9 | 6.1 | 5.0 | 4.9 | 8.3 | 33 |
| <i>Ash Fusion Temperatures – Oxidizing Conditions (°C)²</i> | | | | | | | |
| | JB1 | JB2 | PRB | Lignite | Bituminous | Petcoke | HFO |
| Initial Deformation | 1217 | 1216 | 1156 | 1153 | 1339 | 1237 | >1538 |
| Softening | 1227 | 1224 | 1201 | 1188 | 1359 | 1260 | >1538 |
| Hemispherical | 1242 | 1234 | 1351 | 1196 | 1367 | 1300 | >1538 |
| Fluid | 1293 | 1286 | 1372 | 1216 | 1376 | 1369 | >1538 |
| ¹ Values were taken from Webb et al. (2012). | | | | | | | |
| ² Values were measured at Wyoming Analytical Laboratories, Inc. | | | | | | | |
| ³ Values were taken from Crosby et al. (2008), where they were reported as elemental wt%, and converted to oxide wt%. | | | | | | | |

media in deionized water until an MMD of $\sim 5 \mu\text{m}$ was achieved. The ash was then dried and collected for use. The MMD of each ash is included in Table 3-1. The size distribution for the JB2 ash is shown in Figure 3-7. The size distributions of the rest of the ash samples can be found in Appendix B.

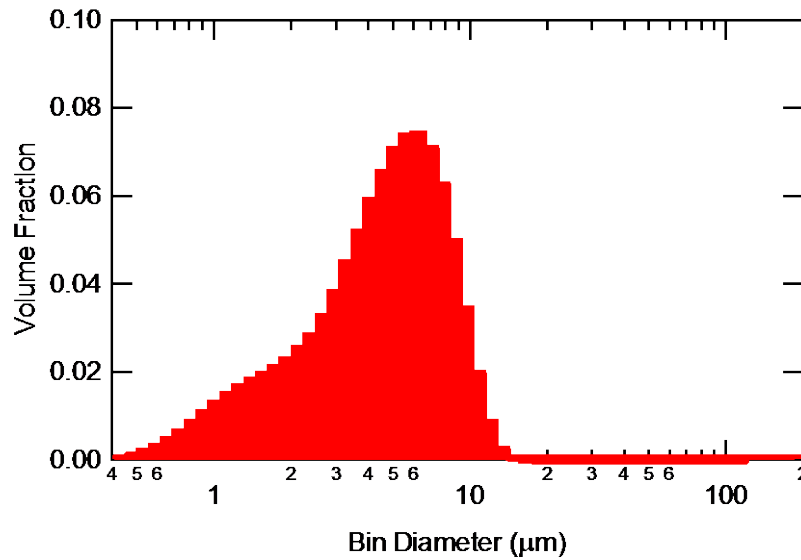


Figure 3-7: Particle size distribution of the JB2 ash.

It is recognized that grinding the ash to obtain a smaller MMD may produce ash particles of the right size but with different chemical composition and physical properties than the small ash particles that form in an actual IGCC gasifier and pass through the filtration system. Samples of actual ash exiting from an IGCC filtration system were not available. The samples and results presented in this study are based on the compositions presented in Table 3-1 and should be considered with that in mind.

The original TADF was designed with an equilibration tube long enough to allow particles up to 40 μm in diameter to come to velocity and thermal equilibrium (95% of the outlet gas velocity and temperature) with the flow (Jensen et al., 2005). The entrainment of particles in the flow was modeled using Stokes flow assumptions and the thermal equilibrium was analyzed using a lumped capacitance model (Jensen, 2004).

To account for the new process conditions and different ash samples with different apparent densities, the velocity and thermal equilibrium were modeled again as follows. The following force balance was applied to the ash particles fed into the combustor

$$F_T = F_g + F_b + F_D \quad (3-1)$$

where F_T is the total force, F_g is the gravitational force, F_b is the buoyant force, and F_D is the drag force acting on the ash particles. Substituting equations in for each of these forces gives

$$\frac{\pi}{6} d_p^3 \rho_p \frac{dv_p}{dt} = \frac{\pi}{6} d_p^3 g (\rho_g - \rho_p) + \frac{\pi}{8} d_p^2 \rho_g (v_g - v_p)^2 f \quad (3-2)$$

$$f = \left(\sqrt{\frac{24}{Re}} + 0.5407 \right)^2 \quad (3-3)$$

$$Re = \frac{\rho_g |v_g - v_p| d_p}{\mu_g} \quad (3-4)$$

where d_p is the particle diameter, ρ_p is the particle density, ρ_g is the gas density, v_p is the particle velocity, v_g is the gas velocity, μ_g is the gas viscosity, g is the gravitational acceleration, Re is the Reynolds number, and f is the friction factor for flow around a sphere (for $Re < 6000$) taken from Bird et al. (2002). This relationship predicts that, for the test conditions presented in this study, 99-100 wt% of particles from the milled coal ash samples reach velocity equilibrium before exiting

the equilibration tube. Similarly, 84 wt% of the unground JB1 ash particles and 93 wt% of the HFO ash particles reach velocity equilibrium before exiting the equilibration tube.

The particle temperature inside the combustor was predicted by performing an energy balance and assuming lumped capacitance, resulting in Eq. (3-5) where h is the convective heat transfer coefficient, T_p is the particle temperature, and c_p is the particle specific heat capacity. The particle specific heat capacity was assumed to be 984 J/(kg·K). This same value was used by Barker et al. (2013) for the JB1 ash. All the particles from all the ash samples reach thermal equilibrium before exiting the equilibration tube.

$$\frac{dT_p}{dt} = \frac{6h(T_g - T_p)}{\pi d_p \rho_p c_p} \quad (3-5)$$

The convective heat transfer coefficient, h , was calculated according to the method outlined in Appendix C.1, except that the Nusselt number correlation for flow around a sphere (Bird et al., 2002) rather than for flow around a cylinder was used, as given in Eq. (3-6).

$$Nu = 2 + 0.6Re^{\frac{1}{2}}Pr^{\frac{1}{3}} \quad (3-6)$$

3.5 Particle Feeding System

A picture of the particle feeding system is shown in Figure 3-8. A syringe filled with ash particles was inserted into the side of a glass bulb. A stepper motor then advanced the plunger in the syringe to push the ash particles out of the syringe, into the bulb. The speed of the stepper motor was regulated by a function generator attached to the stepper motor driver. Air entered the top of the bulb, flowed downward and entrained the ash particles and exited out the bottom of the bulb into a tube that led to the base of the TADF, shown in Figure 3-1. A rotating brush in the bulb

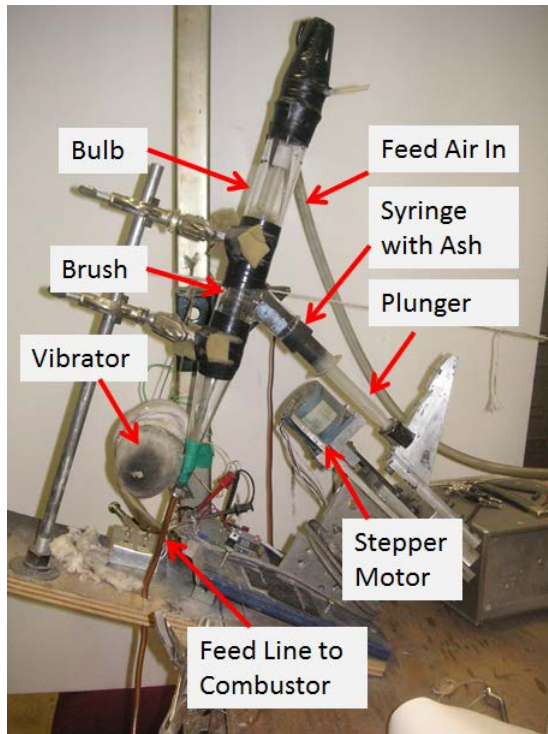


Figure 3-8: Picture of the particle feeding system.

helps to separate the ash particles and a vibrator on the outside of the bulb helps prevent ash particles from adhering to the inside of the bulb.

Before each test, the syringe was filled with ash and vibrated so the ash would settle in the syringe. The syringe was then weighed by itself, inserted into the bulb, and weighed again with the bulb. These initial masses of the syringe and the syringe and bulb combination were recorded. The bulb and syringe were then put in place in the particle feeding system, the brush and vibrator were turned on and the stepper motor was used to advance the plunger in the syringe until ash started to fall out of bottom of the bulb, at which point the stepper motor was stopped. This ash was collected in a cup sitting underneath the bulb until no more ash fell out of the bulb. The brush was turned off and the feed tube was attached to the bulb in preparation for the test. This initial

advancement of the syringe was intended to reduce the lag time between the moment that the particle feeding system was turned on and the moment that ash started to fall through the bulb and was fed into the TADF during the deposition test. The ash that collected in the cup was weighed and the mass was recorded.

After the deposition test was complete, the bulb and syringe combination was removed from the particle feeding system and weighed, then the syringe was weighed by itself and these two final masses were recorded. The final masses and the mass of ash collected in the cup were subtracted from the initial masses to determine the mass of ash fed into the TADF (m_{fed}).

3.6 Temperature Measurement

Two K-type OMEGACLAD[®] XL thermocouples were placed in the outlet stream at the top of the equilibration tube to measure the T_g . The thermocouples were kept in place until the desired T_g was achieved and the system was determined to be at steady state. The thermocouples were removed before starting the particle feeding system so that ash would not deposit on the thermocouples. After the particle feed was turned on, one of the thermocouples would periodically be placed temporarily in the outlet stream to measure the current T_g and adjust the natural gas flow as needed to maintain the desired T_g . The periodic T_g measurements were generally taken about every ten minutes, but were occasionally taken more or less frequently.

Each periodic T_g measurement is the average of several data points that were recorded during each measurement period and filtered to remove the warm-up and cool-down periods resulting from inserting and removing the thermocouple. The data were first filtered by deleting any measurement below 800°C and above 2000°C. This range was chosen because the lowest desired T_g in any of the test series was 1093°C, so any measurement below 800°C was likely from

when the thermocouple was not in the hot gas stream. Any temperature over 2000°C would be a result of a malfunction in the thermocouple. The thermocouple reading changed the fastest when first inserted into or removed from the hot gas stream, as these would be the moments of greatest temperature difference between the thermocouple and its surroundings. The data were filtered further by removing any data point that was not within 20°C of either of its neighbors in an attempt to remove the majority of the warm-up and cool-down data.

After the T_g data had been filtered to this point, each measurement period was defined as a collection of data points where the time between data points was less than 1 minute. In a final effort to remove any lingering warm-up and cool-down data and other artificial fluctuations in the temperature data, a line was fit to the data within a measurement period and the 95% prediction bands were calculated. Any data outside of the prediction bands were filtered out and the process was repeated until no data was filtered out. Figure 3-9a shows the full set of temperature data measured throughout a test, indicating which are removed for being below the 800°C threshold or not having a neighbor within 20°C. Figure 3-9b shows the final data that are retained and removed after iteratively calculating the prediction bands for the measurement period indicated by the green circle in Figure 3-9a.

Occasionally, the process of filtering out data points falling outside of the 95% prediction bands resulted in the removal large clusters of data that may have been good data. An example of the removal of potentially valid data from test F4, which will be discussed in chapter 9, is shown in Figure 3-10. In the cases where this removal of potentially valid data was investigated, the maximum change in the overall average T_g was -2.4°C as a result of removing these data. The decision was made to still filter the data by the normal process to preserve uniformity in the process over all the tests.

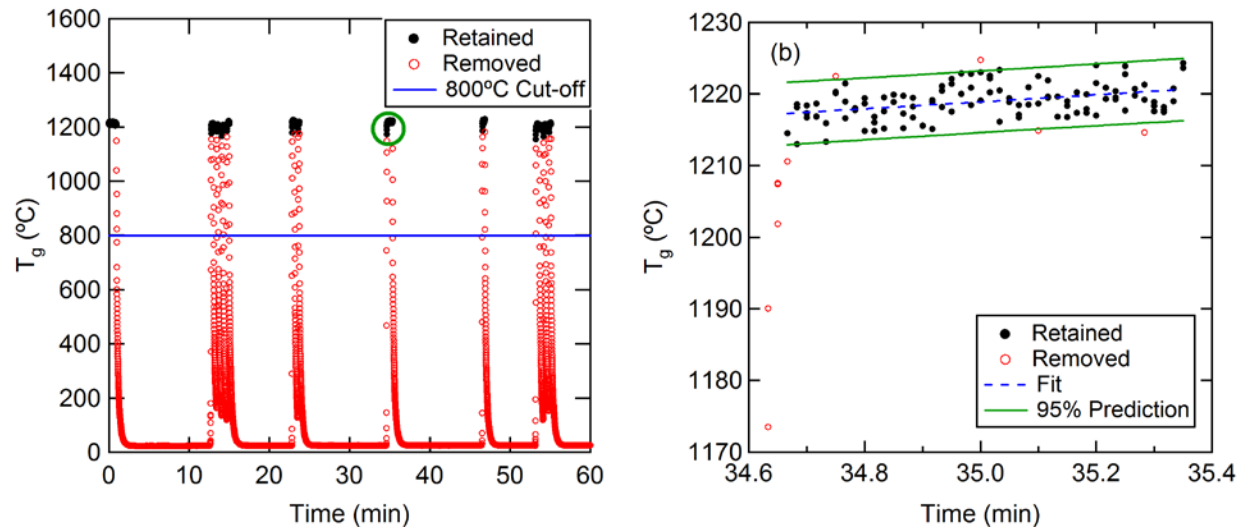


Figure 3-9: Graphs displaying the results from the process used to filter the periodic T_g measurements. The T_g data shown here is from test G3.

The periodic T_g measurements were then averaged together to give an overall average T_g for the test. Occasionally, small pockets of low temperature data points would slip through the filtering process and result in periodic T_g measurements that were the average of only these low temperature measurements. These low periodic T_g were excluded from the overall average T_g .

After the test, the average measured T_g , which is really the average of the thermocouple bead temperature, was then corrected for radiation losses in order to obtain the true gas temperature. The method for this radiation correction is outlined in Appendix C. The T_g reported throughout this study is the radiation-corrected average T_g measured during each test.

According to data found at www.omega.com, the OMEGACLAD[®] XL type K thermocouples are for use up to 1335°C and their accuracy is $\pm 0.75\%$. According to an initial radiation correction analysis, in order to achieve a gas temperature of 1400°C, an uncorrected

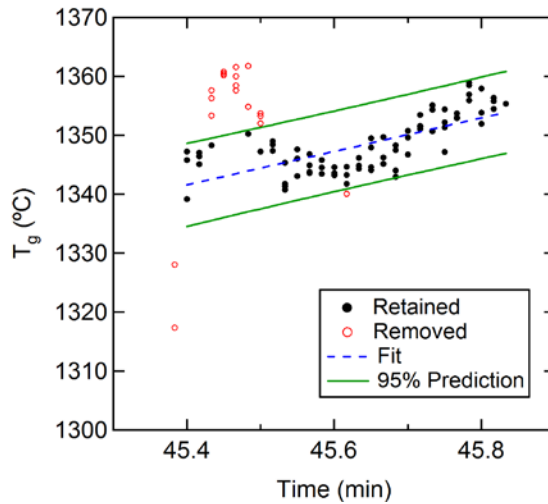


Figure 3-10: Example, from test F4, of potentially valid data being filtered out from the T_g measurements.

thermocouple temperature of 1352°C was desired (the radiation correction analysis was later updated and an uncorrected temperature of 1352°C actually resulted in a corrected temperature of 1413°C to 1415°C). The decision was made to go ahead and use the type K thermocouples with the assumption that although the temperature limit would be exceeded, the additional temperature range would not introduce significant additional error. Before correcting for radiation, the maximum periodic T_g measurement was 1369°C and the maximum average T_g was 1356°C.

Another K-type thermocouple was located at the end of the coolant air inlet tube (4 cm from the back of the coupon for the tests discussed in Chapters 4 and 5, and 2.5 cm from the back of the coupon for the remainder of the tests). This backside temperature was monitored before each test and was used to determine when thermal steady state was achieved, at which point the particle feeder was turned on. When coolant is being used, this thermocouple also measures the temperature of the coolant.

The temperature of the front side of the coupon was measured using two-color and single-color optical pyrometry. An RGB camera was used to take pictures of the coupon, using XCAP image analysis software. A diagram of the camera setup for obtaining the surface temperature is shown in Figure 3-11. The intensity of two color channels (red/blue or red/green) was used to calculate an emissivity and surface temperature (T_s). A temperature map of the whole coupon surface was obtained as well as an average T_s . This method is discussed in more detail by (Svensson et al., 2005), Lu et al. (2009), and Ai (2009). The calibration procedure for the RGB camera is outlined in Appendix C.

The 2-color technique worked well initially. However, due to problems recalibrating the RGB camera for 2-color analysis after replacing a broken sensor, it was necessary to switch to a single color technique using the intensity of the red channel. Using only one color signal, it was no longer possible to simultaneously solve for emissivity and temperature. An assumed emissivity was used to calculate the $T_{s,i}$ of the bare metal coupon. Emissivity tables indicate that nickel-chromium alloys have total emissivities between 0.82 and 0.97 when oxidized (OMEGA, Last visited 2017). An emissivity of 0.9 was chosen to represent the bare coupon. After the $T_{s,i}$ was calculated for the bare metal coupon, it was assumed that a layer of ash had developed on the surface of the coupon for all other T_s calculations. For these calculations, an emissivity of the ash deposit was calculated according to the process outlined by Shimogori et al. (2012) and comprising Eqs. (3-7) - (3-13). The total emissivity is defined as

$$\varepsilon(T) = \frac{\int_{\lambda_1}^{\lambda_2} \varepsilon_{\lambda}(T) E_{b\lambda}(T) d\lambda}{\int_{\lambda_1}^{\lambda_2} E_{b\lambda}(T) d\lambda}, \quad (3-7)$$

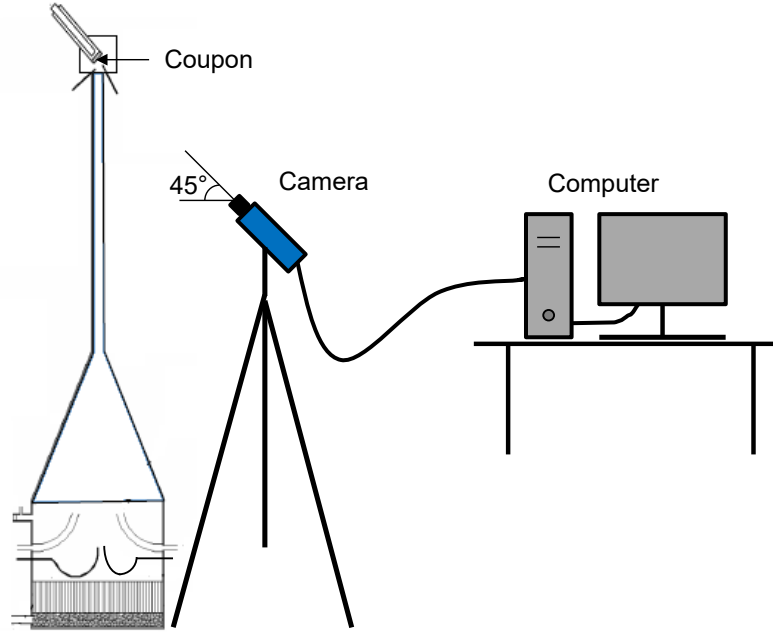


Figure 3-11: RGB camera setup for obtaining coupon and deposit surface temperatures via optical pyrometry.

where λ is wavelength, T is temperature, $\epsilon_{\lambda}(T)$ is the spectral emissivity at T , and $\epsilon(T)$ is the total emissivity at T . The limits of integration, λ_1 and λ_2 , were chosen according to the limits of the spectral responsivity of the red channel in the RGB camera (0.455 μm and 1.15 μm respectively). $E_{b\lambda}(T)$ is the spectral radiance of a blackbody, given by Planck's Law

$$E_{b\lambda}(T) = \frac{2hc^2}{\lambda^5 \left(e^{\frac{hc}{\lambda k_b T}} - 1 \right)}, \quad (3-8)$$

where h is the Planck constant, c is the speed of light and k_b is the Boltzmann constant. The spectral emissivity, $\epsilon_{\lambda}(T)$, is calculated according to Eqs (3-9) through (3-13), where $C_{\text{Fe}_2\text{O}_3}$ is the wt% of iron oxide in the hydrocarbon free ash. The calculated emissivity is used to solve for the surface temperature. However, emissivity is a function of temperature, so the equations are solved iteratively.

$$\varepsilon_{\lambda}(T) = k_1 \lambda^2 (k_2 - \lambda) + k_3 \quad (3-9)$$

$$k_1 = \frac{0.85 - \varepsilon_{1.6}(T)}{229.38} \quad (3-10)$$

$$k_2 = 12 \mu m \quad (3-11)$$

$$k_3 = 1.12 \varepsilon_{1.6}(T) - 0.10 \quad (3-12)$$

$$\varepsilon_{1.6}(T) = (0.164 + 0.25 \log C_{Fe2O3})(0.00176T - 0.584) \quad (3-13)$$

Each analyzed image produced a temperature map of the whole coupon or deposit surface as well as a spatially-averaged surface temperature. When single values are reported for T_s or $T_{s,i}$, they are these spatially averaged surface temperatures from a single image. An example of a temperature map and the corresponding T_s are shown in Figure 3-12.

3.7 Deposit Analysis

The deposits were analyzed after the deposition tests. The following will outline some general procedures for deposit analysis. Some of the procedures were slightly altered from one test series to another due to discoveries about the TADF and its operation, changes in availability of resources, or the time frame in which the analysis could be performed. Analysis procedures specific to a certain test series, or changes made due to discoveries in that test series, will be discussed in the respective chapters.

3.7.1 Capture Efficiency

One of the primary variables calculated and reported in this study is the capture efficiency. The capture efficiency was calculated according to Eq. (3-14) where m_{dep} is the mass of ash that deposited on the coupon, m_{fed} is the mass of ash fed into the TADF (as discussed in Section 3.5) and m_{acc} is the mass of ash that accumulates in the TADF and does not exit the equilibration tube.

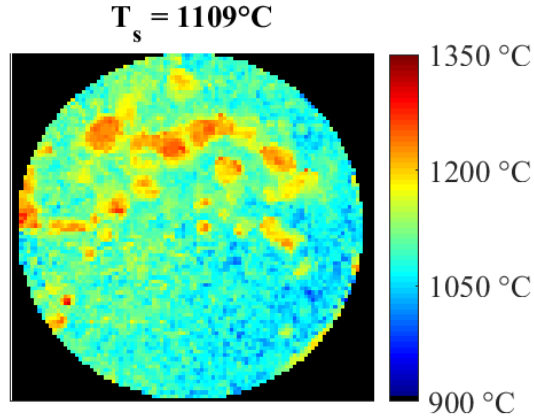


Figure 3-12: Temperature map of test G8 (which will be discussed in Chapter 6) and the spatially-averaged temperature ($T_s = 1109^\circ\text{C}$).

The m_{acc} term initially included just the mass of ash that deposited in the equilibration tube ($m_{tube,e}$), but later included the mass of ash that remained in the feed tube that leads to the base of the combustor ($m_{tube,f}$) after it was discovered that an appreciable amount of ash could remain in the feed tube. This evolution of the definition of the m_{acc} term is discussed more in later chapters. The denominator of Eq. (3-14) represents the mass of ash exiting the equilibration tube and is often referred to as the mass of ash delivered, or m_{del} , in this document.

$$\eta_{cap} = \frac{m_{dep}}{m_{fed} - m_{acc}} \quad (3-14)$$

The value of m_{dep} is determined by weighing the bare coupon before the deposition test and then weighing the coupon with the deposit after the deposition test and subtracting the two masses. In some cases, the deposit layer was quite thin and tenacious and remained on the coupon until it was sanded off. In most cases, the deposit detached from the coupon after cooling down. A padded container was placed below the coupon after the TADF was shut down, but before the holder had completely cooled down, to try to catch any pieces of deposit that fell off the coupon. Sometimes

the recovered deposit was fractured and incomplete. To adjust for this fact, images were taken of each of the recovered deposits and image analysis was conducted to determine what percent of the deposit was missing and what percent was actually recovered. The calculated capture efficiency was then divided by the percent of deposit recovered, giving an adjusted capture efficiency reflecting the mass of the entire deposit including the unrecovered portion.

Because the coupon is held at a 45° to the equilibration tube outlet, the projected view of the coupon down to the tube outlet forms an ellipse with an area smaller than that of the coupon. The inner diameter is also slightly bigger than the diameter of the coupon (27 mm vs. 25 mm). Figure 3-13a shows the projected area of the coupon compared to the area of the equilibration tube outlet. The coupon projection only covers 60% of the outlet area meaning that, if all the particles exited the tube and travelled in straight lines until impinging on either the coupon or the faceplate, only 60% of them would impinge on the coupon. As mentioned in Section 2.3, larger particles will travel in straighter lines while smaller particles will be redirected by the gas flow, meaning that the 60% figure is more of an approximation of the maximum impact efficiency of the particles.

Due to the difference in the projected coupon area and the outlet area, as well as the redirection of smaller particles, not all of the ash that deposited after exiting the tube deposited on the coupon. Some of the ash impinged and deposited on the faceplate surrounding the coupon, as shown in Figure 3-13b-c. This ash was not included in the m_{dep} term when calculating capture efficiency. Only the mass of ash that deposited on the coupon was included in m_{dep} for all deposition tests performed in the TADF. Excluding the ash that deposits on the faceplate from m_{dep} means that the capture efficiencies reported in this study could never reach 100% even if every particle impacted a surface and stuck. However, because the coupon diameter was constant from test to test and the coupon was replaced at the same position and angle relative to the gas flow for

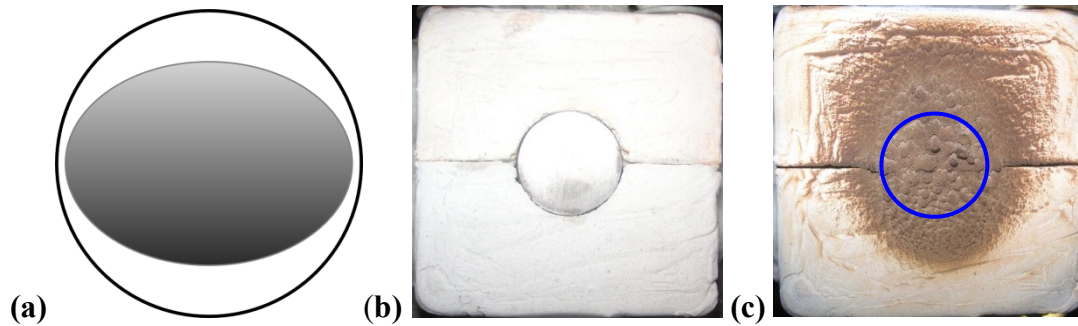


Figure 3-13: (a) Representation of the projected area of the coupon to the area of the equilibration tube outlet, with the shading indicating the distance of the coupon from the tube outlet (darker = closer). (b) Coupon and faceplate before any deposition occurred. (c) Coupon and faceplate after deposition. The circle represents the coupon area. Only ash deposited within this circle was included in m_{dep} .

each test, the capture efficiency, as defined in this section, is still a good indicator of the effect of various process conditions on deposition behavior.

The percentage of the ash that exits the equilibration tube that actually impacts the coupon is known as the impact efficiency. If anything should cause a change in the impact efficiency, this would translate into a change in capture efficiency as well, supposing that the percentage of ash particles that adhered to the surface after impacting remained constant. It is important to determine whether, as the testing conditions are varied, the changes in capture efficiency and deposition behavior are a result of changes in particle and surface characteristics rather than a result of variation in impact efficiency due to changing flow characteristics and the limits of the coupon geometry. Figure 3-14 presents data obtained while performing the CFD work presented in Chapter 10 of this study. The impact efficiency of particles ranging in diameter from $0.4 \mu\text{m}$ to $130 \mu\text{m}$ is presented at 5 different gas temperatures. It can be seen that, as the gas temperature increased from 1263°C to 1411°C , the impact efficiency of each particle size remained relatively constant. This indicates that any changes in the observed deposition behavior as the gas

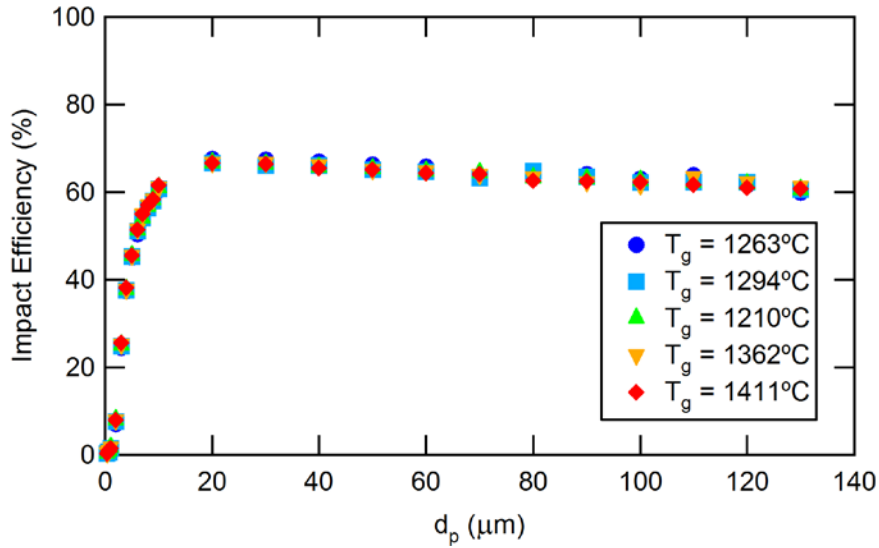


Figure 3-14: CFD results of particle impact efficiency vs. particle size at varying gas temperatures in the TADF.

temperature is varied during the experiments are a result of changing particle properties, and not the limited coupon geometry.

3.7.2 Surface Roughness, Deposit Thickness and Deposit Density

After the ash deposits were collected (if they detached from the coupon), they were taken to a local company (either Wilcox Associates, Inc., or Diversified Metal Services, Inc.) and an optical surface scan of the deposit was performed using a coordinate measuring machine (CMM). These scans provided a cloud of xyz points from which peak and valley heights were obtained. The R_a value was then calculated as

$$R_a = \frac{1}{N} \sum_{i=0}^{N-1} |z_i - \bar{z}|, \quad (3-15)$$

where z is the height of an individual roughness element, \bar{z} is the mean height, and N is the number of roughness elements. Any data from the surface beneath the deposit during scanning, as well as the sloped edges of the deposit, were deleted prior to calculating R_a so that only the peaks and valleys on the top of the deposit were included in the calculation. An example of the area used for the roughness analysis is shown in Figure 3-15.

Given that the CMM scan gives the height of each individual element, the CMM data were also used to obtain the deposit thickness. The deposits were placed on a flat surface while being scanned. Since only the deposit was scanned, the deposit thickness is simply the difference between the lowest point and the highest point measured, illustrated in Figure 3-15b where h_{dep} is deposit thickness. The point clouds were also used to calculate the bulk volume of the deposit (V_{dep}). The volume could then be used along with the deposit mass to calculate the bulk density (including voids) of the deposit as $\rho_{dep} = m_{dep}/V_{dep}$.

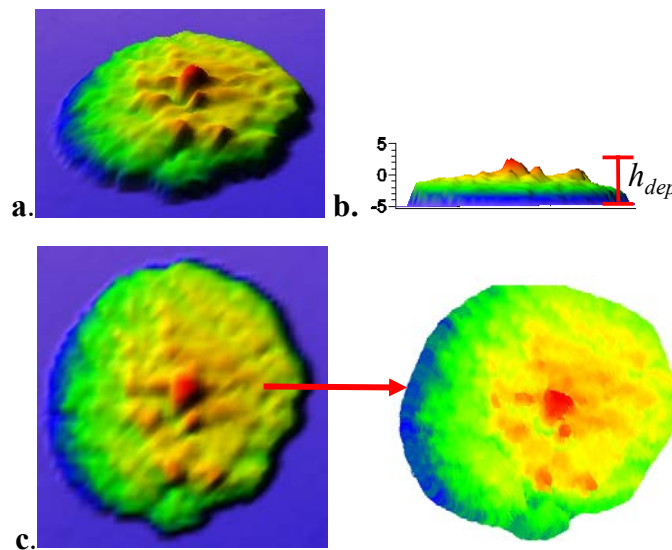


Figure 3-15: (a) 3D surface map of the scan of test T3. (b) Side view of the surface scan. (c) Area used to determine R_a for test T3.

4 COMPARISON WITH THE ORIGINAL FACILITY

This chapter describes efforts to verify that the upgraded TADF produced results similar to those obtained from the original TADF. A series of tests was conducted at test conditions similar to a series conducted on the old facility and the results are discussed here.

4.1 Test Conditions

After the initial modifications to the TADF were completed (a new coupon holder design as outlined in Section 3.2.1 and the full SiC cone and tube as outlined in Section 3.2.2), a series of tests was conducted to compare the operation of the upgraded facility to the original facility. The tests were conducted at T_g ranging from 1130°C to 1188°C using the unground (MMD = 14 μm) JB1 ash. Similar T_g were used on the old facility in a series of tests performed by Ai and Fletcher (2011).

4.2 Results and Discussion

After reviewing video recordings of the deposition tests reported throughout this study, it was determined that occasionally a significant portion of the deposit that formed on the coupon was actually deposit that initially formed on the faceplate downstream and then grew upstream onto the coupon. Figure 4-1 shows a particularly dramatic occurrence of a deposit growing from the faceplate onto the coupon during a test performed as part of a test series that will be discussed in Chapter 6. A ridge of deposit can be seen to form on the edge of the faceplate at the top of the

image and then continue to grow and advance over the top portion of the coupon. When this process was observed and determined to potentially add significantly to the final mass of the deposit, the data for those tests were excluded from the results and discussion of their respective test series. Of the 65 total tests originally included in the various test series for this study, 5 were excluded for this reason. Two of those 5 were part of these comparison tests (one at $T_g = 1131^\circ\text{C}$ and one at $T_g = 1188^\circ\text{C}$).

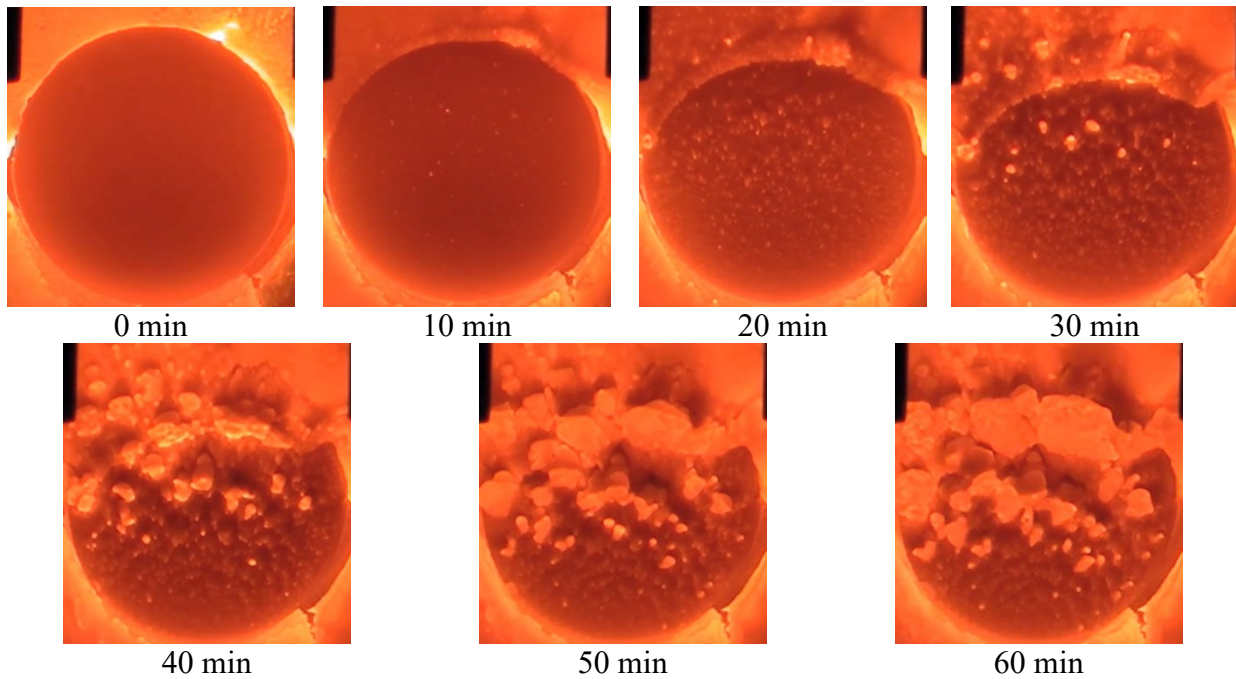


Figure 4-1: Screen captures from the video of test S1. A large deposit can be seen to first form at the edge of the faceplate and then advance onto the coupon.

The main parameter used to compare the performance of the new facility with that of the old was the capture efficiency. Before the final design of the faceplate was established, a number of deposition tests were performed in the TADF with earlier designs. After these first tests were performed on the new facility, it was discovered that deposition was occurring inside the SiC

equilibration tube, which did not occur inside the original Inconel tube. This deposition effectively reduced the amount of ash that reached the deposition surface (i.e. the value of ash fed through the system used in the calculation of capture efficiency). This deposition inside the tube was taken into account by calculating the capture efficiency as

$$\eta_{cap} = \frac{m_{dep}}{m_{fed} - m_{tube,e}}, \quad (4-1)$$

where m_{dep} is the mass deposited on the coupon, m_{fed} is the amount of ash fed into the TADF, and $m_{tube,e}$ is the mass of ash that was deposited on the inside of the equilibration tube, taking the place of m_{acc} in Eq. (3-14). After completing a test, $m_{tube,e}$ was measured by removing the acceleration cone and equilibration tube portion of the combustor and then collecting and weighing the ash deposited in the tube. Of the mass of ash fed in these verification tests, 7.1% and 9.0% deposited in the tube at $T_g = 1132^\circ\text{C}$ and $T_g = 1130^\circ\text{C}$ respectively, and 18% deposited in the tube at $T_g = 1187^\circ\text{C}$. The values of m_{fed} and $m_{tube,e}$ for each test in this study are reported in Appendix A.

Tests were then conducted with the final faceplate design. When $m_{tube,e}$ was taken into account, the calculated capture efficiencies for the upgraded facility were consistent with those obtained from the original facility, as seen in Figure 4-2. The difference between the average measured T_g for the tests in the new facility and the respective comparison tests from the old facility ($T_{g,new} - T_{g,old}$) ranged from -5°C to 7°C . For the tests with a T_g near 1175°C , the capture efficiency obtained in the new facility was 0.39% larger than that obtained in the old facility. For the tests with a T_g near 1130°C , the difference in capture efficiencies was greater, with the capture efficiencies from the new facility being 24.8% and 18.7% lower than that obtained in the old facility.

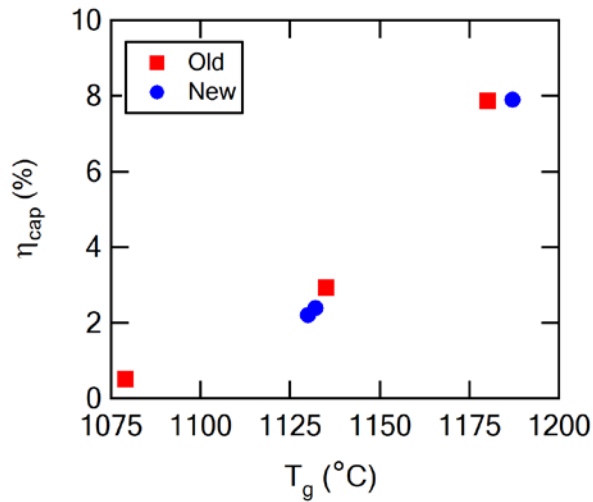


Figure 4-2: Comparison of adjusted capture efficiencies obtained from tests on the upgraded (new) TADF and the previous (old) TADF.

Some of this variation can be attributed to experimental error. Some contributors to experimental error are tube position and fluctuation in T_g . The tube was removed after each test to gather the ash that deposited inside the tube. The tube position was marked before removing the tube to help ensure that it was placed back in its original position. However, some variation in tube position did occur, affecting how much of the ash deposited on the coupon rather than the holder, which then caused variation in the calculated capture efficiency.

T_g was controlled manually by adjusting the mass flow of natural gas to the combustor. During the test, the temperature fluctuated around the average T_g . The sample standard deviation of the periodic T_g measurements used to obtain the overall average T_g ranged from 1.7°C to 4.6°C for the new tests shown in Figure 4-2, indicating small variation in the measured temperature data. The discrepancy between the old and new capture efficiency data is likely more influenced by differences in temperature measurement and analysis between the two sets of data. For example, the radiation corrections applied to the T_g in the old tests from the old facility were, on average,

6°C smaller than the new radiation corrections that would be calculated and applied for the same T_g .

4.3 Summary and Conclusions

The TADF was upgraded in design and material construction to allow for operation at T_g up to 1400°C. Tests were conducted to compare the operation of the new facility and the obtained results with those of the old facility. It was found that the new facility produced results similar to those of the old facility as long as the additional deposition occurring in the SiC equilibration tube was taken into account while calculating the capture efficiency. These results were also used to justify the later modification of using a SiC cone with a quartz tube.

5 TRANSIENT CHARACTERISTICS*

The current particle deposition models applied to gas turbine systems and discussed in Section 2.7 work well to predict capture efficiency at the beginning stages of deposition, but not at later stages after the surface conditions have changed significantly. In order to better understand the transient characteristics of deposit growth, experiments were conducted in the TADF in which the test duration, or length of time over which deposition occurred, was varied and the ash deposit characteristics were analyzed. This included measuring the transient nature of surface temperature, capture efficiency, deposit thickness, deposit roughness, and ash viscosity. This chapter presents the test conditions, analytical procedures and results of the transient deposition test series.

5.1 Test Conditions

The test conditions are summarized in Table 5-1. All of the tests were conducted with a gas temperature close to 1295°C. The 14 μm JB1 flyash was used in 7 of the 9 tests and the 3 μm JB1 flyash was used in the remaining tests. Test times ranged from 20 minutes to 60 minutes. The backside of the test coupon was insulated, so heat flux through the coupon is close to 0.

Combustion air entered the TADF at a rate of 0.0214 kg/s and the natural gas flow was adjusted until T_g reached a value near 1295°C. While the target T_g was achieved very quickly,

* This chapter resulted in the following publication: Laycock, R. G., and T. H. Fletcher, "Time-dependent Deposition Characteristics of Fine Coal Flyash in a Laboratory Gas Turbine Environment," ASME Journal of Turbomachinery, v. 135, n. 2, March 2013

Table 5-1: Summary of test conditions for the transient test series

| Test # | T _g (°C) | MMD (μm) | Time (min) | Particles/m ³ in flow | Void Fraction |
|--------|------------------------|-------------|---------------|-------------------------------------|------------------|
| T1 | 1294 | 14 | 33 | 3.34E6 | 0.9999 |
| T2 | 1298 | 14 | 60 | 3.80E6 | 0.9999 |
| T3 | 1302 | 14 | 60 | 3.86E6 | 0.9999 |
| T4 | 1289 | 14 | 20 | 2.49E6 | 0.9999 |
| T5 | 1291 | 14 | 20 | 2.73E6 | 0.9999 |
| T6 | 1285 [†] | 14 | 40 | 3.57E6 | 0.9999 |
| T7 | 1298 | 14 | 40 | 3.48E6 | 0.9999 |
| T8 | 1295 | 3 | 40 | 4.25E8 | 0.9999 |
| T9 | 1306 | 3 | 20 | 4.02E8 | 0.9999 |

startup of the TADF lasted approximately 1 hour, until the temperature measured by the coolant thermocouple reached steady state. Once steady state was achieved, a picture was taken with the RGB camera to get an initial surface temperature (T_{s,i}) measurement. The particle feeder was then turned on, slowly entraining the flyash into the TADF gas flow. For deposition testing, the time that the particle feeder was turned on was considered t₀ = 0. The full SiC cone and SiC tube was used for the tests in this series.

An image was captured with the RGB camera every 10 minutes until the pre-determined end times were reached. Test T1, however, was shut down early at the 33 minute mark and a final RGB image was not captured after the 30 minute image was captured. In this transient test series, the two-color pyrometry method mentioned in Section 3.6 was used to analyze the RGB images and calculate a surface temperature.

[†] When processing the data to obtain T_g, it appeared that the thermocouple may have malfunctioned at the end of the test. Only the measured data from the first 26:20 (mm:ss) of the test was used to calculate T_g.

After the deposition period, the TADF was slowly shutdown. The coupon and the ash deposit had different coefficients of thermal expansion, causing them to contract at different rates as they cooled. If the rate of contraction differed too greatly, the ash deposit cracked and flaked off of the deposition surface. To avoid cracking and flaking of the deposit, the reactor was shut down slowly over a period of 30 min on average. After the TADF cooled sufficiently (usually overnight), the ash deposit was collected and analyzed.

5.2 Analysis

The three main parameters that were measured and calculated to characterize the ash deposit after testing were capture efficiency (η_{cap}), average surface roughness (R_a), and deposit thickness (h_{dep}). Capture efficiency was calculated according to Eq. (4-1) and R_a and h_{dep} were calculated as outlined in Section 3.7.2. The deposits from this test series were scanned by Wilcox Associates, Inc. using a ROMER INFINITE portable CMM and PC-DMIS metrology software.

The probability that an ash particle will stick to a surface on which it impinges is partly a function of the viscosity of that particle. To better understand the manner in which capture efficiency, surface roughness, and deposit thickness develop over time, the change in particle and deposit viscosity over time was also studied. The viscosity of the ash was calculated using Eq. (2-12) as outlined by Senior and Srinivasachar (1995). The sticking probability was also calculated according to Eq. (2-11) as outlined by Sreedharan and Tafti (2011). This included calculating the critical viscosity of the ash (the viscosity at T_{soft}). For the JB1 ash, μ_{crit} was calculated to be 610 Pa·s.

5.3 Results and Discussion

The results of the deposition experiments in the transient test series are presented here. The discussion is focused on the development of the deposit surface temperature, capture efficiency, thickness, surface roughness, and sticking probability with respect to time.

5.3.1 Surface Temperature

The increase of surface temperature with time can be seen in Figure 5-1 and Figure 5-2. As an example, Figure 5-1 shows the development of T_s over the entire surface of the coupon for test T3. Figure 5-2 shows the increase of the spatially-averaged T_s with time for each test conducted. While each test exhibited its own trend, the overall result was that T_s appeared to increase linearly with time. An interesting result can be seen in Figure 5-2. Tests T1, T3, and T4 each had an initial T_s that differed significantly from the initial T_s of the other tests. However, as time passed and T_s increased for these tests, the T_s became similar to the T_s of the remaining tests. It should also be noted that the T_s cannot increase indefinitely. Although the T_s of the 14 μm tests do not appear to level out in Figure 5-2, the T_s would eventually reach equilibrium.

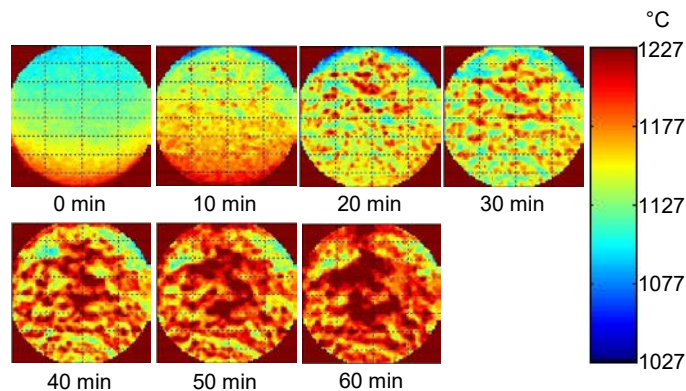


Figure 5-1: Surface temperature maps, at 10 minute increments for test T3 ($T_g = 1302^\circ\text{C}$, $\text{MMD} = 14 \mu\text{m}$).

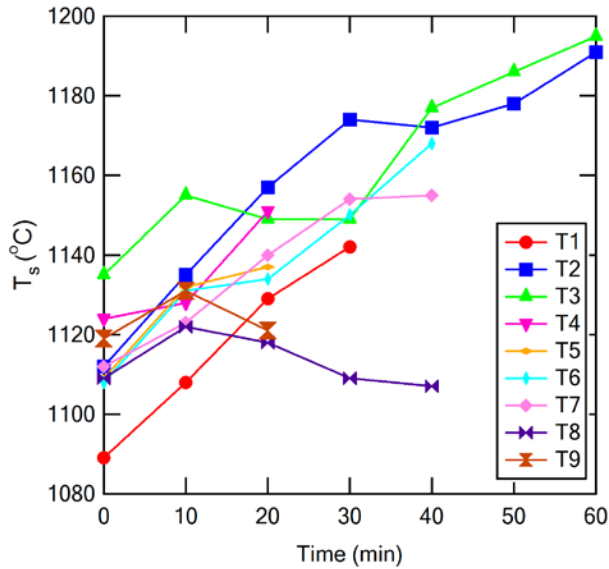


Figure 5-2: Increase of spatially-averaged coupon surface temperature with respect to time.

The T_s of tests T8 and T9, the 3 μm ash tests, increases initially, but then decreases again and the final T_s is within a couple degrees of the initial T_s . As will be shown in the following sections, the 3 μm tests experienced much less deposition and lower capture efficiencies than the 14 μm tests. It is believed that, as the deposit gets thicker over time, less heat is transferred through the deposit and the surface gets hotter. Since the 3 μm tests experienced less deposition, the surface temperature didn't increase as much and fluctuations in T_g may be more apparent in the resulting T_s data. The T_s data for test T3 (MMD = 14 μm) and tests T8 and T9 are shown again in Figure 5-3, along with the periodic T_g measurements from each test. Although there are fewer T_g measurements than T_s measurements, it appears that the T_s of tests T8 and T9 more closely follow the behavior of the respective T_g than does that of test T3.

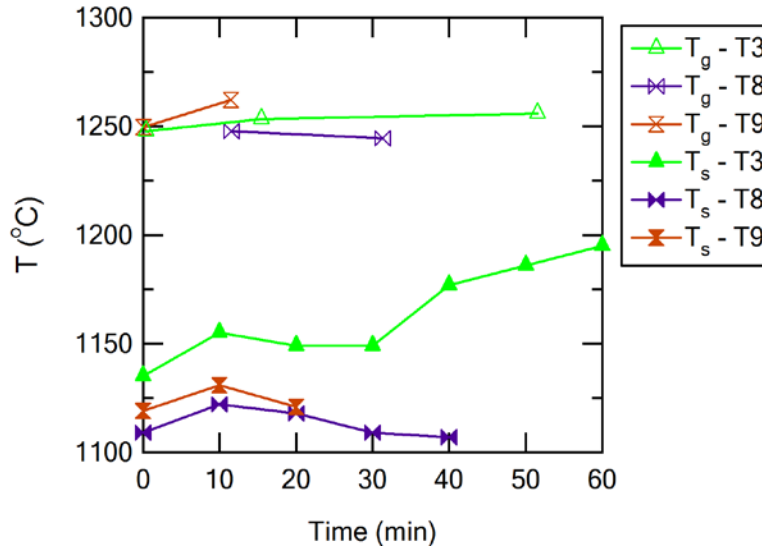


Figure 5-3: T_g and T_s measurements over time for test T3 (MMD = 14 μm) and tests T8 and T9 (MMD = μm).

5.3.2 Capture Efficiency

The capture efficiency was calculated according to Eq. (4-1) for each of the 9 tests and is shown in Figure 5-4. The capture efficiency of the 14 μm ash appeared to increase non-linearly with time, indicating that as an ash deposit forms it becomes a better captor of particles. As time decreases, the capture efficiency levels off. Extrapolating this trend past the collected data suggests that the capture efficiency does not approach zero at t_0 . While the shape of the curve at $t < 20$ minutes is not known, it makes sense that the capture efficiency cannot equal zero at the start of the test, otherwise no ash would deposit during the rest of the test unless the test conditions were changed. The degree to which the capture efficiency approaches zero at t_0 is likely dependent upon several factors, including the gas and surface temperature. In this test series, at these process conditions, the JB1 ash appears to deposit readily at the early stages of the tests.

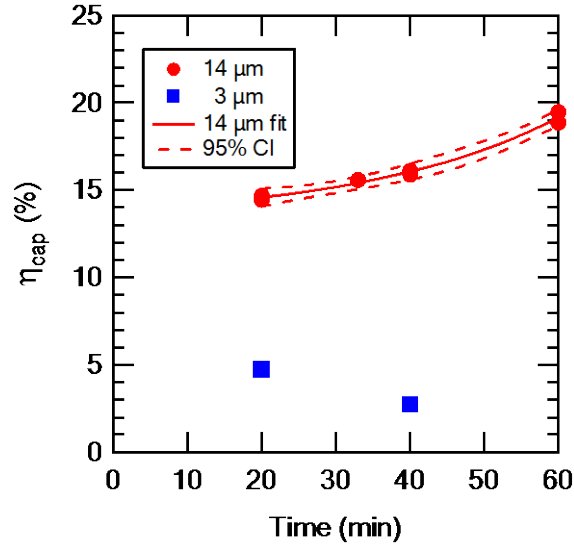


Figure 5-4: Time-dependent growth of capture efficiency. 95% confidence band is shown for the 14 μm fit.

A particle size effect can also be seen in Figure 5-4. The 14 μm particles exhibited capture efficiencies an order of magnitude greater than those of the 3 μm particles. This effect of particle size on capture efficiency was previously reported by Crosby et al. (2008) and Ai et al. (2011a). The current study resulted in a greater difference in capture efficiency between the two particle sizes, but this may be due to the fact that in both of the previous studies, tests were run at a T_g of 1183°C, while the current study used a T_g of 1295°C.

The 14 μm data was fit by the following regressed exponential equation where t is time in minutes.

$$\eta_{cap}(\%) = 0.626e^{0.0374t} + 13.3 \quad (5-1)$$

Only two tests were successfully completed with the 3 μm particles. The capture efficiency dropped from 20 minutes to 40 minutes, which was not expected and does not follow the same trend as the 14 μm ash. The T_g of the 40 minute test (T8) was lower than that of the 20 minute test

(T9), which may have contributed to the lower capture efficiency. With only two data points, however, it is impossible to conclude whether this is normal behavior or just a result of testing variation.

5.3.3 Deposit Thickness

The growth of the deposit thickness with time is shown in Figure 5-5. The deposit thickness increased with time. The best fit linear relationship for the 14 μm data was

$$h_{dep} = 0.108t + 0.0812, \quad (5-2)$$

where h_{dep} is deposit thickness in mm and t is time in minutes. The y-intercept for this equation was close to zero, which should be expected. At time equal to zero, no ash had yet been fed through the TADF, so no deposit had yet formed on the coupon. When the intercept was forced to be exactly zero, the equation simply became

$$h_{dep} = 0.112t, \quad (5-3)$$

resulting in only a 3.6% change in the slope. The slope represents an accrual rate of ash on the coupon, with the rate being 0.112 mm/min.

The effect of particle size on deposition was seen again in deposit thickness growth. Using the 20 and 40 minute data points from the 3 μm series and forcing the intercept to zero, the deposit thickness for 3 μm particulate can be described according to Eq. (5-4), giving an accrual rate of 0.0553 mm/min.

$$h_{dep} = 0.0553t \quad (5-4)$$

The increase in deposit thickness may have contributed to the increase in surface temperature over time as the thicker deposit prevented heat from being transferred away from the surface of the deposit.

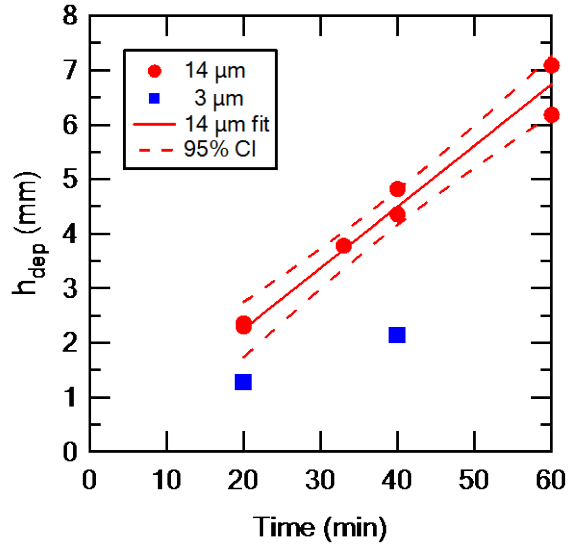


Figure 5-5: Deposit thickness growth with respect to time. 95% confidence band is shown for the 14 μm fit.

5.3.4 Deposit Roughness and Density

The centerline-average roughness, R_a , was calculated according to Eq. (3-15), and the results are shown in Figure 5-6. The R_a of the deposit increased with time. The best fit linear relationship for the 14 μm data was

$$R_a = 12.8t - 77.8. \quad (5-5)$$

It should be noted that the y-intercept of this linear fit is a negative value, which is not physically possible. The initial R_a value of the coupon before testing was 0.3-0.6 μm. Also, it is possible that the coupon surface becomes rougher during startup of the TADF due to heating and possible oxidation of the coupon surface at high temperatures, which would result in a greater R_a value at time equal to zero. One possible explanation for the discrepancy between the y-intercept of the fit and the R_a at t_0 is that the surface roughness may develop slower in the zero to 20 minute range as the deposit is first forming and then shifts to the fit given in Eq. (5-5). Another possible explanation

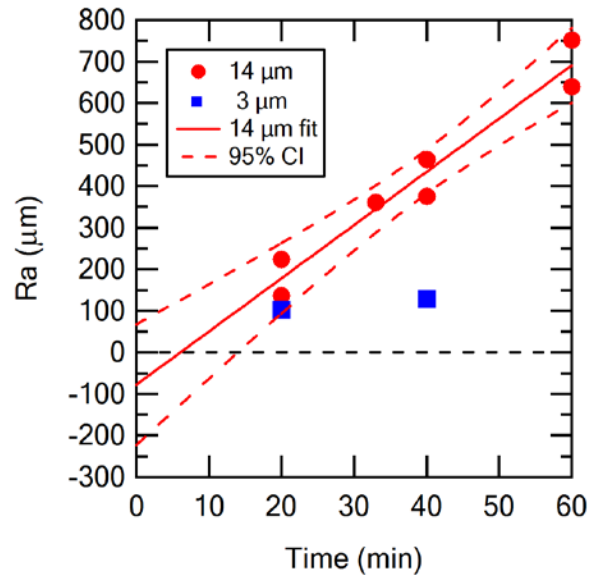


Figure 5-6: Average surface roughness (R_a) development over time. The 95% confidence band is shown for the 14 μm fit and is extrapolated to $t = 0$.

is that the negative y-intercept is simply due to statistical error. When extrapolated to zero, the 95% confidence bands take in positive values of R_a , suggesting that the negative intercept falls within statistical error and that the real value could be positive.

Using the 20 and 40 minute data points, the following best fit linear regression for the 3 μm data was obtained.

$$R_a = 1.28t + 77.2 \quad (5-6)$$

This regression is questionable because it is only based on two data points. More data, particularly at 60 minutes, would be required to obtain a more valid regression.

The increasing surface roughness may have also contributed to the increase in surface temperature by increasing convective heat transfer to the surface.

The density of the deposits (ρ_{dep}) was calculated using the bulk volume of the deposit (obtained from the optical surface scans) and the deposit mass. The ρ_{dep} values are plotted vs. time in Figure 5-7. The ρ_{dep} for the 14 μm tests increased as the test duration increased. This suggests that the porosity of the deposit decreased as the test duration increased. This could be due to the increasing surface temperature which could result in softer deposits, more liquid bridging and increased particle sintering. Kim et al. (1993) observed in some of their tests investigating deposition of volcanic ash that although the flame temperature was held constant, the deposit close to the blade surface was an agglomeration whereas the outer layer of deposit was molten. The molten layer would reasonably have a higher bulk density than the agglomerate layer, suggesting that the bulk density of the entire deposit would increase over time as the molten layer grew.

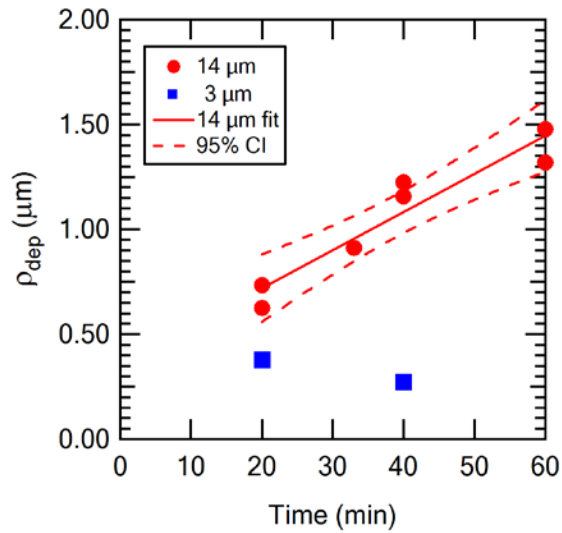


Figure 5-7: Deposit bulk density vs. time.

Robinson et al. (2001) also showed that as porous samples were allowed to sinter in a hot environment, the number of bridges between particles on the outer layer of the deposit increased as the sintering time increased from 1 hour to 12 hours, increasing the solid fraction of the deposit. The sintering times in the Robinson et al. (2001) tests are much longer than the deposition times used in the current test series (1 to 12 hr versus 20 to 60 min), but the deposit temperatures were also much lower than recorded in the current test series (greater than 650°C versus greater than 1189°C). The higher T_s of this test series could increase the rate of sintering and also lead to an increase in deposit bulk density over time.

The bulk density of the deposit from the 3 μm tests decreased as time increased. This could be due to the fact that the surface temperature of the 40 min test was lower than that of the 20 minute test, meaning that less bridging may have occurred in the 40 minute test.

5.3.5 Ash Viscosity and Sticking Probability

The viscosity and sticking probability of the ash were calculated according to Eq. (2-12) and Eq. (2-11). The lowest average T_g reported in Table 5-1 (1285°C) was higher than the softening temperature of the JB1 ash (1227°C), meaning that the sticking probability of ash with T_p equal to T_g was 1.0. The range of T_g reported in Table 5-1, result in a viscosity range of 169 Pa·s to 234 Pa·s. The true particle temperature was likely lower than the measured T_g by the time the particle impinges on the coupon surface. T_g was measured at the outlet of the equilibration tube, and some cooling could occur between the outlet of the equilibration tube and the coupon surface. The center of the coupon was approximately 3.8 cm above the outlet of the equilibration tube.

Figure 5-8 displays particle temperatures (T_p) obtained from CFD simulations, described in detail in Chapter 10, as the particles impact the coupon surface. Four particle sizes are shown ($d_p = 0.4, 1, 2, 3$ and $4 \mu\text{m}$). The vertical dotted line represents the T_{soft} of the JB2 as (1224°C). Figure 5-8 shows that smaller particles are more likely to cool down to temperatures below T_{soft} before impacting the coupon, thus decreasing their probability of sticking upon impact.

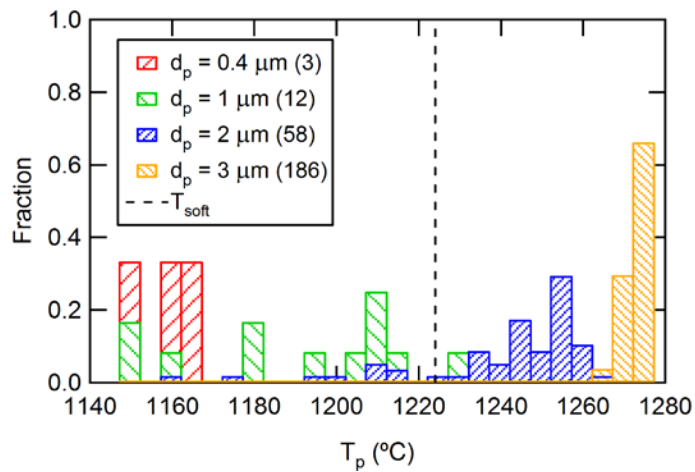


Figure 5-8: Histogram of particle temperatures (T_p) obtained from CFD simulations as the particles impact the coupon. The dotted black line indicates the softening temperature of the JB2 ash and the numbers in parentheses indicate the number of particles that impacted the coupon.

The conditions of the surface on which the particles impinge also have an effect on deposition. For this reason, the viscosity and sticking probability of the ash on the surface of the deposit were calculated as well. The temperature maps, like those shown in Figure 5-1, were used to calculate the viscosity and sticking probability of the surface ash. After deposition started, the measured surface temperature was the temperature of the ash at the surface of the deposit. For this reason, each pixel on the temperature map was treated as an ash particle and the sticking

probability was calculated for each pixel. Rather than representing the probability of a particle at a certain temperature sticking to a surface upon impaction, this probability represents the probability of a particle sticking to a surface ash particle of a particular temperature.

After the P_s values were calculated for each pixel of the temperature map, the P_s values were averaged together, giving a mean P_s for each temperature map. The mean, maximum, and minimum P_s , with respect to time, are shown in Figure 5-9, Figure 5-10, and Figure 5-11 respectively.

The maximum possible T_s at any point was T_g . However, when measuring the surface temperature by taking pictures with the RGB camera, it was possible for the pixel intensity to be too great, resulting in pixel saturation. When a pixel was saturated, the temperature could not be accurately calculated for that pixel, resulting in T_s greater than T_g , which was not physically possible. Any calculated T_s greater than the average T_g for its respective test was omitted from the calculations for P_s . Only 0.01% of the calculated pixel temperatures were omitted.

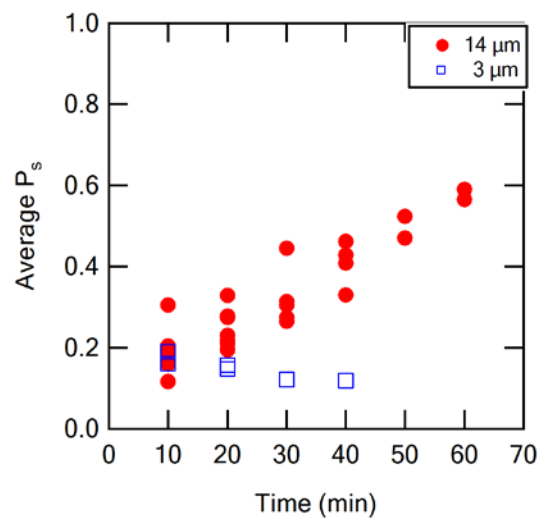


Figure 5-9: Change in average P_s of the surface ash with time.

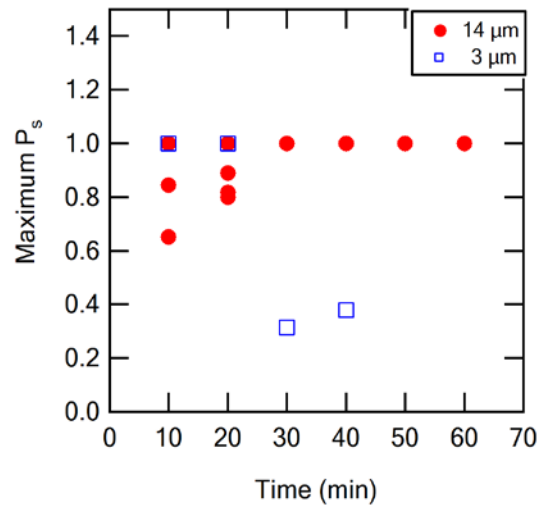


Figure 5-10: Change in the maximum P_s of the surface ash with time.

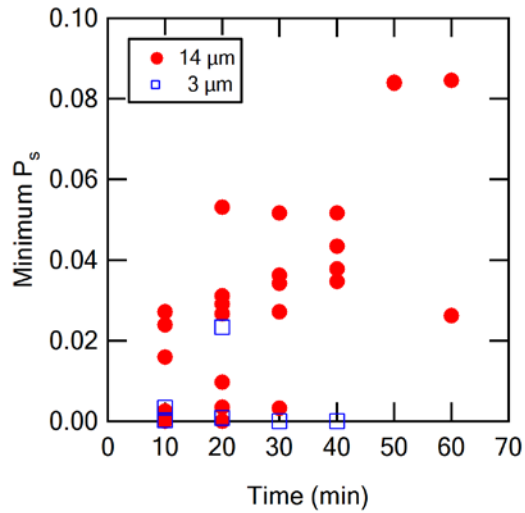


Figure 5-11: Change in the minimum P_s of the surface ash with time.

The average P_s can be seen to increase with time as the surface temperature increases for the 14 μm particles. This increase in average surface P_s could contribute to the increase in capture

efficiency with time. However, the average P_s appeared to increase linearly while the capture efficiency appeared to increase non-linearly. This indicates that other factors aside from T_s , which determines P_s , contribute to the increase in capture efficiency with time. One possibility is that as R_a increases the surface topography allows for better capture of particles.

The average P_s for the 3 μm particles decreased with time, similar to the capture efficiency. There is a dramatic drop in the maximum P_s after 20 minutes, which correlates with the drop in T_s for test T8 while the T_s for tests T1-T3, T6 and T7 increased (tests T2, T3 and T9 ended at 20 minutes). The drop in P_s could have resulted in the drop in capture efficiency for the 3 μm particles.

The distribution of P_s over the entire surface of the deposit for the tests using 14 μm ash is shown in Figure 5-12. The data are split into 100 bins with bin sizes of 0.01. There are two peaks in each distribution. At low P_s the peak in the distribution decreased and the wings of the distribution increased with time. The broadened distributions were due to increased temperatures over more of the deposition surface. The second peak occurred in the final bin where $0.99 < P_s \leq 1.0$. The height of this peak increased as time increased. This indicates that, as time progressed, the T_s exceeded T_{soft} at more points on the surface and P_s maxed out at 1.0 at these points.

5.4 Summary and Conclusions

The time-dependent deposition characteristics for fine coal flyash from a subbituminous coal were measured in the TADF at Brigham Young University. Two different size distributions of flyash were used in this study, with mass mean diameters of 14 μm and 3 μm . The time-dependent nature of surface temperature, capture efficiency, deposit thickness, deposit surface roughness, and ash viscosity were measured and calculated, resulting in the following conclusions for the 14 μm particles:

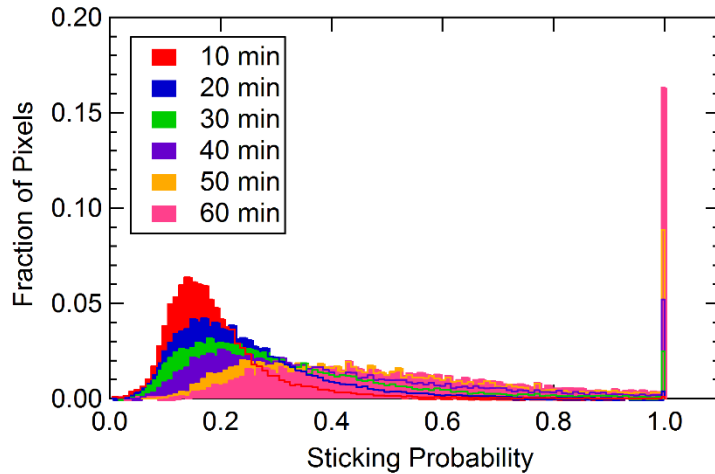


Figure 5-12: Distribution of sticking probability for pixels over the observed face of the coupon as a function of time.

1. Net capture efficiency, surface roughness and deposit thickness all increased with time, with capture efficiency appearing to increase non-linearly.
2. Surface temperature increased with time, possibly due to increasing deposit thickness which increases thermal resistance and reduces conductive heat transfer away from the surface as well as increasing surface roughness which could increase convective heat transfer to the surface. Increasing surface temperature resulted in decreased viscosity and increased probability of a particle sticking to the surface with time.
3. This increase in sticking probability, along with the increase in surface roughness, likely causes the increase in net capture efficiency.

These data and conclusions provide necessary information to be used to further improve and expand current deposition models to allow for transient modeling. The 3 μm particles exhibited capture efficiencies 67%-83% smaller than the 14 μm particles. While the 3 μm particles were

expected to behave similarly to the 14 μm particles but on a smaller scale, the capture efficiency actually decreased with time. There is currently insufficient data to determine if this is the normal behavior or a result of testing variation.

6 TEMPERATURE-DEPENDENT CHARACTERISTICS*

Most of the studies summarized in Table 2-1 were conducted at gas temperatures below 1200°C. Modern technologies allow for higher turbine inlet temperatures in excess of 1400°C (Lebedev and Kostennikov, 2008). At these higher operating temperatures, it is important to understand how the previously mentioned factors continue to contribute to the problem of deposition and if there is a dominating factor. The TADF at BYU has been modified to handle gas temperatures over 1400°C. It has been shown at temperatures below 1400°C that gas and surface temperatures both influence ash deposition, but that the influence of surface temperature can be impacted by the gas temperature (Anderson et al., 1990). This chapter presents the results of two test series that were conducted in the TADF to investigate the individual effects of gas temperature and surface temperature on ash deposition at gas temperatures up to 1400°C.

6.1 Test Conditions

Two test series were conducted in this study. The first series, meant to investigate the individual effect of gas temperature (T_g) on deposition behavior, consisted of tests where the initial surface temperature ($T_{s,i}$) was held constant near 1000°C and T_g was varied from 1261°C to 1413°C. The SiC cone and SiC tube configuration was used for each test in this series. In the

* This chapter resulted in the following publication: Laycock, R. G., and T. H. Fletcher, "Independent Effects of Surface and Gas Temperature on Coal Fly Ash Deposition in Gas Turbines at Temperatures up to 1400 °C," ASME Journal of Engineering for Gas Turbines and Power, v. 138, n. 2, February 2016

second series, meant to investigate the individual effect of $T_{s,i}$, T_g was held constant near 1400°C and $T_{s,i}$ was varied from 894°C to 1142°C. The conditions for each test are summarized in Table 6-1 and Table 6-2. Test S1, shown in Table 6-2, was performed using the SiC cone and SiC tube as well. However, it was at this point that the decision was made to switch from a full SiC cone and SiC tube to a SiC cone and quartz tube. The remaining tests in this series (S2-S15) were performed using the two piece SiC/quartz configuration. The mass of ash delivered (m_{del}) reported in Table 6-1 and Table 6-2 is the final mass of ash that exited the equilibration tube below the coupon. The JB2 ash was used for both test series.

An image was captured with the RGB camera every 10 minutes until the pre-determined end times were reached, or until all of the ash in the syringe had been fed into the TADF, at which point a final image was captured. The two-color pyrometry method mentioned in Section 3.6 was used to analyze the RGB images and calculate surface temperatures for the tests in the constant $T_{s,i}$ test series (tests G1-G9) and for the first test in the constant T_g test series (test S1). The single color technique was used for the remaining constant T_g tests (S2-S15).

Table 6-1: Test conditions and data for the test series varying T_g

| Test # | T_g (°C) | $T_{s,i}$ (°C) | m_{del} (g) |
|-----------------|------------|----------------|---------------|
| G1 | 1299 | 1020 | 7.77 |
| G2 | 1265 | 1026 | 7.92 |
| G3 | 1261 | 969 | 9.91 |
| G4 | 1309 | 1039 | 4.13 |
| G5 | 1315 | 1030 | 7.47 |
| G6 | 1311 | 1027 | 10.61 |
| G7 [†] | 1311 | 1067 | 11.21 |
| G8 | 1413 | 1014 | 9.96 |
| G9 | 1361 | 1001 | 9.96 |

[†] This test is excluded from the data presented in the results and discussion due to excessive faceplate deposit growth onto the coupon, as discussed in Section 4.2.

Table 6-2: Test conditions and data for the test series varying $T_{s,i}$

| Test # | T_g (°C) | $T_{s,i}$ (°C) | m_{del} (g) |
|-----------------|------------|----------------|---------------|
| S1 [‡] | 1406 | 1128 | 11.1 |
| S2 | 1402 | 899 | 12.88 |
| S3 [‡] | 1413 | 1026 | 11.56 |
| S4 | 1414 | 964 | 8.59 |
| S5 | 1414 | 1124 | 7.58 |
| S6 | 1413 | 1075 | 8.95 |
| S7 | 1419 | 930 | 10.36 |
| S8 | 1404 | 1051 | 10.25 |
| S9 | 1412 | 1090 | 10.94 |
| S10 | 1412 | 1096 | 7.2 |
| S11 | 1410 | 961 | 8.63 |
| S12 | 1411 | 1122 | 9.25 |
| S13 | 1410 | 1142 | 8.6 |
| S14 | 1413 | 1130 | 10.81 |
| S15 | 1412 | 894 | 8.85 |

6.2 Analysis

Three parameters were measured and calculated to characterize the ash deposit after testing: capture efficiency (η_{cap}), average surface roughness (R_a), and deposit density (ρ_{dep}). Capture efficiency is still as previously defined and was calculated according to Eq. (4-1) for the constant $T_{s,i}$ test series. However, it was discovered that not only was ash depositing in the equilibration tube, but ash was also settling in the feed tube between the particle feeder and the base of the combustor. After this discovery, the feed tube was removed after each test and the ash inside the feed tube was collected and weighed. Starting with the constant T_g test series, this ash was also taken into account when calculating the capture efficiency, as shown in Eq. (6-1) where m_{dep} is the mass deposited on the coupon, m_{fed} is the amount of ash fed into the TADF, $m_{tube,e}$ is the mass of

[‡] These tests were excluded from the data presented in the results and discussion due to excessive faceplate deposit growth onto the coupon, as discussed in Section 4.2.

ash that was deposited on the inside of the equilibration tube, and $m_{tube,f}$ is the mass of ash that remained in the feed tube ($m_{acc} = m_{tube,e} + m_{tube,f}$).

$$\eta_{cap} = \frac{m_{dep}}{m_{fed} - m_{tube,e} - m_{tube,f}} \quad (6-1)$$

In the case of the single-piece SiC cone and tube configuration, $m_{tube,e}$ was measured by grinding the deposited ash from the inside of the equilibration tube and weighing it after each test. In the case of the 2-piece SiC/quartz configuration, the tube was weighed before and after each test. The difference in weight was the amount of ash that deposited inside the tube. After weighing the quartz tube to determine the amount of ash that had deposited, the inside of the quartz tube was still ground to attempt to remove the ash that had deposited, but not all of the ash could be removed without fear of breaking the tube. The capture efficiency was again adjusted for the percent of deposit recovered, as described in Section 5.2.

XYZ point clouds were again obtained for each deposit from CMM scans. The deposits were taken to a different local company, Diversified Metal Services, Inc., because Wilcox Associates, Inc. was no longer operating locally. The scans at Diversified Metal Services, Inc. were performed using a FaroArm Platinum CMM.

6.3 Results and Discussion

Results of the test series with constant initial surface temperature ($T_{s,i}$) are presented and discussed first, followed by data from the series with constant gas temperature (T_g).

6.3.1 Constant $T_{s,i}$ Series

The following data are discussed in this section: capture efficiency, surface roughness, deposit density, surface temperature, and the physical structure and appearance of the deposit.

6.3.1.1 Capture Efficiency

As can be seen in Table 6-1, the m_{del} was not very consistent, mainly due to the particle feeder malfunctioning in the middle of some of the tests (particularly tests G1-G5). The problem was fixed and the particle feeder functioned properly for the remainder of the tests. Figure 6-1 compares the capture efficiencies for tests G4-G6, which were all conducted at a T_g close to 1300°C and had greatly varying masses of ash delivered. Figure 6-1 also indicates the corresponding $T_{s,i}$ for each of the tests. Although the $T_{s,i}$ decreased very slightly over the first three tests, the capture efficiency increased as the m_{del} increased. This increase in capture efficiency with increasing m_{del} is consistent with the results concerning transient deposition behavior discussed in Chapter 5.

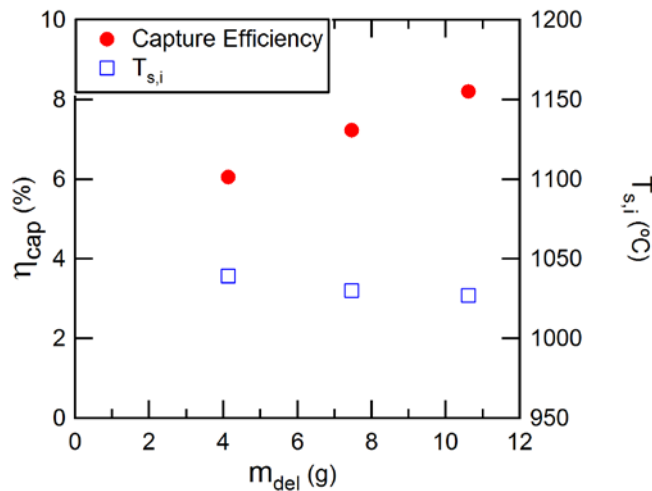


Figure 6-1: Capture efficiency vs. mass of ash delivered for T_g close to 1300°C. The corresponding $T_{s,i}$ for each test are also shown.

Since the m_{del} has an effect on the capture efficiency, the best tests to isolate the effect of T_g are tests G3, G6, G8 and G9, which cover the range of T_g tested and had similar m_{del} . These tests are the red squares in Figure 6-2. The data from the rest of the tests are plotted in Figure 6-2 as well. While the variation in mass of ash fed may contribute to the scatter seen in Figure 6-2, the overall trend with respect to T_g is similar to that of tests G3, G6, G8 and G9, indicating that T_g has a strong effect on particle deposition.

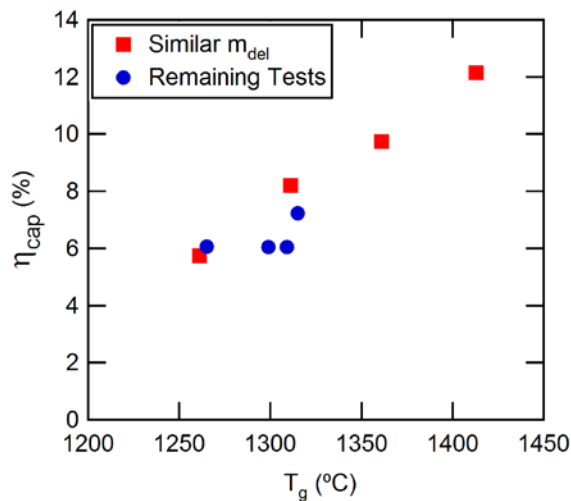


Figure 6-2: Variation in capture efficiency with respect to gas temperature. The red squares represent tests that had a similar m_{del} (G3, G6, G8, and G9). The blue circles represent the rest of the tests included from Table 6-1.

6.3.1.2 Surface Roughness and Density

Figure 6-3 and Figure 6-4 show the effect of T_g on surface roughness and deposit density, respectively. Both R_a and ρ_{dep} are shown to increase with increasing T_g . The increasing roughness can be attributed to the increasing capture efficiency. As more ash deposits, larger structures are formed that increase the average roughness of the surface. The increasing deposit density may be attributed to the ash particles being in a softer or more molten state at higher T_g . More molten

particles could increase the amount of liquid bridging occurring between particles, thus reducing the void space in the deposit.

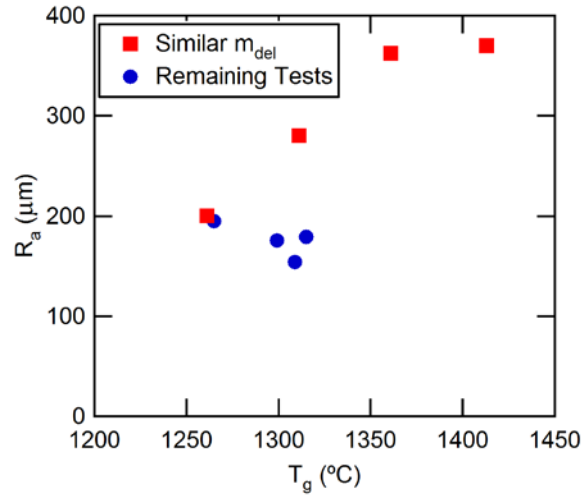


Figure 6-3: Average surface roughness with respect to gas temperature. The red squares represent tests that had a similar m_{del} (G3, G6, G8, and G9). The blue circles represent the rest of the tests included from Table 6-1.

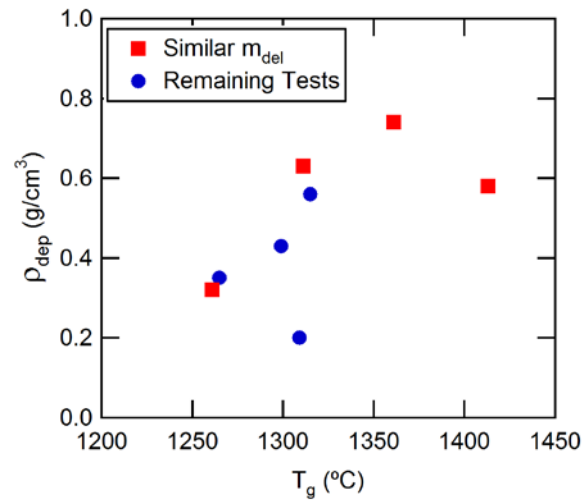


Figure 6-4: Deposit bulk density with respect to gas temperature. The red squares represent tests that had a similar m_{del} (G3, G6, G8, and G9). The blue circles represent the rest of the tests included from Table 6-1.

Figure 6-5 and Figure 6-6 show ESEM images of the deposits from tests G3 ($T_g = 1261^\circ\text{C}$) and G8 ($T_g = 1413^\circ\text{C}$). These images show that at higher T_g , the particles have formed a smoother and more continuous structure, whereas more of the individual particles and agglomerates can be discerned at lower T_g . Comparing the roughness and density data, increased T_g results in larger structures that have smoother surfaces. The calculated density decreases at the highest gas temperature, although the reason for this is not clear. Increasing roughness has a detrimental effect on turbine efficiency (Kurz and Brun, 2001) and increases heat transfer to the turbine surface (Bogard et al., 1998; Bons et al., 2008). However, there is a competing effect on heat transfer. As the deposit gets thicker, the deposit itself forms an insulating layer that reducing heat transfer to the turbine surface.

6.3.1.1 Surface Temperature

The deposit forms an increasingly thicker insulating layer as the test progresses. As the deposit grows thicker, the thermal resistance of the deposit layer increases and less heat is transferred through the deposit and coupon. This decrease in heat transfer increases the instantaneous T_s of the deposit. For the four similar tests highlighted in Figure 6-2, the development of the spatially-averaged T_s over the course of each test is shown in Figure 6-7. Figure 6-8 shows the development of the T_s profile throughout the course of test G8 ($T_g = 1413^\circ\text{C}$). The temperature profile develops in the same manner as the physical deposit. The hot spots on the temperature profile are located at the peaks of the deposit, while the cooler spots are located at the valleys of the deposit and the regions with little deposition.

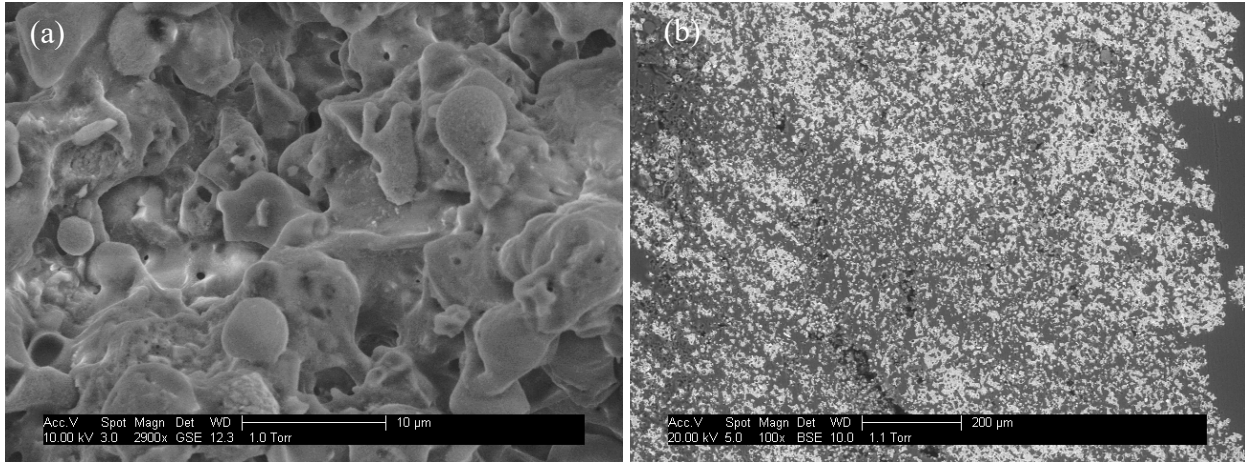


Figure 6-5: ESEM images of deposits from test G3 ($T_g = 1261^\circ\text{C}$). (a) Outer surface and (b) cross-section.

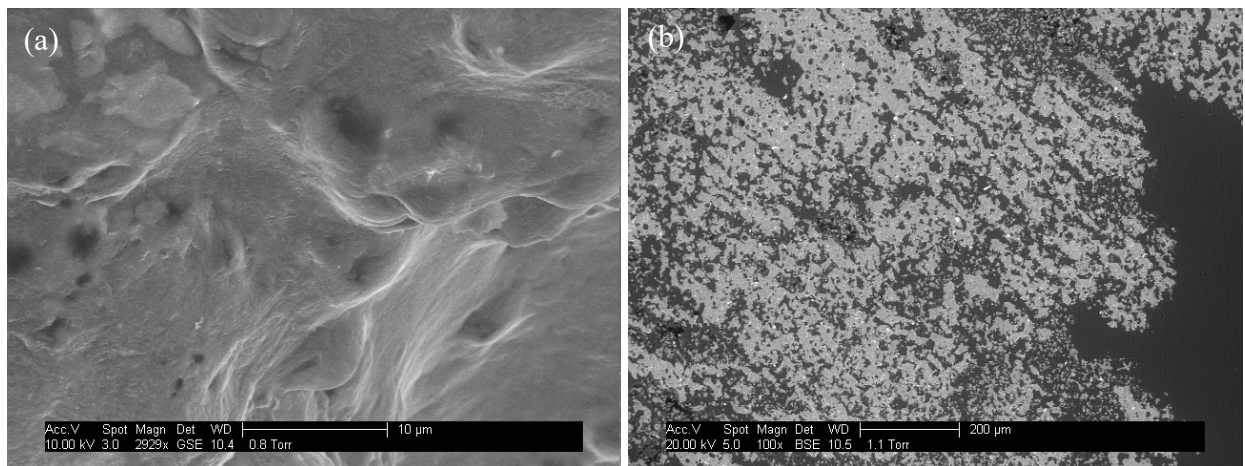


Figure 6-6: ESEM images of deposits from test G8 ($T_g = 1413^\circ\text{C}$). (a) Outer surface and (b) cross-section.

The change in average T_s between the initial value and the value at 60 minutes for the 4 tests is shown in Table 6-3, along with the capture efficiency of each test. It can be seen that as T_g increased, both the capture efficiency increased (more ash was deposited) and the change in surface temperature (ΔT_s) increased.

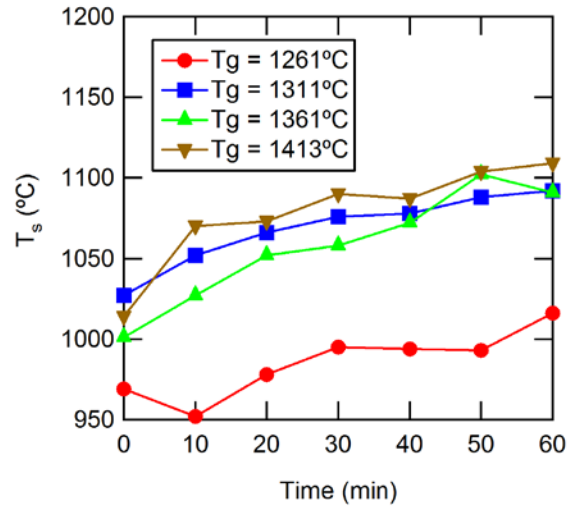


Figure 6-7: Increase in average surface temperature with respect to time for tests G3 ($T_g = 1261^\circ\text{C}$), G6 ($T_g = 1311^\circ\text{C}$), G8 ($T_g = 1413^\circ\text{C}$), and G9 ($T_g = 1361^\circ\text{C}$).

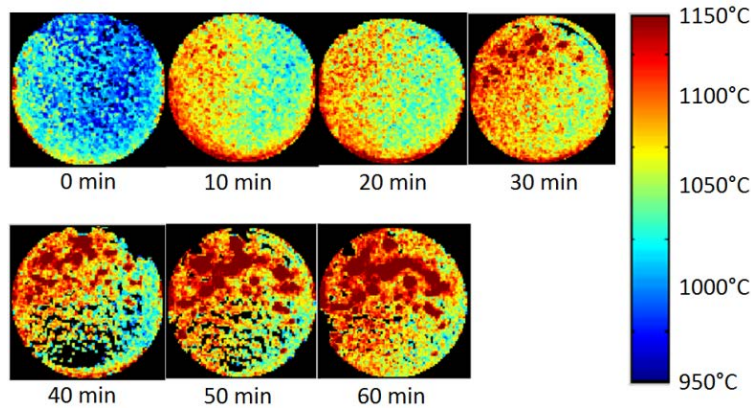


Figure 6-8: Surface temperature profiles measured during test G8 ($T_g = 1413^\circ\text{C}$).

Table 6-3: Dependence of the increase in average surface temperature on gas temperature

| T_g ($^\circ\text{C}$) | Capture Efficiency (%) | ΔT_s ($^\circ\text{C}$) |
|----------------------------|------------------------|-----------------------------------|
| 1261 | 5.75 | 47 |
| 1311 | 8.20 | 65 |
| 1361 | 9.74 | 90 |
| 1413 | 12.15 | 95 |

6.3.1.2 Physical Structure and Appearance

Photos of each deposit were taken after every test. Figure 6-9 presents photos of the deposits from tests G3, G6, G8, and G9. At a T_g of 1261°C, a uniform deposit pattern is apparent, with structures that appear to have grown against the direction of the gas flow (the direction of gas flow is indicated by the arrow). As T_g increased, the formation of large, non-uniform structures that grew in the direction of the flow occurred, implying softening behavior of the ash and influence of the high-speed flow along the surface. To see the effect of deposit thickness on surface temperature, the final image in Figure 6-8 (temperature profile of test G8) can be compared directly to the photo of the deposit from test G8 shown in Figure 6-9. The hottest areas in Figure 6-8 correspond with the biggest formations in Figure 6-9.

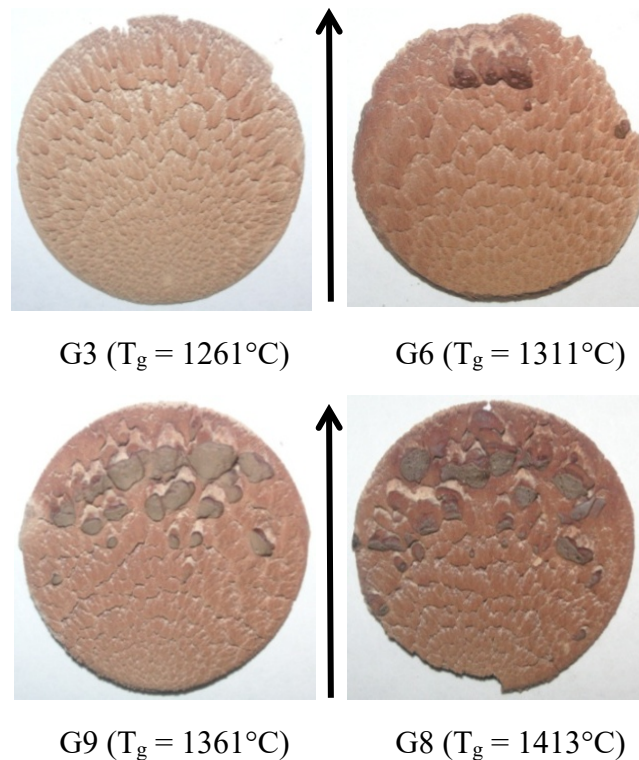


Figure 6-9: Photos of ash deposits collected from tests G3, G6, G9, and G8 respectively. The arrows indicate the direction of the gas flow during deposition.

6.3.2 Constant T_g Series

The following data are discussed in this section: capture efficiency, surface roughness, deposit density, surface temperature, and the physical structure and appearance of the deposit. While the goal was to run all of the tests at a T_g of 1400°C, Table 6-2 shows that there was some variation in the average T_g from test to test, ranging from 1402°C to 1419°C. The mass of ash fed also varied, ranging from 7.2 g to 12.88 g. To account for the undesired variation in T_g and mass of ash fed, the data have been classified into 4 ranges: low T_g (1402°C - 1410°C), high T_g (1411°C - 1419°C), low m_{fed} (7.2g - 9.25g) and high m_{fed} (10.25g -12.88g). The four combinations of the ranges of T_g and m_{fed} are plotted as four separate series.

The results from tests S1 and S3 are not reported here. After reviewing video recordings of the deposition tests, it was determined that a significant portion of the deposit that formed on the coupon in these tests was actually deposit that initially formed on the faceplate downstream and then grew upstream onto the coupon, as shown in the sequence of images in Figure 4-1.

6.3.2.1 *Capture Efficiency*

The effect of $T_{s,i}$ on capture efficiency is shown in Figure 6-10. At lower temperatures ($T_{s,i} = 894^\circ\text{C} - 964^\circ\text{C}$), the capture efficiency increases with increasing $T_{s,i}$. This behavior matches that seen in other studies (Wenglarz and Fox Jr, 1990a; Crosby et al., 2008) and is expected. As $T_{s,i}$ increases, the surface of the deposit softens and is able to trap more particles. However, at higher temperatures ($T_{s,i} = 1026^\circ\text{C} - 1142^\circ\text{C}$) the capture efficiency decreases with increasing $T_{s,i}$. This behavior was not expected. This decrease in capture efficiency could be the result of the deposit viscosity becoming too low, decreasing the stickiness of the deposit and trapping fewer particles. It has also been observed during tests that some ash will detach from the deposit, as shown in

Figure 6-11. It is possible that as $T_{s,i}$ increases, more of the ash is blown off of the deposit later on in the test as T_s continues to increase. The point in Figure 6-10 where the trend changes from increasing capture efficiency to decreasing capture efficiency may represent a transition point where the increase in ash detachment is greater than the increase in ash deposition.

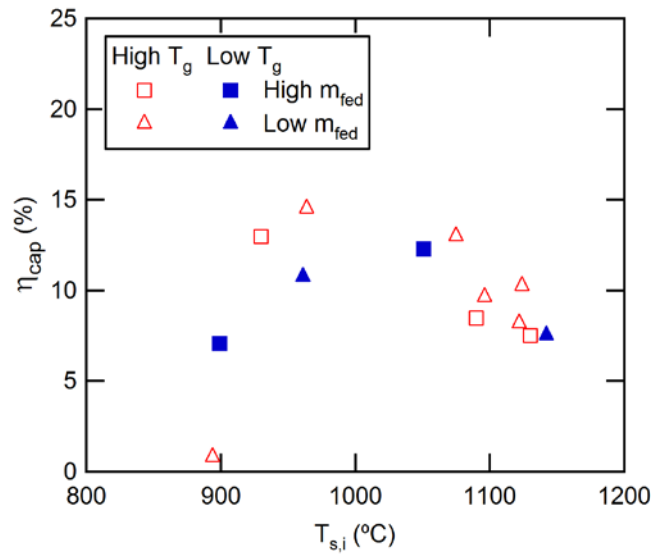


Figure 6-10: Capture efficiency versus initial surface temperature of the coupon.

6.3.2.1 Surface Roughness and Density

Figure 6-12 and Figure 6-13 show the effect of $T_{s,i}$ on surface roughness and deposit density. There is no surface roughness or deposit density data available for tests S5, S10, S12, S13, or S15. The deposits from these tests broke into several pieces either during shutdown or removal from the coupon and were not scanned. Similar to capture efficiency, the surface roughness decreases with increasing $T_{s,i}$. There is no clear trend for the deposit density.

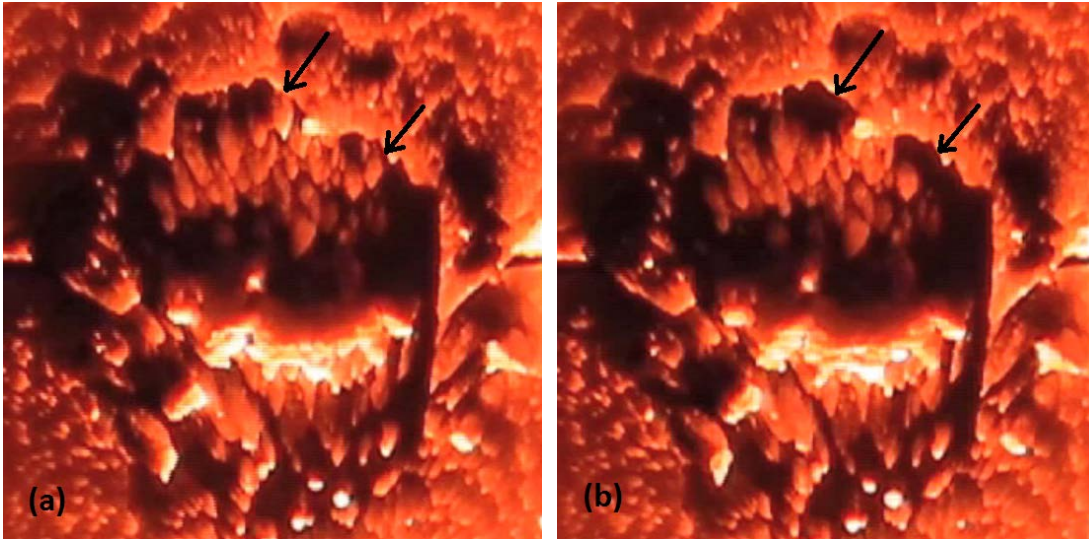


Figure 6-11: Deposit detachment during test S2 ($T_g = 1402^\circ\text{C}$, $T_{s,i} = 899^\circ\text{C}$), (a) before detachment occurs and (b) after detachment occurs. The arrows indicate the locations where the detachment occurs.

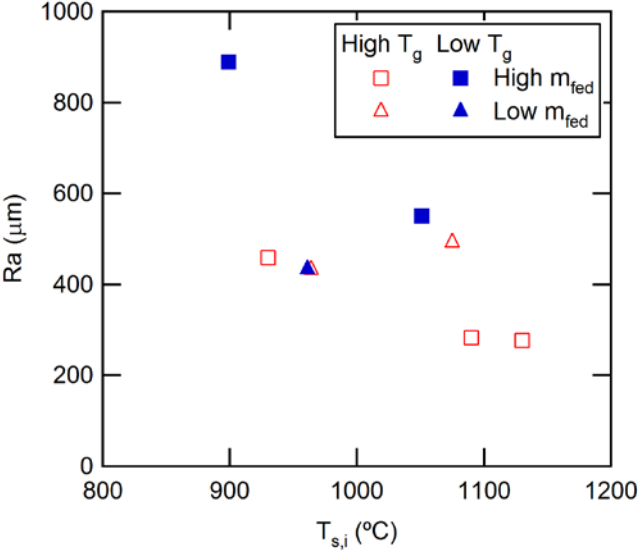


Figure 6-12: Surface roughness versus initial surface temperature of the coupon.

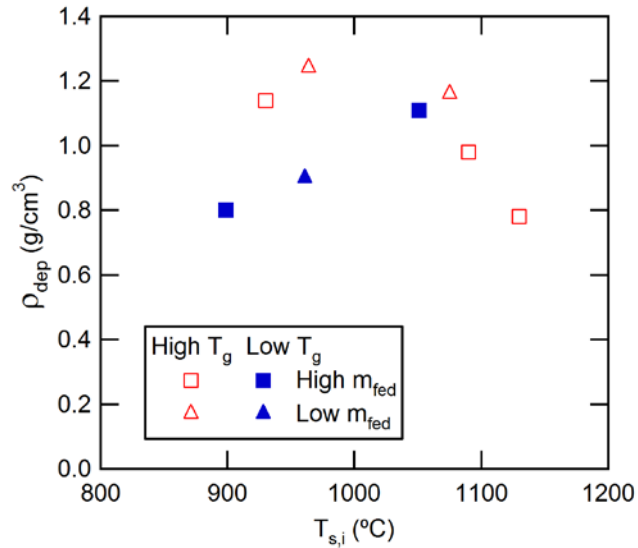


Figure 6-13: Deposit density versus initial surface temperature of the coupon.

6.3.2.2 Physical Structure and Appearance

Figure 6-14 shows photos of deposits collected during the constant T_g series of tests. These tests were all conducted at T_g close to 1400°C. The physical appearance of these deposits is very similar to the fourth image in Figure 6-9 ($T_g = 1413^\circ\text{C}$). $T_{s,i}$ does not appear to have much of an effect on the outward appearance of these deposits.

6.3.3 Equilibration Tube Capture Efficiency

As is reflected by $m_{tube,e}$ in Eq. (6-1), some of the ash fed into the TADF deposits on the inside surface of the equilibration tube. Figure 6-15 presents capture efficiency data for the inside of the equilibration tube. As the gas flow in the tube is parallel to the wall of the equilibration tube, these data show the effect of impact angle on deposition rate. The equilibration tube capture efficiency was calculated according to Eq. (6-2).

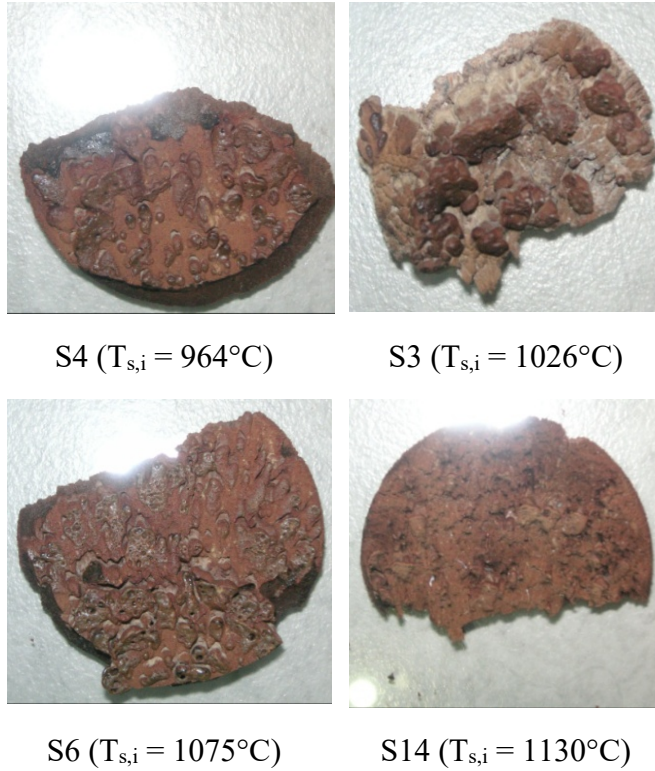


Figure 6-14: Photos of ash deposits collected from tests S4, S3, S6, and S14 respectively.

$$\eta_{cap} = \frac{m_{dep}}{m_{fed} - m_{tube,f}} \quad (6-2)$$

For comparison purposes the equilibration tube capture efficiency was multiplied by the ratio of the coupon surface area to the tube inner surface area, resulting in a capture efficiency per equivalent coupon area.

The surface temperature of the inside wall of the equilibration tube was not measured. However, the equilibration tube was wrapped in insulation and the inner wall temperature was assumed to be close to the local gas temperature. Figure 6-15 shows that the equilibration tube capture efficiency increases linearly with outlet T_g . The capture efficiencies reported here for the

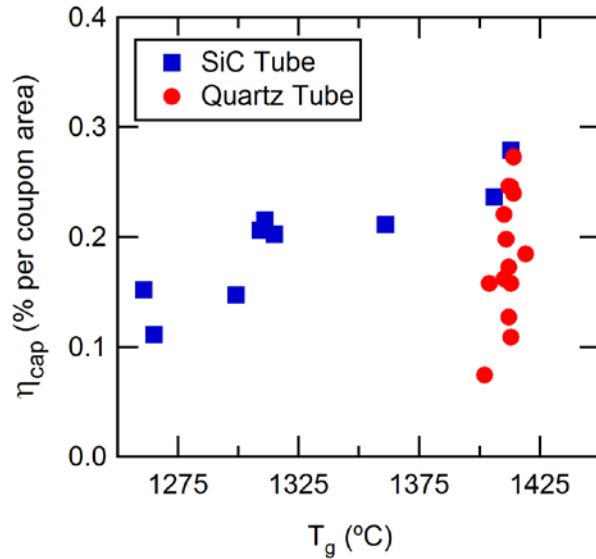


Figure 6-15: Equilibration tube capture efficiency data.

parallel surface are, on average, 97.1% lower than those reported for the coupon at a 45° angle to the flow for the same test. Only test S15, with a tube capture efficiency per coupon area that was 78.2% lower than the capture efficiency recorded on the coupon for the same test, exhibited a tube capture efficiency per coupon area that was less than 96.5% smaller than the corresponding coupon capture efficiency. It can also be seen that the type of surface has an impact on the capture efficiency. Both the SiC and quartz tubes exhibit a similar range of capture efficiency, but the SiC equilibration tube exhibits a trend in T_g while the quartz tube does not. While the quartz tube was cleaned in between each test, less of the deposit was removed than from the SiC tube because of the fragile nature of the quartz tube. The quartz tube was replaced periodically, and the build up process would begin again. It is possible that this build up of ash deposit in the quartz tube affected the scatter in the quartz tube data.

6.4 Summary and Conclusions

The TADF was used to collect deposits from fine particles (MMD $\sim 5 \mu\text{m}$) flowing at approximately 200 m/s and gas temperatures up to 1419°C. These conditions mimic the temperatures and velocities in the first stage of a gas turbine under IGCC conditions, except for the pressure. Two series of experiments were conducted: one series to vary gas temperature with constant initial surface temperature, and a separate series to vary initial surface temperature. The goal is to provide data to permit subsequent models to independently quantify the effects of particle temperature and deposit temperature on capture efficiency.

The experiments that varied gas temperature while holding the initial surface temperature constant showed increases in capture efficiency with increased T_g , as expected. There was some sensitivity of the capture efficiency to the total mass fed. The surface roughness also increased with increasing T_g , while the deposit density first increased then decreased as T_g increased. Time-dependent surface temperature maps were shown, and the average surface temperature increase as a function of time was shown for different values of T_g . Deposits generated were not smooth, and showed clumping that may be caused by the increased softening at higher temperatures as well as the effects of the high speed flows along the surface.

The experiments that held the gas temperature constant and varied the initial surface temperature showed first an increase then a decrease in capture efficiency with increasing $T_{s,i}$. The increasing capture efficiency was similar to other tests, and is a result of increased softening behavior. However, the decrease in capture efficiency at initial surface temperatures above 1000°C was unexpected and is thought to be due to increased deposit shedding as the surface temperature increased. The surface roughness decreased with increasing $T_{s,i}$ as well in these tests.

The impingement angle of the flow onto the deposit surface, as well as the surface material and conditions, affects the rate of deposition, with capture efficiency dropping dramatically when looking at flow that is parallel to the deposit surface.

7 ASH-DEPENDENT CHARACTERISTICS

The previous chapters in this study have focused on how the process conditions can affect deposition behavior in gas turbines. Another important aspect in ash deposition is the ash characteristics. The ash characteristics (ash composition, density, particle size, etc.) determine how the ash particles will react to the process conditions. To explore deposition behavior amongst a variety of ash types, a test series was conducted with ash samples from 4 different types of coal. The results of this test series are presented in this chapter and are compared to results obtained from tests in the constant T_g test series, which used the JB2 ash, at similar process conditions.

7.1 Test Conditions

The tests in the previous series were all performed with subbituminous coal ash from the Jim Bridger Power Plant, either JB1 or JB2. In order to observe the deposition characteristics of other ashes with varying properties, tests were performed with the other coal ashes listed in Table 3-1 (petcoke, lignite, and bituminous), with the major differences being the chemical composition and density of the ash. The test conditions for this series are summarized in Table 7-1.

7.2 Analysis

Capture efficiency (η_{cap}), average surface roughness (R_a), and deposit density (ρ_{dep}) were measured and calculated for each deposit sample as previously described. The 2-piece SiC cone and quartz tube configuration was used for each test in this series, except for the petcoke test

Table 7-1: Summary of test conditions using various types of coal ash

| Test # | Ash Used | T _g (°C) | T _{s,i} (°C) | m _{del} (g) |
|--------|------------|---------------------|-----------------------|----------------------|
| A1 | Petcoke | 1409 | 991 | 2.34 |
| A2 | PRB Sub | 1412 | 1083 | 1.26 |
| A3 | PRB Sub | 1415 | 1095 | 1.89 |
| A4 | Lignite | 1415 | 1061 | 4.46 |
| A5 | Lignite | 1413 | 1072 | 3.97 |
| A6 | Bituminous | 1416 | 1102 | 9.23 |
| A7 | Bituminous | 1415 | 1095 | 10.11 |

which was performed before the change. T_s was also measured, using the single-color method described in Section 3.6 for all tests except for the petcoke test, for which the 2-color method was used.

7.3 Results and Discussion

The results of the deposition tests are summarized below. In order to make comparisons, five tests from the constant T_g test series are included in the figures and discussion (test S4, S6, S9, S10, and S11). All five tests were conducted at a T_g similar to the tests from this series (close to 1400°C). Three of the five tests had a T_{s,i} similar to tests A2-A7 (close to 1100°C) while the remaining two had a T_{s,i} similar to that of test A1 (close to 1000°C).

7.3.1 Capture Efficiency

The effect of T_g on capture efficiency for the 5 ash samples is shown in Figure 7-1. Although the target T_g for each test was 1400°C, resulting in a small temperature range (7°C), a generally upward trend in capture efficiency with T_g can be seen. Although the overall trend is upward, the lignite and PRB subbituminous capture efficiencies decreased with increasing T_g. At 77.4%, the capture efficiency of the petcoke samples was 3.5 times greater than the next highest

capture efficiency (22.2% with the bituminous ash), and 7.2 times greater than that of test S11 (10.7% with the JB2 subbituminous ash) which had the most similar T_g and $T_{s,i}$ to the petcoke ash test.

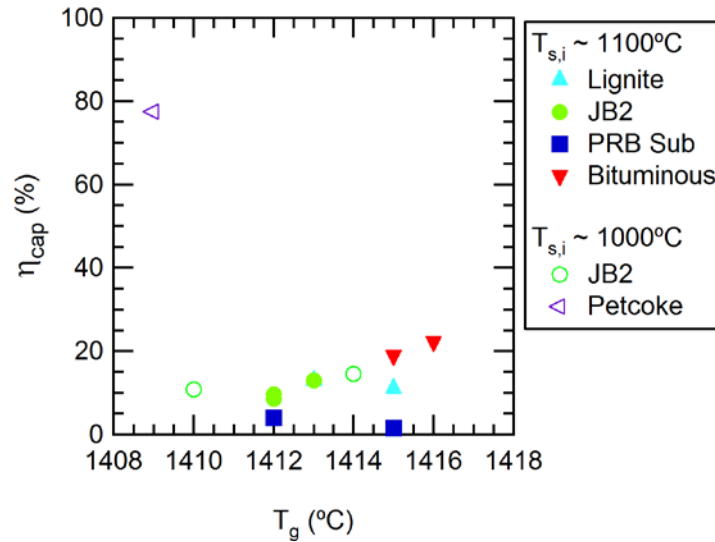


Figure 7-1: Capture efficiency vs. gas temperature for 5 different coal ash samples.

The capture efficiency results were also plotted against the apparent density of the different ash samples and are shown in Figure 7-2. Again, the capture efficiency of the petcoke ash is on a level of its own, but the remaining data show a direct relationship between ash density and capture efficiency. This direct relationship could be due in part to the effect relating to Stokes number as discussed in Section 2.3. According to Eq. (2-1), as the particle density increases, the Stokes number increases. As the Stokes number increases, the likelihood that the particle will follow its own path rather than follow the fluid streamlines increases and the particle is more likely to impact the surface. An increase in impact efficiency then leads to an increase in capture efficiency. The

average capture efficiency increases from 2.78% for the PRB ash with an apparent density of 0.8 g/cm³ to 20.3% for the bituminous ash with an apparent density of 2.5 g/cm³.

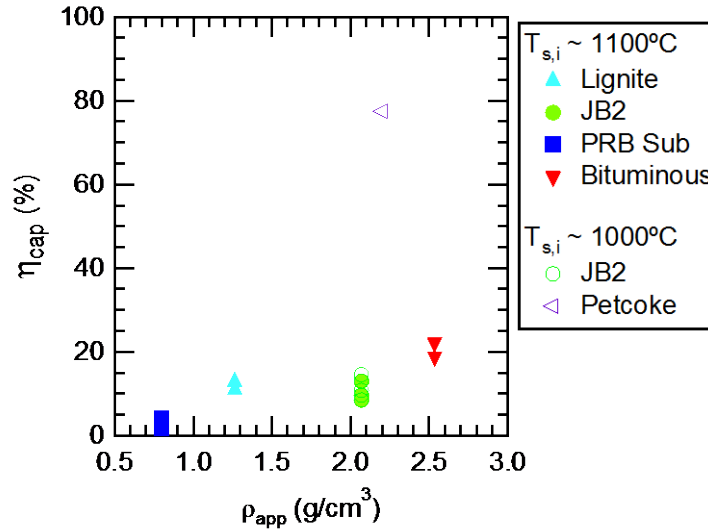


Figure 7-2: Capture efficiency vs. ash apparent density for 5 different coal ash samples.

7.3.2 Surface Roughness and Density

The surface roughness results are plotted in Figure 7-3 and Figure 7-4. Figure 7-5 presents cross-sectional views of some of the deposits formed in this study, along with the deposit from test S6 from the constant T_g test series. It can be seen that the surface of the petcoke ash deposit is quite smooth, but that there is a large variation in the thickness of the deposit. This large change in thickness increased the calculated R_a of the petcoke ash deposit. To account for this, MATLAB was used to fit a polynomial surface to the deposit surface, which was then subtracted from the real deposit surface data to produce a leveled deposit surface. It is the R_a calculated from this leveled surface that is reported in Figure 7-3 and Figure 7-4 for the petcoke ash deposit.

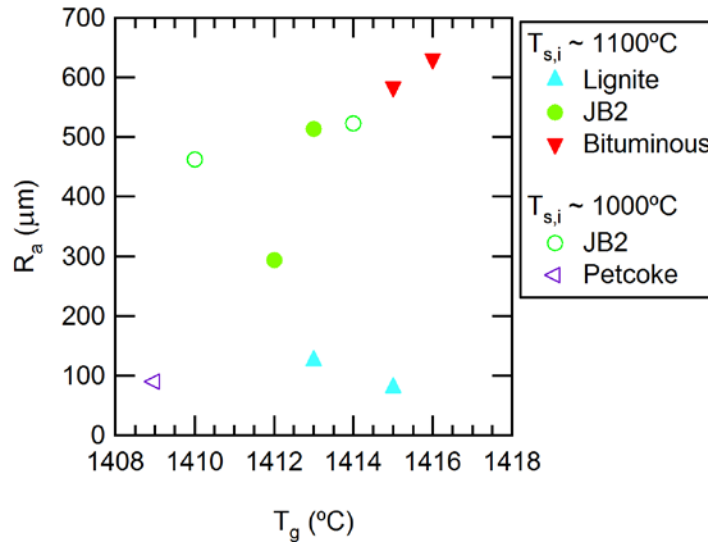


Figure 7-3: Surface roughness vs. gas temperature for 4 different coal ash samples.

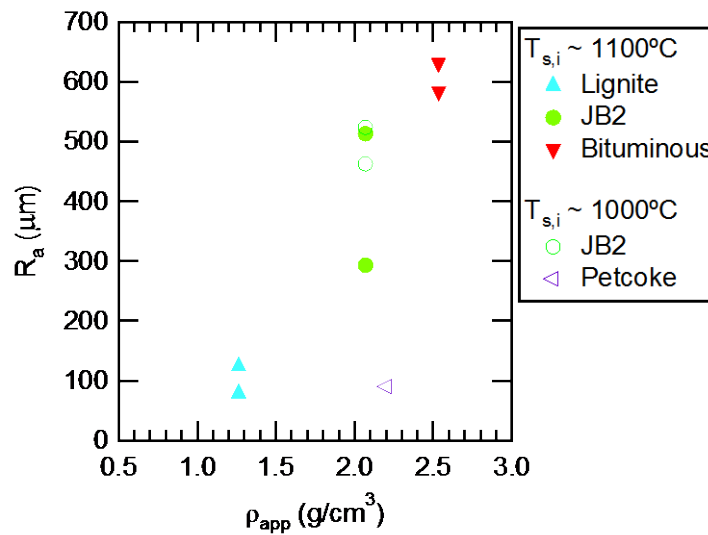


Figure 7-4: Surface roughness vs. ash apparent density for 4 different coal ash samples.

Surface roughness increases with T_g , except in the case of the lignite ash deposits, which have a surface roughness much lower than the other ash deposits at similar T_g and whose R_a decreases with T_g . The capture efficiency also increases as ρ_{app} increases. It was previously noted

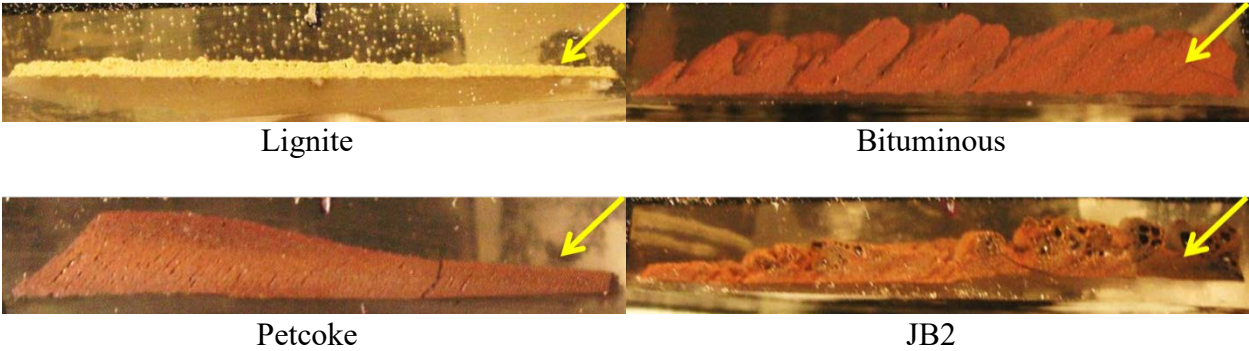


Figure 7-5: Cross-sectional view of deposits from tests using ash from various coal types. The arrows indicate the direction of gas flow as it approaches the coupon and deposit.

in Section 6.3.1 that increased surface roughness could be attributed to increased capture efficiency. Capture efficiency does increase with T_g and ρ_{app} , so it would be expected that surface roughness would also have a direct relationship with these properties. However, it should be noted that the petcoke ash stands out on its own. While the petcoke ash had a capture efficiency many times greater than the other ashes, the petcoke deposit had one of the lowest R_a values which does not fall in line with the other data.

The ρ_{dep} data are presented in Figure 7-6 and Figure 7-7. There is no apparent trend in deposit density with T_g , but ρ_{dep} does increase with increasing ρ_{app} . It would make sense that denser particles would result in a denser deposit. However, it is interesting to note that while ρ_{app} ranges from 0.8-2.5 g/cm³ for the ashes compared here, the ρ_{dep} ranges from 0.65-1.31 g/cm³ which is similar to the deposit densities reported throughout this document for tests using the JB2 ash at T_g near 1400°C. Figure 7-8 shows that the ratio ρ_{dep}/ρ_{app} decreases as ρ_{app} increases.

No surface roughness or deposit density data are reported for the PRB ash tests. While capture efficiency could be calculated from the change in mass of the coupon, the deposits were

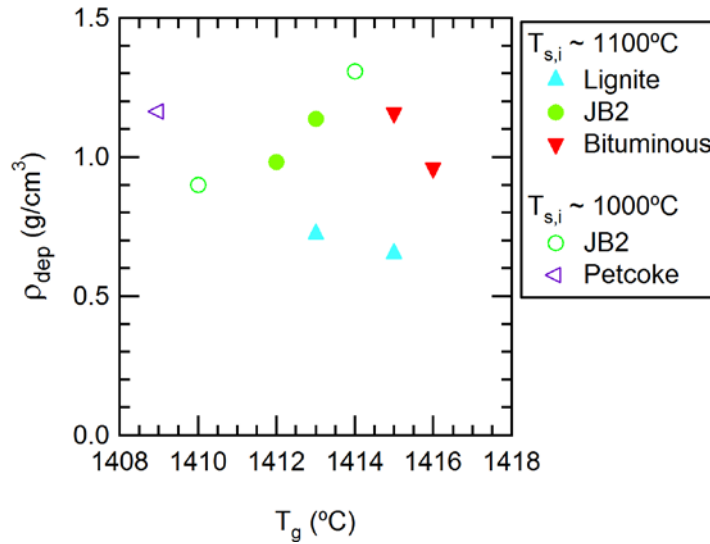


Figure 7-6: Deposit density vs. gas temperature for 4 different coal ash samples.

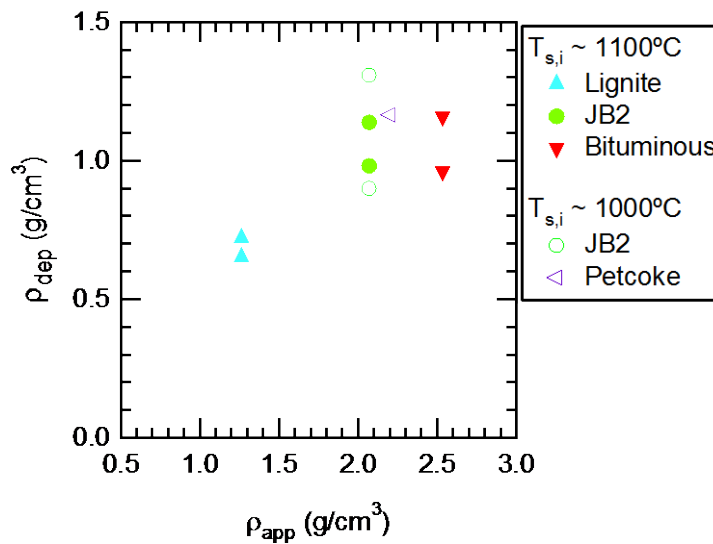


Figure 7-7: Deposit density vs. ash apparent density for 4 different coal ash samples.

too thin to remove from the coupon intact for later analysis. Also, as was mentioned in Section 6.3.2, no surface roughness or deposit density data are available for test S10.

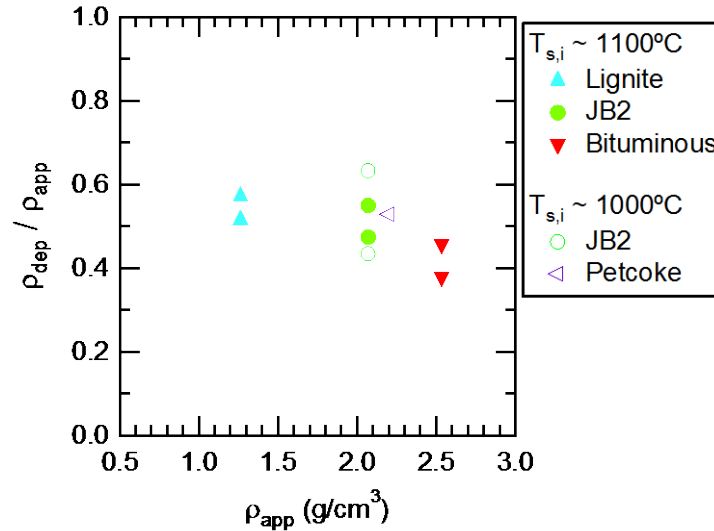


Figure 7-8: Ratio of deposit density to ash apparent density vs. ash apparent density for 4 different coal ash samples.

7.3.3 Surface Temperature

The development of the spatially-averaged surface temperature is shown in Figure 7-9. Several of the tests show a sharp increase in T_s between $t = 0$ and $t = 10$ minutes. This initial increase may be due in part to the formation of deposit, but it is most likely a result of switching from an assumed emissivity of 0.9 for the bare metal surface to a calculated emissivity for the remainder of the test. This sharp increase did not occur with the petcoke ash deposit for which two-color pyrometry was used. Due to this phenomenon, the trends in T_s are examined starting at the 10 minute mark.

Figure 7-9 shows the spatially-averaged T_s with respect to time for each test performed in this test series plus the JB2 ash tests previously compared to this test series. Table 7-2 reports the average capture efficiency and average m_{dep} for each ash sample. The average ΔT_s reported in Table 7-2 is the average difference between T_s at 10 minutes and at the end of the test. For the tests

that had a $T_{s,i}$ near 1100°C , the surface temperature of the lignite, PRB, and bituminous ash deposits behaved as expected where higher amounts of deposition resulted in a larger change in T_s . However, the JB2 ash deposits exhibited the highest average ΔT_s while only having the third highest capture efficiency (second highest m_{dep}). This was also true for the tests that had a $T_{s,i}$ near 1000°C , where the JB2 ash tests had a lower average capture efficiency, but the highest ΔT_s as compared to the petcoke ash test.

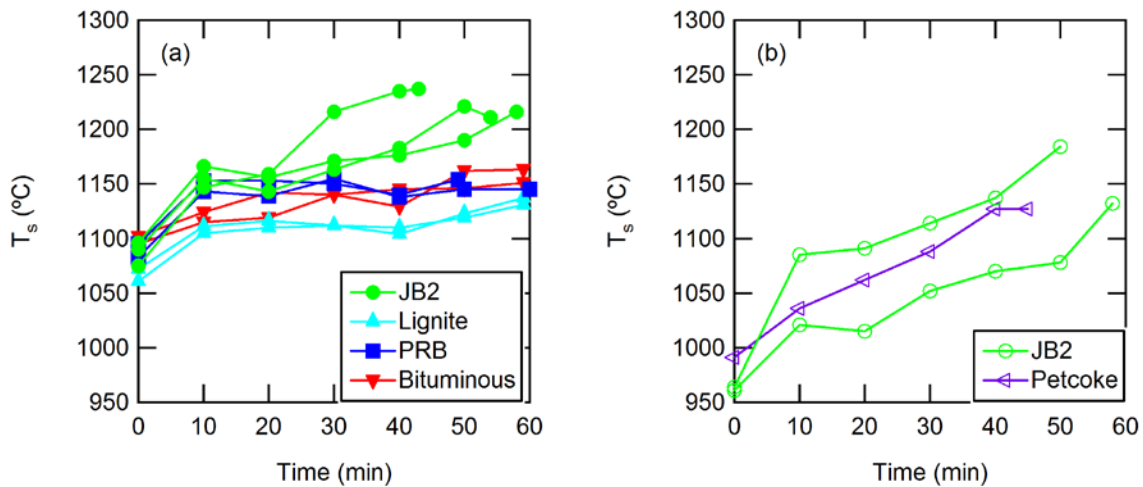


Figure 7-9: Spatially-averaged surface temperature vs. time for various coal ash deposits with (a) $T_{s,i} \sim 1100^{\circ}\text{C}$ and (b) $T_{s,i} \sim 1000^{\circ}\text{C}$.

There are two processes that could contribute to the fact that the JB2 ash tests exhibited greater increases in the surface temperature while depositing less ash throughout the test. Either more heat was transferred to the surface of the deposit or less heat was conducted through the deposit to the coupon or a combination of the two. Two factors that could increase heat transfer to the deposit surface are the temperature of the gas flowing over the deposit and the roughness of

Table 7-2: Averages of the capture efficiency, mass of deposit, and change in surface temperature recorded for each type of ash

| Ash | Average η_{cap} (%) | Average m_{dep} | Average ΔT_s (°C) |
|---------------------------------|---------------------------------|--------------------------|---------------------------|
| <i>T_{s,i} ~ 1100°C</i> | | | |
| Lignite | 11.9 | 0.50 | 26 |
| PRB | 2.8 | 0.04 | 1.5 |
| Bituminous | 20.5 | 1.96 | 38 |
| JB2 | 10.3 | 0.87 | 65 |
| <i>T_{s,i} ~ 1000°C</i> | | | |
| Petcoke | 77.4 | 1.67 | 91 |
| JB2 | 12.6 | 0.99 | 105 |

the deposit surface (Bogard et al., 1998; Bons et al., 2008). The average T_g for the JB2 ash tests represented in Figure 7-9 ranged from 1410°C to 1414°C, which is almost identical to the range for the tests conducted in this series (1409°C to 1416°C), indicating that T_g was not a cause of increased heat transfer to JB2 ash deposits. While R_a is not the most effective roughness statistic to use when determining the effect of surface roughness on heat transfer rates (Bogard et al., 1998), it is compared here for the sake of simplicity. The R_a of the JB2 ash deposits was higher than the R_a of the lignite and petcoke ash deposits and lower than that of the bituminous ash deposits. Increased surface roughness may have improved heat transfer to the JB2 ash deposits, thus increasing the magnitude of ΔT_s , but this could not have accounted for the total difference in ΔT_s between the various ash samples. This is particularly highlighted by the fact that the R_a of the JB2 ash deposits was smaller than the R_a of the bituminous ash deposits, but the ΔT_s of the JB2 ash deposits was larger than that of the bituminous ash deposits.

Less heat conduction through the deposit to the coupon surface could also contribute to the greater ΔT_s of the JB2 ash deposits. The thermal resistance (R) of a material is defined as

$$R = \frac{L}{kA} \quad (7-1)$$

where L is the material's thickness, k is the material's thermal conductivity, and A is the cross-sectional area through which conduction occurs. A is constant for all of the tests. Section 3.7.2 explained that h_{dep} was simply the height of the highest peak of the deposit, measured from the base of the deposit. Using this thickness for L in Eq. (7-1), however, would not give an accurate description of the average thermal resistance of the deposit. Rather, L is taken to be the average deposit thickness of the deposit, calculated as the average of the height of each point in a CMM scan of a deposit. The average value of L for each type of ash deposit for which the data are available is given in Table 7-3. The average L for the JB2 ash deposits is smaller than that for the other deposits, except for the lignite ash deposits. This indicates that, for the thermal resistance of the JB2 ash deposits to be higher than that of the other deposits, the JB2 ash deposits must have a smaller effective thermal conductivity.

Table 7-3: Average values of L for the deposits of the various ash samples, including the sample standard deviation of L

| Ash | Average L (mm) |
|---------------------------------|------------------|
| <i>T_{s,i} ~ 1100°C</i> | |
| Lignite | 1.07 ± 0.07 |
| Bituminous | 3.50 ± 0.98 |
| JB2 | 1.88 ± 0.21 |
| <i>T_{s,i} ~ 1000°C</i> | |
| Petcoke | 2.80 |
| JB2 | 2.23 ± 0.03 |

7.3.4 Physical Structure and Appearance

Images of representative deposits formed from the four ashes used in this test series are presented in Figure 7-10. Images of the deposit formed in test S6 with the JB2 ash are also shown for comparison. The deposits shown in Figure 7-10 are the same deposits for which cross-sections are shown in Figure 7-5, except for the PRB ash deposit for which no cross-section image is available.

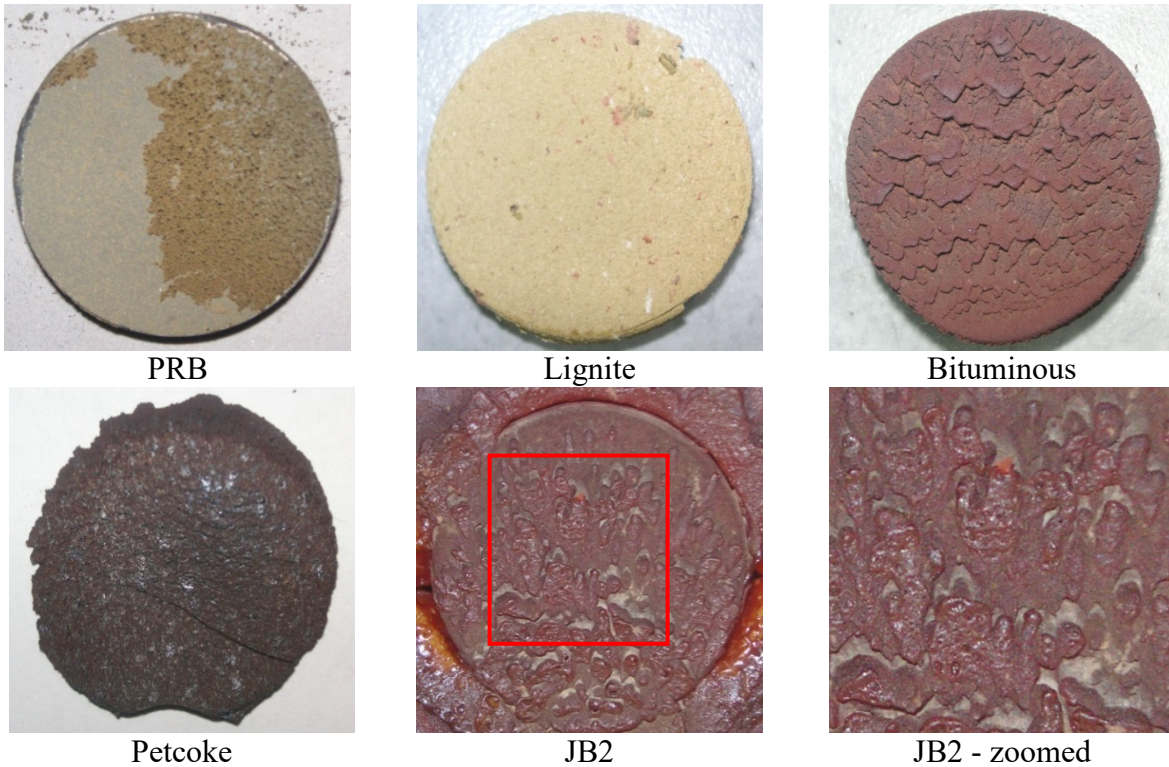


Figure 7-10: Photographs of deposits formed from the four ashes used in this test series plus a deposit formed from the JB2 ash for comparison. The red square in the JB2 image outlines the area shown in the JB2 – zoomed image.

Between the four ashes used in this series, the striking difference is the appearance of the bituminous ash deposit compared to the others. The bituminous ash deposit exhibits the formation

of large, pointed structures that grew and point upstream of the gas flow. This upstream direction of structure growth can also be seen in Figure 7-5. The PRB and lignite ash deposits are much thinner and much more uniform. The petcoke ash deposit, while thicker than the bituminous ash deposit, also has a more uniform surface and an absence of large structures like that found on the bituminous deposit. Although there is an absence of large structures in the petcoke ash deposit, small channels can be seen in the cross-section of the petcoke ash deposit shown in Figure 7-5. These small channels point upstream, indicating that the petcoke ash deposit grew into the flow, similar to the bituminous ash deposit. The large structures that formed on the bituminous ash deposit are similar to those seen on the JB2 ash deposits in Figure 6-9 that were formed at T_g less than 1350°C.

The ash deposits in Figure 6-9 that were formed at T_g greater than 1350°C started to exhibit structures that appear to have passed through a more molten phase and point more downstream and resemble the deposit from test S6, shown in Figure 7-10. While the gas temperature was near 1400°C for all the tests shown in Figure 7-10, which is above the softening temperatures listed in Table 3-1 for the respective ash samples, the average surface temperatures were below the softening temperature in each test, except for those performed with the JB2 ash. This may have contributed to the more molten appearance of the deposits formed with the JB2 ash at high T_g . It appears that less molten particles form structures that grow upstream (against the flow) while more molten particles form structures that grow or deform downstream (with the flow).

7.4 Summary and Conclusions

Ash deposits were formed in the TADF using 4 different types of coal ash in order to compare the effects of ash type on particle deposition behavior. Five deposit samples from the

constant $T_{s,i}$ test series, which used the JB2 ash, were also included in the comparison. Each ash was ground to achieve a similar MMD, ranging from 4.9 to 8.0 μm . It was determined that the apparent density of the ash played a role in ash deposition, with capture efficiency and surface roughness increasing as the ash density increased.

While it appeared that, in general, the increase in surface temperature seemed to correlate with an increase in capture efficiency, this was not true in all cases. The JB2 ash deposits experienced the highest change in T_s despite only having the third highest average capture efficiency. The higher change in T_s is likely due to higher surface roughness (increasing heat transfer to the deposit surface) and lower effective thermal conductivity (reducing heat transfer through the deposit) of the JB2 ash deposits.

8 HEAVY FUEL OIL*

Heavy fuel oil (HFO) is another ash-containing fuel that can be burned in gas turbines. The combustion of HFO can produce a turbine environment with elevated levels of SO₂. There was interest in examining the effect of SO₂, and the resulting SO₃, on deposit formation and the potential interaction of SO₃ with oxides formed from additives injected into the HFO prior to combustion. A series of tests was performed in the TADF in which gaseous SO₂ was introduced into the combustion chamber of the TADF to increase the concentration of SO₂ and the resulting deposits were analyzed. The following chapter discusses the additional analysis performed on the HFO deposits and the results of these tests.

8.1 Test Conditions

The conditions for each test are presented in Table 8-1. T_g was varied from 1101°C to 1219°C between tests. No coolant was used in these tests and the backside of the coupon was insulated. The initial T_s of each test was 167°C lower than the T_g on average due to radiative and conductive heat loss. The initial T_s of test H1 is not reported because of an error in recording the original image data.

* This chapter resulted in the following conference paper : Laycock, R. G., and T. H. Fletcher, "Formation of Deposits from Heavy Fuel Oil Ash in an Accelerated Deposition Facility at Temperatures up to 1206 °C," ASME Turbo Expo 2017: Turbomachinery Technical Conference and Exposition, Charlotte, NC (June 26-30, 2017)

Table 8-1: HFO ash test conditions

| Test # | T _g (°C) | T _{s,i} (°C) | m _{del} (g) |
|-----------------------|---------------------|-----------------------|----------------------|
| H1 | 1101 | - | 1.07 |
| H2 | 1104 | 912 | 0.91 |
| H3 | 1134 | 981 | 1.02 |
| H4 | 1155 | 1020 | 1.03 |
| H5 | 1162 | 991 | 0.85 |
| H6 | 1188 | 1009 | 1.04 |
| H7 | 1218 | 1028 | 0.97 |
| H8 | 1219 | 1019 | 0.98 |
| H9-No SO ₂ | 1106 | 993 | 0.71 |

The m_{del} reported in Table 8-1 is the final mass of ash that exited the equilibration tube below the coupon. During the deposition tests, some ash remained in the ash feed tube or deposited on the walls of the equilibration tube. This mass of ash was subtracted from the mass of ash fed into the TADF, as previously done in Section 6.2. In the case of the HFO ash, m_{del} was also adjusted to take into account the high loss on ignition (LOI, 67.11 wt%, dry) and moisture content (2.45 wt% as received) of the ash so that m_{del} reflects only the mass of inorganics that remained after burning in the TADF.

Magnesium-based additives can be used in HFO to alter deposit characteristics and reduce corrosion. The introduction of magnesium can lead to the formation of MgSO₄ by the reaction of SO₃ with MgO in the resulting ash and ash deposits. Sulfur present in the HFO will combust to SO₂ which then equilibrates with SO₃ in the gas phase. SO₂ was introduced into the TADF at a rate of 12.5 SLPM in order to maintain the SO₂ levels in the exhaust stream at 1.1 mol% to simulate this production of SO₂/SO₃.

NASA-Glenn CEA2 chemical equilibrium software (McBride and Gordon, 2004) was used to predict the equilibrium levels of SO₃ in the exhaust gas at the combustion conditions (temperature, fuel and air flow rates) in the TADF in this study. The results are shown in Table 8-2.

Table 8-2: Calculated equilibrium and outlet SO₃ mol% over the range of planned gas temperatures

| T_g (°C) | Equilibrium SO₃ mol% | Outlet SO₃ mol% (from kinetic model) |
|---------------------------|--|--|
| 1093 | 0.019 | 0.0023 |
| 1149 | 0.012 | 0.0033 |
| 1204 | 0.008 | 0.0043 |

The kinetic model proposed by Burdett et al. (1984) was used to determine the likelihood of SO₂/SO₃ equilibrium being achieved. The kinetic model is given as

$$\frac{d[SO_3]}{dt} = \frac{k_1}{RT} [SO_2][O_2] = \frac{A[SO_2][O_2]}{RT} e^{\left(\frac{-B}{T}\right)} \quad (8-1)$$

for the reaction



where $A = (2.6 \pm 1.3) \times 10^{12} \text{ cm}^3/(\text{mol}\cdot\text{s})$, $B = 23000 \pm 1200 \text{ K}$, and $[SO_2]$, $[O_2]$ and $[SO_3]$ are partial pressures. The conditions for which the model was generated and the conditions in the TADF are compared in Table 8-3. The main differences are the concentration of H₂O and CO₂ and the temperature range. The differences in gas concentrations are not a concern. Belo et al. (2014) showed that H₂O concentration does not have a significant impact on SO₂/SO₃ conversion and that

switching from N₂ to CO₂ atmosphere similarly has no impact in the presence of flyash. The temperature range of the HFO tests is outside of the temperature range of the kinetic model. However, extrapolating the kinetic model to the desired T_g of this study (1093°C to 1204°C) and applying it to the gases in the TADF over the length of the acceleration cone and equilibration tube results in outlet concentrations of SO₃ below the equilibration values, as shown in Table 8-2. A linear temperature profile was assumed over the first six inches of the acceleration cone, with the temperature increasing from an inlet temperature of 25°C to a final temperature equal to the desired outlet T_g. Because the outlet SO₃ mole percent does not reach the equilibrium value, the estimated mole percent of SO₃ in the outlet gas increases with increasing T_g as the rate of reaction increases.

At the temperatures of interest in this study, it is also important to note the potential for decomposition of MgSO₄, which could further reduce the net amount of MgSO₄ remaining in the deposit. Scheidema and Taskinen (2011) performed equilibrium calculations and thermoanalysis experiments in an N₂ atmosphere with varying amounts of CO present as a reducing agent. Their study showed that MgSO₄ will decompose at temperatures ranging from 880°C (90 mol% N₂) to 1085°C (100 mol% N₂). While the exhaust of the TADF is a mixture of combustion products and is not 100% N₂, the amount of CO should be near 0%. The lowest average T_g recorded during the tests (1101°C) is near this threshold of decomposition temperatures.

8.2 Analysis

Capture efficiency, average surface roughness (R_a), and deposit chemical composition were measured and calculated to characterize the ash deposits after testing. The formation of water soluble compounds in the HFO ash deposits and their impact on turbine blade maintenance was an area of great interest in this study. For this reason, the deposits from the HFO tests were analyzed

Table 8-3: Summary of the conditions of the tests used to develop the kinetic model (Burdett et al., 1984) and the conditions in the TADF to which the kinetic model was applied

| | Model | TADF |
|-------------------------------|-------------------|---------------------------------|
| T (°C) | 627-1077 | 25 (inlet) 1093-1204 (final) |
| <i>Gas Composition (mol%)</i> | | |
| CO ₂ | - | 6.8-7.2 |
| H ₂ O | 10 | 13.2-15.2 |
| O ₂ | 0-21 | 3.7-19.4 |
| OH | - | 0.0-0.006 |
| N ₂ | Balance (64.5-90) | 72.1-73.0 |
| NO | - | 0.0-0.044 |
| SO ₂ | 0-5.5 | 1.0-1.1 |

after their initial collection then washed in deionized water, dried and analyzed again. The wash procedure involved placing the coupon with deposit in the bottom of a glass beaker, slowly adding 30 mL of deionized water, allowing the deposit to soak for 25 minutes while recording the water temperature with a K-type thermocouple, then removing the coupon and deposit from the beaker and drying them in a furnace at 50°C for several hours. When discussing the results of this study, “pre-wash” refers to analysis done on the deposits prior to washing them as described and “post-wash” refers to analysis done on the deposits after performing the wash procedure.

The capture efficiency was again calculated according to Eq. (6-1), but applied only to the mass of inorganics by taking into account the high LOI and moisture content of the ash. R_a , however, was not measured with the same equipment as previously described. The HFO ash deposits were taken to Utah Nanofab at the University of Utah and scanned on a Zygo NewView 5000 optical profilometer. The data obtained from the optical profilometer included the average roughness (R_a) which is the value reported in this study. The deposits were too large to be able to

scan the entire surface, so the coupon was scanned at three points along the vertical centerline, as shown in Figure 8-1.

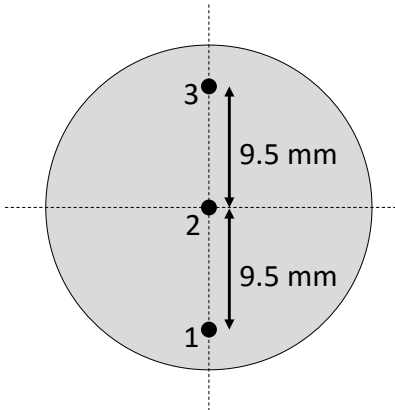


Figure 8-1: Location of markings for scan locations on the HFO ash deposits.

To help ensure that the scans were conducted in the same vicinity before and after the washing procedure, three points were marked on the deposit with a felt pen. The profilometer was then lined up to scan the area directly downstream of the marked point. The area downstream of the marked point was chosen rather than the marking itself so that only ash was being scanned and so the ink from the pen would not interfere with any results.

The chemical composition of the HFO ash deposits was studied before and after washing to determine the extent to which each element was removed by the washing procedure, with sulfur being of particular interest. The chemical analysis was performed by energy dispersive x-ray spectroscopy (EDS) in an FEI XL30 environmental scanning electron microscope (ESEM). The ink markings on the deposit that were used to position the optical profilometer were also visible in the ESEM and were thus used to perform the chemical analysis near the same region as the roughness scans. As with the roughness scans, the EDS analysis was performed on a section of

deposit downstream of the marking so that the ink would not interfere with the results of the analysis. Unless stated otherwise, the chemical composition data obtained from the EDS analysis are presented on an oxygen-free basis. It should be noted that the ESEM/EDS measurements are surface measurements, and hence are only semi-quantitative, complicated even more by a rough surface.

The 2-piece SiC cone and quartz tube configuration was used for each test in this series. T_s was also measured, using the single-color method described in Section 3.6. However, an assumed emissivity of 0.9 was used for each RGB image rather than just the first of each test series. As will be reported, a very small amount of ash deposited on the surface of the coupon and it was assumed that the bare metal surface was more representative of the observed surface throughout the test.

8.3 Results and Discussion

The results of the HFO ash deposition experiments are presented here. The discussion is focused on the effect of gas temperature and sulfur concentration on the physical and chemical characteristics of the ash deposits.

8.3.1 Mass Loss

Each test sample was weighed, washed according to the procedure previously described under Section 8.2, and then weighed again to determine the mass of the deposit that was removed during the wash procedure. The difference in mass before and after washing was attributed to water soluble components of the ash dissolving during the wash process. The percent of deposit mass loss due to washing is reported in Figure 8-2. The deposit mass loss due to washing ranged from 11% to 29% for the tests with injected SO_2 . There appears to be no strong trend between mass loss

and T_g . This indicates that changing the gas temperature in the turbine would not increase the percent of deposit that can be easily removed from the turbine blades and vanes by washing with water. However, changing the gas temperature will not adversely affect the removal of deposits either if it is desired to change the gas temperature for other reasons. The percent mass loss from the deposit from test H9 (19.1%) is also shown in Figure 8-2 and falls within the range of the SO_2 tests, indicating that elevating the levels of SO_2 in the gas stream did not have an effect on the mass of ash that was dissolved or removed from the deposit during the washing procedure.

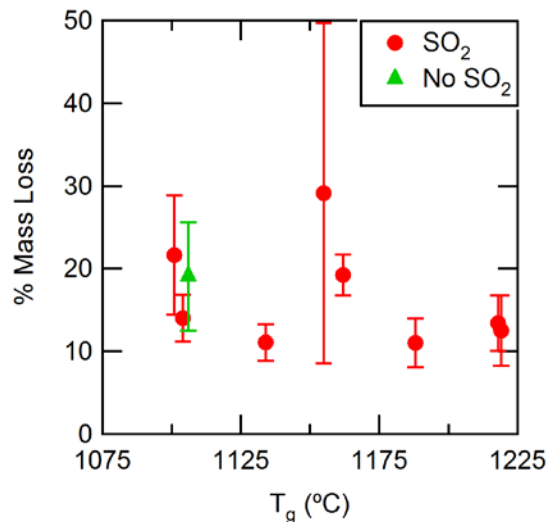


Figure 8-2: Mass loss after washing the HFO flyash deposits. The error bars represent the propagated measurement uncertainty from the mass balances used to weigh the coupons.

8.3.2 Capture Efficiency

The capture efficiency results are shown in Figure 8-3. The data are scattered and exhibit no obvious trend with T_g , with capture efficiencies ranging from 1% to 6%, with the capture efficiency of test H9 again falling within the same range as the tests with injected SO_2 . This lack

of a trend is in contrast with previous findings from the TADF that reported a direct relationship between T_g and capture efficiency (Crosby et al., 2008), including the work presented in Section 6.3.1 of this document. Capture efficiency data from Crosby et al. (2008) are included in Figure 8-3 for comparison. The Crosby et al. (2008) tests were performed with the JB1 ash with a mass mean diameter of 3 μm . The lack of a relationship between T_g and capture efficiency in the HFO ash tests may be a result of competing effects. The first effect would be the expected increase in deposition as T_g increases. The second effect would be greater mass loss at higher temperatures due to one or both of the following: increased particle detachment and increased conversion of ash species into species that evaporate.

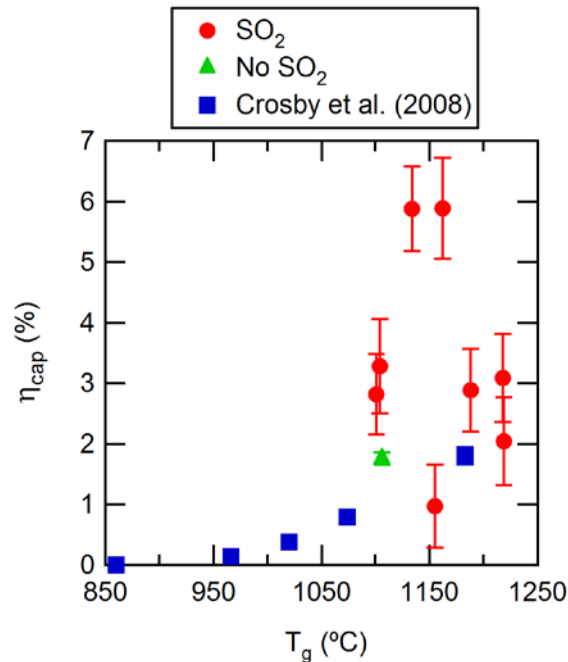


Figure 8-3: Capture efficiency vs. T_g from the HFO tests. The error bars represent the propagated measurement uncertainty from the mass balances used to weigh the coupons. Data from Crosby et al. (2008) is also included for comparison.

The backside of the coupon in the HFO ash test series was insulated during the deposition tests reported here and no cooling was used to control the surface temperature. As a result, the initial surface temperature increased with increasing T_g , as shown in Figure 8-4, which may have resulted in greater particle detachment as discussed in Section 6.3.2 concerning the effect of $T_{s,i}$ on capture efficiency.

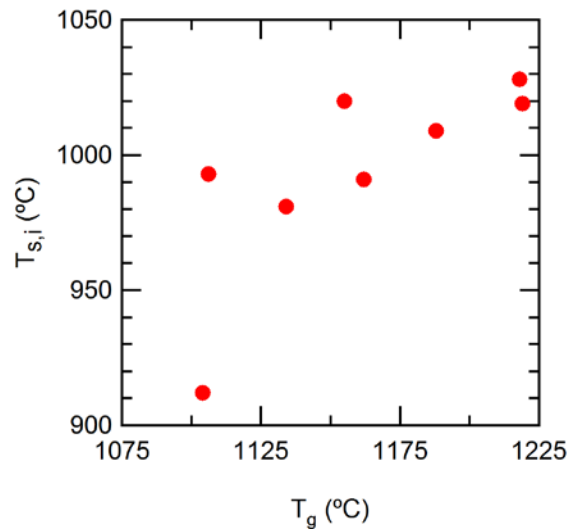


Figure 8-4: Initial surface temperature versus gas temperature for the HFO test series.

The second process that could result in greater mass loss at higher temperatures is ash release. To explore ash release outside of the TADF experiments, samples of the HFO ash were placed in ceramic crucibles and baked for 1 hour at 5 different temperatures representing the range of temperatures in the TADF (both T_g and T_s). The samples were weighed before and after baking. The as-received ash was used for 20 samples (4 at each temperature). All the as-received samples started with 0.61 g of ash. The average percent of ash release (as a percentage of inorganics) after baking at each temperature is presented in Figure 8-5. The ash release results of the as-received

ash showed a large amount of variation. Ten additional samples (2 at each temperature) were baked. These additional samples, however, were each dried and had an LOI test performed before being baked at high temperatures. These samples resulted in much better repeatability (see Figure 8-5, points labeled “Dry, Hydrocarbon Free”). The ash release for the dried, hydrocarbon-free samples increased with increasing temperature and then leveled off at the highest temperatures. This process, as well as increased detachment, may have competed with the normal trend of increasing capture efficiency, resulting in no clear relationship between capture efficiency and T_g .

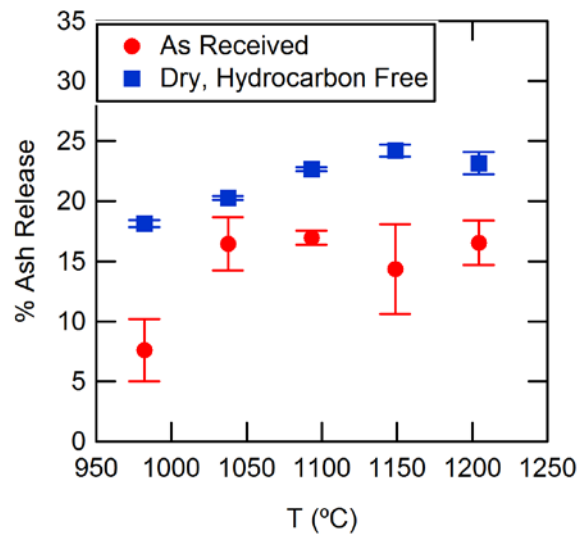


Figure 8-5: Average % ash release after baking the HFO ash samples. The error bars represent the standard error of the mean.

8.3.3 Surface Roughness

The surface roughness data (R_a) for the HFO ash deposition tests are shown in Figure 8-6. The value shown for each test is the average of the data obtained at each of the three locations indicated in Figure 8-1. Only tests H1-H6 are represented in Figure 8-6 because roughness data

for tests H7 through H9 were not available. Figure 8-6 shows that in almost every case, washing the deposit resulted in greater surface roughness. It can also be seen that prior to washing, the R_a displayed scattered values with no trend with respect to T_g . However, the post-wash R_a seems to display a slight inverse relationship with T_g . The error bars (standard error of the mean) do show enough overlap, however, to prevent a trend from being conclusive.

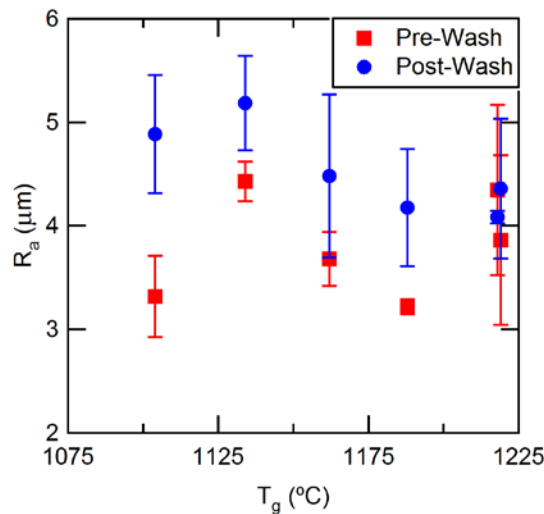


Figure 8-6: Average surface roughness (pre-wash and post-wash) data for the HFO deposits. Error bars show the standard error of the mean.

8.3.4 Chemical Composition

EDS analysis was performed on the HFO ash deposits before and after the wash procedure. The potential formation of water soluble $MgSO_4$ was of particular interest in this study. The mole percent of sulfur and magnesium in the deposits is presented in Figure 8-7. To verify that increasing the concentration of SO_2/SO_3 in the exhaust gas did result in the formation of sulfur compounds in the ash deposit, a single test was conducted without the introduction of extra SO_2

into the TADF. The wt% of sulfur in the deposit formed during the non-SO₂ test is included in Figure 8-7 and is much lower than the wt% of sulfur in the deposits formed with added SO₂ (0.83 wt% without added SO₂ versus 15.1 wt% and 19.9 wt% with added SO₂ at similar T_g). This large difference in deposit sulfur content between the tests with and without added SO₂ indicates that the added SO₂ and subsequent SO₃ did react with the ash in the deposit to form sulfur compounds and thus increased the sulfur content of the deposit. The wt% of magnesium in the deposit formed during the non-SO₂ test did not vary much from that seen in the SO₂ tests. It can also be seen that, while washing the deposits from the SO₂ tests did change the wt% of sulfur and magnesium in the surface of the deposit, there was no such effect on the deposit from the non-SO₂ test. This is interesting to note in light of the fact that the presence of elevated levels of SO₂ created no significant change in the percent mass loss due to washing. Although there was no change in the percent mass loss due to washing, there does seem to have been an effect on which compounds were washed out of the deposit.

The mol% of sulfur in the deposit decreased after washing, which is to be expected if water soluble sulfur compounds were formed in the deposit. However, the mol% of magnesium increased after washing, indicating that while it is possible that some MgSO₄ formed in the deposit and then dissolved during the wash procedure, not all of the sulfur that dissolved was in the form of MgSO₄. Further examination of the EDS data showed that potassium and calcium were also depleted during the washing procedure, as shown in Figure 8-8. It is possible that the SO₂/SO₃ reacted not only with the MgO in the flyash, but also with potassium and calcium to produce potassium sulfate (K₂SO₄) and calcium sulfate (CaSO₄) which are also soluble or slightly soluble in water.

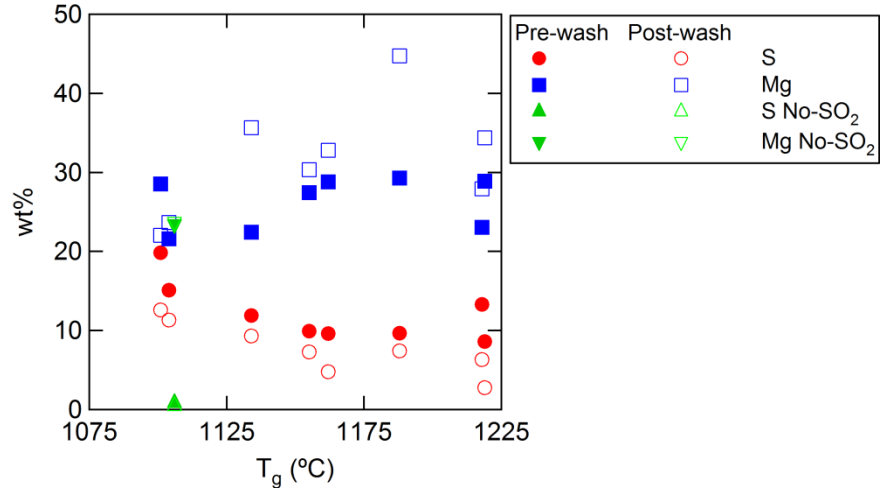


Figure 8-7: wt% of sulfur and magnesium in the HFO deposits with respect to T_g.

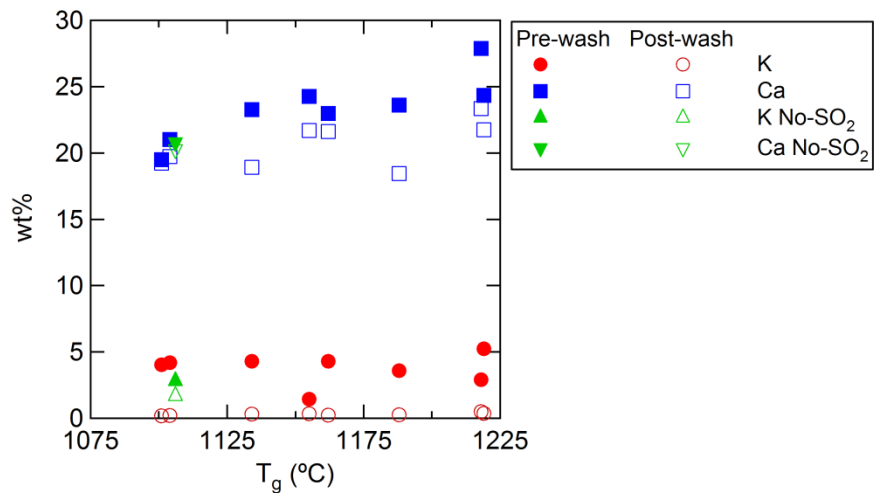


Figure 8-8: wt% of potassium and calcium in the HFO deposits with respect to T_g.

Figure 8-9 shows the relative change in wt% of magnesium, potassium and calcium in the HFO deposits after washing. The relative change in wt% is calculated for each species *i* as

$$Relative\ Change_i = \left(\frac{Postwash\ wt\%_i}{Prewash\ wt\%_i} - 1 \right) \cdot 100\% \quad (8-3)$$

It can be seen that as the wt% of sulfur in the pre-wash deposit increased, magnesium became less enriched after washing and even crossed over into being depleted at the highest levels of sulfur. This relationship between pre-wash sulfur wt% and the relative change in magnesium wt% suggests that when there was more sulfur present in the HFO deposits, a larger portion of the magnesium content was present as $MgSO_4$ which then dissolved during the washing procedure. Potassium became more depleted during washing as the wt% of sulfur increased, but this change was small because most of the potassium was washed out even at low sulfur wt% in the deposit. Calcium, in contrast, became slightly less depleted during washing at high sulfur wt%, possibly due to the lower solubility of $CaSO_4$ compared to $MgSO_4$ and K_2SO_4 . Data from test H9 are also included in Figure 8-9. When no SO_2 was injected into the TADF, the resulting deposit experienced almost no change in magnesium or calcium wt% due to washing. The potassium wt% still decreased with washing, but by a much smaller extent.

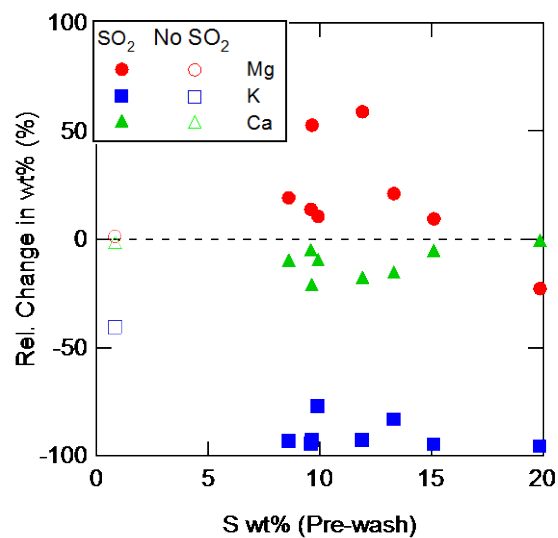


Figure 8-9: Relative change in wt% of Mg, K, and Ca as a function of the pre-wash wt% of S.

8.3.1 Surface Temperature

It has been shown that the average surface temperature increased throughout the duration of a deposition test for the other test series presented in this work. An increase in T_s , however, was not observed in these HFO ash tests. The T_s with respect to time is shown in Figure 8-10. T_s stays relatively constant throughout the duration of the test.

The total mass of ash deposited in the HFO test series was in the range of 0.01-0.06 g, with a mean value of 0.03 g. The total mass of ash deposited in the previous test series, in which an increase in T_s over time was reported, ranged from 0.03 g to 2.93 g, with a mean value of 0.95 g (an order of magnitude greater than that of the HFO ash tests). The significantly smaller amount of ash deposited during the HFO ash tests likely resulted in an ash layer that was too thin to create a noticeable increase in T_s . The difference in the mass of ash deposited between the HFO test series and the other TADF tests, along with the corresponding changes in surface temperature, also supports the idea that the increase in T_s reported in the other TADF tests was a result of increased deposit thickness.

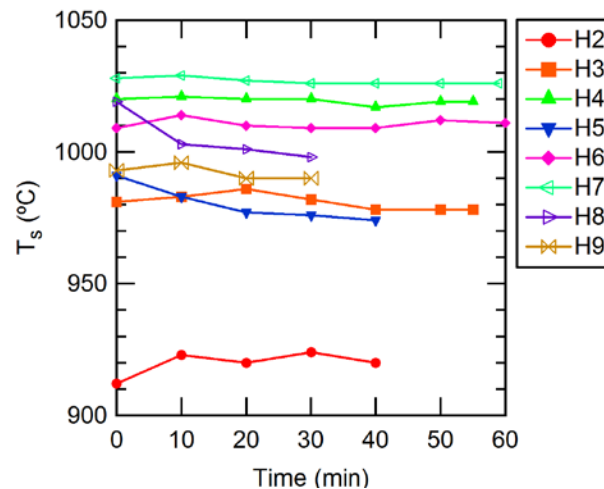


Figure 8-10: Average surface temperature of the HFO ash deposits during the deposit tests.

8.4 Summary and Conclusions

Experiments were conducted in the TADF to study the deposition behavior and deposit characteristics of flyash produced from HFO combustion. The deposits were formed at conditions representative of combustion conditions in industrial gas turbines burning HFO, matching gas temperature, velocity, and SO₂ concentration.

The gas temperature was varied from 1101°C to 1219°C. It was found that varying the gas temperature had no discernable effect on the capture efficiency of the HFO ash in the TADF, possibly due to competing processes of increased deposition tendency and increased detachment or ash release at higher gas temperatures.

The sulfur content of the deposits decreased with increasing temperature. Also, turning off the SO₂ feed to the combustor dramatically reduced the amount of sulfur in the deposit, indicating that feeding extra SO₂ in order to match SO₂ levels found in HFO fueled turbines did result in the SO₂/SO₃ reacting to form sulfur compounds that deposited on the test coupon.

Washing the coupons in distilled water revealed that while some of the magnesium may have formed MgSO₄, most of Mg did not form MgSO₄ and remained in the deposit after washing. The sulfur likely formed K₂SO₄ and CaSO₄ as well from the potassium and calcium in the ash. At lower gas temperatures, when the sulfur content was higher, more of the magnesium was removed during the wash process, indicating that MgSO₄ was more favored to form at lower temperatures with higher sulfur concentrations.

The total mass percent of deposit removed by the water wash procedure did not change with respect to gas temperature, indicating that changing the gas temperature in the turbine would not aid in the formation of easily removed deposits. However, the fact that there was no gas

temperature effect on the amount of deposit removed also indicates that it would not adversely affect the amount of water soluble deposit formed if the gas temperature was changed for other purposes.

9 FILM-COOLING CHARACTERISTICS

To cool and protect turbine blades, film-cooling holes allow coolant air to flow through the turbine blade and over the surface. The processes of film-cooling and particle deposition affect one another as film-cooling can reduce the amount of deposit growth on the blade surface, but deposit formations can affect film-cooling effectiveness and flow paths. Tests were conducted in the TADF at T_g near 1400°C to study the effect of film-cooling on deposition at high gas temperatures.

9.1 Test Conditions

The test conditions for the film-cooling series are summarized in Table 9-1. The T_g was maintained near 1400°C and the blowing ratio (M) was varied between tests from 0.5 to 2.1. The coupons for this test series had 3 film-cooling holes with 1 mm diameter and a spacing of 4.5 mm between holes as shown earlier in Figure 3-6.

Before entering the coupon holder, the film-cooling air passed through an electrical heater attached to a variable autotransformer, which provided some control over the temperature of the film-cooling air. The temperature of the film-cooling air was controlled in order to try to maintain a fairly constant density ratio ($\rho_{\text{coolant}}/\rho_\infty$). Despite these efforts, the average density ratio in these tests varied from 1.8 to 2.8. For certain tests, particularly at high blowing ratio, operating the heater at full power still failed to raise the coolant temperature enough to match

Table 9-1: Summary of test conditions for the film-cooling series

| Test # | T_g (°C) | T_{s,i} (°C) | Blowing Ratio | m_{del} (g) |
|---------------|---------------------------|-----------------------------|--------------------------|----------------------------|
| F1 | 1411 | 1106 | 0.55 | 10.21 |
| F2 | 1410 | 1106 | 1.06 | 8.02 |
| F3 | 1414 | 1039 | 2.13 | 8.47 |
| F4 | 1411 | 1054 | 0.55 | 8.29 |
| F5 | 1411 | 1021 | 2.13 | 8.51 |
| F6 | 1413 | 1093 | 1.08 | 7.82 |
| F7 | 1414 | 1028 | 1.62 | 8.30 |
| F8 | 1412 | 1005 | 2.14 | 8.10 |
| F9 | 1416 | 998 | 1.06 | 9.08 |
| F10 | 1412 | 1053 | 1.62 | 9.48 |
| F11 | 1414 | 1011 | 0.52 | 9.31 |

that of other tests, resulting in a higher density ratio. This test series used the JB2 subbituminous coal ash with properties summarized in Table 3-1.

9.2 Analysis

Capture efficiency (η_{cap}), average surface roughness (R_a), and deposit density (ρ_{dep}) were measured and calculated for each deposit sample as previously described. The two-piece SiC cone and quartz tube configuration was used for all tests in this series except for tests F1 and F2 which used the one-piece SiC configuration. T_s was also measured using the single-color method described in Section 3.6 for all tests except F1 and F2 which used the two-color method.

9.3 Results and Discussion

The results of the deposition experiments with film cooling are presented here. The discussion is focused on the effect of the blowing ratio on the deposit capture efficiency, surface roughness, surface temperature, and physical appearance.

9.3.1 Capture Efficiency

The effect of blowing ratio on capture efficiency is shown in Figure 9-1a. The capture efficiency generally decreased as the blowing ratio increased. There are, however, 2 capture efficiency data points (one at $M = 1.1$ and another at $M = 2.1$), that are much higher than the highest capture efficiency at $M = 0.5$ (16.3% and 15.3% at $M = 1.1$ and 2.1 respectively compared to 12.7% at $M = 0.5$). After reviewing the recorded test conditions and test videos, there is no evidence to indicate that these are bad tests that can be thrown out. However, their distance from the remainder of the data set, particularly at their respective blowing ratios, does indicate the possibility of anomalous deposition behavior. The average capture efficiency at $M = 0.5$ is 12.6% and the average capture efficiency at $M = 2.1$ is 12.3% when including the anomalous data point, and 10.8% when the anomalous data point is excluded.

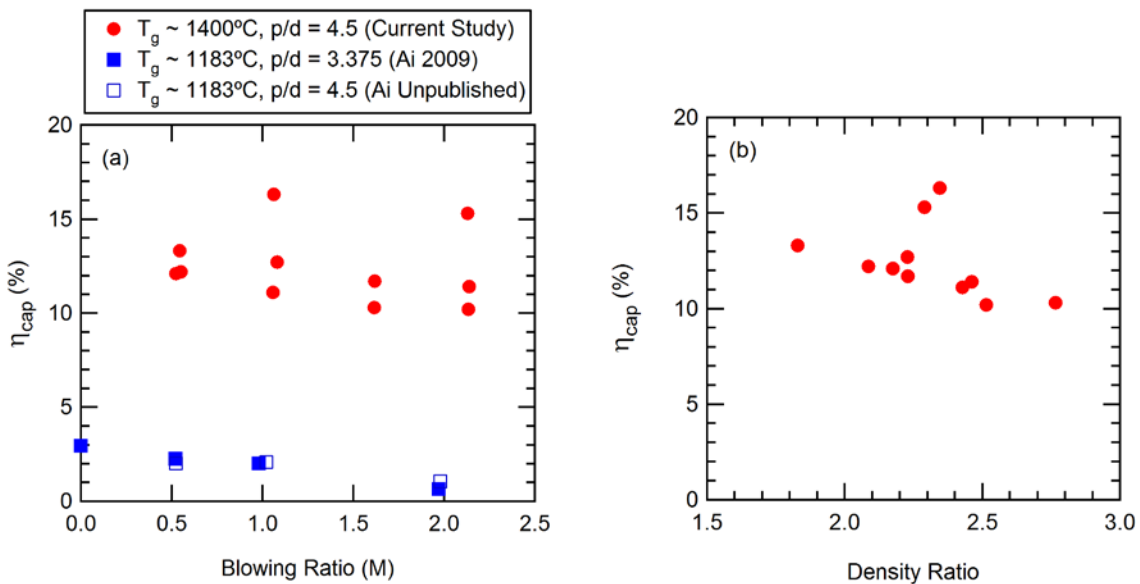


Figure 9-1: Capture efficiency vs. blowing ratio (M) and density ratio for the film-cooling test series.

As noted earlier, the density ratio varied from 1.8 to 2.8. The capture efficiency is also plotted versus density ratio in Figure 9-1b. The capture efficiency decreased as the density ratio increased. While the blowing ratio and density ratio are connected, the capture efficiency data appear to fall much more in line with the density ratio, except for the same two tests mentioned earlier again reinforcing their anomalous behavior.

Ai (2009) performed film-cooling experiments with the JB1 ash with a reported MMD of 4 μm at a T_g of 1183°C. The film-cooling holes were also 1 mm in diameter, but the spacing between holes was 3.375 mm. In Ai's tests, the capture efficiency ranged from 2.27% at $M = 0.5$ to 0.64% at $M = 2.0$ giving an absolute reduction in capture efficiency of 1.63 percentage points or a relative reduction of 72%. Ai did perform other tests that went unpublished, again at a T_g of 1183°C and with the same 4 μm ash, on a bare metal coupon with hole spacings of 4.5 mm. In these tests, the capture efficiency experienced a 48.3% reduction from 2.01% at $M = 0.5$ to 1.04% at $M = 2.0$. In the current test series at T_g near 1400°C, the best case scenario (i.e. excluding the anomalous data points) difference in average capture efficiency between $M = 0.5$ and $M = 2.1$ is 1.7 percentage points, or 14% reduction. This small reduction in capture efficiency, compared to that observed in Ai's tests, indicates that film cooling is less effective at reducing capture efficiency at high T_g than at lower T_g .

There are two primary means by which film cooling reduces particle deposition. The first is that the film-cooling jets sweep away particles before they can impinge on and adhere to the surface. The momentum flux ratio is the ratio of the momentum flux of the coolant jets to the momentum flux of the freestream, or $I = \rho_c U_c^2 / \rho_\infty U_\infty^2$ where ρ_c and ρ_∞ are the density of the coolant jets and the freestream respectively and U_c and U_∞ are the velocities of the coolant jets and freestream respectively. The momentum flux ratio of the current tests and Ai's tests are plotted in

Figure 9-2. The momentum flux ratio from Ai's tests had not previously been reported in other publications. The momentum flux ratios are very similar and it is unlikely that any difference that may exist here is significant enough to account for the observed reduction in the affect that film-cooling has on capture efficiency at high T_g .

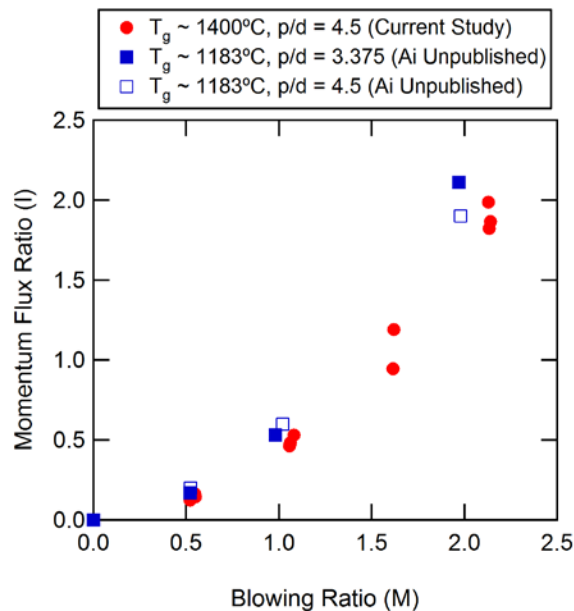


Figure 9-2: Momentum flux ratio (I) vs. blowing ratio (M) for the film-cooling test series.

The particle properties themselves could also contribute to the ease with which the coolant jets can sweep particles away from the surface. Smaller particles have less inertia and could therefore be more easily swept away by film-cooling jets. Ai's tests were performed with the ground JB1 ash (MMD = 3 μm), while the tests in this study were performed with the ground JB2 ash (MMD = 5 μm). The particle size distributions of the two ashes are shown in Figure 9-3. The larger MMD of the JB2 ash could lead to fewer particles being swept away in the high temperature tests. It should also be noted that the density of the JB1 ash is larger than the JB2 ash (see Table

3-1), which further complicates the matter because higher density would increase the inertia of the particle. However, as the mass of a spherical particle is more strongly dependent on particle diameter than on density ($m = \rho_p \pi d_p^3 / 6$), the particle diameter should have a greater influence on the whether or not a particle is swept away by the film-cooling jets.

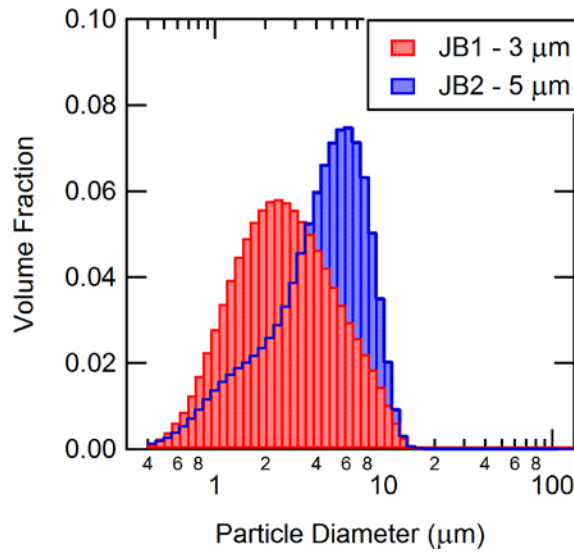


Figure 9-3: Particle size distributions of the ground JB1 and JB2 ash samples.

The second means by which film cooling decreases capture efficiency is by increasing cooling and decreasing the surface temperature. The average $T_{s,i}$ at each blowing ratio for the current test series and for Ai's tests are shown in Table 9-2. While increasing the blowing ratio from 0.5 to 2.1, the average $T_{s,i}$ for the high temperature tests only decreased by 35°C while the average $T_{s,i}$ for the low gas temperature series decreased by 67°C. This smaller reduction in average $T_{s,i}$ could also account for some of the lower effectiveness of film-cooling to reduce capture efficiency at high T_g .

Table 9-2: Average $T_{s,i}$ at each blowing ratio (M)

| $T_g = 1400^\circ\text{C}$, $p/d = 4.5$ | | $T_g = 1183^\circ\text{C}$, $p/d = 3.375$ (Ai, 2009) | |
|--|-------------------------------------|---|-------------------------------------|
| M | <i>Average $T_{s,i}$</i> | M | <i>Average $T_{s,i}$</i> |
| 0.5 | 1057 | 0.5 | 992 |
| 1.1 | 1066 | 1.0 | 961 |
| 1.6 | 1041 | - | - |
| 2.1 | 1022 | 2.0 | 925 |

The capture efficiency data are also plotted with respect to $T_{s,i}$ in Figure 9-4, which also includes the capture efficiency data from the constant T_g series previously reported in Figure 6-10, which did not use film-cooling. The capture efficiencies reported for the film-cooling tests increased with increasing $T_{s,i}$, despite the fact that the range of $T_{s,i}$ for the film-cooling series fell in the range where the constant T_g tests were experiencing decreasing capture efficiency with increasing $T_{s,i}$. After some investigation, the reason for this deposition phenomenon remained unclear and was beyond the scope of this study and is recommended for future work.

9.3.2 Surface Roughness and Density

The surface roughness and deposit density of the ash deposits were measured and the results are shown in Figure 9-5. There is no apparent influence of blowing ratio on either surface roughness or deposit density. Ai (2009) also measured the R_a of the deposits formed in that study and found that R_a dropped dramatically as M increased, dropping from close to $400\ \mu\text{m}$ at $M = 0.5$ to $1.12\ \mu\text{m}$ at $M = 2.0$. No surface roughness or density data are reported for test F1 because the deposit had broken into multiple pieces and was not properly assembled when scanned.

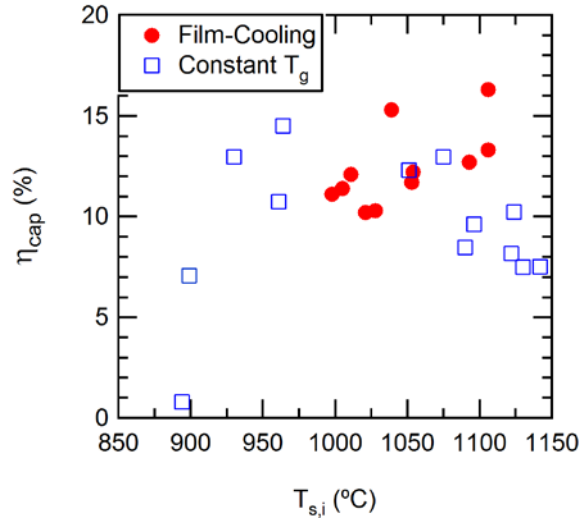


Figure 9-4: The effect of $T_{s,i}$ on capture efficiency during the film-cooling and constant T_g tests series.

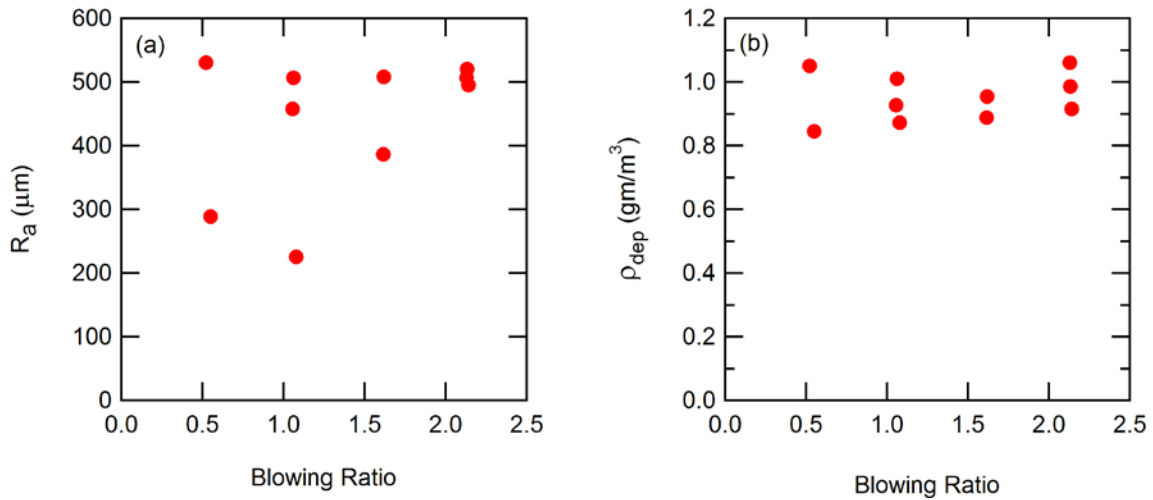


Figure 9-5: Surface roughness and density of deposits formed at $M = 0.5 - 2.1$.

9.3.1 Surface Temperature

The spatially averaged surface temperature for each test is shown in Figure 9-6. The surface temperature increases throughout the duration of each test, but there is no pattern in relation to

blowing ratio. To help illustrate the lack of any effect of blowing ratio on the surface temperature, the average final surface temperature ($T_{s,f}$) at each blowing ratio is reported in Table 9-3. While one would expect the surface temperature to decrease with increasing blowing ratio, the average $T_{s,f}$ at $M = 0.5$ and $M = 2.1$ are equal to each other and the $T_{s,f}$ at $M = 1.1$ and $M = 1.6$ are also equal to each other.

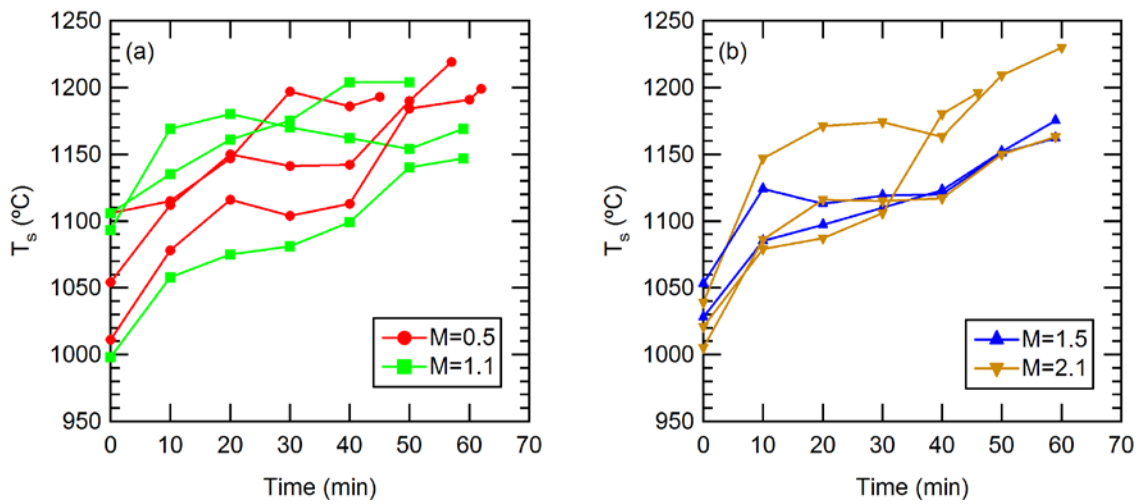


Figure 9-6: Average surface temperature (T_s) vs. deposition time.

Table 9-3: Average final surface temperature ($T_{s,f}$) at each blowing ratio, including standard error on the mean

| Blowing Ratio (M) | Average $T_{s,f}$ (°C) |
|-------------------|------------------------|
| 0.5 | 1204 ± 7.9 |
| 1.1 | 1173 ± 17 |
| 1.6 | 1169 ± 6.5 |
| 2.1 | 1196 ± 19 |

9.3.2 Physical Structure and Appearance

Photographs of deposits formed at $M = 0.5$ to 2.1 are shown in Figure 9-7. The overall appearance does not change much except for the formation of more distinct troughs downstream of the cooling holes at higher blowing ratio. No troughs are visible at $M = 0.5$. Deep troughs are visible on the deposit formed at $M = 1.1$, but only downstream of 2 of the 3 holes. Three wide troughs were formed at $M = 1.6$ and 3 wide and deep troughs were formed at $M = 2.1$. Photographs of the deposits collected from each film-cooling test are included in Appendix B, showing again that the overall appearance is similar for all of the tests. The most consistent characteristic is the lack of troughs at $M = 0.5$.

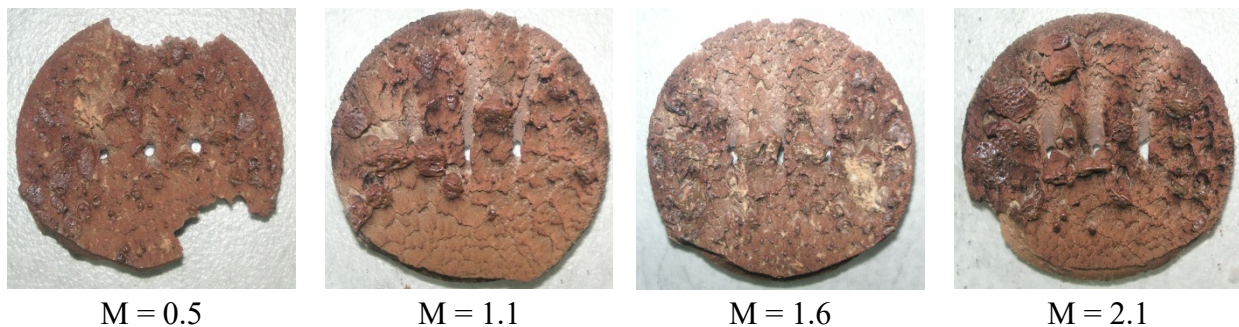


Figure 9-7: Photos of deposits formed at $M = 0.5 - 2.1$ (tests F4, F9, F7 and F8 respectively).

9.4 Summary and Conclusions

Deposition experiments were performed in the TADF using coupons with film-cooling holes. The gas temperature was maintained near 1400°C during each test and the blowing ratio was varied from 0.5 to 2.1 between tests. The capture efficiency decreased slightly as the blowing ratio increased. The major conclusion from this test series is that variation in blowing ratio had a

smaller effect on particle deposition at high gas temperatures (1400°C) than at lower gas temperatures at which other tests have been conducted, possibly due to smaller changes in surface temperatures as the blowing ratio increases. It is possible that there was also a particle size effect as the high temperature tests were conducted with the JB2 ash, which has a higher MMD than the ground JB1 ash. The larger JB2 ash may have been less readily swept away by the film-cooling jets than the smaller JB1 ash. The capture efficiency in these tests was an order of magnitude larger than that observed in similar experiments at lower T_g (1183°C), and experienced a much smaller percent reduction in capture efficiency over the range of blowing ratios. No clear effect on surface roughness, deposit density, surface temperature, or physical structure and appearance was observed with changing blowing ratio, again indicating a reduced effect of film-cooling on deposition behavior at high T_g .

10 DEPOSITION MODELING

Models have been developed to predict particle deposition in gas turbines. To test the applicability of two of these models at temperatures up to 1400°C, gas phase and particle simulations were performed to model the flow dynamics and particle trajectories around the coupon holder in the TADF. Two sticking models, the critical velocity and non-spherical models discussed in Section 2.7, were applied to the impact data obtained from the particle trajectories and the resulting capture efficiencies were compared to those obtained in various test series presented earlier in this study. This chapter describes the process of obtaining the gas phase solutions and particle trajectories and the application of the sticking models.

10.1 Computational Setup

The particle deposition modeling consisted of three steps. The first step was to obtain a steady-state solution to the gas phase flow dynamics. The second step was to then introduce particles into the gas phase and solve the particle trajectories and obtain the particle physics at the moment of impact. The final step was to use the particle impact physics in sticking and detachment calculations to determine the impact, sticking, and capture efficiencies. All CFD modeling was performed in the CFD software STAR-CCM+ version 11.04.010. The sticking and detachment calculations were performed in MATLAB 2016b.

10.1.1 Gas Phase Simulation

Steady-state gas phase simulations were performed in STAR-CCM+ version 11.04.010 using the Reynolds-Averaged Navier-Stokes (RANS) transport equations and the SST $k-\omega$ turbulence model. The gas phase was modeled as a multi-component gas consisting of O₂, CO₂, H₂O, and N₂. Continuity, momentum, and energy equations were solved in the gas phase to solve for gas temperature and velocity and associated parameters (density, wall shear stress, etc.)

The geometry for the simulations was modeled after the real geometry of the TADF within the heat shield (equilibration tube outlet, coupon, faceplate, coupon holder, and inlet and outlet of the heat shield), as shown in Figure 10-1. A large volume above the heat shield and coupon holder was included in the gas phase simulation to avoid problems caused by recirculation at the pressure outlet, which can be caused by an outlet being located too close to an obstacle in the flow (the holder in this case). The ambient inlets are velocity inlets meant to represent the flow of ambient air caused by the fan in the exhaust hood above the TADF. Due to the symmetry of the region within the heat shield, the geometry was cut in half and an axis of symmetry boundary was applied at the cross-section. The boundary conditions for the CFD simulation are summarized in Table 10-1.

10.1.1.1 Mesh Refinement

To reduce error introduced by insufficient grid resolution, a grid study was performed to ensure that a fine enough grid was used. Six meshes of increasing resolution were generated with polyhedral cells, and the CFD solutions obtained with each grid were compared. The number of cells in each grid is reported in Table 10-2. The three columns labeled “Faceplate,” “Jet,” and “Coupon” report the number of cells contained within 3 nested regions of interest of the same

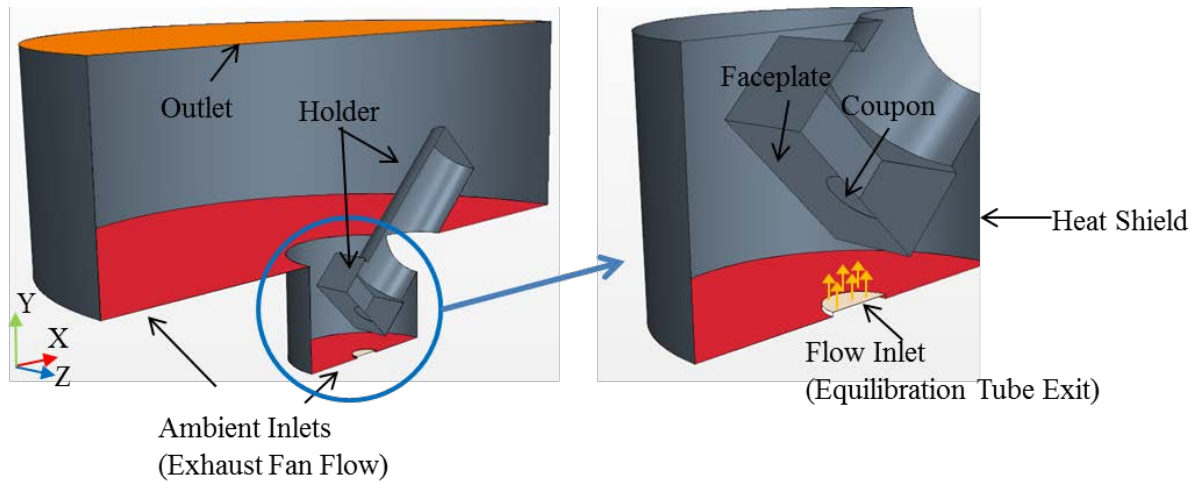


Figure 10-1: Holder and gas phase geometry used in STAR-CCM+. The yellow arrows represent the direction of flow at the flow inlet.

Table 10-1: Boundary conditions for the gas phase CFD simulation

| Jet Inlet | | | | | |
|--------------------------------|--------------------------------|----------------------|---------------------------|-----------------------|-----------------------|
| <i>Mass Flow Rate (kg/s)</i> | <i>Total Temperature (°C)</i> | <i>N₂</i> | <i>O₂</i> | <i>H₂O</i> | <i>CO₂</i> |
| 0.01075 – 0.011265 | 1263-1411 | 0.70954 | 0.00583 | 0.17993 | 0.10456 |
| Ambient Inlets | | | | | |
| <i>Velocity (m/s)</i> | <i>Static Temperature (°C)</i> | <i>N₂</i> | <i>O₂</i> | <i>H₂O</i> | <i>CO₂</i> |
| 2.5 | 27 | 0.79 | 0.21 | 0 | 0 |
| Outlet | | | | | |
| <i>Pressure (Pa)</i> | <i>Static Temperature (°C)</i> | <i>N₂</i> | <i>O₂</i> | <i>H₂O</i> | <i>CO₂</i> |
| Local Value | Local Value | Local Value | Local Value | Local Value | Local Value |
| Coupon | | | All Other Surfaces | | |
| <i>Static Temperature (°C)</i> | | | Adiabatic Wall | | |
| 962-1211 | | | | | |

names, as shown in Figure 10-2. The “Faceplate” region is the group of cells below the faceplate and coupon in the y-direction. The “Jet” region is the group of cells in the region formed by sweeping the flow inlet up from the equilibration tube to the coupon and faceplate. The “Coupon” region is derived from the “Jet” region, but includes only the cells within 2 mm of the coupon and faceplate surfaces. These three regions are where a majority of the cell refinement occurred because it is these regions that are of most importance in reference to particle physics before and during impact.

Table 10-2: Cell count in each of the grids used in the grid study

| Grid # | Region of Interest | | | Total Cells |
|--------|--------------------|--------|-----------|-------------|
| | Coupon | Jet | Faceplate | |
| 1 | 1507 | 2184 | 6122 | 324566 |
| 2 | 5987 | 7613 | 15872 | 326773 |
| 3 | 14083 | 21246 | 81028 | 506743 |
| 4 | 25134 | 54408 | 236434 | 926735 |
| 5 | 26390 | 83601 | 471538 | 1592190 |
| 6 | 57716 | 151519 | 1071118 | 2112231 |

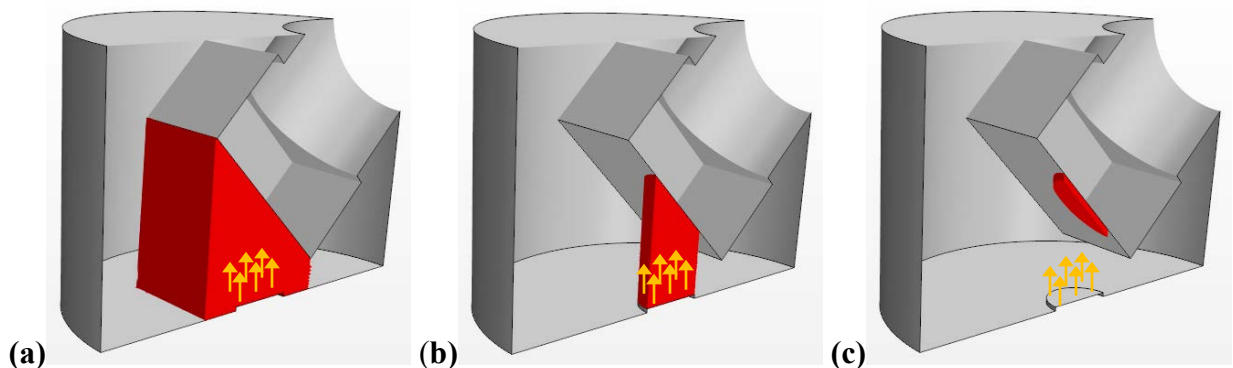


Figure 10-2: Regions of greatest importance in the CFD simulation: (a) Faceplate, (b) Jet and (c) Coupon. The yellow arrows represent the direction of flow at the flow inlet.

The solutions from each grid were compared to each other by calculating the root mean square (RMS) of 5 quantities obtained from the gas phase solution: temperature, velocity magnitude, and the three velocity vector components (i, j, k). When calculating the RMS, the individual quantities taken from each cell were weighted by the cell volume. The percent change in RMS from one grid to the next (i.e. #1 to #2, #2 to #3, etc.) was calculated and the results are shown in Figure 10-3. The case # along the x-axis refers to which grids are compared and are outlined in Figure 10-3a. As can be seen, there is not much change in the RMS values by refining past grid #4, so grid #4 was used to reduce error due to grid resolution but to also save on computational resources in performing other gas-phase simulations and modeling the particle phase. Figure 10-4 also shows gas temperature and velocity profiles across the centerline of the coupon. Again it can be seen that the profiles of meshes #4-6 are very similar, justifying the use of mesh #4.

10.1.1.1 Temperature Cases

The experimental data were obtained at a variety of gas and surface temperatures. Subsequently, gas-phase solutions were obtained for a variety of jet inlet temperature and coupon surface temperature combinations applicable to the actual experimental conditions. The temperatures used in the various solutions are given in Table 10-3.

10.1.2 Particle Phase Simulation

After the gas phase solution was obtained, particles were introduced into the simulation. The discrete element method (DEM) was used along with a coupled energy model. The particles were modeled as spherical particles. The turbulent dispersion model, which uses a random walk technique, was implemented to model the effect of turbulence on the particle trajectories. The

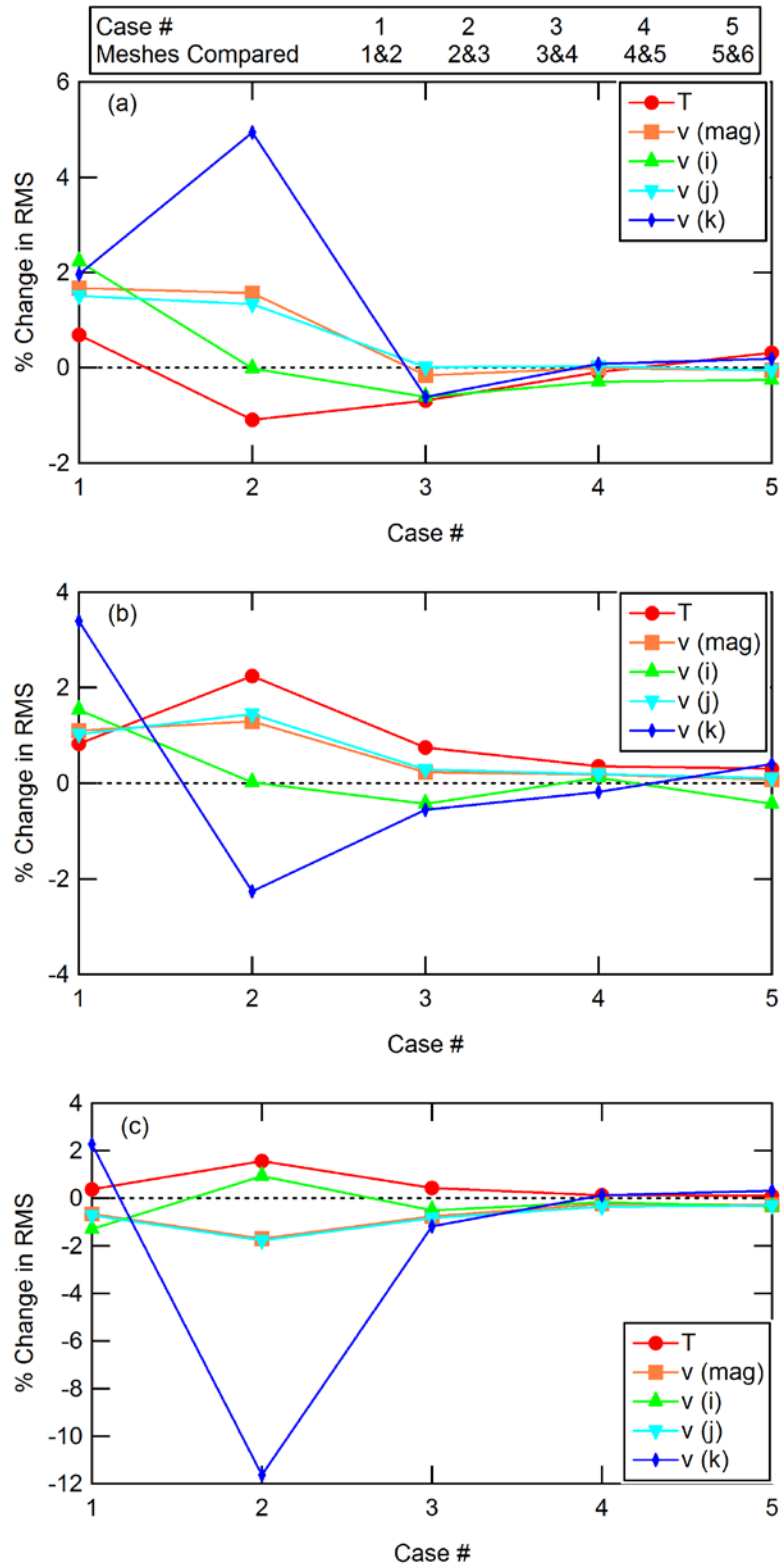


Figure 10-3: % Change in RMS between grid solutions for (a) Faceplate, (b) Jet and (c) Coupon.

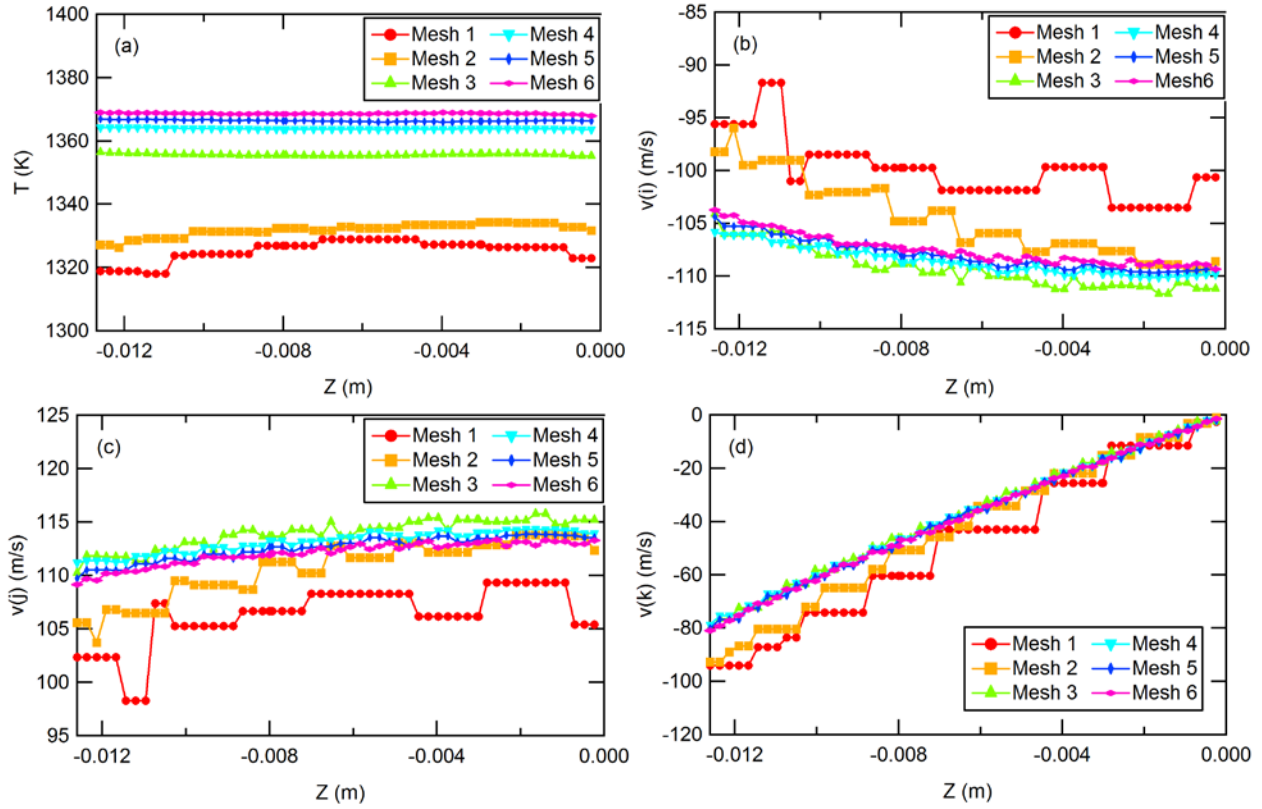


Figure 10-4: (a) Temperature and (b-d) velocity profiles across the centerline of the coupon.

Table 10-3: Temperature cases for the gas-phase simulations

| Case | Inlet Total T (°C) | Coupon T (°C) |
|------|--------------------|---------------|
| 1 | 1263 | 985 |
| 2 | 1263 | 1047 |
| 3 | 1294 | 1045 |
| 4 | 1294 | 1136 |
| 5 | 1310 | 1060 |
| 6 | 1310 | 1110 |
| 7 | 1362 | 1058 |
| 8 | 1362 | 1174 |
| 9 | 1411 | 962 |
| 10 | 1411 | 1047 |
| 11 | 1411 | 1108 |
| 12 | 1411 | 1167 |
| 13 | 1411 | 1211 |

particles were injected 1.6 mm above the flow inlet with velocities and temperatures matching that of the gas phase at their injection points. The average particle injection temperature and velocity for each temperature case is presented in Table 10-4. Boundary sampling was used to obtain particle impact data (temperature, velocity and position) as well as gas-phase properties at the point of impact. These data were then used in sticking and detachment models to determine the impact efficiency, sticking efficiency, and capture efficiency.

Table 10-4: Average particle injection temperature and velocity for each temperature case

| Case | T (°C) | v_i (m/s) | v_j (m/s) | v_k (m/s) |
|------|--------|-------------|-------------|-------------|
| 1 | 1244 | -0.00898 | 210 | 0.473 |
| 2 | 1245 | 0.0252 | 210 | 0.634 |
| 3 | 1274 | -0.0123 | 215 | 0.489 |
| 4 | 1274 | -1.09 | 214 | 1.04 |
| 5 | 1290 | 0.00557 | 217 | 0.536 |
| 6 | 1290 | 0.0278 | 217 | 0.652 |
| 7 | 1342 | -0.000250 | 217 | 0.545 |
| 8 | 1342 | 0.0701 | 217 | 0.613 |
| 9 | 1390 | 0.00463 | 220 | 0.564 |
| 10 | 1390 | 0.00541 | 220 | 0.564 |
| 11 | 1390 | 0.00465 | 220 | 0.565 |
| 12 | 1390 | 0.00372 | 220 | 0.564 |
| 13 | 1390 | 0.00394 | 220 | 0.564 |

The relationship between impact efficiency and the number of particle trajectories was investigated. Particle phase simulations were conducted at $T_g = 1400^\circ\text{C}$ and $T_s = 1000^\circ\text{C}$. Three different particle sizes (2 μm , 6 μm and 10 μm) and 8 different quantities of injection points (10, 25, 50, 75 and 100 particles) were tested. 10 particles were injected at each injection point, resulting in $10n$ particle trajectories in each test case, where n is the number of injection points.

The impact efficiency was then calculated for each case and is reported in Table 10-5. There is some change in impact efficiency as the number of injection points increases, but the impact efficiency levels off above 50 injection points. The decision was made to use 75 particle injection points (750 total trajectories) for all other cases in this study in order to obtain an accurate view of particle impact while conserving computational resources. The location of the 75 injection points is shown in Figure 10-5.

Table 10-5: Impact efficiency of particles with different particle sizes and at different quantities of particle trajectories

| # of Trajectories | Impact Efficiency (%) | | |
|-------------------|-----------------------|-------------|--------------|
| | <i>2 μm</i> | <i>6 μm</i> | <i>10 μm</i> |
| 10 | 10.0 | 56.0 | 60.0 |
| 25 | 6.4 | 46.8 | 57.6 |
| 50 | 9.0 | 50.6 | 59.0 |
| 75 | 8.0 | 51.5 | 61.6 |
| 100 | 8.1 | 54.0 | 63.6 |
| 125 | 8.3 | 51.7 | 62.3 |
| 150 | 7.8 | 52.5 | 61.7 |
| 200 | 7.8 | 50.8 | 61.9 |

10.1.1 Sticking and Detachment Models

The particle deposition models were written as MATLAB routines. After the gas and particle phase solutions were obtained from STAR-CCM+, the particle impact data were exported and read into MATLAB and the overall impact efficiency, sticking efficiency, and capture efficiency were calculated. Two deposition models were examined in this study: the critical velocity model (described earlier in Section 2.7.1) and the non-spherical model (described earlier in Section 2.7.4).

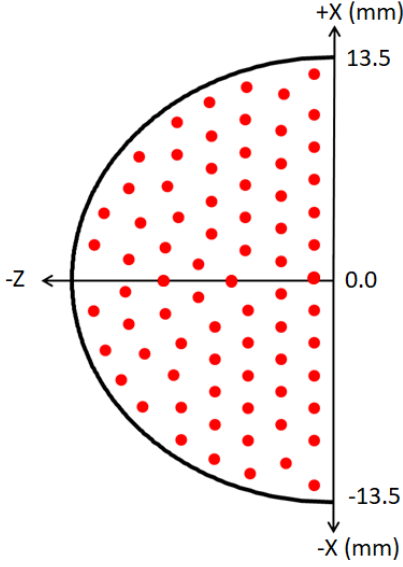


Figure 10-5: Injection points for 75 particle trajectories.

10.1.1.1 Critical Velocity Model

The critical velocity model, developed by Brach and Dunn (1992) and presented as Eqs. (2-3) through (2-7) was used in conjunction with the detachment model outlined in Eqs. (2-8) through (2-10). These equations are repeated here for reference.

$$v_{cr}^2 = -\frac{1 + \eta^2}{R^2} \frac{2W_A}{m} \quad (2-3)$$

$$\eta = \frac{v_t}{v_n} \quad (2-4)$$

$$W_A = -\left[\frac{5}{4}\rho\pi^{\frac{9}{2}}(k_1 + k_2)\right]^{\frac{2}{5}} \gamma r^2 |v_n|^{\frac{4}{5}} \quad (2-5)$$

$$k_1 = \frac{1 - v_s^2}{\pi E_s} \quad (2-6)$$

$$k_2 = \frac{1 - v_p^2}{\pi E_p} \quad (2-7)$$

$$u_{tc}^2 = \frac{CuW_A}{\rho D_p} \left(\frac{W_A}{d_p K_c} \right)^{\frac{1}{3}} \quad (2-8)$$

$$K_c = \frac{4}{3} \left[\frac{(1 - \nu_s^2)}{E_s} + \frac{(1 - \nu_p^2)}{E_p} \right]^{-1} \quad (2-9)$$

$$u_w = \sqrt{\frac{\tau_w}{\rho}} \quad (2-10)$$

A constant value of 0.8 was assumed for γ and a constant value of 0.174, calculated by Whitaker and Bons (2015) for the JB1 ash, was assumed for the Poisson's ratio of the particle and the deposit surface. The coefficient of restitution, R, as used in the critical velocity model, is defined as the coefficient in the absence of adhesion effects. A constant value of 0.5 was assumed, allowing for some loss in energy upon impact. Plastic deformation and energy losses could be taken into account by choosing appropriate values of R. A particle is predicted to deposit if its normal impact velocity is lower than the normal component of the critical velocity.

10.1.1.2 Non-Spherical Model

The non-spherical particle deposition model, developed by Bons et al. (2016) and described earlier in Section 2.7.4, was implemented and these equations are repeated here for reference. The same linear yield stress relation that was used by Bons et al. (2016) was used in this study and is given as Eq. (10-1). As a reminder, the available normal rebound kinetic energy is calculated by subtracting the work of adhesion (W_A) from the stored elastic energy evaluated at the point of transition from elastic to plastic deformation (w_{crit}). The shear drag calculated using Eq. (2-21) essentially increases the available normal rebound kinetic energy. If the resulting rebound normal

kinetic energy, and thus the normal rebound velocity, is positive, the particle rebounds. Otherwise, the particle sticks.

$$E_c = (\pi k_1 + \pi k_2)^{-1} \quad (2-16)$$

$$E_{el} = \int_0^{w_{el}} \frac{E_c A}{l} w dw = \left(\frac{E_c A}{l} \right) \frac{w_{el}^2}{2} \quad (2-17)$$

$$E_{k,n1} = E_{el,crit} + \int_{w_{crit}}^{w_{max}} \sigma_y A dw \quad (2-18)$$

$$W_A = A_{cont} \gamma \quad (2-19)$$

$$\frac{A_{cont}}{A_{crit}} = a + b \left(\frac{w_{max}}{w_{crit}} \right)^c \quad (2-20)$$

$$M_{drag} = \frac{\rho_f^3 u_\tau^4 dl^4}{8\mu^2} + \frac{3\rho_f^{\frac{5}{3}} d^{\frac{1}{3}} u_\tau^{\frac{8}{3}} l^{\frac{10}{3}}}{2\mu^{\frac{2}{3}}} \quad (2-21)$$

$$\sigma_y(T) = 200 - 0.225(T - 1000) \text{ MPa} \quad (10-1)$$

10.1.2 Determination of Final Capture Efficiency

Particle impact data were obtained for 25 particle sizes from the CFD simulations, ranging from 0.4 μm to 130 μm in diameter. At each particle size 750 particle trajectories were used, as shown in Figure 10-5. The use of a constant number of trajectories at each particle size results, however, in a particle size distribution different from the real particle size distribution of the ash used in the experiments. The measured particle size distribution was taken into account when calculating the final capture efficiency.

The total mass of ash impinging and sticking to the coupon surface was calculated for each particle diameter. Each of these masses was then multiplied by the ratio of the real size distribution to the CFD size distribution to obtain the real mass of ash that would have impinged and stuck had

the real distribution been used in producing the trajectories. These masses were then summed across all particle diameters to obtain a final impact, sticking and capture efficiency.

10.2 Results and Discussion

Particle deposition simulations were performed using the two models discussed earlier. The test data from the constant $T_{s,i}$ test series were used in each of the models to fit an expression for the Young's modulus as a function of temperature. Two fits, one linear and one exponential, were generated for each model. The Young's moduli of the particle and of the surface were assumed to follow the same expression, but were calculated at the particle and surface temperatures respectively. The following sections report the results of those fits and how well they simulate other deposition data.

10.2.1 Critical Velocity Model

The linear and exponential fits of the Young's modulus using the critical velocity model are given in Eq. (10-2) and Eq. (10-3) respectively. Figure 10-6 shows the measured capture efficiencies from the $T_{s,i}$ constant test series and the capture efficiencies obtained from the critical velocity model using each of the Young's modulus fits. Using the linear fit (Eq. (10-2)), the sum of squared error (SSE) on the capture efficiencies was 7.08. Using the exponential fit (Eq. (10-3)), the SSE was 3.16.

$$E(T) = -7.94 \times 10^3 T + 1.34 \times 10^7 \quad (10-2)$$

$$E(T) = 1.49 \times 10^{14} \cdot e^{-0.0122T} \quad (10-3)$$

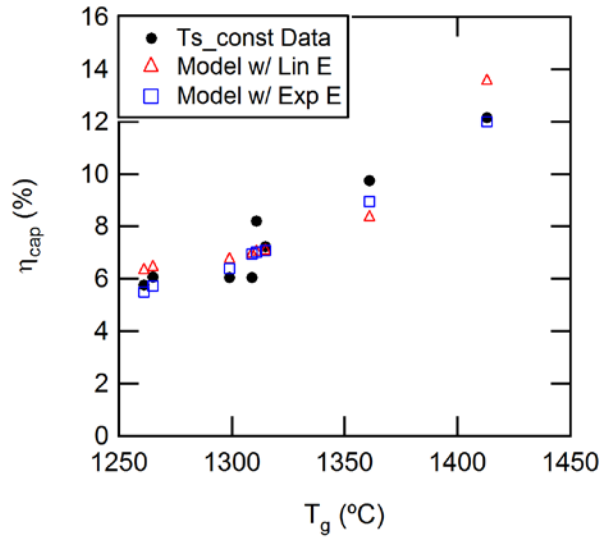


Figure 10-6: Capture efficiency data from the constant $T_{s,i}$ test series and the results from the critical velocity model using the linear and exponential Young's modulus fits.

To test the generality of the critical velocity model with the Young's modulus relations obtained from fitting the constant $T_{s,i}$ test series, the model was applied to the constant T_g test series as well as the transient test series. The results are plotted in Figure 10-7 and the SSE values for each test series and each fit are reported in Table 10-6. Looking at the results for the constant T_g series (Figure 10-7a), the model produced capture efficiencies that matched closest to the peak capture efficiencies. The model capture efficiencies increased slightly with increasing temperature when using the exponential Young's modulus fit. As reported earlier, an increase in capture efficiency would normally be the behavior expected with an increase in surface temperature, but the measured data show that at a gas temperature of 1400 $^{\circ}C$ and above a threshold surface temperature, the real capture efficiency of the JB2 ash began to decrease with increasing surface temperature. The only temperature dependent variables in the model equations

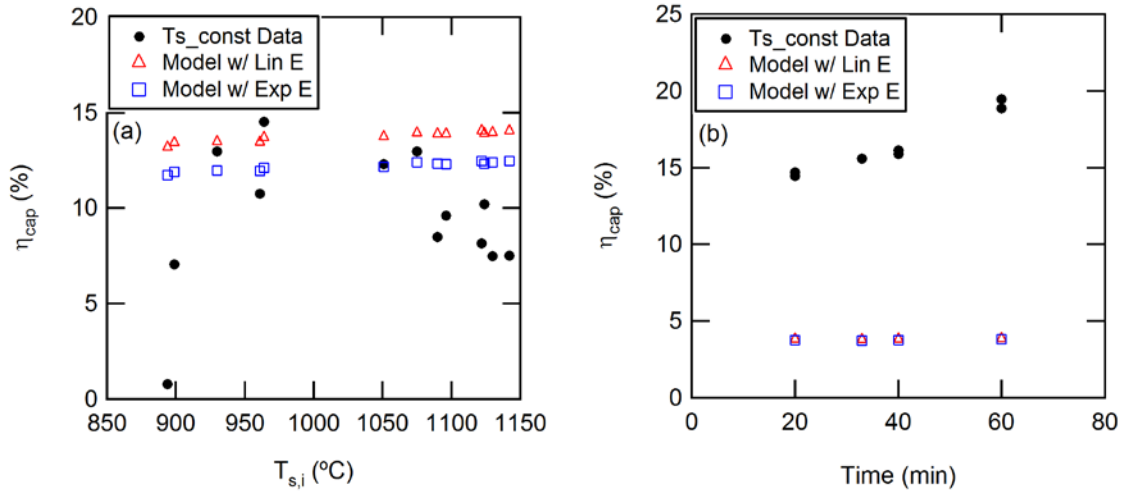


Figure 10-7: Comparison of experimental data and model results for (a) the constant T_g test series and (b) the transient test series using the critical velocity model and Young's modulus fits from the constant $T_{s,i}$ test series.

Table 10-6: SSE values for the results from the critical velocity model for the constant $T_{s,i}$, constant T_g , and transient test series using both Young's modulus fits

| Type of Fit | Constant $T_{s,i}$ | SSE | |
|-------------|--------------------|----------------|-----------|
| | | Constant T_g | Transient |
| Linear | 7.08 | 385 | 1137 |
| Exponential | 3.16 | 245 | 1145 |

are the Young's moduli. As the Young's moduli decrease, the capture velocity increases, meaning that a larger percentage of the particles will be predicted to deposit at higher temperatures.

The model did not predict any detachment in these cases, but decreasing the Young's modulus decreases K_c which leads to a larger u_{tc} which would also reduce any detachment that could possibly occur in other scenarios. This reduction in modeled detachment would also increase the modeled capture efficiency at higher temperatures (lower Young's modulus). In order to

accurately model deposit growth at high temperatures, the model would need to take into account increased particle and agglomeration detachment at higher gas and surface temperatures.

Figure 10-7b shows that the model greatly under-predicted the capture efficiencies of the transient test series. To see what the cause of this could be, the differences between the two test series were considered. The transient test series was conducted with the unground JB1 ash (MMD = 14 μm , $\rho_{\text{app}} = 2.8 \text{ g/cm}^3$), whereas the constant $T_{s,i}$ test series was conducted with the JB2 ash (MMD = 4.9 μm , $\rho_{\text{app}} = 2.1 \text{ g/cm}^3$). The model was run again for the constant $T_{s,i}$ and transient test series, this time using 4 combinations of particle size distribution and apparent density. The exponential Young's modulus fit was used in these cases. The results are shown in Figure 10-8. Changing ρ_{app} had a slight effect on the predicted capture efficiencies for the smaller particle size distribution and almost none for the larger particle size distribution. Changing the particle size distribution had a large effect on the predicted capture efficiencies. The agreement between the model and the transient test series data is still quite poor at each of the 4 combinations.

Looking at the model results using a ρ_{app} of 2100 g/cm^3 , switching from the smaller particle size distribution of the JB2 ash to the larger particle size distribution of the unground JB1 ash caused a relative reduction in the capture efficiency of 47% and 48% for the constant $T_{s,i}$ and transient test series respectively. This reduction in capture efficiency is the opposite of what would be expected. Crosby et al. (2008) performed tests with the JB1 ash and showed that capture efficiency increased with increasing mass mean particle diameter. The size distribution of the JB2 ash was given in Figure 3-7, but is shown again in Figure 10-9 along with the size distribution of the JB1 ash for comparison. The two distributions are similar up to about 2 μm ,

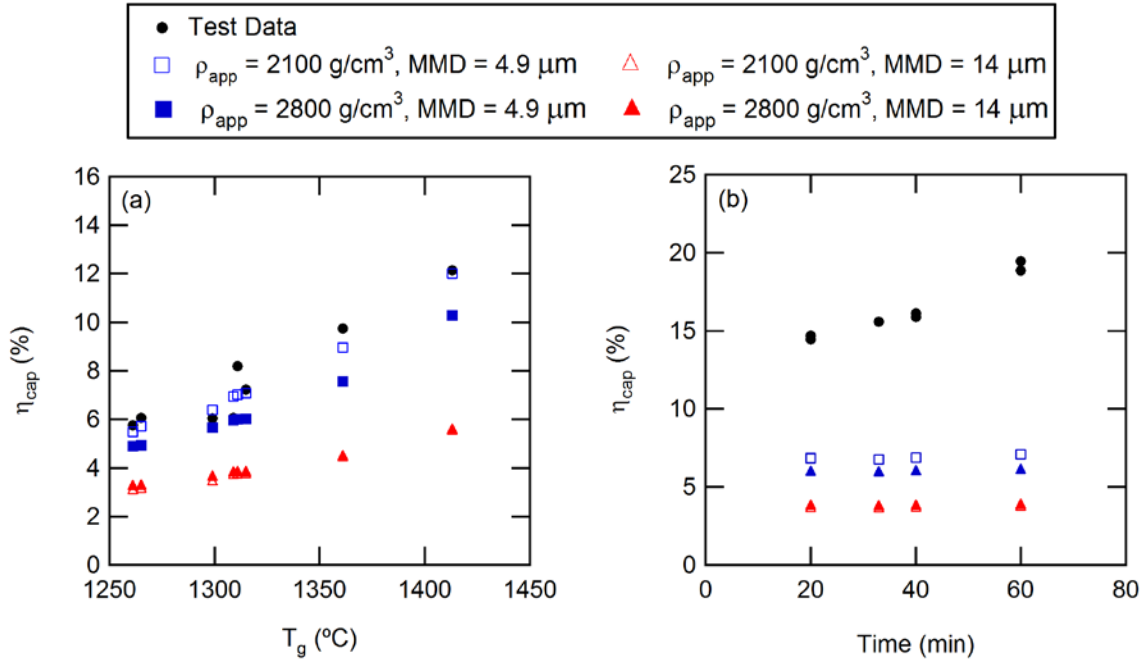


Figure 10-8: Graphs showing the model predictions using four combinations of ρ_{app} and particle size distribution for the (a) constant $T_{s,i}$ test series and (b) transient test series using the critical velocity model and exponential Young's modulus fit (Eq. (10-3)).

but then depart from one another. About 98% of the JB2 ash particles are 10.5 μ m in diameter or smaller, whereas only about 59% of the unground JB1 ash particles fall in that same range. It is likely that the critical velocity model is under-predicting the number of larger particles that deposit, thus driving down the capture efficiency when the unground JB1 ash size distribution is used.

One possible explanation for the under-prediction of large particle deposition is the use of a constant coefficient of restitution ($R = 0.5$). Lawrence (2013) measured the coefficient of restitution of coal ash particles and showed that R decreased with increasing particle diameter and increasing impact velocity. As stated by Brach and Dunn (1992), the R used in Eq. (2-3) is R in the absence of adhesion effects. Bons et al. (2016) showed that the normal R in the absence of adhesion effects, otherwise identified as the ideal normal R , of non-spherical particles is not a

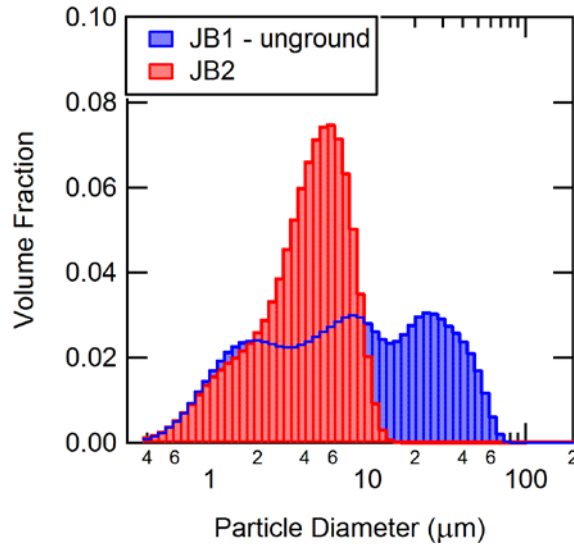


Figure 10-9: Size distributions of the unground JB1 ash and the JB2 ash.

function of d_p . They also indicated that this is generally true for spherical particles as well. The ideal normal R , however, decreases with increasing normal impact velocity.

Figure 10-10 shows the average normal impact velocity (v_n) obtained from the particle trajectories calculated in this study. It can be seen that the average v_n increases with particle size. This is due to the fact that larger particles are more likely to maintain their trajectory and impinge more directly on the target, whereas the smaller particles are more likely to follow the fluid flow and impinge at a shallower angle, thus decreasing the normal component of their impact velocity. Thus, while the particle size does not directly affect the ideal R of the particles, larger particles should have a lower ideal R due to their increased impact velocity, which would then increase the critical velocity in Eq. (2-3) which would lead to the predicted deposition of some larger particles.

Figure 10-10 also shows the effect of changing R on the critical velocity. The exponential Young's modulus fit was used and R was changed from 0.5 to 0.3. Decreasing R to 0.3 increased

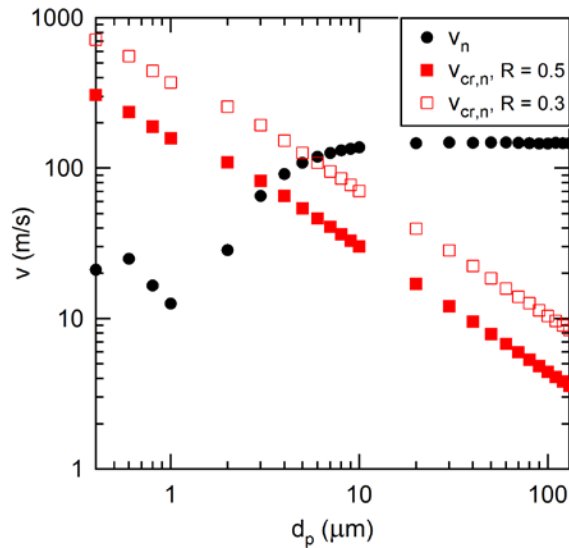


Figure 10-10: Average normal impact velocity (v_n) as a function of particle diameter (d_p). Also included is the average normal component of the critical velocity ($v_{cr,n}$) as a function of d_p , calculated with constant values of R (0.3 and 0.5) and using the exponential Young's modulus fit Eq. (10-3) ($T_g = 1294^\circ\text{C}$, $T_s = 1136^\circ\text{C}$).

the capture velocity. Figure 10-11 shows the effect of R and T_s on the sticking efficiency (the percent of impacting particles that adhere to the surface) at conditions representative of the transient test series. The sticking efficiency increased with increasing T_s . Decreasing R from 0.5 to 0.3 increased the sticking efficiency. While these figures show the effect that R has on modeling particle deposition and the role it can play in the critical velocity model, it should be noted that a constant R is still being used in these cases and that the Young's modulus fit used for these calculations was generated using $R = 0.5$. In order to accurately incorporate real values of R and improve implementation of this model, an appropriate relation for R as a function of particle properties should be used, including during the fitting process for the Young's modulus. This development of relationships for R was beyond the scope of this study.

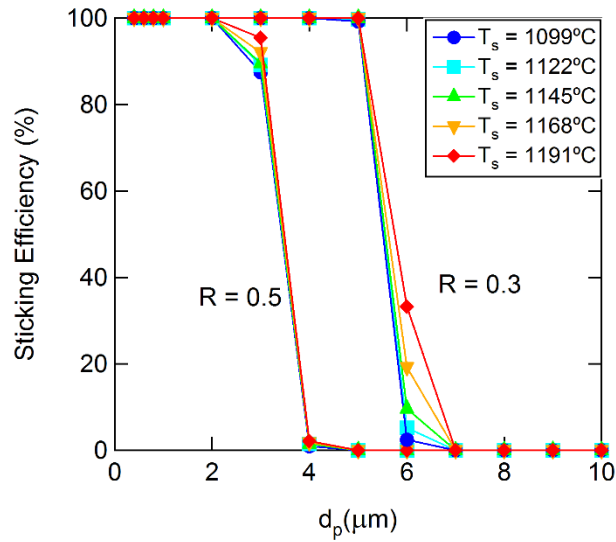


Figure 10-11: Particle sticking efficiency as a function of particle size (d_p) calculated with the critical velocity model using constant values of R (0.5 and 1.0) and using the exponential Young's modulus fit Eq. (10-3) ($T_g = 1288^\circ\text{C}$).

There are other potential contributors to the low predicted capture efficiencies of the transient test series. One is the fact that the model, as implemented here, only takes into account the first impact of a particle. The impact data from STAR-CCM+ were exported and post-processed in MATLAB to apply the sticking models. As such, the rebound velocities calculated in STAR-CCM+ are likely too high and any subsequent behavior of the particle after impact, whether there be additional impacts or no additional impacts, is not reliable. However, it is possible that, in reality, appropriate rebound velocities would result in multiple impacts by a particle that does not initially stick. These additional impacts would be characterized by lower impact velocities, and large particles that did not stick on the first impact could stick on the second impact, resulting in a higher sticking efficiency of large particles than is predicted here.

Another potential contributor to the low predicted capture efficiencies in the transient series is the lack of any consideration of the changing nature of the deposit surface and the resulting flow

around it. As the real deposit grows thicker and rougher, flow near the surface changes and impact angles and velocities could change, and deposit structures could present new obstacles after the initial impact that aren't present in the current simulation geometry.

10.2.2 Non-Spherical Model

Bons et al. (2016) applied their non-spherical model to tests run by Ai and Fletcher (2011). These tests were run with the JB1 ash. As material property values for the JB1 ash, Bons et al. (2016) used a constant Young's modulus (136 GPa), constant Poisson's ratio (0.174) and a temperature dependent yield stress in their model. They tuned the yield stress relationship in order to achieve the best match between the predicted and measured capture efficiencies, resulting in Eq. (10-1). These same material property values were used in applying the non-spherical model to the constant $T_{s,i}$ test series in this study. The predicted capture efficiencies were much greater than the measured capture efficiencies, but an increase in capture efficiency with increasing T_g was still observed. The yield stress relationship was then adjusted to produce a good match between the measured and predicted capture efficiencies, resulting in Eq. (10-4), showing that the non-spherical model can still match deposition trends with T_g up to 1400°C. The model results using both Eq. (10-1) and Eq. (10-4) are shown in Figure 10-12.

$$\sigma_y(T) = 154 - 0.0267(T - 1000)\text{MPa} \quad (10-4)$$

As used above, the only temperature dependent value in the non-spherical model is the yield stress, which is determined by the particle temperature. The surface temperature is not taken into account. The data from Chapter 6 of this study show that the surface temperature can have a significant effect on the capture efficiency. To try to account for the surface temperature, the Young's modulus was again treated as temperature-dependent and the linear and exponential

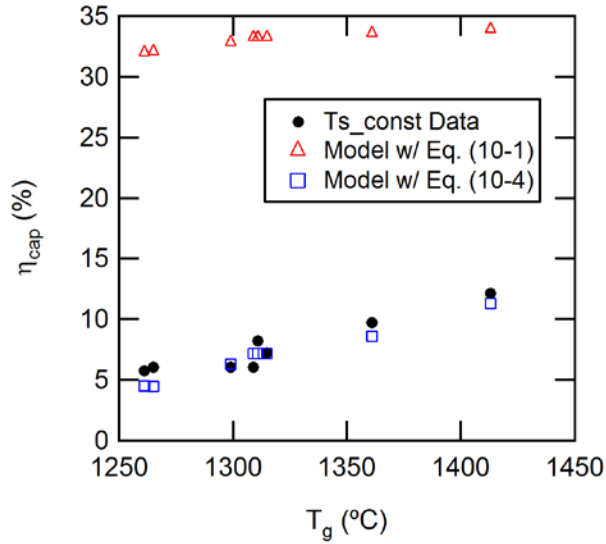


Figure 10-12: Constant $T_{s,i}$ capture efficiency data and the non-spherical model results using Eqs. (10-1) and (10-4) for the yield stress relationship.

relationships were adjusted to try to match the constant $T_{s,i}$ capture efficiencies. Eq. (10-1) was used for the yield stress. The linear and exponential fits of the Young's modulus using the non-spherical model are given in Eq. (10-5) and Eq. (10-6) respectively. Figure 10-13 shows the measured capture efficiencies from the $T_{s,i}$ constant test series and the capture efficiencies obtained from the non-spherical model using each of the Young's modulus fits. Using the linear fit, the sum of squared error (SSE) on the capture efficiencies was 47.0. Using the exponential fit, the SSE was 41.4.

$$E(T) = -1.61 \times 10^8 T + 2.79 \times 10^{11} \quad (10-5)$$

$$E(T) = 1.23 \times 10^{15} \cdot e^{-0.00698T} \quad (10-6)$$

The behavior of the model exhibited in Figure 10-13 is much more scattered than that seen in Figure 10-12. It is believed that this is due to the introduction of a second temperature dependent term. Taking both the particle and surface temperatures into account when calculating the

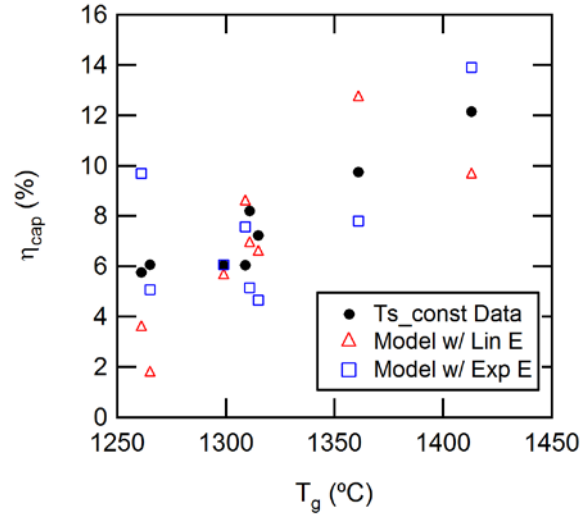


Figure 10-13: Capture efficiency data from the constant $T_{s,i}$ test series and the results from the non-spherical model using the linear and exponential Young's modulus fits.

composite Young's modulus may account for this behavior. As the particle and surface temperatures increase, the composite Young's modulus (E_c) decreases which would increase the stored elastic energy for rebound in the model. However, as the particle temperature increases, the yield stress (σ_y) also decreases which decreases the stored elastic energy for rebound.

Figure 10-14 presents the model results for the constant T_g test series and the transient test series, and Table 10-7 reports the SSE values for each test series and each fit using the non-spherical model. For the non-spherical model, the linear Young's modulus relation produces the closest match to the data, except for the $T_{s,i}$ constant model. In the constant T_g test series (Figure 10-14a), the modeled capture efficiencies are seen to generally decrease with increasing surface temperature, much like the measured capture efficiency data. In the case of the model, this decrease in capture efficiency is likely due to the relatively constant yield stress (T_g is maintained at 1400°C, resulting in more constant particle temperatures across each test) and decreasing E_c as the T_s increases. To demonstrate that the yield stress is mostly constant in the constant T_g test series, the

average particle temperature (T_p) of impacting particles as a function of T_s is shown in Figure 10-15 for 5 different particle sizes. The data presented in Figure 10-15 are those generated by the model for each test in the constant T_g test series. It can be seen that the smaller particles exhibit a larger variation in T_p as T_s increases. However, as the particle size increases, the T_p becomes nearly constant with respect to T_s , meaning that σ_y is nearly constant as well.

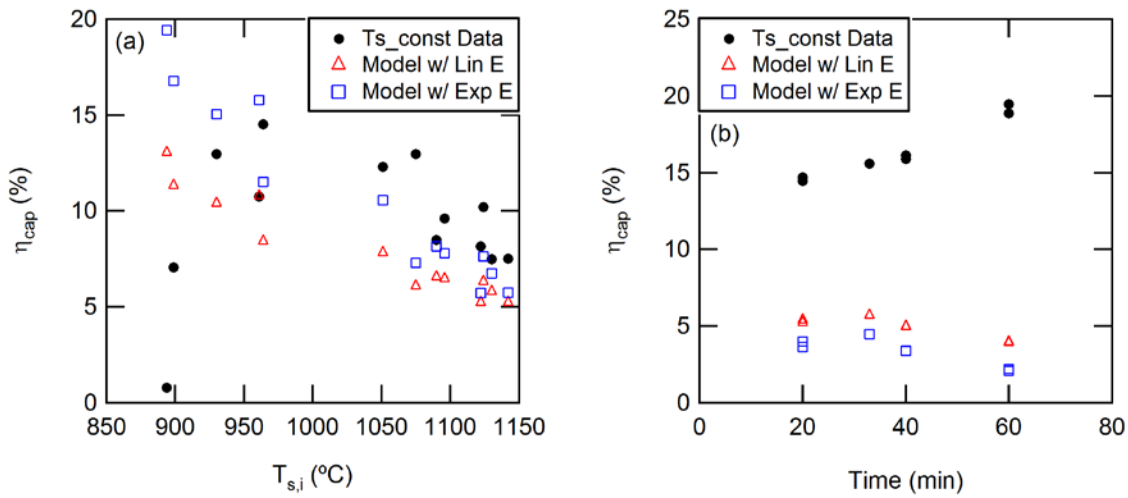


Figure 10-14: Comparison of experimental data and model results for (a) the constant T_g test series and (b) the transient test series using the non-spherical model and Young's modulus fits from the constant $T_{s,i}$ test series.

Table 10-7: SSE values for the results from the non-spherical model for the constant $T_{s,i}$, constant T_g , and transient test series using both Young's modulus fits

| Type of Fit | Constant $T_{s,i}$ | SSE | |
|-------------|--------------------|----------------|-----------|
| | | Constant T_g | Transient |
| Linear | 47.0 | 325 | 977 |
| Exponential | 41.4 | 535 | 1253 |

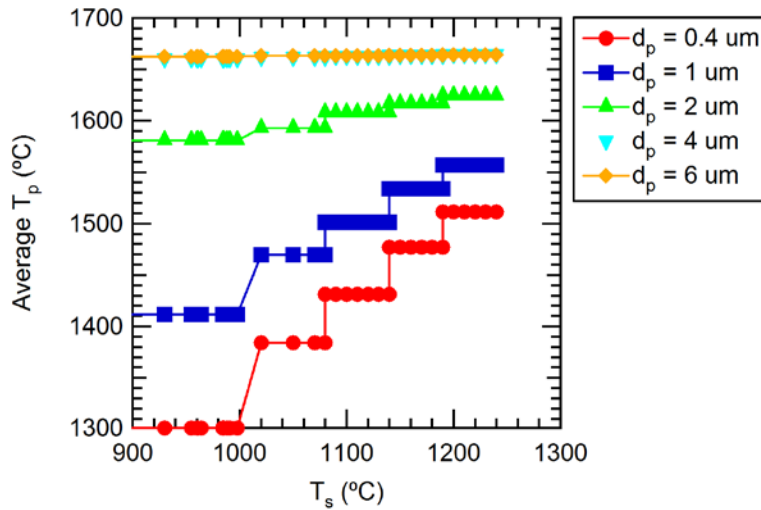


Figure 10-15: Average particle temperature from the constant T_g test series plotted against surface temperature.

Figure 10-14b shows the model results for the transient test series. The non-spherical model, with the linear Young's modulus fit, does produce somewhat higher capture efficiencies than the critical velocity model, but they are still well below the measured capture efficiencies. Figure 10-16 presents the model results from the non-spherical model using the same 4 combinations of particle density and particle size distribution as Figure 10-8. Switching to the size distribution of the unground JB1 ash still lowers the capture efficiency in the non-spherical model. The non-spherical model is much more sensitive to the particle density as well.

Sticking efficiency results obtained from the non-spherical model at conditions representative of the transient test series are presented in Figure 10-17. The sticking efficiency was calculated for each particle size at 5 different surface temperatures. The sticking efficiency peaks at $d_p = 5 \mu\text{m}$ at each T_s , except the hottest where the peak shifts to $d_p = 4 \mu\text{m}$. As the T_s increases, the peak sticking efficiency decreases. The non-spherical model predicted that particles up to $7 \mu\text{m}$ in diameter would deposit, whereas the critical velocity model ($R = 0.5$) predicted that only

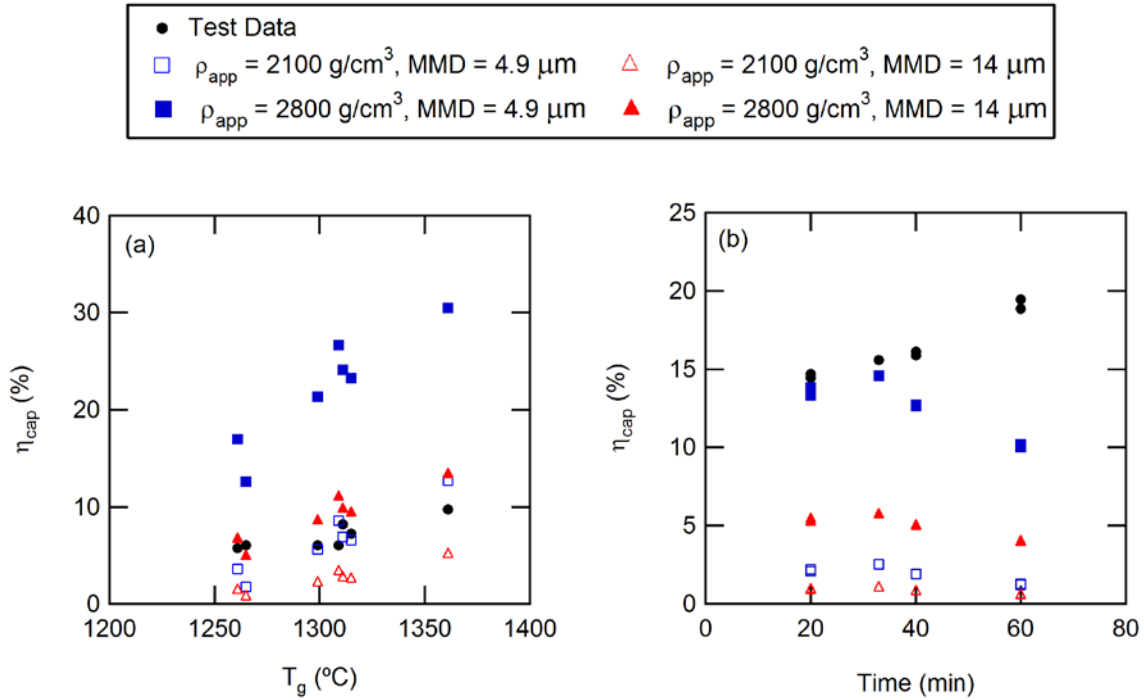


Figure 10-16: Graphs showing the model predictions using four combinations of ρ_{app} and particle size distribution for the (a) constant $T_{s,i}$ test series and (b) transient test series using the non-spherical model and linear Young's modulus fit (Eq. (10-5)).

particles up to 4 μm would deposit. This increase in the size of deposited particles could explain the slight increase in capture efficiency in the non-spherical model. However, looking at the particle size distributions in Figure 10-9, the sizes of particles depositing are still in the range that encompasses the majority of the JB2 ash and only a fraction of the unground JB1 ash. Thus, shifting to the unground JB1 particle size distribution still reduces the overall capture efficiency rather than increasing it. This indicates that, even when calculating R for each particle, the non-spherical model still under-predicts the deposition of large particles (above 10 μm in diameter) that would contribute to the capture efficiency of the unground JB1 ash. Secondary impacts and the changing layout of the deposit surface (altered flow and impact angles, more obstacles) play

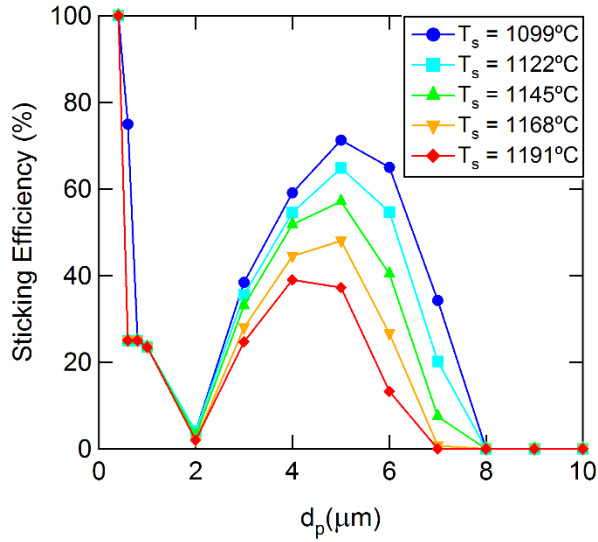


Figure 10-17: Particle sticking efficiency as a function of particle size (d_p) calculated with the non-spherical model and using the linear Young's modulus fit Eq. (10-5) ($T_g = 1288^\circ\text{C}$).

an important role in the deposition process, particularly of large particles that are predicted to rebound initially.

10.3 Summary and Conclusions

Gas-phase simulations were performed to model the fluid flow dynamics around the coupon holder in the TADF. The discrete element method and a coupled energy model were implemented to model particle trajectories and obtain particle impact data at the coupon surface. The impact data were then used in two different particle deposition models to obtain temperature dependent regressions for the Young's modulus of the ash particles that allowed the models to best predict the capture efficiencies from the constant $T_{s,i}$ test series. These fits were then used in the respective models to test the applicability of the models to the constant T_g test series and the transient test series.

An exponential fit for the Young's modulus resulted in the best predictions from the critical velocity model, and a linear fit worked best for the non-spherical model (except for the constant $T_{s,i}$ data). The critical velocity model fit the constant $T_{s,i}$ test data better than the non-spherical model, but the non-spherical model did a better job of predicting the capture efficiencies from the transient test series, although the predictions were still quite poor. Both models had similar SSE values in predicting the constant T_g capture efficiencies, but the non-spherical model better matched the trend in increasing $T_{s,i}$.

Neither model was designed to account for detachment of large agglomerations of particles, the latter process having been observed in experiments at high T_g . Also, some of the gas temperatures are above the softening temperature of the ashes modeled in this study. At these high temperatures it may be necessary to switch from particle deformation/rebound models to models that account for viscous flow of the particles.

11 SUMMARY AND CONCLUSIONS

Experiments were performed in the Turbine Accelerated Deposition Facility (TADF) at Brigham Young University in order to investigate particle deposition behavior at modern gas turbine temperatures. To make these experiments possible, modifications were made to the TADF that increased the maximum operating temperature from 1200°C to 1400°C. These modifications included switching to materials that could withstand higher temperatures (i.e. SiC and quartz vs. Inconel) for the acceleration cone and equilibration tube and redesigning the coupon holder so that a SiO₂ faceplate could be attached to protect the rest of the holder while still allowing the coupon to be flush with the front surface of the holder/faceplate.

After verifying that the upgraded facility produced results similar to those obtained from the previous facility, test series were conducted that varied the deposition time, gas temperature (while aiming for a constant initial surface temperature), initial surface temperature (while aiming for a constant gas temperature), ash type, and film-cooling blowing ratio. The deposits were analyzed to obtain capture efficiency, surface roughness, deposit density, and deposit chemical composition data.

CFD simulations were also performed to obtain fluid dynamics data and particle trajectories near the coupon holder. These data were then used in two different particle deposition models, a critical velocity model (Brach and Dunn, 1992) and a non-spherical model (Bons et al.,

2016), to produce temperature-dependent fits for the value of the Young's modulus of the ash and to see how well these two models predict particle deposition at high gas temperatures.

The following sections summarize the results and conclusions from the experimental test series and the modeling that was performed.

11.1 Transient Characteristics

The time-dependent deposition characteristics for fine coal flyash from a subbituminous coal were measured in the TADF at Brigham Young University at gas temperatures near 1295°C. Two different size distributions of flyash were used in this study, with mass mean diameters of 14 μm and 3 μm . The time-dependent nature of surface temperature, capture efficiency, deposit thickness, deposit surface roughness, and ash viscosity were measured and calculated. It was determined that the net capture efficiency, surface roughness, deposit density, deposit thickness and deposit surface temperature all increased with time. The increasing surface temperature lowered the viscosity and increased the probability of a particle sticking to the surface, which likely led to the increase in net capture efficiency.

These data and conclusions provide necessary information to be used to further improve and expand current deposition models to allow for transient modeling. While the 3 μm particles are believed to behave in a similar manner to the 14 μm particles, there is currently insufficient data to determine the functionality of the behavior.

11.2 Temperature-Dependent Characteristics

The experiments that varied gas temperature while holding the initial surface temperature constant showed increases in capture efficiency with increased T_g , as expected. There was some

sensitivity of the capture efficiency to the total mass fed. The surface roughness also increased with increasing T_g , while the deposit density first increased then decreased as T_g increased. Time-dependent surface temperature maps were shown, and the surface temperature was shown to increase throughout the duration of the tests, much like in the transient test series. The increase in average surface temperature increased as the gas temperature and capture efficiency increased. Deposits were not smooth, and showed clumping that may be caused by increased softening at higher temperatures as well as the effects of the high speed flows along the surface.

The experiments that held the gas temperature constant and varied the initial surface temperature showed first an increase then a decrease in capture efficiency with increasing initial surface temperature ($T_{s,i}$). The increasing capture efficiency was similar to other tests, and is a result of increased softening behavior. However, the decrease in capture efficiency at initial surface temperatures above 1000°C was unexpected. The surface roughness decreased with increasing $T_{s,i}$ as well in these tests.

The data comparing the capture efficiency on the inside of the equilibration tubes (both the SiC and quartz tubes) showed that the impingement angle of the flow onto the deposit surface, as well as the surface material and conditions, affects the rate of deposition. The shallower angle of the tube surface (parallel to the gas flow) resulted in capture efficiencies that were 97% lower on average than on the coupon held at a 45° angle to the flow.

11.3 Ash-Dependent Characteristics

Ash deposits were formed in the TADF using 4 different types of coal ash in order to compare the effects of ash type on particle deposition behavior. Five deposit samples from the constant $T_{s,i}$ test series, which used the JB2 ash, were also included in the comparison. Each ash

was ground to achieve a similar MMD, ranging from 4.9 to 8.0 μm . It was determined that the apparent density of the ash played a role in ash deposition, with capture efficiency and surface roughness increasing as the ash density increased.

While it appeared that, in general, the increase in surface temperature seemed to correlate with an increase in capture efficiency, this was not true in all cases. The JB2 ash deposits experienced the highest change in T_s despite only having the third highest average capture efficiency. The higher change in T_s is likely due to higher surface roughness (increasing heat transfer to the deposit surface) and lower effective thermal conductivity (reducing heat transfer through the deposit) of the JB2 ash deposits.

11.4 Heavy Fuel Oil Characteristics

Experiments were conducted in the TADF to study the deposition behavior and deposit characteristics of flyash produced from HFO combustion. The deposits were formed at gas temperature from 1101°C to 1219°C and the SO_2 concentration was increased to 1.1 mol% to match conditions representative of HFO combustion in industrial gas turbines.

Increasing the SO_2 concentration did increase the amount of sulfur in the deposit from baseline levels. The sulfur content of the deposits decreased with increasing gas temperature. Increasing the surface temperature, however, had no discernable effect on the capture efficiency of the HFO ash in the TADF, possibly due to competing processes of increased deposition tendency and increased detachment or ash release at higher gas temperatures.

Washing the coupons in distilled water revealed that while some of the magnesium may have formed MgSO_4 , most of Mg did not form MgSO_4 and remained in the deposit after washing. The sulfur likely formed K_2SO_4 and CaSO_4 as well from the potassium and calcium in the ash. At

lower gas temperatures, when the sulfur content was higher, more of the magnesium was removed during the wash process, indicating that MgSO_4 was more favored to form at lower temperatures with higher sulfur concentrations.

The total mass percent of deposit removed by the water wash procedure did not change with respect to gas temperature, indicating that changing the gas temperature in the turbine would not aid in the formation of easily removed deposits. However, this also shows that it would not adversely affect the amount of water soluble deposit formed if the gas temperature was changed for other purposes.

11.5 Film-Cooling Characteristics

Deposition experiments were performed in the TADF using coupons with film-cooling holes. The gas temperature was maintained near 1400°C during each test and the blowing ratio was varied from 0.5 to 2.0 between tests. The capture efficiency decreased slightly as the blowing ratio increased. The main conclusion from this test series is that variation in blowing ratio has a smaller effect on particle deposition at high gas temperatures (1400°C) than at lower gas temperatures at which other tests have been conducted. The capture efficiency in these tests was an order of magnitude larger than that observed in similar experiments at lower T_g (1183°C), and experienced a much smaller percent reduction in capture efficiency over the range of blowing ratio. Variation in particle size between the low and high temperature tests may have also contributed to the difference in the observed effect of blowing ratio on capture efficiency. No clear effect on surface roughness, deposit density, surface temperature, or physical structure and appearance was observed with changing blowing ratio, again indicating a reduced effect of film-cooling on deposition behavior at high T_g .

11.6 Deposition Modeling

After obtaining particle impact data from CFD simulations and using the data in the two particle deposition models used in this study, it was found that an exponential fit for the Young's modulus resulted in the best predictions from the critical velocity model, and a linear fit worked best for the non-spherical model (except for the constant $T_{s,i}$ data). The critical velocity model fit the constant $T_{s,i}$ test data better than the non-spherical, but the non-spherical model did a better job of predicting the capture efficiencies from the transient test series, although the predictions were still quite poor. Both models had similar SSE values in predicting the constant T_g capture efficiencies, but the non-spherical model better matched the trend in increasing $T_{s,i}$.

Neither model was designed to account for detachment of large agglomerations of particles, the latter process having been observed in experiments at high T_g . Also, some of the gas temperatures are above the softening temperature of the ashes modeled in this study. At these high temperatures, it may be necessary to switch from particle deformation/rebound models to models that account for viscous flow of the particles.

11.7 Recommendations for Future Work

The capture efficiency in the transient test series increased exponentially with time. It would be of value to perform experiments at longer exposure times to determine how the deposit continues to develop over time as the capture efficiency cannot grow exponentially indefinitely. Experiments with wax droplets (Albert and Bogard, 2012) have shown that the deposit thickness can reach equilibrium. If this thickness equilibrium were to occur with ash, it would be interesting to observe if the other deposit characteristics (surface roughness, density, etc.) also reach equilibrium, or if the roughness would continue to change (possibly decreasing due to peaks

reaching equilibrium and valleys being filled in, such as what was observed by Wammack et al. (2008) at $T_g = 1150^\circ\text{C}$) and if density would change due to increased sintering time. If the deposit density were to reach equilibrium, the capture efficiency would be expected to drop over time due to a constant deposit mass but increasing mass of ash fed. It would also be interesting to perform these transient tests at higher temperature than the 1295°C gas temperature used in this test series to observe how temperature affects the functionality of the capture efficiency growth and, if equilibrium is achieved, how it affects the equilibrium values and speed at which they are attained.

The results from the constant T_g test series that showed decreasing capture efficiency with increasing $T_{s,i}$ were unexpected. Further investigation of this phenomenon would be valuable. Does the capture efficiency continue decrease at even higher $T_{s,i}$, or does the trend shift? It is recognized that the tests performed in this study used bare metal coupons and that increasing surface temperatures necessitates the use of TBC coatings (both in experiments and industrial application). Experiments performed on TBC would provide valuable information and show if similar trends occur when TBC is applied. Also, deposition experiments that focus on observing and quantifying detachment mechanisms of particle agglomerations would add valuable insight to the deposit formation process at high gas and surface temperatures.

The film-cooling experiments showed that blowing ratio had a relatively smaller effect on particle deposition at high gas temperatures (1400°C) than in tests previously performed by Ai (2009) at lower gas temperatures (1183°C). Tests at blowing ratios (greater than 2.0) could reveal if, at higher gas temperatures, there is a threshold blowing ratio below which there is little effect on deposition but above which there is a similar effect as in the lower gas temperature tests. Also, more investigation into why the capture efficiency increased with increasing $T_{s,i}$ rather than decreasing, as seen in the constant T_g test series at similar T_g and $T_{s,i}$, is recommended.

Finally, as more information and insight about particle deposition behavior at high temperatures is becoming available (and more if the work recommended here is carried out), more work can be done on particle deposition models to incorporate and account for high temperature phenomena, such as agglomeration detachment. Accounting for changing surface topography could increase accuracy while looking at various exposure times and different experiment geometries. Also, many deposition models depend on knowledge of the Young's modulus of the ash, but little empirical data are available concerning ash Young's modulus at high temperatures; the collection of this kind of data for a variety of ash types would be a great addition to this field.

REFERENCES

Administration, U. S. E. I., "International Energy Outlook 2016," U. S. E. I. Administration, Washington, D.C (2016).

Agency, I. E., "Key Coal Trends, Exerpt From: Coal Information," International Energy Agency (2016).

Ai, W., "Deposition of Particulate from Coal-Derived Syngas on Gas Turbine Blades near Film Cooling Holes," PhD Dissertation, Chemical Engineering Department, Brigham Young University (2009).

Ai, W. and T. H. Fletcher, "Computational Analysis of Conjugate Heat Transfer and Particulate Deposition on a High Pressure Turbine Vane," *Journal of Turbomachinery*, **134**(4), 041020 (2011).

Ai, W., R. G. Laycock, D. S. Rappleye, T. H. Fletcher and J. P. Bons, "Effect of Particle Size and Trench Configuration on Deposition from Fine Coal Flyash near Film Cooling Holes," *Energy and Fuels*, **25**, 1066-1076 (2011a).

Ai, W., N. Murray, T. H. Fletcher, S. Harding and J. P. Bons, "Effect of Hole Spacing on Deposition of Fine Coal Flyash near Film Cooling Holes," *Journal of Turbomachinery*, **134**(4), 041021 (2011b).

Ai, W., N. Murray, T. H. Fletcher, S. Harding, S. Lewis and J. P. Bons, "Deposition near Film Cooling Holes on a High Pressure Turbine Vane," *Journal of Turbomachinery*, **134**(4), 041013 (2011c).

Albert, J. E. and D. G. Bogard, "Experimental Simulation of Contaminant Deposition on a Film Cooled Turbine Airfoil Leading Edge," *Journal of Turbomachinery*, **134**(5), 051014 (2012).

- Albert, J. E. and D. G. Bogard, "Experimental Simulation of Contaminant Deposition on a Film-Cooled Turbine Vane Pressure Side with a Trench," *Journal of Turbomachinery*, **135**(5), 051008 (2013).
- Anderson, D. W., R. Viskanta and F. P. Incropera, "Effective Thermal Conductivity of Coal Ash Deposits at Moderate to High Temperatures," *Journal of Engineering for Gas Turbines and Power*, **109**, 215-221 (1987).
- Anderson, R. J., R. G. Logan, C. T. Meyer and R. A. Dennis, "A Combustion/Deposition Entrained Reactor for High-Temperature/Pressure Studies of Coal and Coal Minerals," *Review of Scientific Instruments*, **61**(4), 1294 (1990).
- Barker, B., B. Casaday, P. Shankara, A. Ameri and J. P. Bons, "Coal Ash Deposition on Nozzle Guide Vanes-Part II: Computational Modeling," *Journal of Turbomachinery*, **135**(1) (2013).
- Barroso, J., F. Barreras and J. Ballester, "Behavior of a High-Capacity Steam Boiler Using Heavy Fuel Oil: Part I. High-Temperature Corrosion," *Fuel Processing Technology*, **86**(2), 89-105 (2004).
- Baxter, L. L., "Ash Deposition During Biomass and Coal Combustion. A Mechanistic Approach," *Biomass and Bioenergy*, **4**, 85-102 (1993).
- Beer, J. M., A. F. Sarofim and L. E. Barta, "From Properties of Coal Mineral Matter to Deposition Tendencies of Fly Ash. A Modelling Route," *Journal of the Institute of Energy*, **65**(462), 55-62 (1992).
- Belo, L. P., L. K. Elliott, R. J. Stanger, R. Spörl, K. V. Shah, J. Maier and T. F. Wall, "High-Temperature Conversion of SO₂ to SO₃: Homogeneous Experiments and Catalytic Effect of Fly Ash from Air and Oxy-Fuel Firing," *Energy & Fuels*, **28**(11), 7243-7251 (2014).
- Bird, R. B., W. E. Stewart and E. N. Lightfoot, *Transport Phenomena*, Second Edition, New York, John Wiley & Sons, Inc. (2002).
- Bogard, D. G., D. L. Schmidt and M. Tabbita, "Characterization and Laboratory Simulation of Turbine Airfoil Surface Roughness and Associated Heat Transfer," *Journal of Turbomachinery*, **120**(2), 337-342 (1998).
- Bons, J. P., J. Crosby, J. E. Wammack, B. I. Bentley and T. H. Fletcher, "High-Pressure Turbine Deposition in Land-Based Gas Turbines from Various Synfuels," *Journal of Engineering for Gas Turbines and Power*, **129**(1), 135-143 (2005).

- Bons, J. P., J. E. Wammack, J. Crosby, D. Fletcher and T. H. Fletcher, "Evolution of Surface Deposits on a High-Pressure Turbine Blade—Part II: Convective Heat Transfer," *Journal of Turbomachinery*, **130**(2), 021021-021021-7 (2008).
- Bons, J. P., R. Prenter and S. Whitaker, "A Simple Physics-Based Model for Particle Rebound and Deposition in Turbomachinery," ASME Turbo Expo 2016: Turbomachinery Technical Conference and Exposition, GT 2016, June 13, 2016 - June 17, 2016, Seoul, South Korea, 5B (2016).
- Borom, M. P., C. A. Johnson and L. A. Peluso, "Role of Environmental Deposits and Operating Surface Temperature in Spallation of Air Plasma Sprayed Thermal Barrier Coatings," *Surface and Coatings Technology*, **86-87**, 116-126 (1996).
- Brach, R. M. and P. F. Dunn, "A Mathematical Model of the Impact and Adhesion of Microspheres," *Aerosol Science and Technology*, **16**(Compendex), 51-64 (1992).
- Burdett, N. A., W. E. Langdon and R. T. Squires, "Rate Coefficients for the Reaction SO₂ Plus O₂ Yields SO₃ Plus O in the Temperature Range 900-1350 K," *Journal of the Institute of Energy*, **57**(432), 373-376 (1984).
- Casaday, B., R. Prenter, C. Bonilla, M. Lawrence, C. Clum, A. A. Ameri and J. P. Bons, "Deposition with Hot Streaks in an Uncooled Turbine Vane Passage," *Journal of Turbomachinery*, **136**(4) (2014).
- Cengel, Y. A., *Introduction to Thermodynamics and Heat Transfer*, Boston, Massachusetts, Irwin/Mcgraw-Hill (1997).
- Crosby, J. M., "Particle Size, Gas Temperature, and Impingement Cooling Effects on High Pressure Turbine Deposition in Land Based Gas Turbines from Various Synfuels," Master Thesis, Mechanical Engineering Department, Brigham Young University (2007).
- Crosby, J. M., S. Lewis, J. P. Bons, W. Ai and T. H. Fletcher, "Effects of Temperature and Particle Size on Deposition in Land Based Turbines," *Journal of Engineering for Gas Turbines and Power*, **130**(5), 051503 (2008).
- Davidson, F. T., D. A. Kistenmacher and D. G. Bogard, "A Study of Deposition on a Turbine Vane with a Thermal Barrier Coating and Various Film Cooling Geometries," *Journal of Turbomachinery*, **136**(4) (2013).

- Delimont, J. M., M. K. Murdock, W. F. Ng and S. V. Ekkad, "Effect of Temperature on Microparticle Rebound Characteristics at Constant Impact Velocity - Part II," *Journal of Engineering for Gas Turbines and Power*, **137**(11) (2015).
- El-Batsh, H. and H. Haselbacher, "Numerical Investigation of the Effect of Ash Particle Deposition on the Flow Field through Turbine Cascades," Proceedings of the ASME Turbo Expo 2002: Turbomachinery, June 3, 2002 - June 6, 2002, Amsterdam, Netherlands, 5B (2002).
- Franco, A. and A. R. Diaz, "The Future Challenges for "Clean Coal Technologies": Joining Efficiency Increase and Pollutant Emission Control," *Energy*, **34**, 348-354 (2009).
- Jackson, R. L. and I. Green, "A Finite Element Study of Elasto-Plastic Hemispherical Contact against a Rigid Flat," *Journal of Tribology*, **127**(2), 343-354 (2005).
- Jensen, J. W., "The Development of an Accelerated Testing Facility for the Study of Deposits in Land-Based Gas Turbine Engines," Master Thesis, Mechanical Engineering Department, Brigham Young University (2004).
- Jensen, J. W., S. W. Squire, J. P. Bons and T. H. Fletcher, "Simulated Land-Based Turbine Deposits Generated in an Accelerated Deposition Facility," *Journal of Turbomachinery*, **127**, 462-470 (2005).
- Johnson, K. L., K. Kendall and A. D. Roberts, "Surface Energy and the Contact of Elastic Solids," *Proceedings of the Royal Society of London. Series A, Mathematical and Physical Sciences*, **324**(1558), 301-313 (1971).
- Kim, J., M. G. Dunn, A. J. Baran, D. P. Wade and E. L. Tremba, "Deposition of Volcanic Materials in the Hot Sections of Two Gas Turbine Engines," *Journal of Engineering for Gas Turbines and Power*, **115**, 641-651 (1993).
- Kurz, R. and K. Brun, "Degradation in Gas Turbine Systems," *Journal of Engineering for Gas Turbines and Power*, **123**, 70-77 (2001).
- Kurz, R., "Gas Turbine Performance," 34th Turbomachinery Symposium, September 12 - 15, 2005, Houston, TX (2005).
- Lawrence, M. J., "An Experimental Investigation of High Temperature Particle Rebound and Deposition Characteristics Applicable to Gas Turbine Fouling," Master's Thesis, Mechanical and Aerospace Engineering Department, The Ohio State University (2013).

- Lawson, S. A. and K. A. Thole, "Simulations of Multiphase Particle Deposition on Endwall Film-Cooling Holes in Transverse Trenches," *Journal of Turbomachinery*, **134**(5), 051040 (2012).
- Lawson, S. A., K. A. Thole, Y. Okita and C. Nakamata, "Simulations of Multiphase Particle Deposition on a Showerhead with Staggered Film-Cooling Holes," *Journal of Turbomachinery*, **134**(5), 051041 (2012).
- Lebedev, A. S. and S. V. Kostennikov, "Trends in Increasing Gas-Turbine Units Efficiency," *Thermal Engineering (English translation of Teploenergetika)*, **55**(6), 461-468 (2008).
- Lu, H., L. T. Ip, A. Mackrory, L. Werrett, J. Scott, D. Tree and L. Baxter, "Particle Surface Temperature Measurements with Multicolor Band Pyrometry," *Aiche Journal*, **55**(1), 243-255 (2009).
- McBride, B. and S. Gordon, ""Chemical Equilibrium with Applications"," NASA-Glenn (2004).
- OMEGA, "Emissivity of Common Materials," OMEGA (Last visited 2017).
- Pequeno, C. and M. Severin, "Experiences with Heavy Fuel-Oil Firing in a Steam Reformer," *Process Safety Progress*, **18**(2), 82-88 (1999).
- Prenter, R., S. M. Whitaker, A. Ameri and J. P. Bons, "The Effects of Slot Film Cooling on Deposition on a Nozzle Guide Vane," ASME Turbo Expo 2014: Turbine Technical Conference and Exposition, GT 2014, June 16, 2014 - June 20, 2014, Dusseldorf, Germany, 3A (2014).
- Prenter, R., A. Ameri and J. P. Bons, "Deposition on a Cooled Nozzle Guide Vane with Nonuniform Inlet Temperatures," *Journal of Turbomachinery*, **138**(10) (2016).
- Pruschek, R., G. Oeljeklaus, G. Haupt, G. Zimmermann, D. Jansen and J. S. Ribberink, "The Role of IGCC in CO₂ Abatement," *Energy Conversion and Management*, **38**, S153-S158 (1997).
- Richards, G. A., R. G. Logan, C. T. Meyer and R. J. Anderson, "Ash Deposition at Coal-Fired Gas Turbine Conditions: Surface and Combustion Temperature Effects," *Journal of Engineering for Gas Turbines and Power*, **114**, 132-138 (1992).

- Robinson, A. L., S. G. Buckley, N. Yang and L. L. Baxter, "Experimental Measurements of the Thermal Conductivity of Ash Deposits: Part 2. Effects of Sintering and Deposit Microstructure," *Energy and Fuels*, **15**, 75-84 (2001).
- Rocca, E., P. Steinmetz and M. Moliere, "Revisiting the Inhibition of Vanadium-Induced Hot Corrosion in Gas Turbines," *Journal of Engineering for Gas Turbines and Power*, **125**(3), 664-669 (2003).
- Scheidema, M. N. and P. Taskinen, "Decomposition Thermodynamics of Magnesium Sulfate," *Industrial & Engineering Chemistry Research*, **50**(16), 9550-9556 (2011).
- Schmidt, P. F., *Fuel Oil Manual*, New York, Industrial Press (1985).
- Senior, C. L. and S. Srinivasachar, "Viscosity of Ash Particles in Combustion Systems for Prediction of Particle Sticking," *Energy and Fuels*, **9**, 277-283 (1995).
- Sharma, S. D., M. Dolan, D. Park, L. Morpeth, A. Ilyushechkin, K. McLennan, D. J. Harris and K. V. Thambimuthu, "A Critical Review of Syngas Cleaning Technologies — Fundamental Limitations and Practical Problems," *Powder Technology*, **180**(1–2), 115-121 (2008).
- Shimogori, M., H. Yoshizako and Y. Matsumura, "Determination of Coal Ash Emissivity Using Simplified Equation for Thermal Design of Coal-Fired Boilers," *Fuel*, **95**, 241-246 (2012).
- Singh, S. and D. Tafti, "Predicting the Coefficient of Restitution for Particle Wall Collisions in Gas Turbine Components," ASME Turbo Expo 2013: Turbine Technical Conference and Exposition, GT 2013, June 3, 2013 - June 7, 2013, San Antonio, TX, United states, 6B (2013).
- Sreedharan, S. S. and D. K. Tafti, "Composition Dependent Model for the Prediction of Syngas Ash Deposition in Turbine Gas Hotpath," *International Journal of Heat and Fluid Flow*, **32**(1), 201-211 (2011).
- Svensson, K. I., A. J. MacKrorry, M. J. Richards and D. R. Tree, "Calibration of an RGB, CCD Camera and Interpretation of Its Two-Color Images for KL and Temperature," 2005 SAE World Congress, April 11, 2005 - April 14, 2005, Detroit, MI, United states (2005).
- Topper, J. M., P. J. I. Cross and S. H. Goldthorpe, "Clean Coal Technology for Power and Cogeneration," *Fuel*, **73**, 1056-1063 (1994).

- Tovar, D., D. Ellis, V. Ravi-Kumar and D. R. Tree, "Particle Morphology and Composition of Ash from Heavy Fuel Oil Fired at Atmospheric Conditions with Various Spray Injection Pressures," 8th US National Combustion Meeting, Park City, UT, United States, 2 (2013).
- Wammack, J. E., J. Crosby, D. Fletcher, J. P. Bons and T. H. Fletcher, "Evolution of Surface Deposits on a High-Pressure Turbine Blade—Part I: Physical Characteristics," *Journal of Turbomachinery*, **130**(2), 021020 (2008).
- Webb, J., B. Casaday, B. Barker, J. P. Bons, A. D. Gledhill and N. P. Padture, "Coal Ash Deposition on Nozzle Guide Vanes-Part I: Experimental Characteristics of Four Coal Ash Types," *Journal of Turbomachinery*, **135**(2), 021033 (2012).
- Wenglarz, R. A. and R. G. Fox Jr, "Physical Aspects of Deposition from Coal-Water Fuels under Gas Turbine Conditions," *Journal of Engineering for Gas Turbines and Power*, **112**, 9-14 (1990a).
- Wenglarz, R. A. and R. G. Fox Jr, "Chemical Aspects of Deposition/Corrosion from Coal-Water Fuels under Gas Turbine Conditions," *Journal of Engineering for Gas Turbines and Power*, **112**, 1-8 (1990b).
- Whitaker, S. M. and J. P. Bons, "Evaluation of Elastic-Plastic Rebound Properties of Coal Fly Ash Particles for Use in a Universal Turbine Deposition Model," ASME Turbo Expo 2015: Turbine Technical Conference and Exposition, GT 2015, June 15, 2015 - June 19, 2015, Montreal, QC, Canada, 1 (2015).
- Yin, C., Z. Luo, M. Ni and K. Cen, "Predicting Coal Ash Fusion Temperature with a Back-Propagation Neural Network Model," *Fuel*, **77**, 1777-1782 (1998).

APPENDIX A TEST DATA

A.1 Verification Test Series

Table A-1: Deposition data for the verification test series

| Test # | m_{fed} (g) | $m_{tube,e}$ (g) | m_{del} (g) | m_{coupon} Before (g) | m_{coupon} After (g) | η_{cap} (%) | % Deposit Recovered | Adjusted η_{cap} (%) |
|--------|------------------|---------------------|------------------|-------------------------------|------------------------------|---------------------|------------------------|---------------------------------|
| V1 | 20.11 | 3.62 | 16.49 | 10.4 | 11.7 | 7.88 | 99.800 | 7.90 |
| V2* | 21.44 | 4.17 | 17.27 | 10.18 | 11.52 | 7.76 | 99.401 | 7.81 |
| V3 | 20.3 | 1.44 | 18.86 | 11.04 | 11.49 | 2.39 | 99.825 | 2.39 |
| V4* | 22.38 | 2.32 | 20.06 | 10.83 | 11.57 | 3.69 | 99.650 | 3.70 |
| V5 | 20.55 | 1.85 | 18.7 | 10.73 | 11.13 | 2.14 | 96.584 | 2.21 |

Other Information

| | |
|----------------------------|---------|
| Ash: | JB1 |
| Ash MMD (μm): | 14 |
| Tube/Cone Material: | SiC/SiC |
| Deposition Duration (min): | 60 |

* These tests were excluded from the data presented in the results and discussion due to excessive faceplate deposit growth onto the coupon, as discussed in Section 4.2.

Table A-2: Temperature data for the verification test series

| Test # | T _g (°C) | T _s (°C) | | | | | | |
|--------|---------------------|---------------------|--------|--------|--------|--------|--------|--------|
| | | 0 min | 10 min | 20 min | 30 min | 40 min | 50 min | 60 min |
| V1 | 1187 | 1048 | 1059 | 1062 | 1071 | 1103 | 1119 | 1122 |
| V2* | 1188 | 1029 | 1022 | 1031 | 1082 | 1076 | 1105 | 1113 |
| V3 | 1132 | 996 | 993 | 1028 | 1040 | 1019 | 1019 | 1046 |
| V4* | 1131 | 1001 | 1023 | 1024 | 1019 | 1029 | 1050 | 1067 |
| V5 | 1130 | 995 | 989 | 1025 | 1026 | 1018 | 1037 | 1065 |

Other Information

Camera Calibration: 2-color, Red/Blue

No coolant (insulated backside)

* These tests were excluded from the data presented in the results and discussion due to excessive faceplate deposit growth onto the coupon, as discussed in Section 4.2.

A.2 Transient Test Series**Table A-3: Deposition data for the transient test series**

| Test # | Deposition Duration (min) | Ash MMD (μm) | m _{fed} (g) | m _{tube,e} (g) | m _{del} (g) | m _{coupon Before} (g) | m _{coupon After} (g) | η _{cap} (%) | % Deposit Recovered | Adjusted η _{cap} (%) |
|--------|---------------------------|--------------|----------------------|-------------------------|----------------------|--------------------------------|-------------------------------|----------------------|---------------------|-------------------------------|
| T1 | 33 | 14 | 10.61 | 3.12 | 7.49 | 10.25 | 11.39 | 15.2 | 97.76 | 15.6 |
| T2 | 60 | 14 | 21.95 | 7.40 | 14.55 | 9.94 | 12.61 | 18.4 | 97.32 | 18.9 |
| T3 | 60 | 14 | 22.28 | 6.82 | 15.46 | 9.63 | 12.56 | 19.0 | 97.33 | 19.5 |
| T4 | 20 | 14 | 4.79 | 1.30 | 3.49 | 9.2 | 9.7 | 14.3 | 97.61 | 14.7 |
| T5 | 20 | 14 | 5.25 | 1.06 | 4.19 | 9.97 | 10.57 | 14.3 | 99.12 | 14.4 |
| T6 | 40 | 14 | 13.73 | 3.27 | 10.46 | 9.68 | 11.31 | 15.6 | 96.72 | 16.1 |
| T7 | 40 | 14 | 13.39 | 4.89 | 8.50 | 9.35 | 10.64 | 15.2 | 95.54 | 15.9 |
| T8 | 40 | 3.2 | 9.96 | 1.68 | 8.28 | 8.17 | 8.39 | 2.66 | 98.65 | 2.69 |
| T9 | 20 | 3.2 | 4.71 | 1.21 | 3.50 | 8.75 | 8.82 | 2.00 | 42.25 | 4.73 |

Other Information

Ash: JB1

Tube/Cone Material: SiC/SiC

Table A-4: Temperature data for the transient test series

| Test # | T _g (°C) | T _s (°C) | | | | | | |
|--------|---------------------|---------------------|--------|--------|--------|--------|--------|--------|
| | | 0 min | 10 min | 20 min | 30 min | 40 min | 50 min | 60 min |
| T1 | 1294 | 1089 | 1108 | 1129 | 1142 | - | - | - |
| T2 | 1298 | 1112 | 1135 | 1157 | 1174 | 1172 | 1178 | 1191 |
| T3 | 1302 | 1135 | 1155 | 1149 | 1149 | 1177 | 1186 | 1195 |
| T4 | 1289 | 1124 | 1128 | 1151 | - | - | - | - |
| T5 | 1291 | 1109 | 1132 | 1137 | - | - | - | - |
| T6 | 1285 | 1108 | 1131 | 1134 | 1150 | 1168 | - | - |
| T7 | 1298 | 1112 | 1123 | 1140 | 1154 | 1155 | - | - |
| T8 | 1295 | 1109 | 1122 | 1118 | 1109 | 1107 | - | - |
| T9 | 1306 | 1119 | 1131 | 1121 | - | - | - | - |

Other Information

Camera Calibration: 2-color, Red/Blue

No coolant (insulated backside)

Table A-5: Surface scan data for the transient test series

| Test # | Deposit R _a (μm) | Deposit Volume (cm ³) | Deposit mass (g) | ρ _{dep} (g/cm ³) |
|--------|--------------------------------|---|------------------------|--|
| T1 | 361.205 | 1.24831 | 1.140 | 0.913 |
| T2 | 639.576 | 1.808142 | 2.670 | 1.477 |
| T3 | 751.568 | 2.22019 | 2.930 | 1.320 |
| T4 | 136.482 | 0.799269 | 0.500 | 0.626 |
| T5 | 224.185 | 0.817885 | 0.600 | 0.734 |
| T6 | 464.834 | 1.329579 | 1.630 | 1.226 |
| T7 | 374.844 | 1.113696 | 1.290 | 1.158 |
| T8 | 128.263 | 0.80494 | 0.220 | 0.273 |
| T9 | 102.744 | 0.184906 | 0.070 | 0.379 |

A.3 Constant $T_{s,i}$ Test Series

Table A-6: Deposition data for the constant $T_{s,i}$ test series

| Test # | m_{fed} (g) | $m_{tube,e}$ (g) | $m_{tube,f}$ (g) | m_{del} (g) | m_{coupon} Before (g) | m_{coupon} After (g) | η_{cap} (%) | Tube η_{cap} (% per coupon area) |
|--------|---------------|------------------|-------------------|---------------|-------------------------|------------------------|------------------|---------------------------------------|
| G1 | 9.65 | 1.88 | - | 7.77 | 10.26 | 10.73 | 6.05 | 0.147 |
| G2 | 9.28 | 1.36 | - | 7.92 | 10.25 | 10.73 | 6.06 | 0.111 |
| G3 | 12.4 | 2.49 | - | 9.91 | 11.07 | 11.64 | 5.75 | 0.152 |
| G4 | 5.68 | 1.55 | - | 4.13 | 10.22 | 10.47 | 6.05 | 0.206 |
| G5 | 10.21 | 2.74 | - | 7.47 | 11.1 | 11.64 | 7.23 | 0.203 |
| G6 | 14.83 | 4.22 | - | 10.61 | 10.21 | 11.08 | 8.20 | 0.215 |
| G7* | 15.55 | 4.34 | - | 11.21 | 11.05 | 12.15 | 9.81 | 0.211 |
| G8 | 15.78 | 5.82 | 0.71 [†] | 9.96 | 10.98 | 12.19 | 12.1 | 0.279 |
| G9 | 13.84 | 3.88 | 1.04 [†] | 9.96 | 10.99 | 11.96 | 9.74 | 0.212 |

Other Information

| | | | |
|----------------------------|---------|----------------------------|------|
| Ash: | JB2 | Deposition Duration (min): | 60 |
| Ash MMD (μm): | 4.9 | % Deposit Recovered: | 100% |
| Tube/Cone Material: | SiC/SiC | | |

* This test is excluded from the data presented in the results and discussion due to excessive faceplate deposit growth onto the coupon, as discussed in Section 4.2.

[†]The value of $m_{tube,f}$ was not incorporated into the m_{del} and η_{cap} results for consistency with the rest of the constant $T_{s,i}$ tests for which $m_{tube,f}$ was not measured.

Table A-7: Temperature data for the constant $T_{s,i}$ test series

| Test # | T_g (°C) | T_s (°C) | | | | | | | Average Coolant Air Rotameter Setting | Average Coolant Water Flow (mL/min) |
|--------|------------|------------|--------|--------|--------|--------|--------|--------|---------------------------------------|-------------------------------------|
| | | 0 min | 10 min | 20 min | 30 min | 40 min | 50 min | 60 min | | |
| G1 | 1299 | 1020 | 1035 | 1039 | 1043 | 1058 | 1060 | 1062 | 30 | - |
| G2 | 1265 | 1026 | 1037 | 1036 | 1047 | 1056 | 1066 | 1064 | 20 | - |
| G3 | 1261 | 969 | 952 | 978 | 995 | 994 | 993 | 1016 | 21 | - |
| G4 | 1309 | 1039 | 1046 | 1027 | 1027 | 1025 | 1027 | 1052 | 104 | - |
| G5 | 1315 | 1030 | 1054 | 1054 | 1080 | 1096 | 1113 | 1107 | 50 | - |
| G6 | 1311 | 1027 | 1052 | 1066 | 1076 | 1078 | 1088 | 1092 | 49 | - |
| G7* | 1311 | 1067 | 1083 | 1086 | 1090 | 1100 | 1119 | 1135 | 72 | - |
| G8 | 1413 | 1014 | 1070 | 1073 | 1090 | 1087 | 1104 | 1109 | 59 | 21 |
| G9 | 1361 | 1001 | 1027 | 1052 | 1058 | 1072 | 1102 | 1091 | 60 | 18 |

Other Information

Camera Calibration: 2-color, Red/Green

* This test is excluded from the data presented in the results and discussion due to excessive faceplate deposit growth onto the coupon, as discussed in Section 4.2.

Table A-8: Surface scan data for the constant $T_{s,i}$ test series

| Test # | Deposit R_a (μm) | Deposit Volume (cm^3) | Scanned Deposit Mass (g) | ρ_{dep} (g/cm^3) |
|--------|---------------------------------|----------------------------------|--------------------------|--|
| G1 | 112.02617 | 1.066491 | 0.4577 | 0.4291645 |
| G2 | 136.09232 | 1.305208 | 0.4557 | 0.3491398 |
| G3 | 163.88312 | 1.581601 | 0.5092 | 0.3219523 |
| G4 | 129.63964 | 0.657614 | 0.1315 | 0.1999652 |
| G5 | 125.75384 | 1.027858 | 0.5775 | 0.561848 |
| G6 | 284.44577 | 1.32434 | 0.8349 | 0.6304273 |
| G7* | 146.19143 | 1.143106 | 1.102 | 0.9640404 |
| G8 | 327.3796 | 1.999586 | 1.171 | 0.585621 |
| G9 | 372.254 | 1.299496 | 0.9716 | 0.747675 |

* This test is excluded from the data presented in the results and discussion due to excessive faceplate deposit growth onto the coupon, as discussed in Section 4.2.

A.4 Constant T_g Test Series

Table A-9: Deposition data for the constant T_g test series

| Test # | Deposition Duration (min) | m _{fed} (g) | m _{tube,e} (g) | m _{tube,f} (g) | m _{del} (g) | m _{coupon} Before (g) | m _{coupon} After (g) | η _{cap} (%) | Tube η _{cap} (% per coupon area) | % Deposit Recovered | Adjusted η _{cap} (%) |
|--------|---------------------------|----------------------|-------------------------|-------------------------|----------------------|--------------------------------|-------------------------------|----------------------|---|---------------------|-------------------------------|
| S1* | 60 | 16.16 | 5.06 | - | 11.1 | 11.03 | 12.85 | 16.4 | 0.237 | 100.00 | 16.4 |
| S2 | 40 | 14.83 | 1.13 | 0.82 | 12.88 | 10.95 | 11.86 | 7.07 | 0.0744 | 100.00 | 7.07 |
| S3* | 40 | 15.72 | 2.38 | 1.78 | 11.56 | 11.33 | 12.7 | 11.9 | 0.158 | 96.00 | 12.3 |
| S4 | 60 | 13.57 | 3.62 | 1.36 | 8.59 | 11.35 | 12.51 | 13.5 | 0.273 | 93.09 | 14.5 |
| S5 | 50 | 12.79 | 2.67 | 2.54 | 7.58 | 11.05 | 11.74 | 9.10 | 0.240 | 89.12 | 10.2 |
| S6 | 43 | 13.73 | 3.25 | 1.53 | 8.95 | 10.84 | 12 | 13.0 | 0.245 | 100.00 | 13.0 |
| S7 | 59 | 15.3 | 2.59 | 2.35 | 10.36 | 11.25 | 12.37 | 10.8 | 0.184 | 83.38 | 13.0 |
| S8 | 54 | 14.23 | 2.11 | 1.87 | 10.25 | 10.98 | 12.24 | 12.3 | 0.158 | 100.00 | 12.3 |
| S9 | 54 | 14.29 | 1.75 | 1.6 | 10.94 | 10.8 | 11.64 | 7.68 | 0.127 | 90.55 | 8.48 |
| S10 | 58 | 11.7 | 2.62 | 1.88 | 7.2 | 11.21 | 11.81 | 8.33 | 0.246 | 86.76 | 9.60 |
| S11 | 58 | 13.33 | 1.84 | 2.86 | 8.63 | 10.92 | 11.74 | 9.50 | 0.162 | 88.44 | 10.7 |
| S12 | 50 | 13.4 | 2.54 | 1.61 | 9.25 | 10.72 | 11.33 | 6.59 | 0.198 | 80.79 | 8.16 |
| S13 | 46 | 13.52 | 2.7 | 2.22 | 8.6 | 11.15 | 11.62 | 5.47 | 0.220 | 72.78 | 7.51 |
| S14 | 43 | 14.55 | 1.44 | 2.3 | 10.81 | 10.86 | 11.67 | 7.49 | 0.109 | 100.00 | 7.49 |
| S15 | 42 | 12.85 | 2.04 | 1.96 | 8.85 | 10.61 | 10.68 | 0.791 | 0.172 | 100.00 | 0.791 |

Other Information

Ash: JB2
 Ash MMD (μm): 4.9
 Tube/Cone Material: SiC/Quartz (Except test S1 which used SiC/SiC)

* These tests were excluded from the data presented in the results and discussion due to excessive faceplate deposit growth onto the coupon, as discussed in Section 4.2.

Table A-10: Temperature data for the constant T_g test series

| Test # | T _g (°C) | T _s (°C) | | | | | | | Average Coolant Air Rotameter Setting | Average Coolant Water Flow (mL/min) |
|--------|---------------------|---------------------|--------|--------|--------|--------|-------------------|-------------------|---------------------------------------|-------------------------------------|
| | | 0 min | 10 min | 20 min | 30 min | 40 min | 50 min | 60 min | | |
| S1* | 1406 | 1128 | 1148 | 1185 | 1203 | 1236 | 1303 | 1277 | 59 | No Data |
| S2 | 1402 | 899 | 988 | 1022 | 1067 | 1112 | | | 61 | 15 |
| S3* | 1413 | 1026 | 1025 | 1116 | 1155 | 1169 | | | 60 | 7.1 |
| S4 | 1414 | 964 | 1085 | 1091 | 1114 | 1137 | 1184 | No Data | 60 | 4.9 |
| S5 | 1414 | 1124 | 1190 | 1166 | 1153 | 1186 | 1194 | | 60 | 0.0 |
| S6 | 1413 | 1075 | 1147 | 1159 | 1216 | 1235 | 1237 [†] | | 60 | 3.1 |
| S7 | 1419 | 930 | 961 | 998 | 1053 | 1110 | 1159 | 1130 [†] | 59 | 26 |
| S8 | 1404 | 1051 | 1116 | 1105 | 1094 | 1158 | 1225 | 1222 [†] | 60 | 12 |
| S9 | 1412 | 1090 | 1155 | 1143 | 1163 | 1183 | 1221 | 1211 [†] | 61 | 2.6 |
| S10 | 1412 | 1096 | 1166 | 1156 | 1171 | 1176 | 1190 | 1216 [†] | 60 | 12 |
| S11 | 1410 | 961 | 1021 | 1015 | 1052 | 1070 | 1078 | 1132 [†] | 59 | 24 |
| S12 | 1411 | 1122 | 1196 | 1201 | 1197 | 1209 | 1232 | | 60 | 0 |
| S13 | 1410 | 1142 | 1194 | 1190 | 1202 | 1215 | 1228 [†] | | 60 | 2.6 |
| S14 | 1413 | 1130 | 1177 | 1175 | 1185 | 1225 | 1227 [†] | | 60 | 0 |
| S15 | 1412 | 894 | 960 | 955 | 984 | 991 | 985 [†] | | 60 | 24 |

Other Information

Camera Calibration: 1-color, Red (Except test S1 which used the 2-color Red/Green calibration)

* These tests were excluded from the data presented in the results and discussion due to excessive faceplate deposit growth onto the coupon, as discussed in Section 4.2.

[†]The time of the final temperatures in these tests correspond to the actual end of the deposition test (the deposition duration shown in Table A-9) rather than the time indicated at the top of the column.

Table A-11: Surface scan data for the constant T_g test series

| Test # | Deposit R _a (μm) | Deposit Volume (cm ³) | Scanned Deposit Mass (g) | ρ _{dep} (g/cm ³) |
|--------|--------------------------------|---|--------------------------------|--|
| S1* | 621.6959 | 1.441418 | 1.6892 | 1.171902 |
| S2 | 888.8006 | 0.608825 | 0.4845 | 0.795795 |
| S3* | 936.3959 | 0.926602 | 0.8852 | 0.955319 |
| S4 | 431.4466 | 0.572059 | 0.7481 | 1.307733 |
| S5 | - | - | - | - |
| S6 | 491.2912 | 0.833904 | 0.9483 | 1.137181 |
| S7 | 458.9832 | 0.856488 | 0.9764 | 1.140005 |
| S8 | 550.2535 | 1.127827 | 1.2473 | 1.105932 |
| S9 | 283.146 | 0.640401 | 0.6284 | 0.98126 |
| S10 | - | - | - | - |
| S11 | 432.3929 | 0.645429 | 0.58 | 0.898627 |
| S12 | - | - | - | - |
| S13 | - | - | - | - |
| S14 | 276.8627 | 0.631365 | 0.4929 | 0.78069 |
| S15 | 621.6959 | 1.441418 | 1.6892 | 1.171902 |

* This test is excluded from the data presented in the results and discussion due to excessive faceplate deposit growth onto the coupon, as discussed in Section 4.2.

A.5 Various Coal Ashes Test Series

Table A-12: Deposition data for the various coal ash type test series

| Test # | Ash* | Deposition Duration (min) | m _{fed} (g) | m _{tube,e} (g) | m _{tube,f} (g) | m _{del} (g) | m _{coupon Before} (g) | m _{coupon After} (g) | η _{cap} (%) | % Deposit Recovered | Adjusted η _{cap} (%) |
|--------|------------|---------------------------------|-------------------------|----------------------------|----------------------------|-------------------------|---------------------------------------|--------------------------------------|-------------------------|------------------------|-------------------------------------|
| A1 | Petcoke | 45 | 16.05 | 13.71 | 0.00 | 2.34 | 10.96 | 12.63 | 71.4 | 92.17 | 77.4 |
| A2 | PRB | 60 | 3.55 | 0.54 | 1.75 | 1.26 | 11.09 | 11.14 | 3.97 | - | - |
| A3 | PRB | 49 | 2.68 | 0.00 | 0.79 | 1.89 | 10.85 | 10.88 | 1.59 | - | - |
| A4 | Lignite | 59 | 7.86 | 0.99 | 2.41 | 4.46 | 10.5 | 10.98 | 10.8 | 98.57 | 10.9 |
| A5 | Lignite | 59 | 8.22 | 1.19 | 3.06 | 3.97 | 10.78 | 11.29 | 12.8 | 100.00 | 12.8 |
| A6 | Bituminous | 59 | 15.17 | 4.95 | 0.99 | 9.23 | 10.49 | 12.51 | 21.9 | 98.55 | 22.2 |
| A7 | Bituminous | 59 | 15.62 | 4.5 | 1.01 | 10.11 | 10.94 | 12.84 | 18.8 | 100.00 | 18.8 |

Other Information

Tube/Cone Material: SiC/Quartz (Except test A1 which used SiC/SiC)

* See Table 3-1 for ash properties.

Table A-13: Temperature data for the various coal ash type test series

| Test # | T _g (°C) | T _s (°C) | | | | | | | Average Coolant Air Rotameter Setting | Average Coolant Water Flow (mL/min) |
|--------|---------------------|---------------------|--------|--------|--------|--------|-------------------|-------------------|---------------------------------------|-------------------------------------|
| | | 0 min | 10 min | 20 min | 30 min | 40 min | 50 min | 60 min | | |
| A1 | 1409 | 991 | 1036 | 1062 | 1088 | 1127 | 1127 [†] | - | 60 | 4.1 |
| A2 | 1412 | 1083 | 1143 | 1139 | 1155 | 1138 | 1145 | 1145 | 60 | No Data |
| A3 | 1415 | 1095 | 1153 | 1153 | 1150 | 1140 | 1154 [†] | | 60 | No Data |
| A4 | 1415 | 1061 | 1105 | 1110 | 1112 | 1110 | 1119 | 1131 [†] | 60 | - |
| A5 | 1413 | 1072 | 1111 | 1116 | 1112 | 1104 | 1123 | 1137 [†] | 60 | - |
| A6 | 1416 | 1102 | 1124 | 1142 | 1140 | 1129 | 1162 | 1163 [†] | 60 | - |
| A7 | 1415 | 1095 | 1115 | 1119 | 1140 | 1145 | 1146 | 1151 [†] | 60 | - |

Other Information

Camera Calibration: 1-color, Red (Except test A1 which used the 2-color Red/Green calibration)

* These tests were excluded from the data presented in the results and discussion due to excessive faceplate deposit growth onto the coupon, as discussed in Section 4.2.

[†]The time of the final temperatures in these tests correspond to the actual end of the deposition test (the deposition duration shown in Table A-12) rather than the time indicated at the top of the column.

Table A-14: Surface scan data for the various coal ash type test series

| Test # | Deposit R _a (μm) | Deposit Volume (cm ³) | Scanned Deposit Mass (g) | ρ _{dep} (g/cm ³) |
|--------|-----------------------------|-----------------------------------|--------------------------|---------------------------------------|
| A1 | 90.24578837* | 1.381786 | 1.6086 | 1.164145 |
| A2 | - | - | - | - |
| A3 | - | - | - | - |
| A4 | 78.65153 | 0.525896 | 0.3425 | 0.651269 |
| A5 | 124.5775 | 0.585707 | 0.4224 | 0.72118 |
| A6 | 630.713 | 1.810385 | 1.7355 | 0.958636 |
| A7 | 583.3619 | 1.321561 | 1.529 | 1.156965 |

* The surface R_a obtained for the petcoke ash test was calculated from a leveled surface, as described in Section 7.3.2.

A.6 Heavy Fuel Oil Test Series

Table A-15: Deposition data for the HFO test series

| Test # | Deposition Duration (min) | m_{fed} (g) | Inorganics m_{fed} (g) | $m_{\text{tube,e}}$ (g) | $m_{\text{tube,f}}$ (g) | m_{del} (g) | m_{coupon} Before (g) | m_{coupon} After (g) | η_{cap} (%) | m_{coupon} Dry, Prewash (g) | m_{coupon} Dry, Postwash (g) | Mass Loss During Wash (%) |
|--------|---------------------------|----------------------|---------------------------------|-------------------------|-------------------------|----------------------|--------------------------------|-------------------------------|-------------------------|--------------------------------------|---------------------------------------|---------------------------|
| H1 | 50 | 3.32 | 1.07 | 0.00 | 0.00 | 1.07 | 10.32 | 10.35 | 2.82 | 10.9757 | 10.9707 | 14.0 |
| H2 | 40 | 2.85 | 0.914 | 0.00 | 0.00 | 0.91 | 10.94 | 10.97 | 3.28 | 11.3789 | 11.3695 | 19.2 |
| H3 | 55 | 3.18 | 1.02 | 0.00 | 0.00 | 1.02 | 10.84 | 10.90 | 5.88 | 11.1123 | 11.1095 | 12.6 |
| H4 | 55 | 3.34 | 1.07 | 0.04 | 0.00 | 1.03 | 10.79 | 10.80 | 0.969 | 10.4391 | 10.4352 | 13.4 |
| H5 | 40 | 2.71 | 0.869 | 0.02 | 0.00 | 0.85 | 11.33 | 11.38 | 5.89 | 10.8806 | 10.8761 | 11.1 |
| H6 | 60 | 3.25 | 1.04 | 0.00 | 0.01 | 1.04 | 10.66 | 10.69 | 2.89 | 10.6908 | 10.6874 | 11.0 |
| H7 | 59 | 3.31 | 1.06 | 0.09 | 0.00 | 0.97 | 10.41 | 10.44 | 3.09 | 10.3380 | 10.3341 | 21.7 |
| H8 | 30 | 3.05 | 0.978 | 0.00 | 0.00 | 0.98 | 11.09 | 11.11 | 2.04 | 10.7979 | 10.7956 | 29.1 |
| H9 | 33 | 2.28 | 0.712 | 0.00 | 0.00 | 0.71 | 10.5748 | 10.5873 | 1.76 | 10.5858 | 10.5837 | 19.1 |

Other Information

Ash: HFO
 Ash MMD (μm): 32.8
 wt% inorganics in ash: 32.1%
 Tube/Cone Material: SiC/Quartz (Except test A1 which used SiC/SiC)

Table A-16: Temperature data for the HFO test series

| Test # | T_g (°C) | T_s (°C) | | | | | | |
|--------|------------|------------|---------|---------|------------------|---------|---------|-------------------|
| | | 0 min | 10 min | 20 min | 30 min | 40 min | 50 min | 60 min |
| H1 | 1101 | No Data | No Data | No Data | No Data | No Data | No Data | - |
| H2 | 1104 | 912 | 923 | 920 | 924 | 920 | | |
| H3 | 1134 | 981 | 983 | 986 | 982 | 978 | 978 | 978 [†] |
| H4 | 1155 | 1020 | 1021 | 1020 | 1020 | 1017 | 1019 | 1019 [†] |
| H5 | 1162 | 991 | 983 | 977 | 976 | 974 | | |
| H6 | 1188 | 1009 | 1014 | 1010 | 1009 | 1009 | 1012 | 1011 |
| H7 | 1218 | 1028 | 1029 | 1027 | 1026 | 1026 | 1026 | 1026 [†] |
| H8 | 1219 | 1019 | 1003 | 1001 | 998 | | | |
| H9 | 1106 | 993 | 996 | 990 | 990 [†] | | | |

Other Information

Camera Calibration: 1-color, Red (Except test A1 which used the 2-color Red/Green calibration)
 No coolant (insulated backside)

[†]The time of the final temperatures in these tests correspond to the actual end of the deposition test (the deposition duration shown in Table A-15) rather than the time indicated at the top of the column.

Table A-17: Surface scan data for the HFO test series

| Test # | Prewash Deposit R_a (μm) | | | Postwash Deposit R_a (μm) | | |
|--------|--|-------|-------|---|-------|-------|
| | Location | | | Location | | |
| | 1 | 2 | 3 | 1 | 2 | 3 |
| H1 | | | | | | |
| H2 | 2.54 | 3.796 | 3.621 | 5.87 | 3.896 | 4.889 |
| H3 | 4.353 | 4.79 | 4.146 | 5.845 | 5.404 | 4.313 |
| H4 | | | | | | |
| H5 | 3.643 | 3.252 | 4.147 | 3.03 | 4.671 | 5.737 |
| H6 | 3.092 | 3.343 | 3.223 | 5.307 | 3.524 | 3.698 |
| H7 | 3.417 | 3.636 | 5.981 | 3.994 | 4.063 | 4.201 |
| H8 | 4.641 | 2.222 | 4.722 | 5.701 | 3.565 | 3.809 |
| H9 | | | | | | |

A.7 Film-Cooling Test Series

Table A-18: Deposition data for the film-cooling test series

| Test # | Deposition Duration (min) | m_{fed} (g) | $m_{\text{tube,e}}$ (g) | $m_{\text{tube,f}}$ (g) | m_{del} (g) | m_{coupon} Before (g) | m_{coupon} After (g) | η_{cap} (%) | % Deposit Recovered | Adjusted η_{cap} (%) |
|--------|---------------------------|----------------------|-------------------------|-------------------------|----------------------|--------------------------------|-------------------------------|-------------------------|---------------------|----------------------------------|
| F1 | 45 | 16.67 | 5.38 | 1.08 | 10.21 | 10.26 | 11.56 | 12.7 | 95.68 | 13.3 |
| F2 | 50 | 15.79 | 6.65 | 1.12 | 8.02 | 10.21 | 11.52 | 16.3 | 100.00 | 16.3 |
| F3 | 60 | 14.47 | 4.11 | 1.89 | 8.47 | 10.1296 | 11.4089 | 15.1 | 98.67 | 15.3 |
| F4 | 57 | 13.56 | 3.04 | 2.23 | 8.29 | 10.01 | 10.88 | 10.5 | 85.81 | 12.2 |
| F5 | 46 | 13.03 | 3.14 | 1.38 | 8.51 | 9.94 | 10.77 | 9.75 | 95.26 | 10.2 |
| F6 | 59 | 13.95 | 3.47 | 2.66 | 7.82 | 9.87 | 10.71 | 10.7 | 84.59 | 12.7 |
| F7 | 59 | 13.9 | 3.76 | 1.84 | 8.30 | 9.79 | 10.61 | 9.88 | 95.78 | 10.3 |
| F8 | 59 | 14.47 | 4.29 | 2.08 | 8.10 | 9.72 | 10.62 | 11.1 | 97.86 | 11.4 |
| F9 | 59 | 14.48 | 2.8 | 2.6 | 9.08 | 9.57 | 10.58 | 11.1 | 100.00 | 11.1 |
| F10 | 59 | 14.71 | 3.47 | 1.76 | 9.48 | 9.5 | 10.57 | 11.3 | 96.58 | 11.7 |
| F11 | 62 | 13.44 | 2.76 | 1.37 | 9.31 | 9.47 | 10.58 | 11.9 | 98.43 | 12.1 |

Other Information

| | |
|----------------------------|--|
| Ash: | JB2 |
| Ash MMD (μm): | 4.9 |
| Tube/Cone Material: | SiC/Quartz (Except test A1 which used SiC/SiC) |

Table A-19: Temperature data for the film-cooling test series

| Test # | T _g (°C) | T _s (°C) | | | | | | M | DR | I | |
|--------|------------------------|---------------------|--------|--------|--------|--------|-------------------|-------------------|------|------|--------|
| | | 0 min | 10 min | 20 min | 30 min | 40 min | 50 min | | | | 60 min |
| F1 | 1411 | 1106 | 1115 | 1147 | 1197 | 1186 | 1193 [†] | 0.51 | 1.83 | 0.15 | |
| F2 | 1410 | 1106 | 1135 | 1161 | 1175 | 1204 | 1204 | 0.99 | 2.35 | 0.42 | |
| F3 | 1414 | 1039 | 1147 | 1171 | 1174 | 1163 | 1209 | 1230 | 1.99 | 2.29 | 1.74 |
| F4 | 1411 | 1054 | 1112 | 1150 | 1141 | 1142 | 1190 | 1219 [†] | 0.52 | 2.09 | 0.13 |
| F5 | 1411 | 1021 | 1079 | 1087 | 1106 | 1180 | 1196 [†] | 2.00 | 2.51 | 1.60 | |
| F6 | 1413 | 1093 | 1169 | 1180 | 1170 | 1162 | 1154 | 1169 [†] | 1.01 | 2.23 | 0.47 |
| F7 | 1414 | 1028 | 1085 | 1097 | 1110 | 1123 | 1152 | 1175 [†] | 1.51 | 2.77 | 0.83 |
| F8 | 1412 | 1005 | 1086 | 1116 | 1115 | 1117 | 1150 | 1163 [†] | 2.01 | 2.46 | 1.64 |
| F9 | 1416 | 998 | 1058 | 1075 | 1081 | 1099 | 1140 | 1147 [†] | 0.99 | 2.43 | 0.41 |
| F10 | 1412 | 1053 | 1124 | 1113 | 1119 | 1120 | 1151 | 1162 [†] | 1.52 | 2.23 | 1.05 |
| F11 | 1414 | 1011 | 1078 | 1116 | 1104 | 1113 | 1184 | 1191 [‡] | 0.49 | 2.17 | 0.11 |

Other Information

Camera Calibration: 1-color, Red (Except tests F1 and F2 which used the 2-color Red/Green calibration)

of Film-Cooling Holes: 3

Film-Cooling Hole Dimensions: Diameter = 3 mm, P/d = 4.5

[†]The time of the final temperatures in these tests correspond to the actual end of the deposition test (the deposition duration shown in Table A-18) rather than the time indicated at the top of the column.

[‡]This test ran for 62 minutes. The final T_s at 62 minutes was 1199°C

Table A-20: Surface scan data for the film-cooling test series

| Test # | Deposit R _a (μm) | Deposit Volume (cm ³) | Scanned Deposit Mass (g) | ρ _{dep} (g/cm ³) |
|--------|--------------------------------|--------------------------------------|-----------------------------|--|
| F1 | - | - | - | - |
| F2 | 506.6725 | 1.28924 | 1.2959 | 1.005166 |
| F3 | 506.5612 | 1.18305 | 1.2557 | 1.061409 |
| F4 | 288.4818 | 0.770765 | 0.6516 | 0.845394 |
| F5 | 519.7875 | 0.813714 | 0.8021 | 0.985727 |
| F6 | 225.139 | 0.648392 | 0.5655 | 0.872157 |
| F7 | 386.0115 | 0.862258 | 0.7658 | 0.888133 |
| F8 | 494.8906 | 0.98631 | 0.9025 | 0.915027 |
| F9 | 457.7424 | 0.993946 | 0.9217 | 0.927314 |
| F10 | 507.7503 | 1.060826 | 1.0122 | 0.954162 |
| F11 | 530.3713 | 1.02559 | 1.0766 | 1.049737 |

APPENDIX B ADDITIONAL FIGURES

B.1 Particle Size Distributions

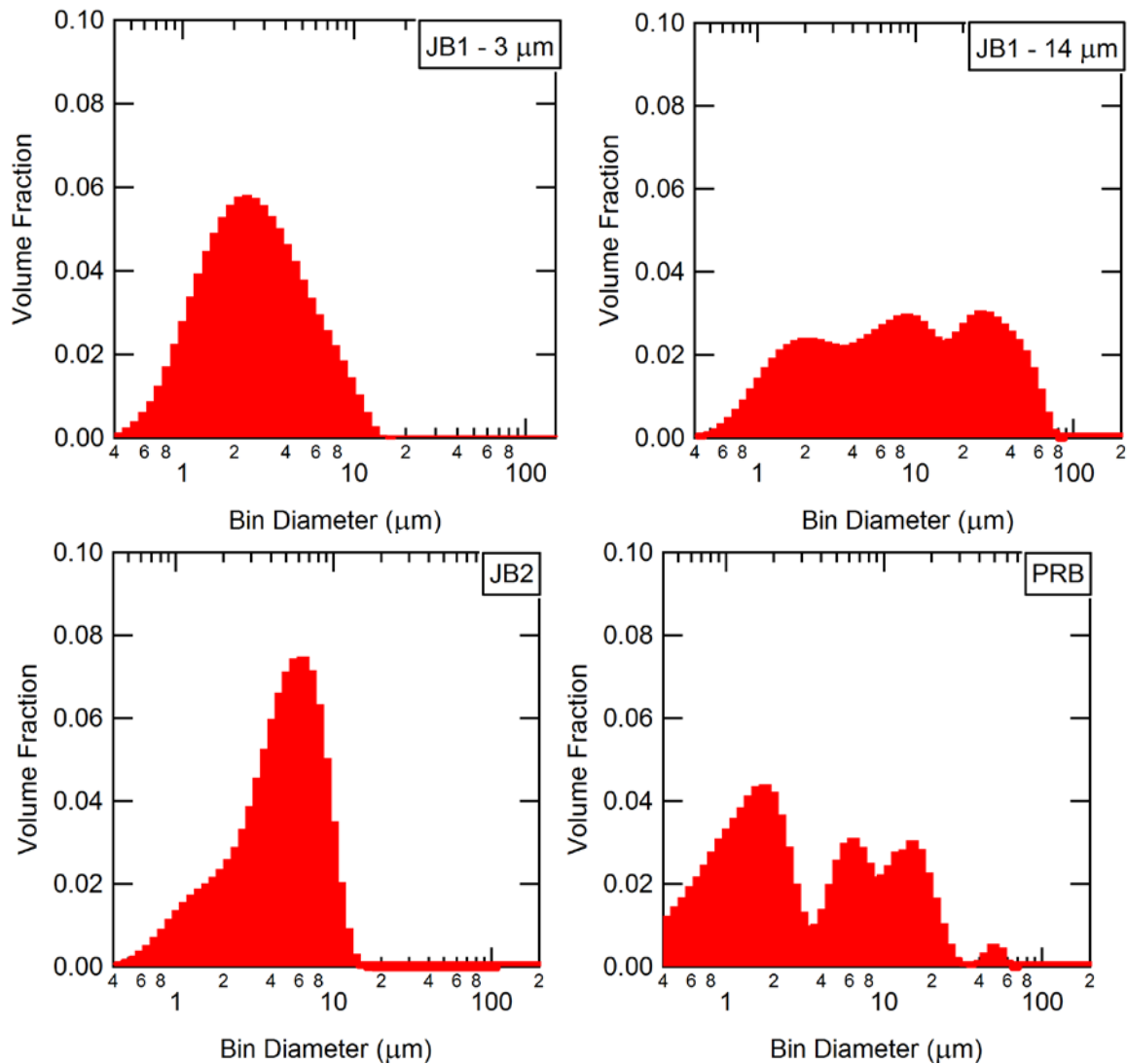


Figure B-1: Particle size distributions for the JB1 (MMD = 3 μm and 14 μm), JB2 and PRB ash samples.

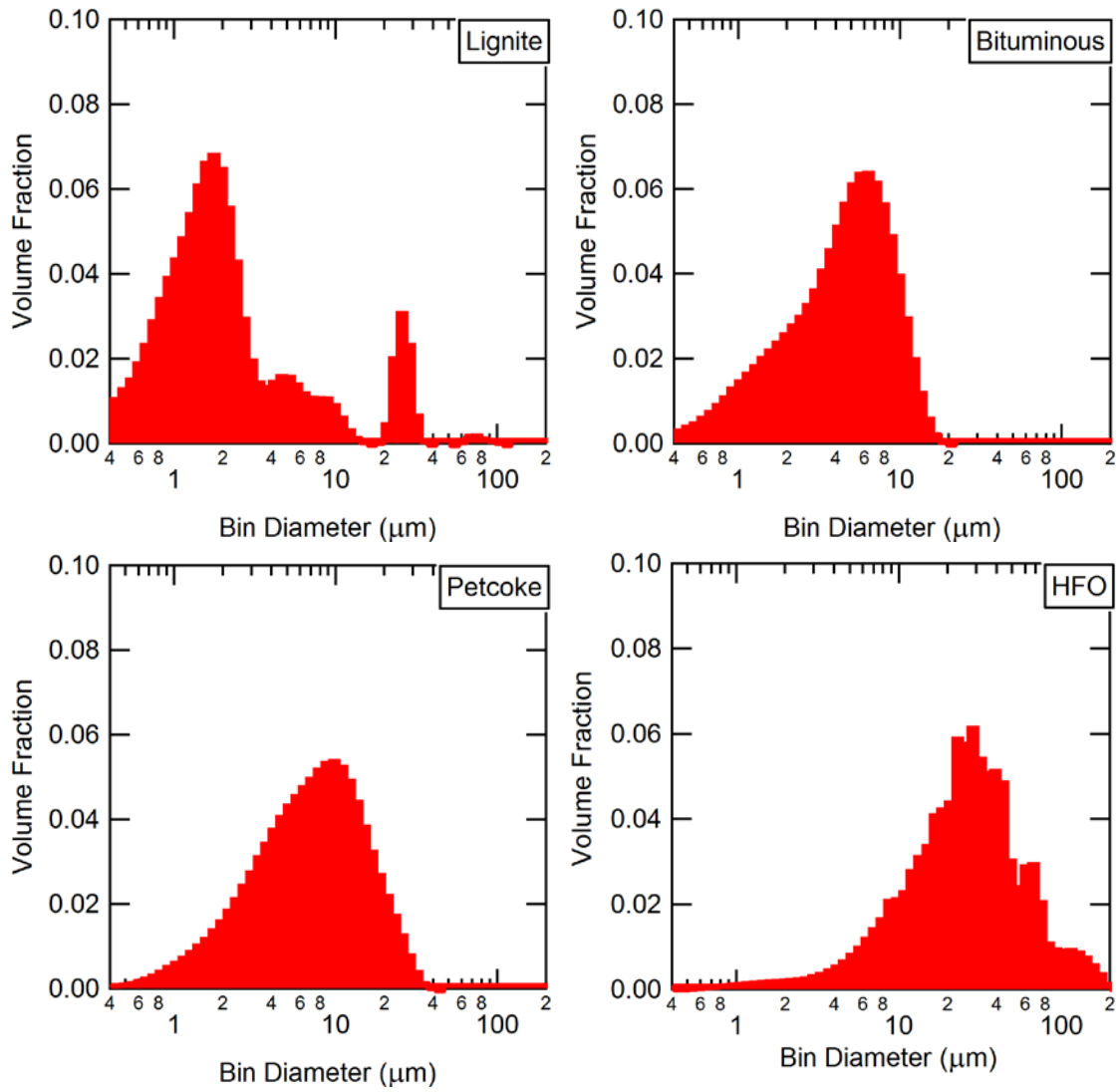


Figure B-2: Particle size distributions for the lignite, bituminous, petcoke and HFO ash samples.

B.2 Deposit Photos



V1



V2



V3



V4



V5

Figure B-3: Photos of the deposits collected during the verification test series.



T1



T2



T3



T4



T5



T6



T7



T8



T9

Figure B-4: Photos of the deposits collected during the transient test series.



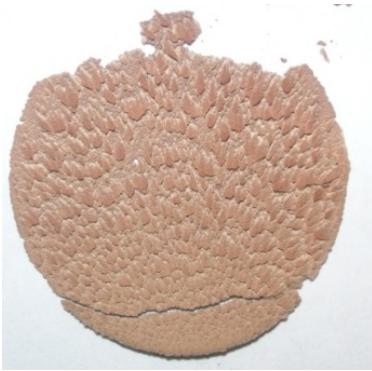
G1



G2



G3



G4



G5



G6



G7



G8



G9

Figure B-5: Photos of the deposits collected during the constant $T_{s,i}$ test series.



S1



S2



S3



S4



S5



S6



S7



S8



S9



S10



S11



S12



S13



S14

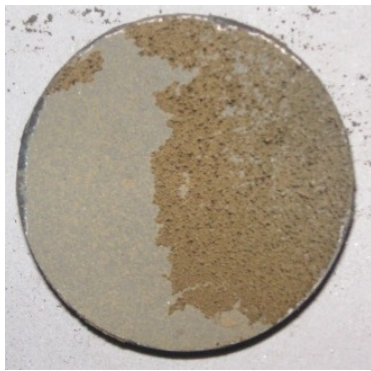


S15

Figure B-6: Photos of the deposits collected during the constant T_g test series.



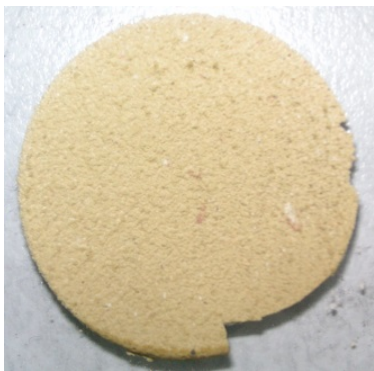
A1



A2



A3



A4



A5



A6



A7

Figure B-7: Photos of the deposits collected during the various coal ash type test series.

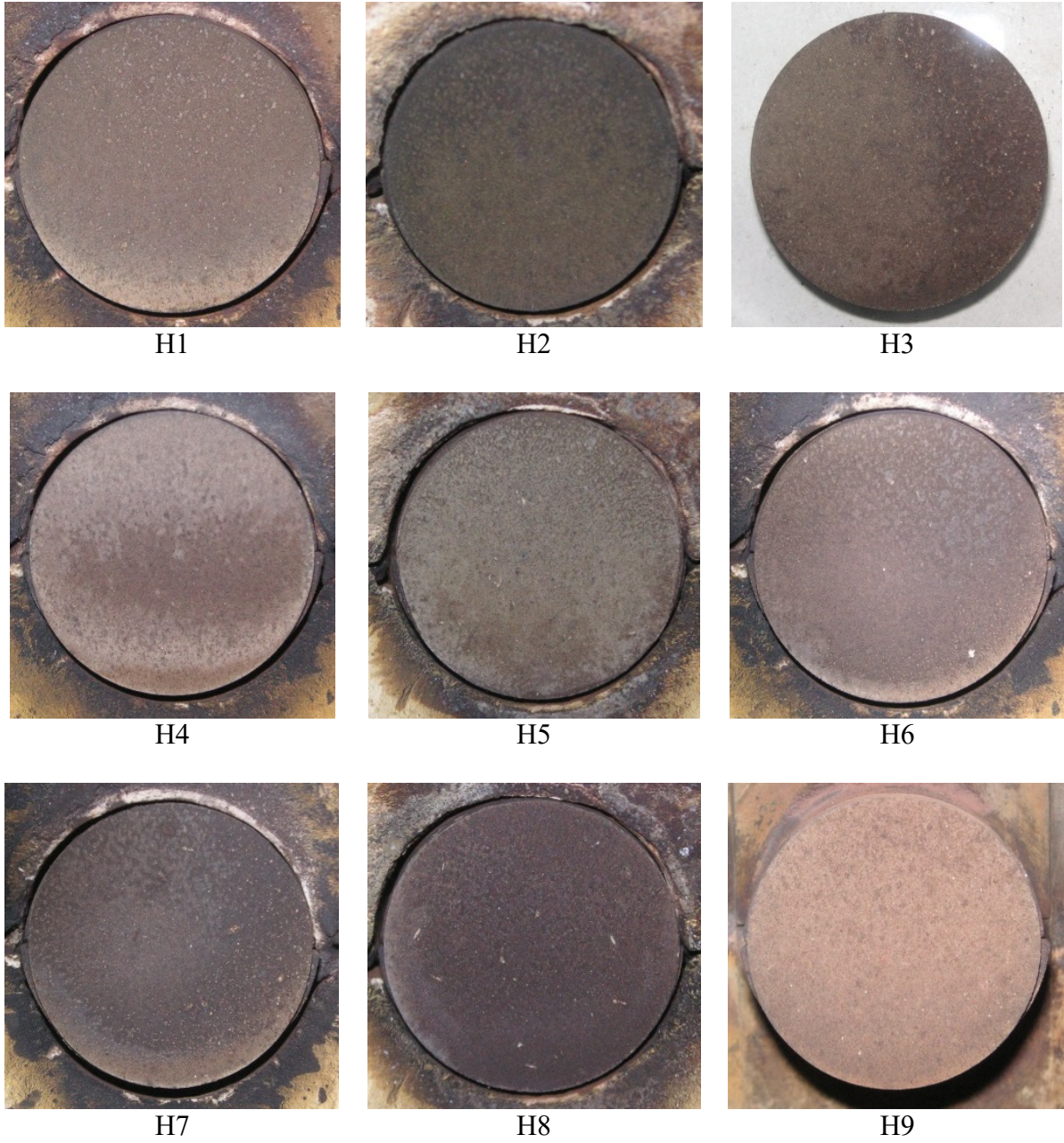


Figure B-8: Photos of the deposits collected during the HFO test series.



F1



F2



F3



F4



F5



F6



F7



F8



F9



F10



F11

Figure B-9: Photos of the deposits collected during the film-cooling test series.

APPENDIX C TEMPERATURE MEASUREMENT

C.1 Thermocouple Radiation Correction

When measuring the gas temperature, the tip of the thermocouple sheath would glow red and was visible to many surroundings of various temperatures (the inside of the equilibration tube, the coupon surface, the faceplate, the radiation shield, and the rest of the lab) meaning that heat would be radiated away from the tip of the thermocouple. It was necessary to correct the measured temperature from the thermocouple for these radiation losses. To do so, it was assumed that the only heat transferred to the thermocouple was from convection from the hot combustion gases (Q_{conv}) and that the only heat transferred away from the thermocouple was radiation from the thermocouple to its surroundings (Q_{rad}). This resulted in the following energy balance

$$Q_{\text{conv}} = Q_{\text{rad}} \quad (\text{C-1})$$

which can be expanded to

$$hA(T_g - T_{th}) = \sum A\varepsilon\sigma F_{\text{bead} \rightarrow i} (T_{th}^4 - T_i^4) \quad (\text{C-2})$$

where h is the convective heat transfer coefficient, A is the surface area of the tip of the thermocouple, T_{th} is the thermocouple temperature, ε is the thermocouple emissivity, σ is the Stefan-Boltzmann constant, $F_{\text{bead} \rightarrow i}$ is the view factor from the tip of the thermocouple to surface i , and T_i is the temperature of surface i . Eq. (C-2) can be rearranged to solve for the true (corrected) T_g .

The view factors were obtained from STAR-CCM+. The same geometry used for the CFD analysis in Chapter 10, but reflected about the symmetry plane to create the full geometry, was used to obtain the view factors. A cylinder (radius = 1.02 mm, length = 1.02 mm), was added to the geometry 1.6 mm above the outlet of the equilibration tube at a 27.9° angle as shown in Figure C-1. The view factor calculator in STAR-CCM+ was then used to calculate the view factor from the cylinder (excluding the lower circular face as this would technically be inside the thermocouple if the whole thermocouple had been included). The view factors are given in Table C-1.

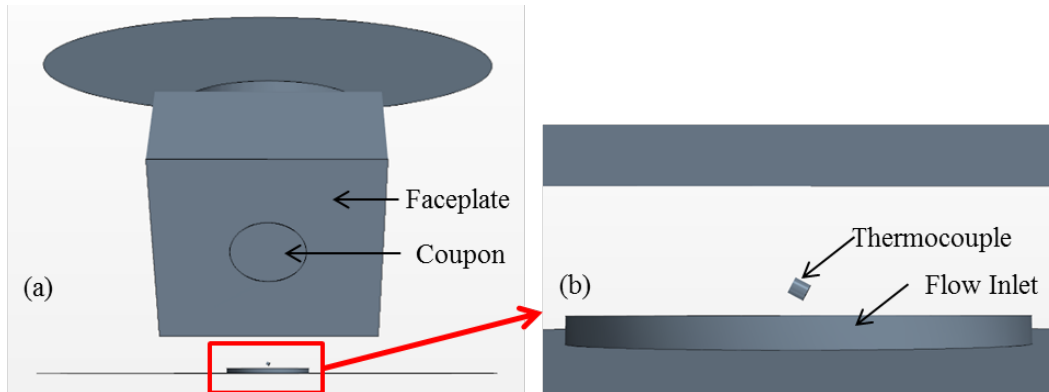


Figure C-1: Placement of the thermocouple tip in the CFD geometry for calculating the radiation view factors. The heat shield is not shown in this view.

Table C-1: Radiation view factors from the thermocouple to the other visible surfaces. The temperature of each surface is also provided

| | Tube | Coupon | Faceplate | Heat Shield | Lab |
|-------------|-------------|---------------|------------------|--------------------|------------|
| View Factor | 0.39194 | 0.027499 | 0.20128 | 0.32269 | 0.056299 |

The temperature of each surface that the thermocouple sees affects the magnitude of the radiation temperature correction. The temperature of the equilibration tube was assumed to be T_g .

The temperature of the lab was assumed to be 26.85°C (300 K). The coupon temperature was taken as the average of the values of T_s reported for each test in Appendix A. However, because radiative heat transfer is dependent on T_i^4 , the average was calculated as

$$T_{s,ave} = \left(\frac{\sum T_s^4}{n} \right)^{\frac{1}{4}} \quad (C-3)$$

where n is the number of T_s values reported for each test in Appendix A.

The temperatures of the faceplate and heatshield were obtained from CFD data generated with T_g ranging from 1250°C to 1400°C and T_s ranging from 1050°C to 1150°C, all in 50°C increments. The area average temperatures were calculated according to Eq. (C-4), where A_i is the area of each cell face, and fit to T_g and T_s according to Eqs. (C-5) and (C-6).

$$T_{ave} = \left(\frac{\sum T_i^4 A_i}{\sum A_i} \right)^{\frac{1}{4}} \quad (C-4)$$

$$T_{faceplate} = 0.420T_g + 0.0246T_{s,i} + 472 \quad (C-5)$$

$$T_{HeatShield} = 0.260 * T_g + 0.0465 * T_{s,i} + 176 \quad (C-6)$$

The tip of the sheathed thermocouple was treated as a cylinder in cross-flow and the convective heat transfer coefficient, h , was calculated according to Eqs. (C-7)-(C-10). The Nusselt number correlation for flow over a cylinder (Eq. (C-8)) was taken from Cengel (1997) and the values of c and m are given in Table C-2.

$$h = \frac{Nu \cdot k_g}{d_p} \quad (C-7)$$

$$Nu = c \cdot Re^m Pr^{\frac{1}{3}} \quad (C-8)$$

$$Pr = \frac{c_{p,g}\mu_g}{k_g} \quad (\text{C-9})$$

$$p = \sum p_i y_i \quad (\text{C-10})$$

Table C-2: Values of c and m for Eq. (C-8), based on the value of Re

| Re | c | m |
|----------------|----------|----------|
| 0.4 – 4 | 0.989 | 0.330 |
| 4 – 40 | 0.911 | 0.385 |
| 40 – 4000 | 0.683 | 0.466 |
| 4000 – 40000 | 0.193 | 0.618 |
| 40000 – 400000 | 0.027 | 0.805 |

The p in Eq. (C-10) refers to either of the fluid properties ($c_{p,g}$, k_g , and μ_g), p_i is the corresponding fluid property for each major chemical component of the exhaust gas (N_2 , O_2 , H_2O , CO_2 , and SO_2) and y_i is the mole fraction of each component. The fluid properties were calculated at the film temperature (average of T_g and T_p) according to correlations available on the Design Institute for Physical Properties (DIPPR®) website (dippr.byu.edu). The mole fractions were calculated with the NASA-Glenn CEA2 chemical equilibrium software (McBride and Gordon, 2004) according to the approximate air, gas, and SO_2 flows required to achieve the target gas temperatures. As many of the values required for the radiation temperature correction depend upon T_g , the calculation is performed iteratively.

The total mass flow through the TADF was used to calculate the gas velocity at the exit of the equilibration tube. The total mass flow for each individual test was not used. Rather, approximated mass flows based on the desired test conditions were used. Of primary concern here was the mass flow of the natural gas. The mass flow of the natural gas was not consistently

recorded from test to test. The mass flow was simply adjusted to achieve the desired temperature. The level on the natural gas rotameter at the beginning of the test was recorded for a small number of tests. These values were used to approximate the natural gas mass flow for each target gas temperature. Table C-3 gives the approximate mass flows of air, natural gas, and SO₂ (only for the HFO tests) for each desired test condition.

Table C-3: Approximate mass flows of air, natural gas and sulfur dioxide for each desired gas temperature

| T_g (°C) | \dot{m}_{air} (kg/s) | \dot{m}_{CH_4} (kg/s) | \dot{m}_{SO_2} (kg/s) |
|----------------------------|-------------------------------|--------------------------------|--------------------------------|
| 1250 | 0.0214 | 0.00105 | - |
| 1288 | 0.0214 | 0.00110 | - |
| 1300 | 0.0214 | 0.00113 | - |
| 1350 | 0.0205 | 0.00128 | - |
| 1400 | 0.0203 | 0.00120 | - |
| <i>With SO₂</i> | | | |
| 1093 | 0.0214 | $9.01 \cdot 10^{-4}$ | $5.46 \cdot 10^{-4}$ |
| 1149 | 0.0214 | $9.76 \cdot 10^{-4}$ | $5.46 \cdot 10^{-4}$ |
| 1204 | 0.0214 | 0.00105 | $5.46 \cdot 10^{-4}$ |

C.2 RGB Camera Calibration

C.2.1 First Calibration (2-Color, Red/Blue)

A two-color pyrometry technique, taken from Svensson et al. (2005) and Lu et al. (2009) had been used by Ai (2009) to measure the surface temperature of the bare metal coupon and the deposit during deposition tests. An RGB camera (SVS285CLCS Sony Exview HAD CCD) was used to obtain images of the coupon and deposit surface. A calibration was performed that allowed the color signals to be converted into temperature and emissivity data. The calibration performed

by Ai (2009) was only performed over a temperature range of 900°C to 1250°C. For the current study, the calibration was redone over a temperature range of 900°C to 1450°C and the process is outlined below.

Each pixel on a CCD sensor in an RGB camera collects light and produces three signals (one red, one green, and one blue) that are represented by digitized integers, the pixel count (P), which can be represented by the following equation

$$P_i = \int_{t_1}^{t_2} S_i \int_{\lambda_1}^{\lambda_2} \varepsilon I_{\lambda} \beta_{\lambda} \tau_{\lambda} d\lambda dt \quad (\text{C-11})$$

where i represents the respective value for each color, ε is the emissivity of the light source, $E_{b\lambda}$ is the spectral radiance given by Planck's law (Eq. (3-8)) and is a function of temperature, β_{λ} is the spectral responsivity of the camera system, τ_{λ} is the transmittance of any additional optics in front of the camera, S_i is a sensitivity constant specific to the camera, t is exposure time, and λ is wavelength. If S_i , β_{λ} , and τ_{λ} are known and if S_i is not a function of exposure time or spectral radiance (the detector is linear), then the pixel count is only a function of emissivity and temperature. At this point, any two signals and their respective equations for P_i can be used to solve for the two unknowns of emissivity and temperature Svensson et al. (2005)

The process of calibrating the RGB camera for two-color pyrometry is essentially the process of determining the values of S_i , β_{λ} , and τ_{λ} . The spectral responsivity, β_{λ} , of the camera had previously been measured and is shown in Figure C-2. No additional optics (filters, windows, etc.) were placed in front of the camera, eliminating τ_{λ} from Eq. (C-11).

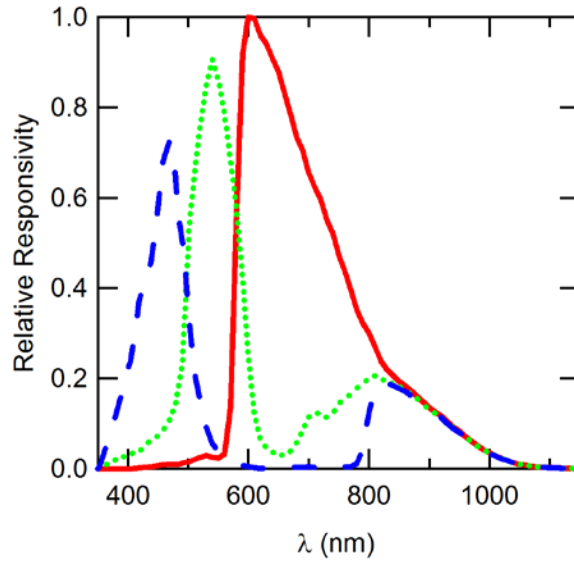


Figure C-2: Spectral responsivity curve for the Sony RGB camera.

To solve for S_i , the camera was placed in front of a Mikron M330 blackbody calibration source with a known effective emissivity of 0.99. The temperature of the blackbody was varied from 900°C to 1450°C in 50°C increments. Five images were taken with the RGB camera at each temperature and the average P was obtained for each color at each temperature. Then, if S_i is not a function of exposure time, Eq. (C-11) can be rearranged to solve for S_i at each temperature as follows

$$s_i = \frac{P_i}{\Delta t \int_{\lambda_1}^{\lambda_2} \epsilon I_\lambda \beta_\lambda \tau_\lambda d\lambda} \quad (C-12)$$

The S_i obtained at each temperature were then averaged together to obtain a single value of S_i . The resulting S_i were then used along with the average P values to calculate the temperature of the blackbody using all three combinations of color equations (red/blue, red/green, green/blue). The final S_i values and temperature calculations are given in Table C-4. It can be seen that the

red/blue combination produced temperatures closest to the set blackbody temperatures, although significant error was observed at temperatures less than 1000°C. When using the camera during deposition experiments, the camera was aimed perpendicular to the coupon and placed so the camera was the same distance from the coupon as it was from the opening of the blackbody during calibration.

Table C-4: Temperatures calculated using the three combinations of color signal, plus the sensitivity constants for each color

| Blackbody T (°C) | Calculated T (°C) | | |
|---------------------|----------------------|----------------------|----------------------|
| | <i>Red/Blue</i> | <i>Red/Green</i> | <i>Green/Blue</i> |
| 900 | 780 | 741 | 860 |
| 950 | 923 | 920 | 930 |
| 1000 | 1006 | 1015 | 988 |
| 1050 | 1056 | 1064 | 1040 |
| 1100 | 1106 | 1115 | 1091 |
| 1150 | 1164 | 1178 | 1141 |
| 1200 | 1214 | 1091 | 1397 |
| 1250 | 1258 | 1274 | 1237 |
| 1300 | 1306 | 1326 | 1280 |
| 1350 | 1347 | 1368 | 1322 |
| 1400 | 1389 | 1411 | 1364 |
| 1450 | 1428 | 1453 | 1403 |
| SSE | 16343 | 41198 | 46073 |
| | S_R | S_B | S_G |
| | 0.275 | 0.288 | 0.287 |

C.2.2 Second Calibration (2-Color, Red/Green)

The camera that was used during the first part of this study was on loan from another research group. It became necessary to return this camera part way through the study. Another camera was made available. This camera, a UNIQ UC-600CL, needed to be calibrated for the

experimental setup and conditions of this study. The calibration was carried out as detailed in Appendix C.2.1 over a temperature range of 1000°C to 1400°C in 50°C increments. In this case, the red/green combination of equations produced better results. There were a few differences between this calibration and the first calibration, which are described below.

Using a new camera necessitated obtaining a new spectral responsivity curve. Lu et al. (2009) showed that the measured responsivity curve for a specific camera and CCD sensor system can vary slightly from the sensor responsivity curve provided by the manufacturer. Attempts were made at measuring the spectral responsivity for the new camera, but these did not produce reliable results. As a result, it was decided to use the spectral responsivity curve found in the user's manual for the UNIQ camera.

There were also problems with obtaining constant S_i values during calibration. As a result, the camera settings (exposure time and aperture) were held constant for all conditions. The S_i still varied with temperature during calibration. To account for this, the S_i were plotted vs the P_i and curve fits were obtained. These curve fits were then used during the temperature calculation process to calculate S_i based on P_i . The S_i data and curve fits are shown in Figure C-3.

The S_i fits were then used to calculate the blackbody temperatures from the RGB images used in calibration. The results are plotted in Figure C-4a. The calculated temperatures deviate slightly from the measured values. The error between the blackbody and calculated temperatures was fit to two linear lines and used to create a temperature correction based on the calculated temperature. This temperature correction was added to the temperature calculation algorithm and the new results are plotted in Figure C-4b. After adding the temperature correction, some additional images were taken of the blackbody and the temperatures calculated from

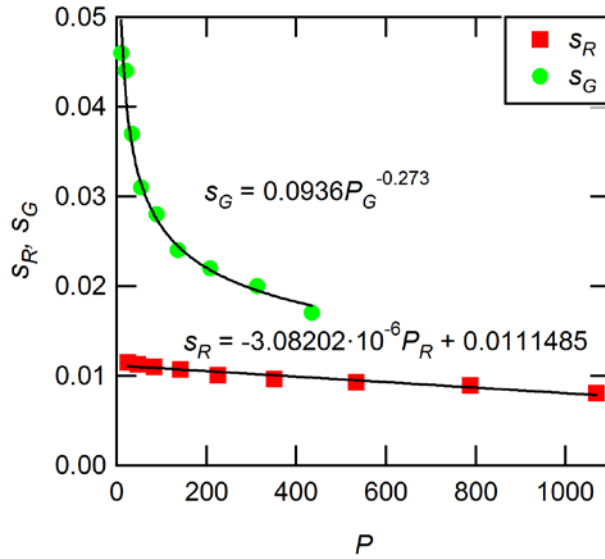


Figure C-3: Spectral sensitivity data obtained for the UNIQ RGB camera.

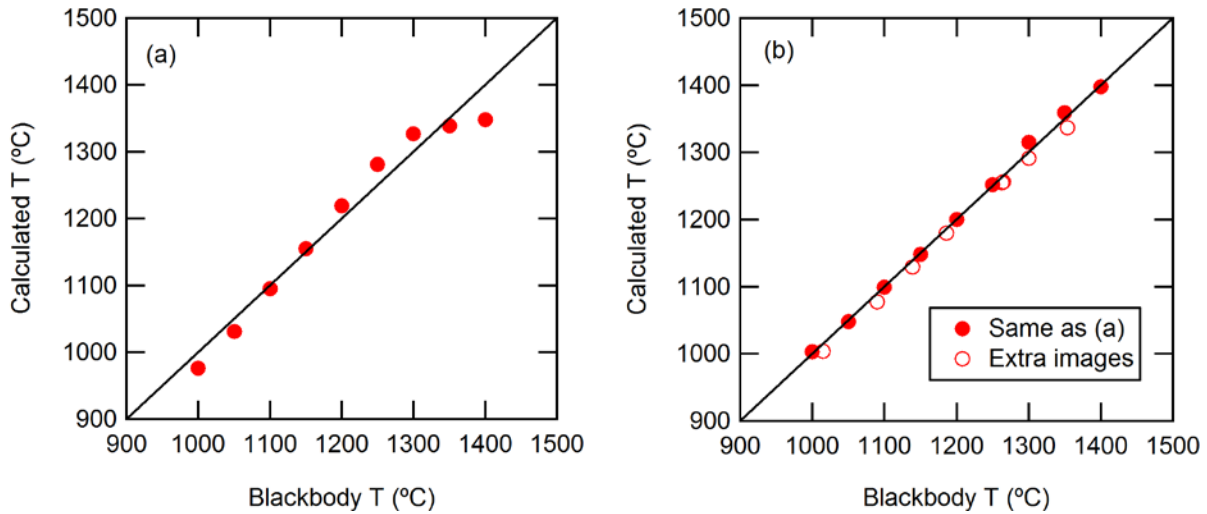


Figure C-4: Calculated vs. blackbody temperatures (a) without the temperature correction and (b) with the temperature correction.

these additional images are included in Figure C-4b as well to show that the temperature correction can be applied generally over the temperature range of the calibration.

C.2.3 Third Calibration (1-Color, Red)

About a year and a half after the second calibration was completed, the CCD sensor on the UNIQ camera malfunctioned. After a performance check, it was found that the previous calibration did not work with the new sensor. A new calibration was performed with images taken over the temperature range 800°C to 1400°C. After several failed attempts to get a good two-color calibration, the decision was made to only use one color equation to calculate the temperature. This required a known emissivity, so an assumed emissivity of 0.9 was used for the bare metal coupon and the emissivity of the ash deposit was calculated according to the method outlined in Section 3.6.

The same manufacturer-provided spectral responsivity curve that was used in the second calibration was used in this third calibration. The manufacturer-provided curve did not include the infrared region. For this calibration, the responsivity data from the infrared region from the curve shown in Figure C-2 was added to the manufacturer curve, even though the two data sets are for two different sensors.

A constant value for S_R did not work well with this calibration either. Rather than fitting S_R to P , a table was constructed from which the appropriate S_R value could be selected based on the exposure time and aperture setting of the camera and is provided in Table C-5.

Table C-5: SR table used for the single-color calibration

| Aperture Setting | Exposure Time (msec) | | | | | | | |
|------------------|----------------------|----------|----------|----------|----------|----------|----------|----------|
| | 0.016 | 0.032 | 0.05 | 0.067 | 0.08 | 0.1 | 0.125 | 0.167 |
| 7 | 0.04716 | 0.087147 | 0.116353 | 0.153887 | 0.187456 | 0.211386 | 0.277368 | 0.324186 |
| 11 | 0.207395 | 0.357573 | 0.466495 | 0.613358 | 0.744562 | 0.796336 | 1.041161 | 1.286246 |
| 14 | 0.431434 | 0.759303 | 1.04882 | 1.376442 | 1.418601 | 1.394714 | 1.810968 | 2.220184 |
| Aperture Setting | Exposure Time (msec) | | | | | | | |
| | 0.2 | 0.25 | 0.5 | 1 | 2 | 4 | 8 | |
| 7 | 0.361785 | 0.447147 | 0.794426 | 1.483499 | 2.554855 | 5.081965 | 9.409796 | |
| 11 | 1.444375 | 1.673426 | 3.162172 | 6.24773 | 11.54953 | 14.38904 | 28.66059 | |
| 14 | 2.628766 | 3.23051 | 6.492185 | 8.7662 | 16.15755 | 32.374 | 64.06857 | |

Another alteration to the surface temperature measurement that was introduced with the single-color calibration was the combination of multiple images to obtain one surface temperature map. As the deposits built up on the coupon, the presence of high temperature peaks and low temperature valleys made it impossible to get a high color signal over the entire deposit surface at a single exposure time without saturating the signal at the high temperature areas. Images were taken at multiple exposure times. Then, when the images were processed, areas that either had a low signal or a saturated signal were omitted from the temperature map. The resulting temperature maps were spliced together to form a complete map. Whenever overlap occurred between the spliced images, the temperature values were averaged together. An example of this process is shown in Figure C-5. Figure C-6 shows the amount of overlap between the separate temperature maps used to obtain the final temperature map shown in Figure C-5, with the different colors indicating the number of temperature maps that overlapped at a particular location.

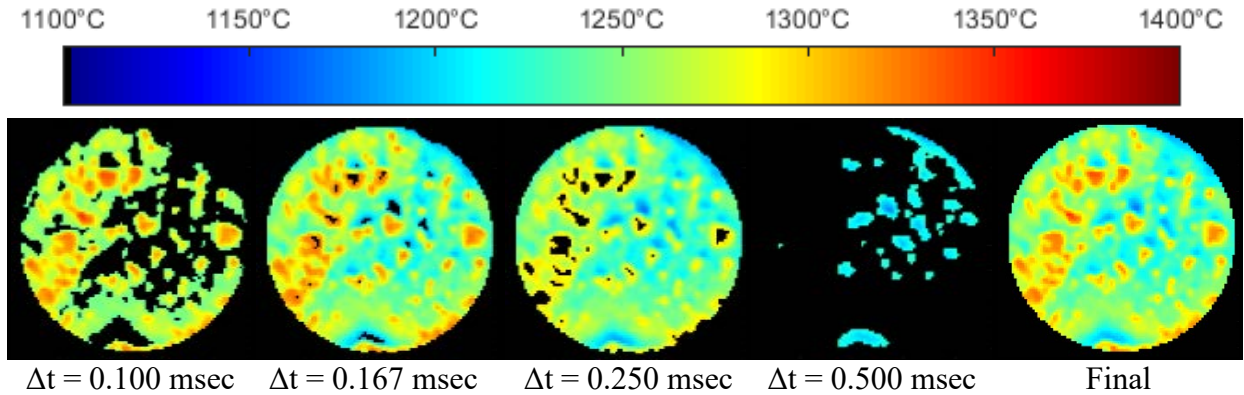


Figure C-5: Example of temperature maps created from images taken at different exposure times and the final temperature map created by splicing/averaging the images together.

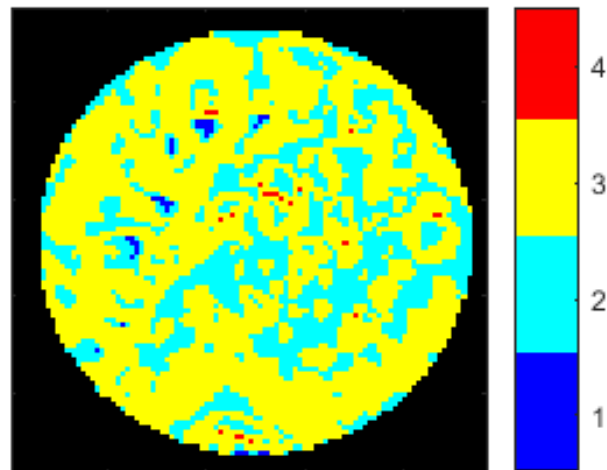


Figure C-6: Map showing how many temperature maps overlapped at each pixel of the final temperature map shown in Figure C-5.

After the calibration with the blackbody was completed, tests were conducted to compare the T_s obtained from the RGB camera using the single-color calibration with the T_s obtained from an Ircon Ultimax UX-10 infrared thermometer. A bare metal coupon was placed in the TADF and the gas temperature was raised to 1400°C. Backside cooling air and water were used to vary the temperature of the coupon surface. The IR thermometer was used to measure the T_s of the coupon,

while the emissivity setting on the thermometer was varied from 0.1 to 1.0 in increments of 0.1. Images were taken with the RGB camera with varying aperture settings and exposure times and the T_s was calculated from the images, using the same range of emissivity. Table C-6 gives the temperatures measured with the IR thermometer and Table C-7 gives the temperatures calculated from the RGB images. Figure C-7 shows the temperature difference between the T_s obtained from the IR thermometer and the RGB images. The temperature difference was fit to a curve, shown in Figure C-7, and applied as a temperature correction to the T_s obtained from the RGB camera when using the single-color calibration.

Table C-6: Coupon temperature measured by an IR thermometer

| Coolant Water Flow (mL/min) | T_s (°C) | | | | | | | | | |
|-----------------------------------|------------------|------|------|------|------|------|------|------|------|------|
| | $\epsilon = 0.1$ | 0.2 | 0.3 | 0.4 | 0.5 | 0.6 | 0.7 | 0.8 | 0.9 | 1.0 |
| 24 | 1065 | 1013 | 976 | 960 | 945 | 930 | 921 | 911 | 900 | 895 |
| 18 | 1220 | 1150 | 1116 | 1093 | 1074 | 1056 | 1043 | 1031 | 1020 | 1015 |
| 12 | 1325 | 1249 | 1204 | 1174 | 1162 | 1134 | 1120 | 1107 | 1095 | 1085 |
| 5.6 | 1375 | 1291 | 1237 | 1208 | 1185 | 1170 | 1155 | 1142 | 1131 | 1123 |
| 0 | 1382 | 1304 | 1259 | 1226 | 1205 | 1185 | 1167 | 1150 | 1143 | 1128 |
| 12 | 1281 | 1200 | 1155 | 1127 | 1107 | 1090 | 1078 | 1069 | 1060 | 1053 |
| 24 | 1167 | 1108 | 1066 | 1047 | 1022 | 1002 | 977 | 963 | 949 | 946 |

Table C-7: Coupon temperature calculated from RGB images

| Coolant Water Flow (mL/min) | Δt (msec) | Aperture Setting | RGB Camera - Red | | | | | | | | | |
|--------------------------------------|----------------------|---------------------|------------------|------|------|------|------|------|------|------|------|------|
| | | | $\epsilon = 0.1$ | 0.2 | 0.3 | 0.4 | 0.5 | 0.6 | 0.7 | 0.8 | 0.9 | 1.0 |
| 24 | 2000 | 14 | 1126 | 1052 | 1012 | 985 | 964 | 948 | 935 | 923 | 913 | 905 |
| 24 | 4000 | 14 | 1123 | 1050 | 1010 | 983 | 962 | 946 | 933 | 922 | 912 | 903 |
| 18 | 250 | 14 | 1275 | 1188 | 1140 | 1108 | 1084 | 1065 | 1049 | 1036 | 1024 | 1014 |
| 18 | 500 | 14 | 1271 | 1184 | 1137 | 1105 | 1081 | 1062 | 1046 | 1033 | 1021 | 1011 |

Table C-7 Continued

| Coolant Water Flow (mL/min) | Δt (msec) | Aperture Setting | RGB Camera - Red | | | | | | | | | |
|--------------------------------------|----------------------|---------------------|---------------------|------|------|------|------|------|------|------|------|------|
| | | | $\varepsilon = 0.1$ | 0.2 | 0.3 | 0.4 | 0.5 | 0.6 | 0.7 | 0.8 | 0.9 | 1.0 |
| 12 | 250 | 14 | 1389 | 1290 | 1237 | 1201 | 1174 | 1153 | 1135 | 1120 | 1107 | 1096 |
| 12 | 1000 | 7 | 1374 | 1276 | 1223 | 1188 | 1161 | 1140 | 1123 | 1108 | 1096 | 1084 |
| 12 | 2000 | 7 | 1407 | 1306 | 1251 | 1215 | 1187 | 1166 | 1148 | 1133 | 1120 | 1108 |
| 5.6 | 500 | 7 | 1429 | 1326 | 1270 | 1233 | 1205 | 1183 | 1164 | 1149 | 1136 | 1124 |
| 5.6 | 1000 | 7 | 1438 | 1334 | 1278 | 1240 | 1212 | 1190 | 1171 | 1156 | 1142 | 1130 |
| 5.6 | 2000 | 7 | 1460 | 1353 | 1296 | 1257 | 1229 | 1206 | 1187 | 1171 | 1157 | 1145 |
| 0 | 500 | 7 | 1451 | 1345 | 1288 | 1250 | 1222 | 1199 | 1180 | 1165 | 1151 | 1139 |
| 0 | 1000 | 7 | 1461 | 1354 | 1296 | 1258 | 1229 | 1206 | 1188 | 1172 | 1158 | 1146 |
| 12 | 250 | 14 | 1339 | 1245 | 1194 | 1160 | 1134 | 1114 | 1097 | 1083 | 1071 | 1060 |
| 12 | 500 | 14 | 1337 | 1243 | 1192 | 1158 | 1132 | 1112 | 1095 | 1081 | 1069 | 1058 |
| 12 | 2000 | 7 | 1335 | 1241 | 1191 | 1157 | 1131 | 1111 | 1094 | 1080 | 1068 | 1057 |
| 12 | 4000 | 7 | 1342 | 1248 | 1197 | 1163 | 1137 | 1117 | 1100 | 1086 | 1073 | 1062 |
| 24 | 500 | 14 | 1222 | 1139 | 1095 | 1064 | 1042 | 1024 | 1009 | 996 | 985 | 975 |
| 24 | 1000 | 14 | 1268 | 1181 | 1133 | 1102 | 1078 | 1059 | 1043 | 1030 | 1019 | 1008 |

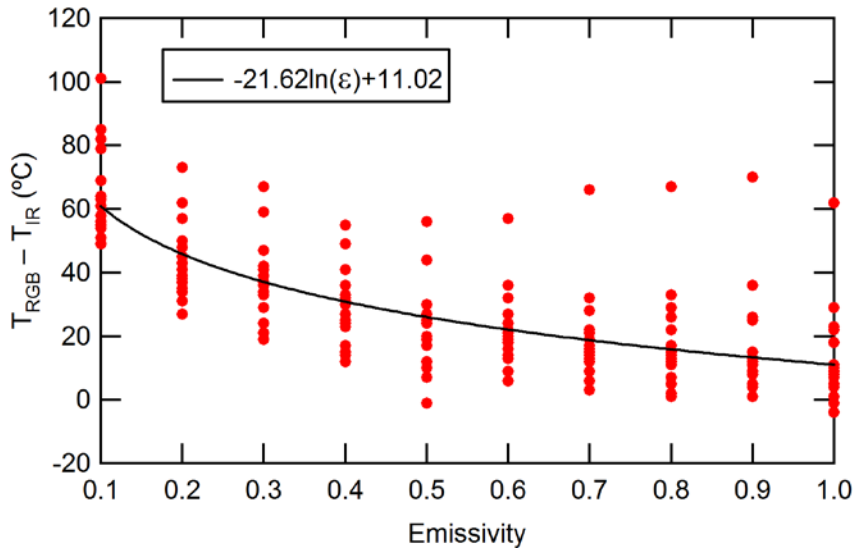


Figure C-7: Difference between the T_s calculated with the RGB camera and measured with the IR camera vs. emissivity.

Figure C-8 presents the temperatures calculated from a sampling of the blackbody images that were used in the calibration plotted against the respective blackbody temperature. The temperatures in Figure C-8 were calculated using an emissivity of 0.99 and have already been reduced by 11°C according to the data presented in Figure C-7. For blackbody temperatures of 1000°C or greater, the calculated temperatures are within $\pm 18^\circ\text{C}$ of the blackbody temperature. At a blackbody temperature of 800°C, the calculated temperature was as low as 753°C.

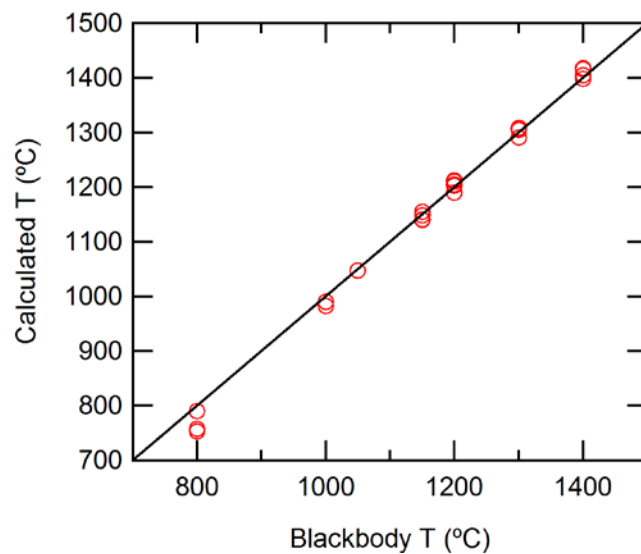


Figure C-8: Calculated vs. blackbody temperatures for the single color calibration, with a temperature correction of -11.24°C applied to the calculated temperatures.

APPENDIX D DEPOSITION MODEL CODES

D.1 Importing Data and Calling Models

```
%PREPARES CFD AND IMPACT DATA AND CALLS THE SPECIFIED STICKING MODEL

clear

%Load cfd and impact data

Test_Data = load('Rho_2800_Data_Poly_Coup.mat');
Distribution = load('JB_1_dist.mat'); %MeanBinDiameter Vol%

Data = Test_Data.Data_Coup;
tau_w = Test_Data.tau_w;
Distribution = Distribution.Distribution;

Total_Particle_count = 750; % The number of particles that were injected in
each particle size case
T_soft = 1497; %Ash softening temperature (K) ***USER SPECIFY***
PR = 0.174; %Poisson ratio ***USER SPECIFY***
Points = load('Points_Transient_new.mat');
Ts = Points.Ts%(i,:);
t = Points.t%(i,:);
ydata = Points.ydata%(:,i);
Tg = Points.Tg%(:,i);

if size(Ts,1)>size(Ts,2)
    Ts = transpose(Ts);
end

cases = [1 1263 985
         2 1263 1047
         3 1294 1045
         4 1294 1136
         5 1310 1060
         6 1310 1110
         7 1362 1058
         8 1362 1174
         9 1411 962
        10 1411 1047
        11 1411 1108
        12 1411 1167
        13 1411 1211];
```

```

for i = 1:size(Ts,2)
    if size(Ts{i},2) > 1
        for j = 1:size(Ts{i},2)-1
            Ts_int{i}(j) = mean([Ts{i}(j) Ts{i}(j+1)]);
            t_int{i}(j) = t{i}(j+1)-t{i}(j);
        end
    else
        Ts_int{i} = Ts;
        t_int{i} = 10;
    end

    for j = 1:size(Ts_int{i},2)
        f = cases(:,2) - Tg(i)';
        f2 = cases(:,3) - Ts_int{i}(j)';

        [c idx] = min(abs(f));
        k = 1;
        STOP = 0;
        while STOP == 0
            if f(idx+k) == f(idx)
                k = k+1;
                STOP = 0;
                if idx+k == size(f,1)
                    STOP = 1;
                    idx2 = idx + k;
                end
            else
                k = k-1;
                STOP = 1;
                idx2 = idx + k;
            end
        end
        [c idx3] = min(abs(f2(idx:idx2)));
        case_idx{i}(j) = cases(idx+idx3-1,1);
    end
end

for i = 1:13
    F{i} =
    scatteredInterpolant(tau_w{i}(:,2),tau_w{i}(:,3),tau_w{i}(:,4),tau_w{i}(:,1))
    ;
end

Coeff = [-1.61,8,2.79,11]; %Coefficients in Young's Modulus equation

fun4 = @(x) (fun_model4(x,Data, tau_w, Total_Particle_count, T_soft, PR, Ts,
t, case_idx, Distribution, F));

cap = fun4(Coeff);

```

```

function f = fun_model4(x, Data, tau_w, Total_Particle_count, T_soft, PR, Ts,
t, case_idx, Distribution, F)

for i = 1:size(case_idx,2)
    cap(i) = StickModel_Bons_17(x, Data, tau_w, Total_Particle_count, T_soft,
PR, Ts{i}, t{i}, case_idx{i}, Distribution, F)*100;
end

f = cap;

```

D.2 Critical Velocity Model

```

function cap = StickModel_CV_18(Coeff, Data, tau_w, Total_Particle_count,
T_soft, PR, Ts, t, case_idx, Distribution, F)

masses = zeros(1,size(Data,2));
for j = 1:size(Data,2)
    i = 1;
    while masses(j) == 0
        if isempty(Data{i,j}) == 1
            i = i + 1;
        else
            masses(j) = Data{i,j}(1,9);
        end
    end
end

if size(Ts,2) > 1
    for i = 1:size(Ts,2)-1
        Ts_int(i) = mean([Ts(i)+273.15 Ts(i+1)+273.15]);
        t_int(i) = t(i+1)-t(i);
    end
else
    Ts_int = Ts+273.15;
    t_int = 10;
end

set = 1;
for k = 1:size(case_idx,2)
    T_s = Ts_int(k);
    Dp2 = [];
    vcrn3 = [];
    vn2 = [];

    for j = 1:size(Data,2)
        if isempty(Data{case_idx(k),j}) == 1
            Imp_Stats{j} = [0 0 0 0 masses(j)*Total_Particle_count];
            Stick_Stats{j} = zeros(1,4);
            Cap_Stats{j} = zeros(1,2);
            EffOut{j} = zeros(1,2);
            Info{j} = zeros(6,1);
        end
    end
end

```

```

StickMass_init{j} = 0;
Detach_mass{j} = 0;
StickTable4{j} = zeros(1,3);
else
S1 = size(Data{case_idx(k), j},1);

PID = Data{case_idx(k), j}(:,1); %Parcel Index

[~,idxPID] = unique(PID);

PID = PID(idxPID,:);
S1 = size(PID,1);
rho_g = Data{case_idx(k), j}(idxPID,2); %Gas density (kg/m^3)
mu_g = Data{case_idx(k), j}(idxPID,3); %Gas dynamic viscosity
(Pa*s)
rho_p = Data{case_idx(k), j}(idxPID,4); %Particle density
(kg/m^3)
D_p = Data{case_idx(k), j}(idxPID,5); %Particle diameter (m)
vp_i = Data{case_idx(k), j}(idxPID,6); %Particle impact velocity
[i] (m/s)
vp_j = Data{case_idx(k), j}(idxPID,7); %Particle impact velocity
[j] (m/s)
vp_k = Data{case_idx(k), j}(idxPID,8); %Particle impact velocity
[k] (m/s)
m_p = Data{case_idx(k), j}(idxPID,9); %Particle mass (kg)
T_p = Data{case_idx(k), j}(idxPID,10); %Particle temperature (K)
X_p = Data{case_idx(k), j}(idxPID,11); %Particle impact location
[x] (m)
Y_p = Data{case_idx(k), j}(idxPID,12); %Particle impact location
[y] (m)
Z_p = Data{case_idx(k), j}(idxPID,13); %Particle impact location
[z] (m)
T_g = Data{case_idx(k), j}(idxPID,14); %Gas temperature (K)

Total_Particle_mass = Total_Particle_count*m_p(1);

vp_ni = (vp_i*(1/sqrt(2))+vp_j*(1/sqrt(2))+vp_k*(0))*(1/sqrt(2));
vp_nj = (vp_i*(1/sqrt(2))+vp_j*(1/sqrt(2))+vp_k*(0))*(1/sqrt(2));
vp_nk = (vp_i*(1/sqrt(2))+vp_j*(1/sqrt(2))+vp_k*(0))*(0);

vp_n = sqrt(vp_ni.^2+vp_nj.^2+vp_nk.^2);

vp_ti = vp_i-vp_ni;
vp_tj = vp_j-vp_nj;
vp_tk = vp_k-vp_nk;

vp_t = sqrt(vp_ti.^2+vp_tj.^2+vp_tk.^2);

%Sticking Model
%Young's modulus of the particle (Pa)
for i = 1:S1
E_p(i,1) =
Coeff(1)*(10^Coeff(2))*exp((Coeff(3)*10^Coeff(4))*T_p(i)); %Exponential E
%
E_p(i,1) =
Coeff(1)*(10^Coeff(2))*T_p(i)+Coeff(3)*(10^Coeff(4)); %Linear E

```

```

%           E_p(i,1) = Coeff(1)*10^Coeff(2); %Constant E
if E_p(i,1) < 0
    E_p(i,1) = 2000;
end
end

%Young's modulus of the surface (Pa)
E_s =
Coeff(1)*(10^Coeff(2))*exp((Coeff(3)*10^Coeff(4))*T_s); %Exponential E
%           E_s =
Coeff(1)*(10^Coeff(2))*T_s+Coeff(3)*(10^Coeff(4)); %Linear E
%           E_s = Coeff(1)*10^Coeff(2); %Constant E
if E_s < 0
    E_s = 2000;
end

k1 = (1-PR^2)./(pi*E_s);
k2 = (1-PR^2)./(pi*E_p);
gamma = 0.8;
eta = vp_t./vp_n;
Wa = -
(1.25.*rho_p.*pi.^(9/2).*(k1+k2)).^(2/5).*gamma.*(D_p./2).^2.*vp_n.^(4/5);
a_m =
(15./8.*pi.*(k1+k2).*(D_p./2).^2.*(1/2).*m_p.*vp_n.^2).^1/5);
E = 1.5*gamma*(5*(pi^2)*(k1+k2)./(4*rho_p.^(3/2))).^(2/5);

for i = 1:S1
    v_crn(i) = vp_n(i); %setting up variables for iteration
    v_crt(i) = vp_t(i); %setting up variables for iteration
    diff = 1; %setting up variables for iteration

    while diff > 0.001
        %           Wa = 0.039; %Adhesion force, from literature (El-Batsh)
        Wa2(i) = -
(1.25.*rho_p(i).*pi.^(9/2).*(k1+k2(i))).^(2/5).*gamma.*(D_p(i)./2).^2.*v_crn(
i).^(4/5);
        v_cr(i) = ((-
2*Wa2(i).*(1+eta(i)).^2)./m_p(i))./(0.5^2)).^0.5;
        v_crn2(i) = (v_cr(i)^2./(1+eta(i)^2)).^0.5;
        v_crt2(i) = eta(i)*v_crn2(i);
        diff = abs(v_crn - v_crn2(i));
        v_crn(i) = v_crn2(i);
    end
end

for i = 1:S1
    if vp_n(i) <= v_crn(i)
        Stick(i,1) = 1;
    else
        Stick(i,1) = 0;
    end
end

Stick2 = Stick(find(Stick));
PID2 = PID(find(Stick));

```

```

%Detachment Model

tau_w_interp = F{case_idx(k)}(X_p,Y_p,Z_p);

Cu = 1+2*(68E-9)./D_p.*(1.257+0.4*exp(-0.55*D_p./(68E-
9))); %Cunningham correction factor for air
Kc = (4/3)*(k1*pi+k2*pi).^-1;

u_tc =
(Cu.*abs(Wa./(pi.*a_m.^2))./(rho_g.*D_p).*(abs(Wa./(pi.*a_m.^2))./(D_p.*Kc)).
^(1/3)).^0.5;
u_w = (tau_w_interp./rho_g).^0.5;

u_tc2 = u_tc(find(Stick));
u_w2 = u_w(find(Stick));
m_p2 = m_p(find(Stick));

StickMass_init{j} = sum(m_p2);

StickTable = [PID2, Stick2, u_tc2, u_w2, m_p2];

if isempty(StickTable) == 0
    [~,idx] = unique(StickTable(:,1));
    StickTable2 = StickTable(idx,:);
else
    StickTable2 = [0 0 0 0 0];
end
ST = size(StickTable2);

Detach_mass{j} = 0;
if sum(StickTable2) == 0
    Stick3 = 0;
else
    for i = 1:ST(1)
        if StickTable2(i,4) >= StickTable(i,3)
            Stick3(i,1) = 0;
            Detach_mass{j} = Detach_mass{j} + StickTable(i,5);
        else
            Stick3(i,1) = 1;
        end
    end
end

Stick4 = Stick3(find(Stick3));
PID4 = PID2(find(Stick3));
m_p4 = m_p2(find(Stick3));

if isempty(Stick4) == 0
    StickTable4{j} = [PID4, Stick4, m_p4];
else
    StickTable4{j} = [0 0 0];
end

```

```

%Efficiency Calculations
SizeUnique = size(unique(PID));

[~,idxPID] = unique(PID(:,1));
m_p_unique = m_p(idxPID,:);

Imp_num = SizeUnique(1);
Imp_mass = sum(m_p_unique);
Imp_Eff_num = Imp_num/Total_Particle_count;
Imp_Eff_mass = Imp_mass/Total_Particle_mass;

Imp_Stats{j} = [Imp_num Imp_mass Imp_Eff_num Imp_Eff_mass
Total_Particle_mass];

Stick_Eff_num = sum(StickTable4{j}(:,2))/Imp_num;
Stick_Eff_mass = sum(StickTable4{j}(:,3))/Imp_mass;

Stick_Stats{j} = [sum(StickTable4{j}(:,2))
sum(StickTable4{j}(:,3)) Stick_Eff_num Stick_Eff_mass];

Cap_Eff_num = Imp_Eff_num*Stick_Eff_num;
Cap_Eff_mass = Imp_Eff_mass*Stick_Eff_mass;

Cap_Stats{j} = [Cap_Eff_num Cap_Eff_mass];

EffOut{j} = [Imp_Eff_mass Stick_Eff_mass Cap_Eff_mass];

Info{j} = [mean(E_p); E_s; mean(E); Imp_mass;
sum(StickTable4{j}(:,3)); Cap_Eff_mass];

Dp2 = [Dp2; D_p];
vcrn3 = [vcrn3; v_crn'];
vn2 = [vn2; vp_n];

clear E_p E_s Stick Stick3 v_cr v_crn v_crn2 v_crt v_crt2
end
end

FileIndex2 = [1 2 3 4 5 6 7 8 9 10 11 12 13 14 15 16 17 18 19 20 21 22 23
24 25];

SizeTable = [1 0.4 % [FileIndex2 ParticleDiameter]
2 0.6
3 0.8
4 1
5 2
6 3
7 4
8 5
9 6
10 7
11 8
12 9
13 10

```

```

        14 20
        15 30
        16 40
        17 50
        18 60
        19 70
        20 80
        21 90
        22 100
        23 110
        24 120
        25 130];

BinEdges(1) = 0;
for i = 1:size(SizeTable,1)-1
    BinEdges(i+1) = (SizeTable(i,2)+SizeTable(i+1,2))/2;
end
BinEdges(size(SizeTable,1)+1) = 1000;

for i = 1:size(SizeTable,1)
    [indx_i, indx_j] = find(SizeTable(:,1)==FileIndex2(i));
    PartSize(i,1) = SizeTable(indx_i, 2);
    PartSize(i,2) = 0;
    for j = 1:size(Distribution,1)
        if Distribution(j,1) >= BinEdges(i) && Distribution(j,1) <=
BinEdges(i+1)
            PartSize(i,2) = PartSize(i,2) + Distribution(j,2);
        end
    end
end

for i = 1:size(Imp_Stats,2)
    M_tot(i) = Imp_Stats{i}(5);
end

M_percent = M_tot./sum(M_tot);

for i = 1:size(Imp_Stats,2)
    M_tot_new(i) = PartSize(i,2)/M_percent(i)*Imp_Stats{i}(5);
    Imp_mass_new(i) = PartSize(i,2)/M_percent(i)*Imp_Stats{i}(2);
    Stick_mass_new(i) = PartSize(i,2)/M_percent(i)*Stick_Stats{i}(2);
    Detach_mass_new(i) = PartSize(i,2)/M_percent(i)*Detach_mass{i};
    StickMass_init_new(i) = PartSize(i,2)/M_percent(i)*StickMass_init{i};
end

Imp_mass_new_sum(set) = sum(Imp_mass_new);
Stick_mass_new_sum(set) = sum(Stick_mass_new);
Detach_mass_new_sum(set) = sum(Detach_mass_new);
StickMass_init_new_sum(set) = sum(StickMass_init_new);
M_tot_new_sum(set) = sum(M_tot_new);

set = set+1;
end
%Standard time between T_s readings is 10 minutes.

```

```

    %Multiply masses by t/10 before summing to account for shorter
measurement periods (typically at end of test)
    Imp_mass_final = sum(Imp_mass_new_sum.*(t_int/10));
    Stick_mass_final = sum(Stick_mass_new_sum.*(t_int/10));
    Detach_mass_final = sum(Detach_mass_new_sum.*(t_int/10));
    StickMass_init_final = sum(StickMass_init_new_sum.*(t_int/10));
    M_tot_final = sum(M_tot_new_sum.*(t_int/10));

    Imp_eff_mass_final = Imp_mass_final/M_tot_final;
    Stick_eff_mass_final = Stick_mass_final/Imp_mass_final;
    Detach_eff_mass_final = Detach_mass_final/StickMass_init_final;
    Cap_eff_mass_final = Stick_mass_final/M_tot_final;

cap = Cap_eff_mass_final;

```

D.3 Non-Spherical Model

```

function Cap = StickModel_Bons_17(Coeff, Data, tau_w, Total_Particle_count,
T_soft, PR, Ts, t, case_idx, Distribution, F)

```

```

masses = zeros(1,size(Data,2));
for j = 1:size(Data,2)
    i = 1;
    while masses(j) == 0
        if isempty(Data{i,j}) == 1
            i = i + 1;
        else
            masses(j) = Data{i,j}(1,9);
        end
    end
end

if size(Ts,2) > 1
    for i = 1:size(Ts,2)-1
        Ts_int(i) = mean([Ts(i)+273.15 Ts(i+1)+273.15]);
        t_int(i) = t(i+1)-t(i);
    end
else
    Ts_int = Ts+273.15;
    t_int = 10;
end

set = 1;
Ts3 = [];
Tp2 = [];
Dp2 = [];
EEem2 = [];
EEadj2 = [];
Wa2 = [];
Sy2 = [];
Ep2 = [];
Es3 = [];

```

```

for k = 1:size(case_idx,2)
    T_s = Ts_int(k);
    for j = 1:size(Data,2)
        if isempty(Data{case_idx(k),j}) == 1
            Imp_Stats{j} = [0 0 0 0 masses(j)*Total_Particle_count];
            Stick_Stats{j} = zeros(1,4);
            Cap_Stats{j} = zeros(1,2);
            EffOut{j} = zeros(1,2);
            Info{j} = zeros(6,1);
        else
            S1 = size(Data{case_idx(k), j},1);

            PID = Data{case_idx(k), j}(:,1); %Parcel Index
            rho_g = Data{case_idx(k), j}(:,2); %Gas density (kg/m^3)
            mu_g = Data{case_idx(k), j}(:,3); %Gas dynamic viscosity (Pa*s)
            rho_p = Data{case_idx(k), j}(:,4); %Particle density (kg/m^3)
            D_p = Data{case_idx(k), j}(:,5); %Particle diameter (m)
            vp_i = Data{case_idx(k), j}(:,6); %Particle impact velocity [i]
(m/s)
            vp_j = Data{case_idx(k), j}(:,7); %Particle impact velocity [j]
(m/s)
            vp_k = Data{case_idx(k), j}(:,8); %Particle impact velocity [k]
(m/s)

            m_p = Data{case_idx(k), j}(:,9); %Particle mass (kg)
            T_p = Data{case_idx(k), j}(:,10); %Particle temperature (K)
            X_p = Data{case_idx(k), j}(:,11); %Particle impact location [x]
(m)
            Y_p = Data{case_idx(k), j}(:,12); %Particle impact location [y]
(m)
            Z_p = Data{case_idx(k), j}(:,13); %Particle impact location [z]
(m)

            T_g = Data{case_idx(k), j}(:,14); %Gas temperature (K)

            Total_Particle_mass = Total_Particle_count*m_p(1);

            l_p = D_p.*(2/3); %length of non-spherical particle (cylinder)
            A_p = pi.*(D_p./2).^2; %cross-sectional area of non-spherical
particle (cylinder)

            vp_ni = (vp_i*(1/sqrt(2))+vp_j*(1/sqrt(2))+vp_k*(0))*(1/sqrt(2));
            vp_nj = (vp_i*(1/sqrt(2))+vp_j*(1/sqrt(2))+vp_k*(0))*(1/sqrt(2));
            vp_nk = (vp_i*(1/sqrt(2))+vp_j*(1/sqrt(2))+vp_k*(0))*(0);

            vp_n = sqrt(vp_ni.^2+vp_nj.^2+vp_nk.^2);

            vp_ti = vp_i-vp_ni;
            vp_tj = vp_j-vp_nj;
            vp_tk = vp_k-vp_nk;

            vp_t = sqrt(vp_ti.^2+vp_tj.^2+vp_tk.^2);

            for i = 1:S1

```

```

        alpha(i,1) = acos(( [vp_i(i) vp_j(i) vp_k(i)]*[vp_ti(i)
vp_tj(i) vp_tk(i)]')/(norm([vp_i(i) vp_j(i) vp_k(i)])*norm([vp_ti(i) vp_tj(i)
vp_tk(i)])));
        if alpha(i,1) > pi/2
            alpha(i,1) = pi - alpha(i,1);
        end
    end

    %Sticking Model
    %Young's modulus of the particle (Pa)
    for i = 1:S1
    %
        E_p(i,1) =
    Coeff(1)*(10^Coeff(2))*exp((Coeff(3)*10^Coeff(4))*T_p(i)); %Exponential E
        E_p(i,1) =
    Coeff(1)*(10^Coeff(2))*T_p(i)+Coeff(3)*(10^Coeff(4)); %Linear E
    %
        E_p(i,1) = 136*10^9; %Constant E
        if E_p(i,1) < 0
            E_p(i,1) = 2000;
        end
    end

    %Young's modulus of the surface (Pa)
    %
        E_s =
    Coeff(1)*(10^Coeff(2))*exp((Coeff(3)*10^Coeff(4))*T_s); %Exponential E
        E_s = Coeff(1)*(10^Coeff(2))*T_s+Coeff(3)*(10^Coeff(4)); %Linear
    E
    %
        E_s = 136*10^9; %Constant E
        if E_s < 0
            E_s = 2000;
        end

    k1 = (1-PR^2)./(pi*E_s);
    k2 = (1-PR^2)./(pi*E_p);
    Eprime = 1./(k1*pi+k2*pi); %Composite Young's Modulus

    for i = 1:S1
        if T_s > T_p(i)
            T_Sy(i,1) = T_s;
        else
            T_Sy(i,1) = T_p(i);
        end
    end

    Sy = (200 - 0.225.*(T_Sy-1000)).*(10^6); %USER DEFINED %Sy is
that of surface that yields first (most likely particle)

    w_c = Sy.*l_p./Eprime; %particle deformation (critical - point of
transition to plastic deformation)
    EE_c = (Eprime.*A_p./l_p).*(w_c.^2)./2; %Elastic Energy (critical
- point of transition to plastic deformation)
    KE_n1 = 0.5.*m_p.*vp_n.^2; %Normal kinetic energy of particle
impact

    for i=1:S1
        if KE_n1(i) <= EE_c(i)

```

```

        w_m(i,1) =
((16./(3*pi)).*KE_n1(i)./(D_p(i).*Eprime(i))).^0.5;
        EE_m(i,1) = KE_n1(i,1);
        else
            w_m(i,1) = l_p(i)-exp(log(l_p(i)-w_c(i))-(KE_n1(i)-
EE_c(i))./(Sy(i).*A_p(i).*l_p(i))); %maximum particle deformation
            EE_m(i,1) = EE_c(i,1);
        end
    end

v_n2i = (2.*EE_m./m_p).^0.5; %ideal normal rebound velocity

CoR_ni = v_n2i./vp_n; %ideal normal coefficient of restitution

a = 0.1; % As used by Bons. Adjust if justified.
b = 1/7; % As used by Bons. Adjust if justified.
c = 0.5; % As used by Bons. Adjust if justified.
gamma = 0.8; % As used by Bons. Adjust if justified.

A_cont = A_p.*(a+b.*(w_m./w_c).^c);
Wa = A_cont.*gamma.*sin(alpha); %Work of adhesion to overcome
adhesive forces

tau_w_interp = F{case_idx(k)}(X_p,Y_p,Z_p);
u_w = sqrt(tau_w_interp./rho_g);

M_drag =
(rho_g.^3).*(u_w.^4).*D_p.*(l_p.^4)./(8.*mu_g.^2)+(3.*(rho_g.^(5/3)).*(D_p.^(
1/3)).*(u_w.^(8/3)).*(l_p.^(10/3)))./(2.*mu_g.^(2/3));
a_cont = (A_cont./pi).^0.5;
k_spring = Eprime.*A_p./l_p;

Del_Fel = 1.7.*M_drag./a_cont; %Change in elastic force due to
shear
Del_wel = Del_Fel./k_spring; %Change in deflection due to shear
wel = sqrt(2*EE_m./k_spring);
EE_adj = 0.5.*k_spring.*(wel+Del_wel).^2;

EE_real = EE_adj-Wa;

for i = 1:S1
    if EE_real(i) >= 0
        v_2n(i,1) = (2.*EE_real(i)./m_p(i)).^0.5;
    else
        v_2n(i,1) = 0;
    end
end

CoR_n = v_2n./vp_n;

for i = 1:S1
    if v_2n(i) <= 0
        Stick(i,1) = 1;
    end
end

```

```

        else
            Stick(i,1) = 0;
        end
    end

Stick2 = Stick(find(Stick));
PID2 = PID(find(Stick));
m_p2 = m_p(find(Stick));

StickTable = [PID2, Stick2, m_p2];

if isempty(StickTable) == 0
    [~,idx] = unique(StickTable(:,1));
    StickTable2{j} = StickTable(idx,:);
else
    StickTable2{j} = [0 0 0];
end
ST = size(StickTable2{j});

%Efficiency Calculations
SizeUnique = size(unique(PID));

[~,idxPID] = unique(PID(:,1));
m_p_unique = m_p(idxPID,:);

Imp_num = SizeUnique(1);
Imp_mass = sum(m_p_unique);
Imp_Eff_num = Imp_num/Total_Particle_count;
Imp_Eff_mass = Imp_mass/Total_Particle_mass;

Imp_Stats{j} = [Imp_num Imp_mass Imp_Eff_num Imp_Eff_mass
Total_Particle_mass];

Stick_Eff_num = sum(StickTable2{j}(:,2))/Imp_num;
Stick_Eff_mass = sum(StickTable2{j}(:,3))/Imp_mass;

Stick_Stats{j} = [sum(StickTable2{j}(:,2))
sum(StickTable2{j}(:,3)) Stick_Eff_num Stick_Eff_mass];

Cap_Eff_num = Imp_Eff_num*Stick_Eff_num;
Cap_Eff_mass = Imp_Eff_mass*Stick_Eff_mass;

Cap_Stats{j} = [Cap_Eff_num Cap_Eff_mass];

EffOut{j} = [Imp_Eff_mass Stick_Eff_mass Cap_Eff_mass];

Info = [mean(E_p); E_s; mean(Eprime); Imp_mass;
sum(StickTable2{j}(:,3)); Cap_Eff_mass];

Ts2 = ones(size(PID,1),1).*T_s;
Es2 = ones(size(PID,1),1).*E_s;

Ts3 = [Ts3; Ts2];
Tp2 = [Tp2; T_p];

```

```

Dp2 = [Dp2; D_p];
EEm2 = [EEm2; EE_m];
EEadj2 = [EEadj2; EE_adj];
Wa2 = [Wa2; Wa];
Sy2 = [Sy2; Sy];
Ep2 = [Ep2; E_p];
Es3 = [Es3; Es2];

clear alpha E_p E_s Sy w_m EE_m v_2n Stick T_Sy
end
end

FileIndex2 = [1 2 3 4 5 6 7 8 9 10 11 12 13 14 15 16 17 18 19 20 21 22 23
24 25];

SizeTable = [1 0.4 % [FileIndex ParticleDiameter]
2 0.6
3 0.8
4 1
5 2
6 3
7 4
8 5
9 6
10 7
11 8
12 9
13 10
14 20
15 30
16 40
17 50
18 60
19 70
20 80
21 90
22 100
23 110
24 120
25 130];

BinEdges(1) = 0;
for i = 1:size(SizeTable,1)-1
    BinEdges(i+1) = (SizeTable(i,2)+SizeTable(i+1,2))/2;
end
BinEdges(size(SizeTable,1)+1) = 1000;

for i = 1:size(SizeTable,1)
    [indx_i, indx_j] = find(SizeTable(:,1)==FileIndex2(i));
    PartSize(i,1) = SizeTable(indx_i, 2);
    PartSize(i,2) = 0;
    for j = 1:size(Distribution,1)
        if Distribution(j,1) >= BinEdges(i) && Distribution(j,1) <=
BinEdges(i+1)
            PartSize(i,2) = PartSize(i,2) + Distribution(j,2);

```

```

        end
    end
end

for i = 1:size(Imp_Stats,2)
    M_tot(i) = Imp_Stats{i}(5);
end

M_percent = M_tot./sum(M_tot);

for i = 1:size(Imp_Stats,2)
    M_tot_new(i) = PartSize(i,2)/M_percent(i)*Imp_Stats{i}(5);
    Imp_mass_new(i) = PartSize(i,2)/M_percent(i)*Imp_Stats{i}(2);
    Stick_mass_new(i) = PartSize(i,2)/M_percent(i)*Stick_Stats{i}(2);
end

Imp_mass_new_sum(set) = sum(Imp_mass_new);
Stick_mass_new_sum(set) = sum(Stick_mass_new);
M_tot_new_sum(set) = sum(M_tot_new);

set = set+1;
end

Imp_mass_final = sum(Imp_mass_new_sum.*(t_int/10));
Stick_mass_final = sum(Stick_mass_new_sum.*(t_int/10));
M_tot_final = sum(M_tot_new_sum.*(t_int/10));

Imp_eff_mass_final = Imp_mass_final/M_tot_final;
Stick_eff_mass_final = Stick_mass_final/Imp_mass_final;
Cap_eff_mass_final = Stick_mass_final/M_tot_final;

[Dp2 Tp2 Ts3 EEm2 Wa2 Sy2 Ep2 Es3];

Cap = Cap_eff_mass_final;

```